

TIME-LAPSE SEISMIC MONITORING OF SUBSURFACE STRESS DYNAMICS

PROEFSCHRIFT

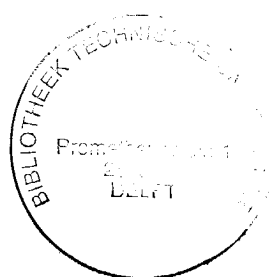
ter verkrijging van de graad van doctor
aan de Technische Universiteit Delft,
op gezag van de Rector Magnificus prof. ir. K.F. Wakker,
voorzitter van het College voor Promoties,
in het openbaar te verdedigen op dinsdag 19 december 2000 om 10.30 uur

door

Meindert Wichert Pieter DILLEN

mijnbouwkundig ingenieur

geboren te Kampen



Dit proefschrift is goedgekeurd door de promotoren:

Prof. dr. ir. J.T. Fokkema

Prof. dr. ir. C.P.A. Wapenaar

Samenstelling promotiecommissie:

Rector Magnificus,

voorzitter

Prof. dr. ir. J.T. Fokkema,

Technische Universiteit Delft, promotor

Prof. dr. ir. C.P.A. Wapenaar,

Technische Universiteit Delft, promotor

Prof. dr. ir. P.M. van den Berg,

Technische Universiteit Delft

Prof. ir. C.P.J.W. van Kruijsdijk,

Technische Universiteit Delft

Prof. dr. ir. S.M. Luthi,

Technische Universiteit Delft

Prof. M. Landrø,

Norwegian U. of Sc. & Techn., Trondheim

Dr. rer. nat. B.C. Lehr,

Shell, Rijswijk

ISBN 90-9014406-4

Copyright © 2000 by M. W. P. Dillen, Section of Applied Geophysics and Petro-
physics, Department of Applied Earth Sciences, Faculty of Civil Engineering and
Geosciences, Delft University of Technology.

cover design by: Corinne van den Bosch

The research reported in this thesis has been financially supported by the Nederlandse Aardolie Maatschappij B.V.

All rights reserved. No parts of this publication may be reproduced, stored in a retrieval system or transmitted, in any form or by any means, electronic, mechanical, photocopying, recording, or otherwise, without the prior written permission of the author.

Stellingen

behorende bij het proefschrift:

“*Time-lapse seismic monitoring of subsurface stress dynamics*”
van Menno Dillen

Stelling 1 De integraalrepresentatie van het tijd-convolutietype, gegeven als

$$\begin{aligned}\check{I}^{\text{conv}}(x_3; \mathbf{x}_T^R, x_3^R, \mathbf{x}_T^S, x_3^S, \omega) \\ = \int_{\mathbf{x}_T \in \mathbb{R}^2} \left[\check{v}_3^{(1)}(\mathbf{x}_T, x_3; \mathbf{x}_T^R, x_3^R, \omega) \check{p}^{(2)}(\mathbf{x}_T, x_3; \mathbf{x}_T^S, x_3^S, \omega) \right. \\ \left. - \check{p}^{(1)}(\mathbf{x}_T, x_3; \mathbf{x}_T^R, x_3^R, \omega) \check{v}_3^{(2)}(\mathbf{x}_T, x_3; \mathbf{x}_T^S, x_3^S, \omega) \right] d\mathbf{x}_T, \quad x_3 > x_3^R, x_3^S,\end{aligned}$$

met in de integrant het totale golfveld van de referentietoestand $\{\check{p}^{(1)}, \check{v}_3^{(1)}\}$ en het totale golfveld van de herhalingstoestand $\{\check{p}^{(2)}, \check{v}_3^{(2)}\}$, kan worden beschouwd als een verschilgolfveld gegenereerd door temporele contrasten gesitueerd onder de interactiediepte x_3 , terwijl temporele contrasten boven de interactiediepte geen bijdrage leveren aan de interactie-integraal.

Hoofdstukken 6 en 10 van dit proefschrift.

Stelling 2 De integraalrepresentatie van het tijd-correlatietype, gegeven als

$$\begin{aligned}\check{I}^{\text{corr}}(x_3; \mathbf{x}_T^R, x_3^R, \mathbf{x}_T^S, x_3^S, \omega) \\ = - \int_{\mathbf{x}_T \in \mathbb{R}^2} \left[\check{v}_3^{\text{sct},(1)*}(\mathbf{x}_T, x_3; \mathbf{x}_T^R, x_3^R, \omega) \check{p}^{\text{sct},(2)}(\mathbf{x}_T, x_3; \mathbf{x}_T^S, x_3^S, \omega) \right. \\ \left. + \check{p}^{\text{sct},(1)*}(\mathbf{x}_T, x_3; \mathbf{x}_T^R, x_3^R, \omega) \check{v}_3^{\text{sct},(2)}(\mathbf{x}_T, x_3; \mathbf{x}_T^S, x_3^S, \omega) \right] d\mathbf{x}_T, \quad x_3 > x_3^R, x_3^S,\end{aligned}$$

met in de integrant het complex geconjugeerde verstrooide golfveld van de referentietoestand $\{\check{p}^{\text{sct},(1)*}, \check{v}_3^{\text{sct},(1)*}\}$ en het verstrooide golfveld van de herhalingstoestand $\{\check{p}^{\text{sct},(2)}, \check{v}_3^{\text{sct},(2)}\}$, kan worden beschouwd, na normalisatie, als het seismisch equivalent van een radarinterferogram (Massonnet en Feigl 1998).

Didier Massonnet en Kurt L. Feigl. *Radar interferometry and its application to changes in the earth's surface.* Reviews of Geophysics, 36:441-500, 1998.

Stelling 3 Door gebruik te maken van time-lapse data-acquisitiemethodes uit de exploratieseismologie, die gekenmerkt worden door een dichte bedekking van bronnen en ontvangers, wat resulteert in een goede 'belichting' van de ondergrond en een goede bemonstering van het gemeten golfveld, wordt het stress-inversieprobleem beter gesteld dan bij aardbevingsseismologische methodes (Chen et al. 1987), waar gewoonlijk slechts enkele bronnen en ontvangers gebruikt worden.

Tian-Chang Chen, David C. Booth en Stuart Crampin. *Shear-wave polarizations near the North Anatolian Fault - III. Observations of temporal changes.* Geophys. J. R. astr. Soc. 91:287-311, 1987.

Stelling 4 De interactie-integralen van het tijd-convolutie type (Stelling 1) en het tijd-correlatie type (Stelling 2) kunnen gebruikt worden voor het bepalen en afbeelden van de verandering van het ondergrondse stressveld. Gebruik makend van deze technieken zou, door bestudering van de pre-seismische stress-evolutie in de omgeving van suspecte breuken, de onzekerheid over de plaats en tijd van aardbevingen verminderd kunnen worden.

Stelling 5 De kosten van het meten aan geofysische verschijnselen moeten worden afgewogen tegen de kosten die onzekerheid omtrent deze verschijnselementen met zich mee brengt. In de meteorologie is deze balans beter gesteld dan in de aardbevingsseismologie.

Stelling 6 De allocatie van financiële middelen aan de Technische Universiteit Delft wordt gemeten naar de productie van wetenschappelijke publicaties. Om aan een bepaalde norm te voldoen kan men twee strategieën volgen: of men produceert een groot aantal publicaties van relatief lage kwaliteit, of men compenseert een klein aantal publicaties door een relatief hoge kwaliteit. Omdat de eerste optie een lager risico inhoudt dan de tweede, terwijl de beloning hetzelfde is, neigt de wetenschapsbeoefening, onderworpen aan dit allocatiemodel, integraal, naar een lagere kwaliteit, alsmede naar overspecialisatie en een daarbij optredende proliferatie van specialistische tijdschriften en wetenschappelijk jargon.

Stelling 7 Vergelijkbaar met bijvoorbeeld 'venture capital' investeringen en het boren van putten in de olie- en gasexploratie-industrie zou de wetenschapsbeoefening als een hoge risico/hoge beloning activiteit beschouwd moeten worden. Men verwacht dan dat onderzoek slechts in enkele gevallen baanbrekende publicaties zal opleveren. Een zodanige activiteit kan gecreëerd worden als de beloning voor een belangrijke publicatie voldoende hoger is dan voor een minder belangrijke publicatie, de tijdsduur waarover gemeten wordt voldoende lang is en de populatie van wetenschappers waarover gemeten wordt voldoende groot is.

Stelling 8 In vergelijking met onderwijs dat de nadruk legt op de specialisaties, waarbij onvoldoende de abstracte samenhang tussen deze specialisaties wordt onderwezen, levert onderwijs, dat gericht is op het ontwikkelen van algemene wetenschappelijke kennis op basis waarvan specialisaties worden bestudeerd, betere academici af.

Menno Dillen. Eigen ervaringen met studenten van de Katholieke Universiteit Leuven en met studenten van de Technische Universiteit Delft.

Dedicated to my brother John Dillen

Contents

1	Introduction	1
1.1	Outline of Part I	3
1.2	Outline of Part II	4
I	Subsurface stress dynamics	7
2	Poroelasticity	9
2.1	Preliminaries on stress	9
2.2	Constitutive equations of poroelasticity	12
2.2.1	Equivalent fluid model	15
2.2.2	Isotropy	17
2.2.3	Darcy's law	19
2.3	Field equations	19
2.4	Stress diffusion	21
3	Failure of rock	23
3.1	Failure mechanism	23
3.2	Microcrack model	24
3.3	Nonlinear stress-strain behaviour	26
3.3.1	Hysteresis	28
3.3.2	Dilatancy	29
3.4	Granular model	29
3.5	Sub-critical crack growth and creep	30
3.6	Failure criteria	30
3.7	Pore fluid pressure changes	32
3.8	Seismicity	33
3.8.1	Microseismicity	35

3.9	Reservoir stress dynamics	36
3.10	Crack dynamics	38
3.11	Stress and wave velocity	39
4	Description of the experimental set-up and samples	43
4.1	The tri-axial pressure machine	43
4.2	Boundary conditions	44
4.3	Transducers	46
4.4	Sandstone samples	47
4.4.1	Colton sandstone	47
4.4.2	Flechtinger sandstone	48
4.4.3	Niederhausen sandstone	56
4.4.4	Bad Dürckheim sandstone	57
4.5	Stress experiments on cylindrical cores	61
4.5.1	Unconfined experiments	61
4.5.2	Confined experiments	73
5	Experimental results	79
5.1	Introduction	79
5.2	Experiments on the Colton sandstone	80
5.2.1	Introduction	80
5.2.2	Experimental design	80
5.2.3	Experimental results	81
5.2.4	Conclusions	84
5.3	Experiments on the Flechtinger sandstone	88
5.3.1	Introduction	88
5.3.2	Quasi-static experiments	88
5.3.3	Dynamic experiments	94
5.3.4	Sensitivity of wave velocities to stress	104
5.3.5	Conclusions	108
5.4	Experiments on the Niederhausen and Bad Dürckheim sandstones	111
5.4.1	Introduction	111
5.4.2	Quasi-static experiments	111
5.4.3	Dynamic experiments	113
5.4.4	Conclusions	134
5.5	Discussion	135

II Time-lapse seismic monitoring	141
6 Time-lapse contrast formalism	143
6.1 Introduction	143
6.2 The acoustic wave field equations	144
6.3 Wave field decomposition	146
6.4 Reciprocity theorem	147
6.5 Interaction integral	149
6.6 Numerical example	151
7 Acoustic reciprocity theorems	159
7.1 Introduction	159
7.2 The acoustic scalar wave field equations	160
7.3 The acoustic vectorial wave field equation	163
7.4 Acoustic states	165
7.5 Bilinear forms	167
7.6 Time-convolution type reciprocity theorem	169
7.7 Sesquilinear forms	172
7.8 Time-correlation type reciprocity theorem	174
8 Wave field decomposition	179
8.1 Introduction	179
8.2 Wave field equations	180
8.3 Integral representations	182
8.3.1 Incident wave field	182
8.3.2 Scattered wave field	185
8.3.3 Total wave field	187
8.4 Dirichlet-to-Neumann operators	190
8.5 Decomposition operator	191
8.6 Reflection and transmission operators	192
8.7 Symmetry of the D-t-N operators	195
8.7.1 Symmetry of $\hat{\mathcal{Y}}^d$	195
8.7.2 Symmetry of $\hat{\mathcal{Y}}^u$	196
8.7.3 Symmetry of $\hat{\mathcal{Y}}$	198
9 Wave field extrapolation	201
9.1 Introduction	201
9.2 Incident wave field	201

9.3	Scattered wave field	205
9.4	Reflection operator	206
9.5	Inverse extrapolation	208
9.6	Fundamental solutions	211
9.7	Longitudinal invariance	213
10	Acoustic time-lapse interaction	217
10.1	Interaction operator	217
10.2	Symplectic eigenvalue decomposition	222
10.3	Time-lapse imaging	228
10.4	Fundamental solutions	232
10.5	Numerical examples of the interaction integral	236
10.6	Longitudinal invariance	239
10.7	Proposed processing scheme	242
10.8	Discussion	248
A	Notations and conventions	249
B	Integral transformations	251
B.1	Laplace transform with respect to time	251
B.1.1	Causal wave fields	251
B.1.2	Anti-causal wave fields	253
B.1.3	Partial differentiation with respect to time	254
B.2	Spatial Fourier transformation	255
B.2.1	Partial differentiation with respect to the spatial coordinates	255
Summary		267
Samenvatting		271
Acknowledgement		275
Curriculum vitae		277

Chapter 1

Introduction

The earth's response to a changing stress field, caused by tectonic forces or by forces induced by human activities, such as hydrocarbon extraction operations, is to equilibrate these forces by differential displacements (deformation) e.g. along faults. Whenever the rigidity along a section of the fault is high enough to resist the stress build-up a seismogenic zone is created, which eventually will relieve the high stress by brittle failure, as one or several subsequent ruptures along the fault zone. These ruptures are high energy surface sources of elastodynamic waves which can cause major damage to man-made structures when travelling as high amplitude earth surface waves. Due to the catastrophic nature of earthquakes it proved impossible to accurately predict these phenomena in space and time. The predictive power of several precursors to earthquakes has been studied. In this thesis the elastodynamic response of seismic waves to an elastostatic change, caused by a changing stress field, is investigated as a possible precursor to earthquakes. The correlation between the occurrence of earthquakes and man-induced fluid injection or extraction operations offers the opportunity to study earthquake mechanisms in a semi-controlled way.

The objective of this thesis is to investigate the possibility of (Part I), and device (Part II), seismic monitoring techniques of the subsurface stress dynamics. Therefore, we consider the action of quasi-static (earthquake precursor mechanisms) and dynamic (seismic wave propagation) loading on rocks. Rocks are heterogeneous porous solids consisting of a solid phase, comprising of aggregates of crystals and grains, cemented at various degrees, and a fluid phase, which occupies the pores or voids of the material. The boundaries be-

tween crystals represent weaknesses in the structure of the rock. Rocks are permeated by thin cracks, which together with the crystal boundaries determine its micro-mechanical behaviour. On a large scale, discontinuities that separate layers of rocks and faults explain the macro-mechanical phenomena, such as earthquakes. Subsurface deformations depend on the mechanical interaction at a range of spatial, but also temporal scales. Therefore, measurements obtained from the small spatial and temporal scales at which experiments are conducted can be indicative for the observed large spatio-temporal scale of in-situ phenomena. As an example, Fabre et al. (1991) extracted core samples from deep sedimentary rocks from the oil and gas Lacq field, located on the northern side of the Pyrenees in France. Several seismic events had occurred at this site, with local magnitude ranging from 1 to 4.2, which are attributed to the extraction of gas. In the laboratory the samples were subjected to tests under in-situ stress conditions, such as uniaxial and triaxial compression tests, hydraulic fracture tests, acoustic activity during loading and the determination of the brittle-ductile transition of some samples, in order to determine mechanical behaviour of the in-situ rock formations. The inferred mechanical parameters were used to prepare a geomechanical model of the field which could predict the occurrence of seismic activity resulting from the depletion of the reservoir. In this thesis small scale physical laboratory experiments are described which attempt to investigate the possibility of large scale seismic monitoring of the changing in-situ stress field. The rock samples used are not from cores, obtained from wells penetrating the reservoir of interest, but from quarries with outcrops which are representative for the small gas reservoirs, consisting of the Rotliegend sandstone formation, as found in the northern part of the Netherlands. Besides using a representative sample from a quarry to infer the subsurface mechanical behaviour we investigate the seismic method. This technique has the advantage that no physical extraction of a small portion of the material is needed. Instead, the entire reservoir region can be probed in a non-destructive way. The disadvantage is that quasi-static (large spatio-temporal scale) mechanical parameters which govern earthquake precursor mechanisms must be inferred from dynamical (small spatio-temporal scale) mechanical parameters in which terms wave propagation theory is described, which makes mutual calibration difficult. Because time-lapse seismic experiments are elaborate and expensive we will investigate the effect of stress on wave propagation at the ultrasonic scale. At this scale we have better control of the mechanical parameters, which make inferences from observations more reliable.

In Part I of this thesis I give an overview of what is published in the literature regarding stress diffusion and deformation processes which govern the mechanics of earthquakes. Thereafter, I present results from ultrasonic triaxial stress experiments conducted as part of this thesis research. My intention with Part I is to integrate the subsurface stress dynamics theory with the seismic monitoring technique developed in Part II. The ultrasonic stress experiments serve as scaled physical model studies which enable to investigate the relationship between elasto-quasi-static theory, which governs crustal deformation, and elastodynamic theory, describing seismic wave propagation. The time-lapse seismic monitoring theory in Part II is derived for acoustic waves, whereas Part I assumes elastic wave theory. The analysis is done for acoustic waves due to time constraints, and in order to keep the calculations within reasonable limits. The elastic wave theory can be derived in an analogous manner involving similar operators.

1.1 Outline of Part I

In Chapter 2 preliminaries on stress are given, before the partial differential equation are derived, as given in the literature, which govern stress diffusion from a mechanical disturbance, such as a man-induced relatively sudden pore pressure change. The effects of pore pressure are included using the effective stress concept.

Chapter 3 describes several deformation and failure mechanism in a more descriptive way, in order to acknowledge, the essential complex and nonlinear mechanics of rocks, not sufficiently described by the partial differential equations in Chapter 2. The linear stress diffusion theory in Chapter 2, as a model, is possibly valid for small stress changes, in a specific stress range, but does not encompass the full stress-strain behaviour. The micro-crack model is explained and used to describe this full stress-strain behaviour. Also, the granular model, describing many sedimentary rocks, is discussed. The effect of fluid extraction and injection is shown, with respect to the Coulomb failure criterion, using Mohr circles. On a large scale the stress dynamics induced by a hydrocarbon reservoir is discussed. Finally, the effect of stress on wave propagation is explained using examples from laboratory experiments described in the literature.

In Chapter 4 a description of the ultrasonic triaxial pressure machine is

given, on which three series of experiments were conducted, involving the Colton sandstone, the Flechtinger sandstone, and the Niederhausen and Bad Dürckheim sandstones, respectively. Each sandstone, in terms of its mineralogy and mechanical parameters, is described. On the latter two sandstones, used for the third series of experiments, more extensive stress experiments on cylindrical cores were conducted.

The three consecutive series of experiments are described in Chapter 5. Both stress-strain experiments, from which quasi-static elastic moduli were calculated, and ultrasonic experiments, from which compressional- and shear wave velocities and dynamic elastic moduli were calculated as function of stress, were conducted.

1.2 Outline of Part II

In Chapter 6 a time-lapse contrast formalism is derived in terms of an interaction integral of the time-convolution type with respect to the transverse direction. The difference wave field generated by the interaction integral, evaluated for a fixed longitudinal coordinate (perpendicular to the transverse plane, representing depth in surface seismic measurements and inter-well distance in cross-well tomography), is causally related to a source formalism in terms of temporal contrasts, located below the interaction depth (surface seismic experiments).

In Chapter 7, the coupled acoustic wave field equations are rewritten to a single first-order differential equation, with respect to the longitudinal direction, in terms of vector-valued wave field quantities. The parameter in this equation is a matrix operator, containing partial derivatives with respect to the transverse coordinates. The reciprocity theorems of the time-convolution and time-correlation types are derived in terms of bilinear and sesquilinear forms, respectively. Symmetry and adjointness of the matrix operators, associated with bilinear and sesquilinear forms, respectively, are implemented, to obtain reciprocity theorems, which are applied in subsequent chapters.

By introducing a background medium and an associated scattering surface, in Chapter 8, a wave field decomposition is introduced of the total wave field vector into incident and scattered wave field vectors. Using the reciprocity theorems, integral representations, in terms of single- and double-layer potentials, are derived for the incident, scattered and total scalar pres-

sure wave fields. The respective integral representations, at the scattering surface, are obtained by applying a limit operation, producing Cauchy principal value integrals. These latter integrals are used to define single- and double-layer potential boundary integral operators. In terms of these singular integral operators, down- and up-going wave field conditions are derived, with respect to the choice of the background medium. Using this terminology, the incident and scattered wave fields, at the scattering surface, are designated down- and up-going wave fields, respectively, representing so-called one-way wave fields. The singular boundary integral operators involved are pseudo-differential operators. From these operators one can construct, at the scattering surface, Dirichlet-to-Neumann (D-t-N) operators for the incident wave field and the scattered wave field, which transform the first component of the wave field vector, the pressure, to the second component, the vertical component of the particle velocity. In terms of these operators a wave field decomposition matrix operator is obtained which splits the total wave field into a down-going incident wave field and an up-going scattered wave field. With respect to the actual medium the D-t-N map of the total wave field is derived. Application of boundary conditions give the reflection and transmission operators in terms of the D-t-N operators. The symmetry of each D-t-N operator is derived, using the reciprocity theorem of the time-convolution type, and applying boundary conditions towards infinity.

The symmetries of the D-t-N operators are used, in Chapter 9, to obtain forward extrapolation operators for the incident and scattered pressure wave fields. In terms of the extrapolation operators and the reflection operator, the scattered wave field, evaluated above the scattering surface, is shown to be equivalent to the WRW-model (Berkhout (1985)). Application of the reciprocity theorem of the time-correlation type yields the inverse extrapolation operator, which extrapolates the up-going scattered wave field downwards. This is an approximate result because the contribution of one surface integral is neglected by assuming an adjointness relation between the D-t-N operators of the down- and up-going wave fields.

Application of the wave field decomposition operators, in Chapter 10, to the total wave field vectors appearing in the time-lapse interaction integral of the time-convolution type, yields an interaction matrix operator with respect to this bilinear form. A subsequent symplectic eigenvalue decomposition of this interaction matrix operator yields a D-t-N operator valid for both time-lapse wave fields. The resulting new parameterization is used to derive an imaging scheme which generalizes the configuration, for which time-lapse

contrasts above the interaction integral's interaction depth are absent, to a configuration which allows for these contrasts to be present above the interaction depth. In this manner non-repeatability and induced time-shifts are taken into account such that a pure amplitude difference reflectivity is obtained. This procedure also allows for an inversion scheme in which these time-shifts are minimized in a top-down recursive way.

Part I

Subsurface stress dynamics



Chapter 2

Poroelasticity

First, preliminaries on stress are given to introduce the notation and summarize quantities as, normal and shear stress, principal stresses, and the associated construction of Mohr circles. Further, introducing the effective stress concept, the linear elastic theory for solids is generalized to include porous solids. In terms of pore pressure, poroelastic moduli and pore fluid flow parameters the partial differential equations are derived which govern stress diffusion in a linear elastic porous solid.

2.1 Preliminaries on stress

Imagine a closed surface A within a continuum body. Consider a small surface element ΔA of A with a unit vector ν normal to ΔA directed outward from A . To counteract the action of the material inside the surface A , the part of the material on the positive side of the normal exerts a force \mathbf{F} on the part which is on the negative side of the normal. We introduce the assumption that as ΔA tends to zero, the ratio $\Delta \mathbf{F}/\Delta A$ tends to a definite limit $d\mathbf{F}/dA$, and that the moment of the forces acting on the surface ΔA , about any point within the area, vanishes in the limit. The limiting vector

$$\mathbf{t} = \frac{d\mathbf{F}}{dA}, \quad (2.1)$$

is called the stress vector or traction (Fung (1965)). The linear relationship of the stress vector \mathbf{t} acting on a surface and the normal ν is given by Cauchy's

formula, which in subscript notation is given by

$$t_j = \tau_{ij} \nu_i, \quad (2.2)$$

in which τ_{ij} represent the components of the stress tensor $\boldsymbol{\tau}$. The stress vector \mathbf{t} can be written as the sum of two components, according to

$$\mathbf{t} = \mathbf{t}^n + \mathbf{t}^s, \quad (2.3)$$

with the normal stress vector \mathbf{t}^n as the component of the stress vector acting in the direction of the normal $\boldsymbol{\nu}$, and with the shear stress vector \mathbf{t}^s , acting parallel to the plane of the surface with the normal $\boldsymbol{\nu}$. The components of the normal stress vector are given by

$$t_i^n = t_k \nu_k \nu_i = \tau_{mk} \nu_m \nu_k \nu_i = \sigma \nu_i, \quad (2.4)$$

in which $\sigma = \tau_{mk} \nu_m \nu_k$ is the magnitude of the normal stress. When the orientation of the surface is such that its normal $\boldsymbol{\nu}$ is in the direction of the stress vector \mathbf{t} , then the stress vector is a called a principal stress vector, while the direction of the normal $\boldsymbol{\nu}$ is called a principal direction. In a principal direction the shear stress vector \mathbf{t}^s vanishes. To determine such orientations we rewrite Eq. (2.3) to

$$t_j^s = \tau_{ij} \nu_i - \tau_{mk} \nu_m \nu_k \nu_j = \tau_{ij} \nu_i - \sigma \nu_j = (\tau_{ij} - \sigma \delta_{ij}) \nu_i = 0, \quad (2.5)$$

which poses an eigenvalue problem of the stress tensor $\boldsymbol{\tau}$. In this last equation δ_{ij} are the components of \mathbf{I} , the symmetrical unit tensor of rank two (Kronecker tensor). Because the stress tensor is symmetric, Eq. (2.5) has three non-vanishing orthonormal eigenvector solutions $\{\boldsymbol{\nu}^{(1)}, \boldsymbol{\nu}^{(2)}, \boldsymbol{\nu}^{(3)}\}$ associated with three real principal stresses $\{\sigma^{(1)}, \sigma^{(2)}, \sigma^{(3)}\}$, if and only if the determinantal equation satisfies

$$\det(\boldsymbol{\tau} - \sigma \mathbf{I}) = 0. \quad (2.6)$$

Hence, if the Cartesian coordinate frame is rotated such that its axes coincide with the principal axes, we have for the matrix of components of $\boldsymbol{\tau}$,

$$\boldsymbol{\tau} = \begin{pmatrix} \sigma^{(1)} & 0 & 0 \\ 0 & \sigma^{(2)} & 0 \\ 0 & 0 & \sigma^{(3)} \end{pmatrix}. \quad (2.7)$$

In this respect, for a general coordinate frame orientation, the diagonal components of $\boldsymbol{\tau}$ are referred to as the normal stress components, whereas the non-diagonal components are called the shear stress components. Eq. (2.6) can be written as the characteristic equation,

$$-\sigma^3 + I^{(1)}\sigma^2 - I^{(2)}\sigma + I^{(3)} = 0, \quad \sigma \in \{\sigma^{(1)}, \sigma^{(2)}, \sigma^{(3)}\}, \quad (2.8)$$

in which $\{I^{(1)}, I^{(2)}, I^{(3)}\}$ are the invariants of the stress tensor $\boldsymbol{\tau}$, given by

$$I^{(1)} = \tau_{ii} = \sigma^{(1)} + \sigma^{(2)} + \sigma^{(3)}, \quad (2.9)$$

$$I^{(2)} = \frac{1}{2} \epsilon_{klm} \epsilon_{pqr} \tau_{pk} \tau_{ql} = \sigma^{(1)}\sigma^{(2)} + \sigma^{(2)}\sigma^{(3)} + \sigma^{(3)}\sigma^{(1)}, \quad (2.10)$$

$$I^{(3)} = \frac{1}{3} \epsilon_{klm} \epsilon_{pqr} \tau_{pk} \tau_{ql} \tau_{rm} = \sigma^{(1)}\sigma^{(2)}\sigma^{(3)}. \quad (2.11)$$

The first invariant, $I^{(1)}$, equals the trace of $\boldsymbol{\tau}$, the second invariant, $I^{(2)}$, equals the sum of sub-determinants produced with the components of the main diagonal of $\boldsymbol{\tau}$, and the third invariant, $I^{(3)}$, is equivalent to the determinant of $\boldsymbol{\tau}$. In Eqs. (2.10) and (2.11) ϵ_{ijk} represent the components of the antisymmetrical unit tensor of rank three, also known as the Levi-Civita tensor, which is defined as

$$\epsilon_{ijk} = \begin{cases} +1 & \text{when } \{i, j, k\} \text{ is an even permutation of } \{1, 2, 3\}, \\ -1 & \text{when } \{i, j, k\} \text{ is an odd permutation of } \{1, 2, 3\}, \end{cases}$$

and

$$\epsilon_{ijk} = 0 \quad \text{when not all subscripts are different.} \quad (2.12)$$

The normal and shear stress magnitudes, σ and τ , for arbitrary orientations can be obtained by a coordinate transformation. One can show (McDonald (1996)) that any pair $\{\sigma, \tau\}$ obeys the following system of equations

$$\begin{aligned} \left(\sigma - \frac{\sigma^{(2)} + \sigma^{(3)}}{2} \right)^2 + \tau^2 &= \left(\frac{\sigma^{(2)} - \sigma^{(3)}}{2} \right)^2 + \nu_1^2 (\sigma^{(1)} - \sigma^{(2)}) (\sigma^{(1)} - \sigma^{(3)}), \\ \left(\sigma - \frac{\sigma^{(1)} + \sigma^{(3)}}{2} \right)^2 + \tau^2 &= \left(\frac{\sigma^{(1)} - \sigma^{(3)}}{2} \right)^2 + \nu_2^2 (\sigma^{(2)} - \sigma^{(1)}) (\sigma^{(2)} - \sigma^{(3)}), \\ \left(\sigma - \frac{\sigma^{(1)} + \sigma^{(2)}}{2} \right)^2 + \tau^2 &= \left(\frac{\sigma^{(1)} - \sigma^{(2)}}{2} \right)^2 + \nu_3^2 (\sigma^{(3)} - \sigma^{(1)}) (\sigma^{(3)} - \sigma^{(2)}). \end{aligned} \quad (2.13)$$

The admissible $\{\sigma, \tau\}$ values determined by these last equations are plotted as so called Mohr circles in Figure (2.1).

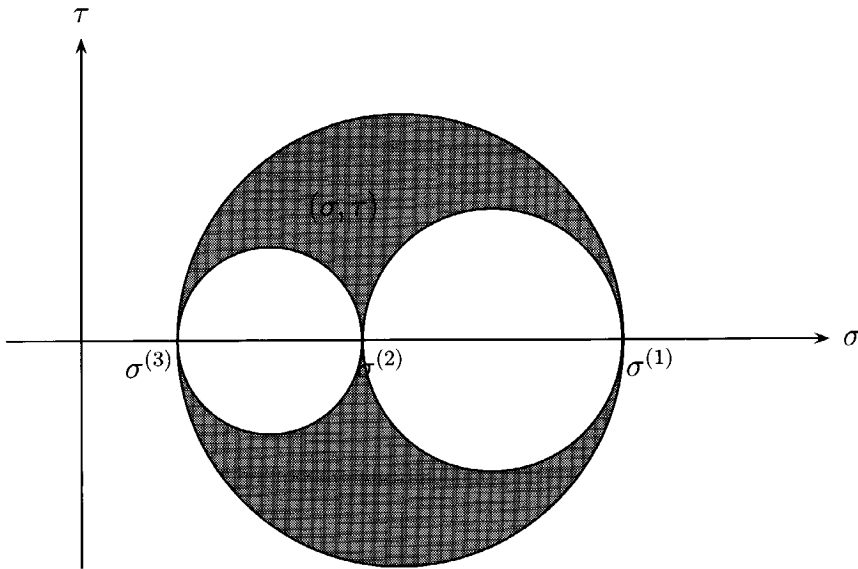


Figure 2.1: *Mohr circles*. The grey area represents admissible magnitudes of normal and shear stress pairs.

2.2 Constitutive equations of poroelasticity

A porous rock can be modelled by a material consisting of a solid phase and a fluid (gas or liquid) phase. Quantities associated with either the solid or fluid phase are represented by ^s and ^f superscripts, respectively. The constitutive equations for a linear elastic fluid-saturated porous rock, according to Biot (1941); Rice and Cleary (1976); Segall (1992); Chen and Nur (1992), are given by

$$\tau_{ij} = C_{ijkl}e_{kl} + \alpha_{ij}P^f, \quad (2.14)$$

and

$$m^f - m_0^f = -\rho^f \alpha_{ij}e_{ij} + \zeta P^f. \quad (2.15)$$

The elasticity relation of Eq. (2.14) is a generalization of Hooke's law to porous solids, by incorporating the effect of the the pore pressure P^f on the strain e , in terms of the dry aggregate stiffness \mathbf{C} and Biot's pore pressure

Symbol	Name	Unit
τ	stress	Pa
P^f	pore fluid pressure	Pa
e	strain (deformation)	
C	stiffness of the dry aggregate	Pa
α	Biot's pore pressure coefficient	
ρ^f	pore fluid volume density of mass	$\text{kg} \cdot \text{m}^{-3}$
m^f	fluid mass per unit volume	$\text{kg} \cdot \text{m}^{-3}$
ζ	scalar quantity	$\text{m}^{-2} \cdot \text{s}^2$

Table 2.1: *poroelastic quantities and their units*

coefficient α . Eq. (2.15) relates the pore pressure to the fluid mass change per unit volume, $m^f - m_0^f$, from some initial state m_0^f , and the strain, in terms of Biot's pore pressure coefficient, pore fluid volume density of mass ρ^f , and a scalar quantity ζ . The poroelastic quantities of Eqs. (2.14) and (2.15) are summarized in Table (2.1). We adopt the convention that compressive stresses are taken positive which is common in rock mechanics. To have positive displacements correspond to positive stresses we take, if \mathbf{u} is the displacement vector of the particle initially at \mathbf{x} , its final position to be

$$\mathbf{x}' = \mathbf{x} - \mathbf{u}, \quad (2.16)$$

(Jaeger and Cook (1979)). The components of the strain tensor are given in terms of differential displacements by

$$e_{ij} = \frac{1}{2} (\partial_j u_i + \partial_i u_j), \quad (2.17)$$

with u_i being a component of the displacement vector. The strain tensor e is, from this last equation, easily seen to be symmetric. For $\Delta m^f = 0$, i.e. undrained conditions, the pore pressure exerts a strain without causing a fluid mass change. In this case the scalar quantity ζ in Eq. (2.15) can be determined as

$$\zeta = \frac{\rho^f \alpha_{ij} e_{ij}}{P^f} \Bigg|_{m^f = m_0^f}. \quad (2.18)$$

Using the symmetry of the stress tensor τ , which follows from the balance of angular momentum, and the symmetry of the strain tensor e , the stiffness

\mathbf{C} has the following symmetry properties

$$C_{ijkl} = C_{jikl} = C_{jilk} = C_{ijlk}. \quad (2.19)$$

The inverse of the stiffness, the compliance \mathbf{S} , is obtained as

$$S_{ijmn}C_{mnkl} = \Delta_{ijkl}^+, \quad (2.20)$$

in which

$$\Delta_{ijkl}^+ = \frac{1}{2} (\delta_{ik}\delta_{jl} + \delta_{il}\delta_{jk}) \quad (2.21)$$

is the symmetrical unit tensor of rank four (de Hoop (1995)[p. 1015]). Using Eq. (2.20), Eq. (2.14) can be rewritten in terms of the compliance tensor,

$$e_{mn} = S_{mni} (\tau_{ij} - \alpha_{ij} P^f), \quad (2.22)$$

in which the symmetry of \mathbf{e} was used. From this last equation it is apparent that within the current model the deformation is completely determined by the effective stress $\boldsymbol{\tau}^{\text{eff}}$,

$$\boldsymbol{\tau}^{\text{eff}} = \boldsymbol{\tau} - \boldsymbol{\alpha} P^f. \quad (2.23)$$

The concept of effective stress was introduced by van Terzaghi (1943) and further developed, amongst others, by Hubbert and Rubey (1959); Nur (1971); Carroll (1979); Chen and Nur (1992). From Eqs. (2.22) and Eq. (2.23) it is apparent that the effective stress is associated with the deformation of the dry aggregate through \mathbf{S} . Hence, the total stress $\boldsymbol{\tau}$ is, according to Eq. (2.23), decomposed into a stress $\boldsymbol{\tau}^{\text{eff}}$, on the solid matrix, and a pressure P^f , on the fluid. The effective stress, and hence the deformation of the porous solid, can be manipulated by changing the total stress or by changing the pore pressure. The effective stress law of Eq. (2.23) enables to simulate deformation with a certain pore pressure (partially drained or undrained condition) by experiments without a pore pressure (drained or dry condition), the latter case being represented by

$$\boldsymbol{\tau}^{\text{eff}} = \boldsymbol{\tau} |_{P^f=0}, \quad (2.24)$$

by taking

$$\boldsymbol{\tau} |_{P^f=0} = \boldsymbol{\tau} - \boldsymbol{\alpha} P^f. \quad (2.25)$$

The triaxial stress experiments described in later chapters were conducted under dry conditions, i.e. no liquid saturant and under atmospheric pore pressure. Using Eq. (2.25), and assuming values for the components of α , these dry experiments can be related to the in-situ reservoir situation, where deformations are induced by pore pressure changes representing hydrocarbon extraction or injection operations.

Biot's coefficient α is derived, by following a superposition procedure in Nur (1971) and Carroll (1979), as

$$\alpha_{ij} = \delta_{ij} - C_{ijkl} S_{klmm}^s, \quad (2.26)$$

in which S^s is the compliance of the solid phase. The deviation of the compliance of the dry aggregate S from S^s is a measure for the porosity. Hence, α depends on the porosity. The components of α vanish for zero porosity because then $S = S^s$. For natural rocks the compliance of the dry aggregate material is often much larger than the compliance of the solid phase. In that case $\alpha \approx 1$. Using Eqs. (2.20) and (2.26), Eq. (2.22) can be rewritten to

$$e_{mn} = S_{mnij} \tau_{ij} - (S_{mnij} - S_{mnij}^s) \delta_{ij} P^f. \quad (2.27)$$

Hence, the larger the difference between the components of S and S^s the larger the component of the deformation induced by the pore pressure.

2.2.1 Equivalent fluid model

Following de Hoop (1995)[p. 343] we consider an equivalent fluid model by taking into account only dilatational deformation. To this end, Eq. (2.27) is contracted yielding

$$e_{mm} = S_{mmij} \tau_{ij} - (\kappa - \kappa^s) P^f, \quad (2.28)$$

in which the dry aggregate compressibility κ and the compressibility for the solid phase κ^s are given by

$$\kappa = S_{mmii} \quad \text{and} \quad \kappa^s = S_{mmii}^s, \quad (2.29)$$

respectively. The invariant e_{mm} is the volumetric strain or compression (negative dilatation). When considering the deformation of a spherical solid to an ellipsoid the volumetric strain is the ratio of the change in area to the original area of the sphere. The volumetric strain e_{mm} is positive when the area

is decreased. The stress tensor is decomposed into an isotropic confinement pressure P and a deviatoric stress according to

$$\tau_{ij} = P\delta_{ij} + (\tau_{ij} - P\delta_{ij}), \quad (2.30)$$

with

$$P = \frac{\tau_{ii}}{3}. \quad (2.31)$$

Multiplying this last equation with S_{mnij} yields the same equation in terms of deformations,

$$S_{mnij}\tau_{ij} = S_{mnij}P\delta_{ij} + S_{mnij}(\tau_{ij} - P\delta_{ij}). \quad (2.32)$$

In accordance with the equivalent fluid model, we neglect the deformation due to the second term in the right-hand side of Eq. (2.32), and approximate Eq. (2.28) by

$$e_{mm} = \kappa P^{\text{eff}}, \quad (2.33)$$

with the effective confining pressure given by

$$P^{\text{eff}} = P - \alpha P^{\text{f}} \quad (2.34)$$

and with the scalar Biot's coefficient α given by,

$$\alpha = 1 - \frac{\kappa^s}{\kappa}. \quad (2.35)$$

This last equation is the expression for α proposed by Geertsma (1957) and Skempton (1960). The effective stress for $\alpha = 1$ is the original form introduced by van Terzaghi (1923). According to Eq. (2.35) $\alpha \approx 1$ if $\kappa \gg \kappa^s$, i.e if the compressibility of the dry aggregate is much larger than the compressibility of the solid phase. This is the case for unconsolidated soils with a high porosity, which settlement under an applied load was the original field of investigation of van Terzaghi (1923). In consolidated rocks with a lower porosity α is smaller than in soils. Assuming dilatational deformation only in Eq. (2.15), we obtain

$$m^{\text{f}} - m_0^{\text{f}} = -\rho^{\text{f}}\alpha\epsilon_{nn} + \zeta P^{\text{f}}, \quad (2.36)$$

with ζ of Eq. (2.18) now given by

$$\zeta = \frac{\rho^f \alpha e_{mm}}{P^f} \Big|_{m^f = m_0^f}, \quad (2.37)$$

which is proportional to the compression (negative dilatation) of the porous solid per unit pore pressure increase under undrained conditions. Eqs. (2.33) and (2.36) are derived by Jaeger and Cook (1979)[p. 211-231] starting from equations with isotropic coefficients. Eq. (2.33) shows that an increase in the confining pressure causes a contraction, whereas a pore pressure increase causes a dilatation of a porous solid. Eq. (2.36) shows how these processes are related to fluid mass changes. A fluid mass increase of $m^f - m_0^f$ causes a dilatation and a pore pressure increase. Consider the following finite difference increments, ΔP^f , ΔP and Δe_{nn} , applied to Eqs. (2.33) and (2.36). Under perfectly constrained conditions there is no change in the volumetric strain, i.e. $\Delta e_{nn} = 0$. Then a fluid mass change of $m^f - m_0^f$ is counterbalanced by a fluid pressure increase of $\Delta P^f = (m^f - m_0^f)/\zeta$, which puts the porous solid under a confining pressure $\Delta P = \alpha \Delta P^f$. If a porous solid is free from constraints, i.e $\Delta P = 0$, then the dilatation equals $-\kappa \alpha \Delta P^f$. Rocks surrounding a reservoir are neither free from constraints nor perfectly constrained. Fluid extraction, for which $m^f < m_0^f$, causes a contraction of a reservoir which under constraining conditions puts it into tension which stresses the surrounding rock (Segall (1992)).

2.2.2 Isotropy

For an isotropic solid we have

$$C_{ijkl} = 3\lambda \Delta_{ijkl}^\delta + 2\mu \Delta_{ijkl}^+, \quad (2.38)$$

and

$$\alpha_{ij} = \alpha \delta_{ij}, \quad (2.39)$$

with the diagonalising unit tensor of rank four given by,

$$\Delta_{ijkl}^\delta = \frac{1}{3} \delta_{ij} \delta_{kl}, \quad (2.40)$$

(de Hoop (1995)[p. 1014]), and the symmetrical unit tensor of rank four Δ^+ given in Eq. (2.21). The scalar Biot's coefficient α is given in Eq. (2.35). The

coefficients λ and μ are known as the Lamé coefficients. Hence, for isotropic symmetry Eqs. (2.14) and (2.15) become

$$2\mu e_{ij} + \lambda e_{nn}\delta_{ij} = \tau_{ij} - \alpha P^f \delta_{ij}, \quad (2.41)$$

$$m^f - m_0^f = -\rho^f \alpha e_{mm} + \zeta P^f, \quad (2.42)$$

respectively. Eliminating the volumetric strain e_{nn} in Eqs. (2.41) and (2.42), by substituting Eq. (2.33), yields

$$2\mu e_{ij} = \tau_{ij} - \frac{3\nu}{1+\nu} P \delta_{ij} - \frac{1-2\nu}{1+\nu} \alpha P^f \delta_{ij}, \quad (2.43)$$

and

$$m^f - m_0^f = -\rho^f \kappa \alpha \left[P - \left(\alpha + \frac{\zeta}{\rho^f \kappa \alpha} \right) P^f \right], \quad (2.44)$$

with

$$\kappa = \left(\lambda + \frac{2}{3} \mu \right)^{-1}. \quad (2.45)$$

In these last calculations we used

$$\lambda = \frac{2\mu\nu}{1-2\nu} \quad \text{and} \quad \kappa = \frac{3(1-2\nu)}{2\mu(1+\nu)}, \quad (2.46)$$

with ν representing Poisson's ratio, defined as the ratio of lateral expansion to longitudinal contraction (see Jaeger and Cook (1979)[p. 110-111]). Introducing Skempton's coefficient B ,

$$B = \left(\alpha + \frac{\zeta}{\rho^f \kappa \alpha} \right)^{-1}, \quad (2.47)$$

Eq (2.44) is rewritten to

$$m^f - m_0^f = -\rho^f \kappa \alpha (P - B^{-1} P^f). \quad (2.48)$$

For undrained conditions Skempton's coefficient is given by

$$B = \frac{P^f}{P} \Big|_{m^f = m_0^f}, \quad (2.49)$$

which is the ratio of the pore pressure to confining pressure, a measure which can be obtained from laboratory experiments.

2.2.3 Darcy's law

The constitutive law which governs pore fluid diffusion is given by Darcy's law,

$$\Phi_i^f + \frac{k\rho^f}{\eta} \partial_i P^f = 0, \quad (2.50)$$

in which the fluid mass flow density Φ^f is related to the gradient of the pore fluid pressure. The constitutive parameters k and η are the permeability and the fluid viscosity, respectively. The quantities describing fluid flow are summarized in Table (2.2).

Symbol	Name	Unit
Φ^f	fluid mass flow density	$\text{kg} \cdot \text{m}^{-2} \cdot \text{s}^{-1}$
k	permeability	m^2
η	fluid viscosity	$\text{Pa} \cdot \text{s}$

Table 2.2: *Fluid flow quantities and their units*

2.3 Field equations

For static phenomena the stress tensor obeys the following equilibrium equation,

$$\partial_j \tau_{ij} = 0. \quad (2.51)$$

The symmetric strain tensor ϵ has in general six independent components. They are however defined, see Eq. (2.17), through the displacement vector which has at most three independent components. To ensure the existence of a single-valued continuous displacement field corresponding to a given strain tensor we need the so called compatibility conditions for the strain (Maugin (1993)[p. 54-57]), given by

$$\epsilon_{ijk} \epsilon_{lmn} \partial_j \partial_m e_{kn} = 0, \quad (2.52)$$

with the Levi-Civita tensor ϵ given in (2.12). In the following derivation we assume that the porous medium is isotropic and homogeneous. Taking twice

the gradient of Eq. (2.41) and substituting the equilibrium equation of Eq. (2.51), yields

$$2\mu\partial_i\partial_j e_{ij} + \lambda\partial_q\partial_q e_{nn} = -\alpha\partial_k\partial_k P^f. \quad (2.53)$$

Contraction of the compatibility conditions of Eq. (2.52) leads to

$$\partial_i\partial_j e_{ij} = \partial_q\partial_q e_{nn}, \quad (2.54)$$

in which we used

$$\epsilon_{ijk}\epsilon_{imn} = 2\Delta_{jkmn}^- \quad \text{and} \quad \Delta_{jkmn}^- = \frac{1}{2}(\delta_{jm}\delta_{kn} - \delta_{jn}\delta_{km}), \quad (2.55)$$

with Δ^- representing the antisymmetrical unit tensor of rank four (de Hoop (1995)[p. 1016-1017]). Substituting Eq. (2.54) into Eq. (2.53) yields the field equation for the volumetric strain,

$$\partial_q\partial_q e_{nn} = -\frac{1}{\lambda + 2\mu}\alpha\partial_k\partial_k P^f. \quad (2.56)$$

For vanishing pore pressure this last equation shows that the volumetric strain obeys Laplace's equation $\partial_q\partial_q e_{nn} = 0$, (Jaeger and Cook (1979)[p. 118]). Subsequently, taking twice the gradient and multiplying twice with the Levi-Civita tensor ϵ , the constitutive equation (2.43) is rewritten, substituting the equilibrium equation (2.51), as

$$\begin{aligned} \epsilon_{pki}\epsilon_{qlj}\partial_k\partial_l\tau_{ij} - \frac{3\nu}{1+\nu}(\delta_{pq}\partial_m\partial_m - \partial_q\partial_p)P \\ - \frac{1-2\nu}{1+\nu}\alpha(\delta_{pq}\partial_r\partial_r - \partial_q\partial_p)P^f = 0. \end{aligned} \quad (2.57)$$

In this last equation we used

$$\epsilon_{pki}\epsilon_{qli} = 2\Delta_{pkql}^-, \quad (2.58)$$

with Δ^- given in Eq. (2.55). Contracting Eq. (2.57), using the equilibrium equation of Eq. (2.51), yields the field equation for the confining pressure,

$$\partial_q\partial_q P = \frac{2(1-2\nu)}{3(1-\nu)}\alpha\partial_k\partial_k P^f. \quad (2.59)$$

2.4 Stress diffusion

The conservation of mass is expressed by

$$\partial_t m^f + \partial_k \Phi_k^f = 0, \quad (2.60)$$

which is also known as the continuity equation of mass flow. Using the constitutive Eqs. (2.44) and (2.50) this last equation is rewritten to

$$\frac{k}{\eta} \partial_i \partial_i P^f + \frac{3\alpha(1-2\nu)}{2\mu(1+\nu)} \partial_t \left[P - \alpha P^f - \frac{2\mu(1+\nu)}{3\rho^f \alpha (1-2\nu)} \zeta P^f \right] = 0. \quad (2.61)$$

Using Eq. (2.59) we obtain

$$\begin{aligned} \partial_q \partial_q \left[P - \alpha P^f - \frac{2\mu(1+\nu)}{3\rho^f \alpha (1-2\nu)} \zeta P^f \right] \\ = -\frac{(1+\nu) [(1-2\nu) \rho^f \alpha^2 + 2\mu(1-\nu) \zeta]}{3(1-\nu)(1-2\nu) \rho^f \alpha} \partial_k \partial_k P^f. \end{aligned} \quad (2.62)$$

Substituting this last equation into Eq. (2.61) we arrive, in terms of Skempton's coefficient B of Eq. (2.47), at

$$\partial_q \partial_q \left[P - \frac{1}{B} P^f \right] - \frac{1}{C} \partial_t \left[P - \frac{1}{B} P^f \right] = 0, \quad (2.63)$$

with the coefficient of consolidation or diffusivity given by

$$C = \frac{k}{\eta} \left[\frac{2\mu(1-\nu)}{\alpha^2(1-2\nu)} + \frac{\rho^f}{\zeta} \right]. \quad (2.64)$$

Eq. (2.63) is the equation derived by Rice and Cleary (1976)). Using the effective stress law of Eq. (2.34), Eq. (2.63) can also, in terms of the effective confining pressure, be written as,

$$\partial_q \partial_q \left[P^{\text{eff}} - \frac{\zeta}{\rho^f \alpha \kappa} P^f \right] - \frac{1}{C} \partial_t \left[P^{\text{eff}} - \frac{\zeta}{\rho^f \alpha \kappa} P^f \right] = 0. \quad (2.65)$$

The diffusivity C has the units of meters squared per second. Hence, the diffusion equation (2.63) can be interpreted as the area expansion of the field $P - B^{-1}P^f$. According to Eq. (2.64) the diffusivity is proportional to the permeability k , and inverse proportional to the fluid viscosity η . Hence, e.g.,

one expects a fast expansion of the stress field $P - B^{-1}P^f$ in case of a high permeable gas saturated rock, as compared to more viscous hydrocarbons saturating low permeable rock. The diffusivity in soils, for which α is close to one (see Eq. (2.35)), is smaller than in consolidated deep reservoir rock, with α smaller than in soils. The porosity dependence of the diffusivity is included through the parameters α of Eq. (2.35) and ζ of Eq. (2.37). A higher porosity leads to a higher compressibility of the dry aggregate, which yields a higher value for α . One expects that a higher porosity also yields a lower value for ρ^f/ζ , which is the pore pressure increase per unit compression under undrained conditions. Hence, through α and ζ , an increase in the porosity gives a decrease in the diffusivity.

Chapter 3

Failure of rock

3.1 Failure mechanism

In the previous chapter the equations have been presented that govern the diffusion of the confining pressure, which equals the trace of the stress tensor divided by three according to Eq. (2.31), and the pore fluid pressure. A stress diffusion process is initiated by a mechanical disturbance which acts as a source function. This source function is a function of time and space, representing e.g. the change of the pore pressure at the well during reservoir production or injection operations. The mechanical stress inequilibrium thus imposed is dissipated away from the well, according to Eq. (2.63), by a dynamic stress field which equilibrates for long time. The source function may also be the stress field associated with a dislocation, which is a spatial discontinuity in the displacement function, equivalent to, according to Eq. (2.17), a singularity in the deformation field. The discontinuous displacement is usually shear but can sometimes be normal depending on the stress conditions. A spatial array of such dislocations, simulates, as a function of time, the propagation of slip along a fault as in aseismic earth faulting (Rice and Cleary (1976)). The poroelastic diffusion equation (2.63) generates the evolution of the confining pressure and pore pressure. Using the field equation of Eq. (2.56) instead of Eq. (2.59) one could also derive a diffusion equation in terms of strain and pore pressure, from which the evolution of deformation can be calculated. To establish if slip (singular strain) will occur within the linear elastic theory a failure criterion is needed. As the state of the material approaches failure, depending on the type of material, several modes of

failure can occur. Brittle failure means a complete loss of cohesion across a plane such that the ability to resist load decreases with increasing deformation. Beyond the failure surface in stress space ductile deformation (fully ductile region according to Jaeger and Cook (1979)) may occur, during which increasing deformation does not impair load resistance. Experiments showing brittle failure and post-failure ductile deformation are shown in Section (4.5), for the Niederhausen and Bad Dürckheim sandstones, the sandstones being described in Section (4.4). Rocks show a transformation from brittle to ductile behaviour upon failure when the confining pressure and/or temperature increases. This behaviour, for several confining pressures, is also shown in Section (4.5). Ductile behaviour is observed in limestone and halite, and other sedimentary rocks, and marble (Jaeger and Cook (1979)). Such materials deform elastically up to a certain yield stress, beyond which no greater stress can be sustained. The super-yield stress flow behaviour is called plastic deformation. The total behaviour is described by elastoplastic theory. The onset of plastic behaviour is determined by a yield criterion which is a relation between the principal stresses. The presence of e.g. relatively ductile rock salt (containing halite), in a reservoir environment of more brittle sandstones, is quite significant for the macro-mechanical elastic behaviour of the reservoir, as is shown with numerical elastoplastic simulations in Nagelhout and Roest (1997); Roest et al. (1999); Roest and Mulders (2000).

3.2 Microcrack model

The dominant mechanism of brittle failure is the nucleation, growth, interaction and coalescence of cracks called microcracks on the laboratory scale and joints and faults on the reservoir scale. The extension of existing microcracks creates new crack surface area and consequently dissipates strain energy. The onset of this process indicates the development of zones of irreversible deformation and may be viewed as a precursor to failure. Ultimate failure is described by crack coalescence on a macroscopic scale into planar shear bands, inclined with respect to the principal stresses (Ouyang and Elsworth (1991)).

Because of the poly-crystalline nature of rocks crack nucleation and growth will occur at regions of high stress concentrations such as the tips of preexisting cracks, pores or contacts between adjacent grains. Therefore the failure stress at those regions in an inhomogeneous rock is smaller than the failure

stress of the single crystal constituents. Another effect of the inhomogeneity of rocks is that failure is initiated over a stress interval rather than a singular stress value, represented by a locus on the failure surface in the principal stress space. By assigning effective failure parameters by averaging the microscopic behaviour one can construct a failure surface in principal stress space which predicts the onset of failure in rocks. A particular stress state, uniquely determined by the orientation and magnitude of the principal stresses, causes, through the process of crack nucleation and growth, a certain orientation and distribution of cracks. By inference, the orientation and distribution of cracks is diagnostic for the orientation of the contemporary and historical principal stresses. Hence, determining the directionality of crack distributions, identified with the anisotropy of the elastic parameters (Crampin (1982)), one can infer a principal stress state, which could produce this geometry. In this respect stress-induced anisotropy is an important concept in stress inference theory.

The effect that a crack-permeated rock has a smaller compressibility than the same rock without cracks was shown by Walsh (1965a) using a simple theoretical model. The compressibility is defined, according to Eq. (2.33), as the fractional volume decrease (equals the volumetric strain e_{mm}) per unit of confining pressure P^{eff} . Walsh (1965a) equates the difference of the effective compressibility of the cracked material, κ , and the compressibility of the same material without cracks, κ^{hp} , to the rate of the decrease of the porosity per unit of confining pressure, according to

$$\kappa = \kappa^{\text{hp}} - \frac{d\phi^{\text{cr}}}{dP^{\text{eff}}}. \quad (3.1)$$

The porosity ϕ^{cr} in this last equation refers to the voids in a porous solid which are susceptible to closure under pressure, making up the so called compliant porosity or crack porosity. The superscript in the compressibility of the rock without cracks is designated $^{\text{hp}}$, because this value can be obtained by applying a sufficient high confining pressure to a cracked rock, such that the compliant cracks get closed. In sedimentary rock like sandstone the compliant porosity ϕ^{cr} is only a small fraction of the total porosity ϕ , whereas in volcanic rocks such as granite the porosity consists often entirely of compliant cracks. Assuming low crack density (no crack interaction because each crack is considered in an infinite field) and penny-shaped cracks, Walsh calculates

for the cracked compressibility,

$$\kappa = \kappa^{\text{hp}} \left(1 + \frac{16}{9} \frac{1 - (\nu^{\text{hp}})^2}{1 - 2\nu^{\text{hp}}} \frac{\bar{l}^3}{\bar{V}} \right), \quad (3.2)$$

in which ν^{hp} is the Poisson's ratio of the uncracked or crack-closed rock, \bar{l} is the average crack length, and \bar{V} is the average volume enclosing one crack, which is a measure for the crack density. Because the average crack length appears in Eq. (3.2) to the third power the compressibility is strongly affected by a few long cracks. The compressibility of the cracked rock, κ , increases with increasing crack density.

3.3 Nonlinear stress-strain behaviour

According to the simple model of Walsh, represented by Eq. (3.1), the compressibility of a rock containing cracks depends on the pressure through a porosity reduction mechanism of compliant crack closure. However, the stress diffusion equation (2.63) is stated in terms of the elastic parameters, the shear modulus μ , Poisson's ratio ν , and the compressibility κ , which are assumed to be constant functions of pressure, within this linear theory. According to experimental results published in the literature, and according to the experiments described in this thesis, elastic parameters of rocks depend on the stress, and vary strongly with stress at low effective stresses. The linear theory described in Chapter 2, assuming stress independent elastic parameters, is therefore an approximation, only accurate enough for sufficiently small stress changes. A nonlinear theory would be more appropriate but possibly too complex to derive analytical solutions. Other parameters occurring in Eq. (2.63), such as e.g. the permeability k , are also stress dependent, and assumed to be constant within the stress range of investigation.

In order to investigate the nonlinear stress-strain behaviour of rocks consider in Fig. (3.1) the unconfined stress-strain curve of a Niederhausen sandstone (Section (4.5)). Stuart (1992) describes the following processes which follow this curve preceding failure. The first part of the curve is convex upwards and results, depending on the orientation of the crack faces, from the progressive closure and opening of pre-existing, possibly randomly oriented cracks. Cracks which are predominantly aligned perpendicular to the axial stress are closed, while cracks parallel to the axial stress are open. Increased

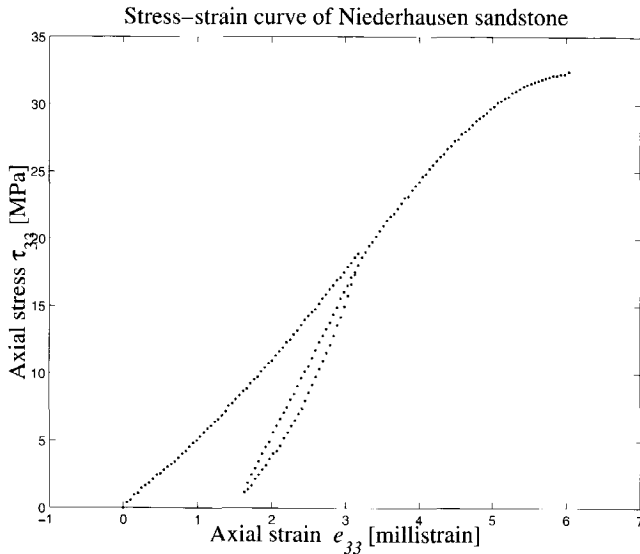


Figure 3.1: Axial strain versus axial stress applied to a Niederhausen sandstone core in an unconfined uniaxial pressure machine. Incorporated is a hysteresis loop.

loading in this first convex upwards part stiffens the rock (Walsh (1965b)). The convexity is explained by the reasoning that increasing increments of stress are needed to cause the same increments of strain, because the fraction of remaining open cracks become increasingly less compliant. A possibly initial superposition of an isotropic rock matrix permeated by randomly oriented flat cracks makes the rock effectively macroscopically isotropic. However, the large influence of relatively few long cracks (see Eq. (3.2)) which share a dominant orientation can make the rock behave anisotropically. The progressive crack closure process in a single direction induces transverse isotropy with respect to the elastic behaviour of the rock. This means that the rock is stiffer in the direction of the axis of symmetry than in the directions perpendicular to it. Three different principal stresses upon a rock with initial intrinsic isotropic symmetry induces an orthorhombic symmetry. Upon unloading, the cracks will open elastically and the small permanent deformation observed is due to the settling of the rock matrix by grain sliding and rotation. Second loading is completely elastic because subsequent unloading shows no extra permanent deformation.

The second approximately linear part of the stress-strain curve in Fig.

(3.1) results probably from a balance due to the superposition of the effects of continued closure, frictional sliding across the closed surfaces, and the extension of cracks. Microcrack propagation (nucleation and extension) is in the direction of the largest principal stress.

The last concave downward part of the stress-strain curve is due to increasing growth and deformation of cracks, parallel and perpendicular to the largest principal stress direction, to form a serrated failure plane connected through crack tips and inclined to the principal stress directions. The rock is progressively less able to sustain stress, a process called strain weakening. The linkage of previously isolated propagating cracks into serrated shear bands results in macroscopic failure (Ouyang and Elsworth (1991)). In this last part the rock becomes more compliant. The damage incurred by the rock is apparent as permanent deformation after unloading. After failure the rock is greatly reduced in strength while the strength itself is determined by the cohesive (frictional) forces across the failure plane rather than by the intact strength of the rock. The phenomenon that strains occur at discrete positions, such as at crack faces, grain contacts and, on a larger scale, ultimately at the shear failure plane, is known as strain localization. This process is also discrete in time due to its so called stick-slip behaviour. Strains are perceived to be continuous when the temporal and spatial scale of the measurement is much larger than the temporal and spatial scale of the phenomenon itself, such as with stress-induced crack growth in laboratory samples.

3.3.1 Hysteresis

Rocks may follow a different stress-strain path when unloaded compared to the loading curve as can be seen from the unloading-loading loop incorporated in Fig. (3.1). This phenomenon is called elastic hysteresis and occurs when more work is done on the body during loading, by the process of frictional sliding of crack faces, than is done during unloading (Walsh (1965b); Jaeger and Cook (1979)). Hence, the apparent Young's modulus during uniaxial loading depends both on the crack closure mechanism as well as on the effective friction coefficient of the opposing two surfaces of a closed crack. According to Walsh (1965b), the initial apparent Young's modulus upon unloading is larger because cracks which have undergone sliding do not immediately slide back. Therefore, Walsh (1965b) suggests that this modulus gives the best estimate of the true modulus of the rock matrix without cracks.

3.3.2 Dilatancy

Another measure of deformation is the invariant volumetric strain e_{nn} , which is the sum of the principal strains. The volumetric strain equals the ratio of the change in volume of the rock during compression to the original volume in the absence of any applied stress. Near failure, under compression, rocks show the behaviour that the volumetric strain becomes negative. This means that under compression the rock increases in volume, a phenomenon known as dilatancy. Dilatancy is caused by the nucleation and growth of open cracks which have their long axis parallel to the direction of the maximum principal stress (Jaeger and Cook (1979)). The opening of cracks is inelastic and occurs at far higher deviatoric stresses than the elastic opening of cracks at the first part of the curve in Fig. (3.1).

3.4 Granular model

In the above description of deformation and failure few remarks were made about actual granular nature of many sedimentary rocks and its effect on these phenomena. Schutjens (1995) reported no uniaxial stress-induced internal grain deformation, which could be identified with inelastic deformation, after inspection with a scanning electron microscope. Therefore Schutjens (1995) suggests that the inelastic deformation is explained by local minute changes in grain contact configurations, caused by grain sliding and/or grain rotation, triggered by inter-granular crack formation, or by intra-crystalline plastic deformation (dislocation propagation within crystal), or by brittle deformation of the weaker minerals in the load-bearing quartz mineral framework, such as corroded feldspars. The inter-granular cracks originate and grow due to breakage of micron-size or sub-micron-size asperities at either grain or cement contact surfaces. Hence, deformation of a sandstone can be explained by failure processes at grain boundaries and inside relatively weaker minerals (Schutjens (1995); Hettema (1996)). Explaining damage by crack mechanics within a rock matrix is a mere conceptual model for sandstones encompassing a range of complex phenomena. In sedimentary rocks, like high porous sandstones, inelastic deformation associated with grain sliding, rotation and crushing can lead to substantial porosity reduction and compaction weakening. Schutjens (1995) shows that the inelastic deformation increases with increasing porosity of quartz-rich sandstones. Other pa-

rameters that influence the deformation behaviour of rock are also cited by Schutjens (1995). For example, a decreasing indentation parameter, which is the average contact length between adjacent quartz grains divided by the average grain diameter, a measure for the inter-granular pressure solution, correlates with an increasing compressibility. A relatively higher concentration of (partly corroded) feldspar grains weakens the quartz load-bearing framework and hence decreases the compressibility.

3.5 Sub-critical crack growth and creep

Crack growth proceeds when the stress at the crack tip exceeds a critical value called the critical stress-intensity factor. Given enough time cracks may grow under sub-critical conditions. The mechanism which can cause sub-critical crack growth are driven chemical effects due to the presence of pore water, such as: stress corrosion, dissolution, diffusion, ion exchange and micro-plasticity (Atkinson (1984); Hettema (1996)). Stress corrosion is probably the main mechanism for sub-critical crack growth. Its effect is that it degrades the strength of rock, subject to small strain rates, over time. Continued stress can also increase the strength of a rock by the frictional related process of strain-hardening. The time-dependent deformation processes are categorized under the term 'creep'. The models describing creep are often power law functions of time. Delayed deformation can explain the randomness in time of failure processes like earthquakes but also impair the possibilities of predicting these phenomena (Evans (1984)).

3.6 Failure criteria

A failure criterion is a surface in the principal stress space at which failure takes place, represented by the functional relationship $\sigma^{(1)} = f(\sigma^{(2)}, \sigma^{(3)})$, in which the principal stresses, $\sigma^{(1)}$, $\sigma^{(2)}$ and $\sigma^{(3)}$, are solution of the determinantal equation (2.6). The simplest failure criterion is the linear Coulomb criterion, which, in case of an anisotropic medium, is given by

$$|\tau| = \tau^0 + \tan \psi (\sigma - \alpha_{ij} \nu_i \nu_j P^f), \quad (3.3)$$

(Jaeger and Cook (1979); Chen and Nur (1992)). Anisotropic failure is very common because rocks have often multiple planes of weakness. The Coulomb

criterion of Eq. (3.3) is shown in Fig. (3.2), together with the Mohr circles in $\{\sigma, \tau\}$ -space. The normal stress magnitude σ and the shear stress magnitude

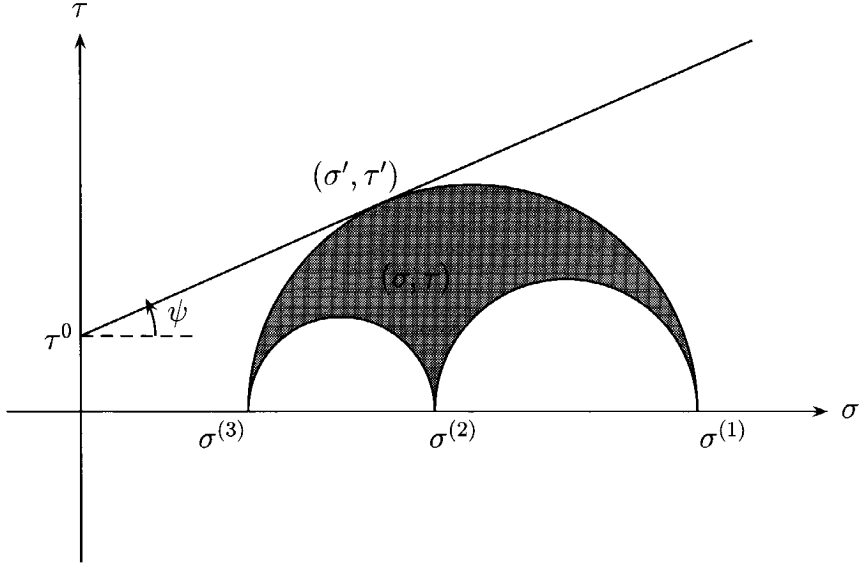


Figure 3.2: Locus of failure (σ', τ') given by a linear Coulomb criterion touching a Mohr circle

τ are solutions of Eq. (2.13), and are depicted in Fig. (2.1). The intercept shear stress τ^0 is the inherent shear strength or cohesion, and ψ is the angle of internal friction, the latter two parameters both depending on the anisotropic properties of the rock. Biot's coefficient α is given in Eq. (2.26). The normal vector to the failure plane is given by ν . Failure takes place at $(\sigma, \tau) = (\sigma', \tau')$, where the shaded area of possible (σ, τ) -values touches the coulomb failure criterion of Eq. (3.3). There are two possible planes of failure oriented in the direction of the intermediate principle stress and making angles of $\pi/4 - \psi/2$ with the direction of the maximum stress (Jaeger and Cook (1979)).

Another failure criterion was proposed by Mohr who hypothesized that normal and shear stress magnitudes are related by the functional relation

$$|\tau| = f(\sigma), \quad (3.4)$$

(Jaeger and Cook (1979)). The curve in (σ, τ) -space associated with Eq. (3.4), which is called a Mohr envelope, can be found experimentally by performing several triaxial experiments under varying stress conditions (See Section (4.5)).

The Griffith criterion is based on the assumption that failure is caused by stress concentrations at the tip of minute Griffith cracks which are supposed to pervade the material. Griffith's failure criterion depends on the balance of consumed surface energy and the supply of mechanical energy for an infinitesimal increase in crack length. This energy balance concept enables to derive the equation of motion of a crack tip. The Griffith criterion is equivalent to the existence of a critical stress-intensity factor, beyond which the crack will extend. (Aki and Richards (1980)). Murrell's extension of the original two-dimensional Griffith criterion to three dimensions represents a paraboloid, with symmetry axis $\sigma^{(1)} = \sigma^{(2)} = \sigma^{(3)}$, in the principal stress space (Jaeger and Cook (1979)).

3.7 Pore fluid pressure changes

To assess the effect of pore fluid pressure changes in a reservoir we review the effective stress law of Eq. (2.23) for the isotropic case,

$$\boldsymbol{\tau}^{\text{eff}} = \boldsymbol{\tau} - \alpha P^{\text{f}} \mathbf{I}, \quad (3.5)$$

with the scalar Biot's coefficient α given in Eq. (2.35), and \mathbf{I} being the unit tensor of rank two. This last equation and Fig. (3.3) show that a pore pressure increase, caused by e.g. fluid injection (dashed semi-circles), decreases the normal effective stress, but has no effect on the shear stress. Decrease of the normal stress on a possible failure plane, e.g. a fault plane, while the shear stress remains constant, destabilizes the fault and can induce slip along the fault. Fault stabilization occurs when the pore pressure decreases, due to e.g. fluid extraction (dotted semi-circles), which increases the normal stress on a plane. Both processes are indicated by the arrow in Fig. (3.3).

Using Eqs. (2.23) and (2.26), Chen and Nur (1992) give examples of the deviatoric effect of pore fluid pressure in anisotropic rocks. This means that the pore pressure also effects the shear stress. They show that, given a certain anisotropy in the stiffness tensor, a pore pressure increase can stabilize a fault, while a pore pressure decrease can have a destabilizing effect, see Fig.

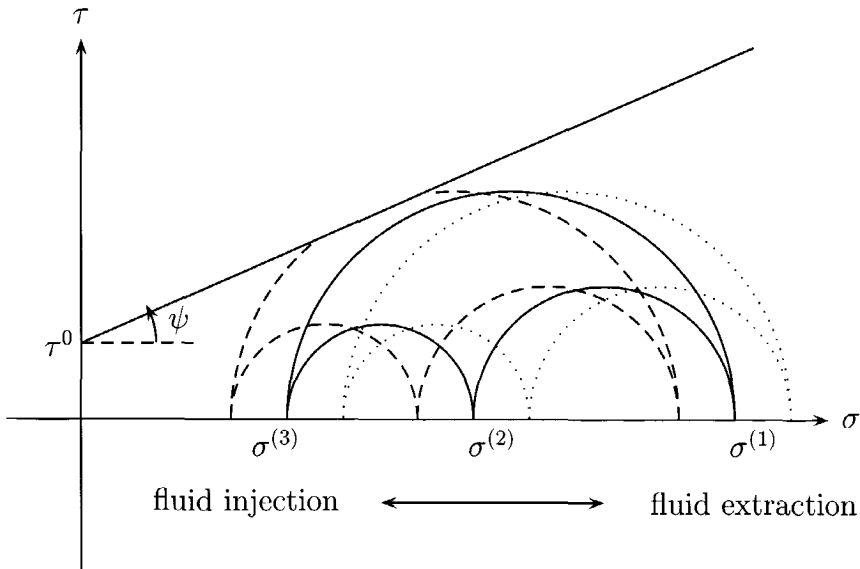


Figure 3.3: Pore fluid pressure changes in an isotropic medium causing translation of the Mohr circles in (σ, τ) -space. Failure induced by fluid injection. Fluid extraction stabilizes material.

(3.4), in contradistinction to the isotropic case, shown in Fig. (3.3). Conversely, the deviatoric effect in anisotropic rock can enhance the stabilization or destabilization compared to the isotropic case where the shear stress does not alter. This latter result is shown in Fig. (3.5), in which a pore pressure increase causes more destabilization on the fault plane, compared to the case shown in Fig. (3.3), whereas a pore pressure decrease stabilizes the fault more for the situation depicted in Fig. (3.5) than in Fig. (3.3).

3.8 Seismicity

Stresses build up in a fault region can suddenly be relaxed by slip along the fault creating an earthquake. In this so called seismogenic zone regions of high strength form, called asperities, which act as barriers to slip causing high stress concentrations in their vicinity. Asperities may act as sites for the nucleation of large earthquakes, while their distribution tend to control the

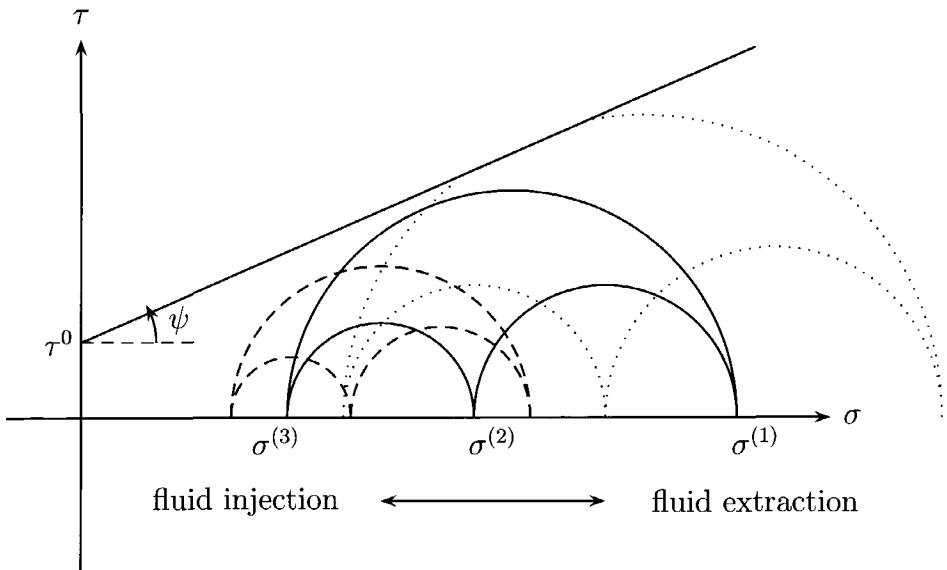


Figure 3.4: *Pore fluid pressure changes in an anisotropic medium causing a translation and a decrease or increase of the Mohr circles in (σ, τ) -space. Failure induced by fluid extraction. Fluid injection stabilizes material.*

propagation of rupture along the fault. Slip along an internal surface can be represented by a continuous array of displacement discontinuities called dislocations. By synchronizing the temporal behaviour of each point dislocation, equivalent to a moving point dislocation, material failure nucleation and the spreading of rupture, together with the rupture velocity, along the surface can be described. This complex mechanism acts as a source for seismic waves. The amplitude of the seismic wave depends on the temporal behaviour of the slip functions. Slow dissipation of built-up strain energy results in a relatively small amplitude wave, which may be below detection threshold of the seismometers. Rapid release of energy, as with brittle fracture, induces high amplitude waves. If the displacement discontinuity across a fault surface is known as a time-dependent function of position on the fault, then seismic motions throughout the medium are completely determined. This enables to interpret the observable seismic motions that radiate from the source region in terms of motions on a fault. The principal stress directions on the fault plane, which eventually reach a certain failure criterion, can be predicted by

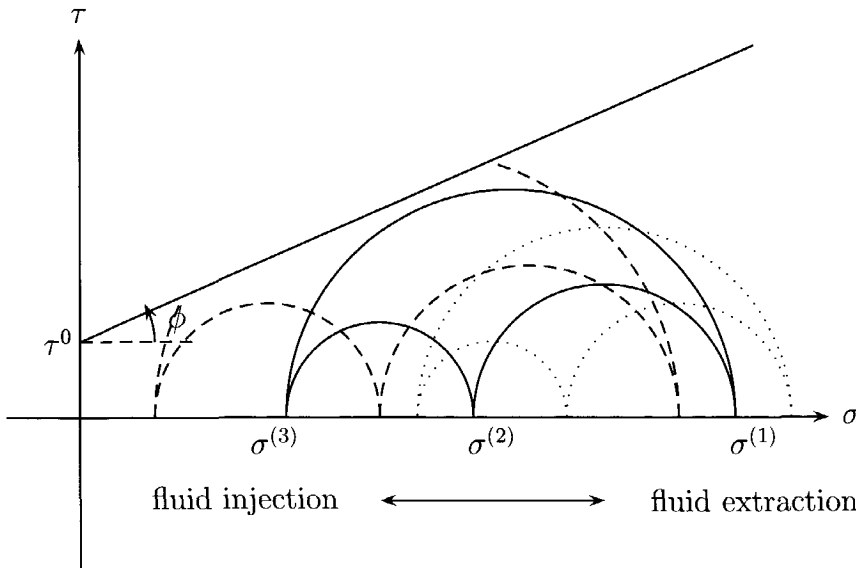


Figure 3.5: *Pore fluid pressure changes in an anisotropic medium causing a translation and a decrease or increase of the Mohr circles in (σ, τ) -space. Failure induced by fluid injection. Fluid extraction stabilizes material. The stabilization/destabilization is enhanced by the deviatoric effect of the pore fluid pressure.*

dynamical modelling of the rupture process, which describes the movement of a fault tip. Hence, studying the seismic waves, inferences can be made about the location of the earthquake source, the orientations of the fault, the principal stress directions and the rupture mechanism (Aki and Richards (1980)).

3.8.1 Microseismicity

At the microcrack scale the elastodynamic energy, associated with crack nucleation, crack growth and inelastic grain consolidation, is generally called acoustic emission or microseismicity. First arrival measurements of acoustic emission wave forms, with ultrasonic transducers, enables to locate the rupture process. Acoustic emission amplitudes indicate the source mechanism as they depend e.g. on the rate of change of incremental crack size (crack extension velocity). In that respect, acoustic emissions are very sensitive to the

small crack length increments, with high extension velocity, in brittle rock, and less sensitive to low extension velocity, large crack length increments, in ductile material (Stuart (1992)). An important measure is the acoustic activity which is the number of acoustic emissions above a certain threshold during an increment of time. It yields information on the overall rate of microcrack growth which is a measure for the damage accumulation rate. The accumulative acoustic activity from the onset of an experiment is a measure for the total damage incurred by the specimen. Stuart (1992) reports no acoustic emissions measurements upon uniaxial loading of Darley Dale sandstone specimens at the first region shown in Fig. (3.1), where elastic opening and closure of microcracks occurs. At the onset of new microcrack growth, in the linear region (40-50 % of the maximum compressive strength), the acoustic activity rises approximately exponentially with increasing stress, until total failure. Schutjens (1995) shows uniaxial compaction data of quartz-rich reservoir rock with a range of porosities. The cumulative amount of acoustic activity of the high porous samples, which show strain weakening and an increase of the compressibility, is one to two orders higher than that of the low porous samples, which show a more elastic response, indicated by a relatively constant and lower compressibility. Upon second loading all samples show a smaller compressibility than when subjected to the first loading. The ratio of second loading compressibility to first loading compressibility decreases with increasing porosity. Second loading acoustic activity is relatively low compared to the first loading. When the effective axial stress of the second loading is increased up to 5 to 10 MPa of the maximum effective axial stress of the first loading a renewed increase of the acoustic activity is observed. This stress memory phenomenon is called the Kaiser effect. Stuart (1992) defines the Kaiser effect as “the absence of acoustic emissions at stresses below a previously applied stress with an abrupt increase when that stress is exceeded”.

3.9 Reservoir stress dynamics

In the literature many cases can be found on the geomechanical effects of reservoir operations. Grasso et al. (1992) lists three categories of sources of mechanical instabilities induced by the recovery of hydrocarbons,

- fluid injection,

- fluid extraction,
- mass transfer and fluid circulation.

As is explained in the previous section a pore pressure change, either an increase due to fluid injection or a decrease due to fluid extraction, can locally destabilize a fault. The local decrease of the effective stress due to fluid injection as a cause for instability is obvious. Seismic instability related to fluid extraction, except for certain cases of anisotropy (see Figs. (3.3), (3.4) and (3.5)), is less clear. On a larger reservoir scale, fault instability due to fluid extraction is explained in Grasso et al. (1992) using the poroelastic stress transfer principle. The interaction between hydraulic diffusivity (permeability) and stress diffusivity, modelled by the diffusion equation (2.63), causes anomalous stress distributions away from the well, particularly at large contrasts in the elastic and flow material parameters, manifested by differential compaction at the edges of a reservoir (Roest and Kuilman (1994)). The diffusive process also explains the apparent time delay of deformation effects like subsidence and seismicity with respect to the time of reservoir operations. Poroelastic stress transfer also plays a role in large fluid injection operations, like secondary recovery methods and pore pressure maintenance operations to facilitate production in nearby wells, whereby stress transfers along pre-existing fractures to areas with seismic unstable faults (Grasso et al. (1992)). When examined on a larger reservoir scale the release of strain energy by deformation associated with transferred stress will occur at the weakest places. Grasso argues that pore fluid pressure manipulations cause predominantly seismic instabilities along preexisting tectonic faults. Small magnitude seismic activity originates from microfracturing in the vicinity of a large effective stress gradient, with small time delay, while large magnitude seismicity occurs at fewer places, often remote from the producing or injecting wells, and with possibly large time delays. The larger events depend on the deformation of the entire reservoir, which settles by differential movements along preexisting tectonic faults. The scale of the magnitude of the events is matched by its dependency on a larger spatial scale of the particular crustal region and the larger temporal scale in which the seismic events can occur. By considering the reservoir as a number of discrete stiff blocks, each with its own geomechanical properties, separated by faults representing planes of weaknesses, the deformation of the entire reservoir can be modelled (Nagelhout and Roest (1997); Roest et al. (1999); Roest and Mulders (2000)).

Secondary recovery involves both fluid injection and extraction. It is part of the third category of Grasso's list given above. The imbalance between depletion and injection zones stresses the rock and can generate fractures. Cold water injection for enhanced oil recovery causes thermal stressing in the vicinity of the cold front. The removal of load by massive oil extraction is known to have been the cause of major seismic events. Poroelastic stress transfer via an aquifer and rocksalt are two mechanism which can cause seismicity at a large distance from the reservoir itself (Barends et al. (1995)). Gas reservoir depletion can affect the aquifer pressure and transmit significant pore pressure. Viscoelastic coupling with rocksalt could trigger a delayed response.

The induced stress perturbations causing seismicity are small (a few bars), according to the hypothesis that the continental crust must be nearly everywhere at a state of stress near failure. In this respect the dynamics of the lithosphere can be described as a self-organized critical phenomenon.

3.10 Crack dynamics

Several mechanisms were discussed in this chapter which explain the relation between the history of the orientations and magnitudes of the principal effective stresses and the present alignment of zones of weaknesses, like faults and cracks. Changes in the arrangements of cracks causes changes in the elastic moduli of the rock. Hence, the crack model explains the susceptibility of the elastic moduli of the rock with cracks to changes in the effective stress. For reservoir rock with relatively compliant pores other mechanisms such as porosity reduction due to pore collapse also explain stress-induced changes in the elastic moduli. At low effective stresses the preferential opening and closure of cracks is a mechanism which affects the elasticity of rocks. Flat cracks with normals predominantly perpendicular to the direction of the largest principal stress will preferentially close, while cracks with normals parallel to the largest principal stress open or stay open. Conditions like that could occur at high pore pressures near the lithostatic pressure. The elastic crack closure in this pressure regime is a practically instantaneous reaction to the changing stress state.

The nucleation and growth of cracks to accommodate a changing stress state requires relatively high deviatoric stresses, i.e. half the failure stress. The question is if the required stress levels are present in a reservoir envi-

ronment to allow crack growth to occur. This might occur during e.g high fluid pressure injection operations such as hydraulic fracturing or due to high deviatoric stresses induced by differential compaction caused by the inhomogeneity of the fluid pressure (sealing faults).

Dilatancy, which involves the preferential growing of cracks aligned in the direction of the largest principal stress, occurs near failure at very high deviatoric stresses. Anomalous high stresses near asperities in the earthquake preparation zone may be loci of dilatancy (Evans (1984)).

Another mechanism as discussed above is the alignment of cracks caused by sub-critical crack growth. Crampin et al. (1984) suggest that sub-critical crack growth causes opening and growth of cracks, parallel to the largest principal stress, throughout a large part of an earthquake preparation by stresses one or two orders of magnitude less than those at which dilatancy occurs. It would explain the occurrence of earthquake precursors at substantial distance away from stress concentrations in the earthquake preparation zone where dilatancy is unlikely to occur. Crampin et al. (1984) call this mechanism extensive-dilatancy anisotropy (EDA).

3.11 Stress and wave velocity

The change in the effective elastic anisotropy, which can be modelled by a change in the alignments of cracks or any other alignment of micro-structural flaws or defects, induced by a changing stress, is known to affect elastodynamic waves. As already mentioned in this chapter Walsh (1965a) derives a model which explains a lower compression modulus (inverse of the compressibility) of a crack permeated solid compared to the same solid without cracks. Increase of the effective pressure on a cracked solid causes crack closure and hence an increase in the compression modulus. Wave velocities, which in elastodynamic theory are a function of the elasticity modulus, are also known to be affected by the presence of cracks and defects.

Wyllie et al. (1956) measured ultrasonic waves, using piezo-electric transducers, through a pile of glass microscope slides in order to affect poor coupling. Ultrasonic velocities measured in the two parallel directions of the glass plate faces were similar to the velocity of a single slide (17,530 ft/s). Velocities measured across the pile, perpendicular to the faces, were considerably lower (1,650 ft/s), hence identifying wave velocity anisotropy. In the same paper ultrasonic velocities of sandstones under uniaxial pressure are

shown to increase with pressure. The increase is at first rapid but decreases with increasing effective pressure until a limiting velocity is attained, except for high porosity samples which collapsed before attaining a limiting velocity. From this result the presence of microcracks or other generic flaws might be inferred which show pressure-induced closure. The limiting velocity is reached when the effective elastic modulus approaches the elastic modulus of the intact rock matrix due to the pressure action. This latter assumption is confirmed by the observation, described in a later paper by Wyllie et al. (1958), that different samples from the same rock may show variations in velocities for fixed effective pressures but the limiting velocities are constant. Wyllie et al. (1958) also verify that wave velocities depend on the effective stress of Eq. (2.23) by reporting constant velocities (first arrivals) with samples subjected to an increasing external stress, accompanied by a simultaneous increase in the fluid pressure.

In Birch (1960) experimental data on igneous and metamorphic rock of ultrasonic velocity versus pressure up to 1000 MPa are reported. For example, Barre granite and Sacred Heart granite show a rapid increase of compressional wave velocity up to 100 MPa, after which the increase slopes down to small velocity increments per unit pressure at 1000 MPa. Texture dependent anisotropy is apparent on several samples by the lower velocities of waves which propagate perpendicular to the foliation or schistosity.

In Nur and Simmons (1969) uniaxial stress experiments are described up to 30 MPa under dry conditions which concentrate on the effect of stress on wave velocity anisotropy in rocks. Nur and Simmons (1969) loaded a cylindrical sample of Barre granite normal to its axis and measured velocities parallel to the axis, and also normal to the cylindrical axis, but with variable angles to the applied load. Compressional-wave velocities, perpendicular to the axis, increased with pressure in all directions, but the increase becomes smaller with increasing angle with the applied load, from a maximum at 0 degrees down to a minimum at 90 degrees. Hence, they observe a stress-induced anisotropy, which increases with pressure. For shear-waves which travel perpendicular to the axis, polarizations parallel to the axis show a larger stress-induced anisotropy than polarizations perpendicular to the cylindrical axis. Nur and Simmons (1969) also verify the occurrence of acoustic double refraction or shear-wave splitting. Shear-waves, which propagate in the cylindrical axis direction and are polarized at angles from zero to ninety degrees with respect to the loading direction, show at intermediate angles an interference pattern of two wave forms, which can be identified as two shear-waves form-

ing a split shear-wave pair. This pair comprises a fast and a slow shear-wave with velocities comparable to the wave velocities in the loading direction and perpendicular to it, respectively.

Chapter 4

Description of the experimental set-up and samples

4.1 The tri-axial pressure machine

The experiments described Chapter 5 were conducted on the tri-axial pressure machine, located in the Laboratory of Rock Mechanics at the Delft University of Technology, and shown in Fig. (4.1). The machine was designed by J. Gramberg. Each of the three axes of the pressure machine can build up a computer-controlled maximum force of 3,500 kN. It is not possible to apply a controlled pore pressure to the rock since it is an open system. Each uni-axial part of the machine has a piston on one side and a pressure plate on the other side. All plates, except the bottom plate, are equipped with spherical seats, which allow for small rotations of the pressure plates, in case the sides of the sandstone sample are not parallel. The sides of the sandstone block are longer than the pressure plates to prevent the plates from touching each other. The forces and displacements are recorded, either every 10 seconds, or after a change of force of 10 kN, or after a change of displacement of 0.01 mm, whatever happens first. The displacements in each of the three axis directions are monitored by two linear variable differential transformers (LVDT's). Because of small rotations of the spherical seats of the pressure plates the average of both LVDT's is taken to measure the axial strain. Three ceramic piezo-electric transducers with a center frequency of 1 MHz were mounted in each pressure plate.

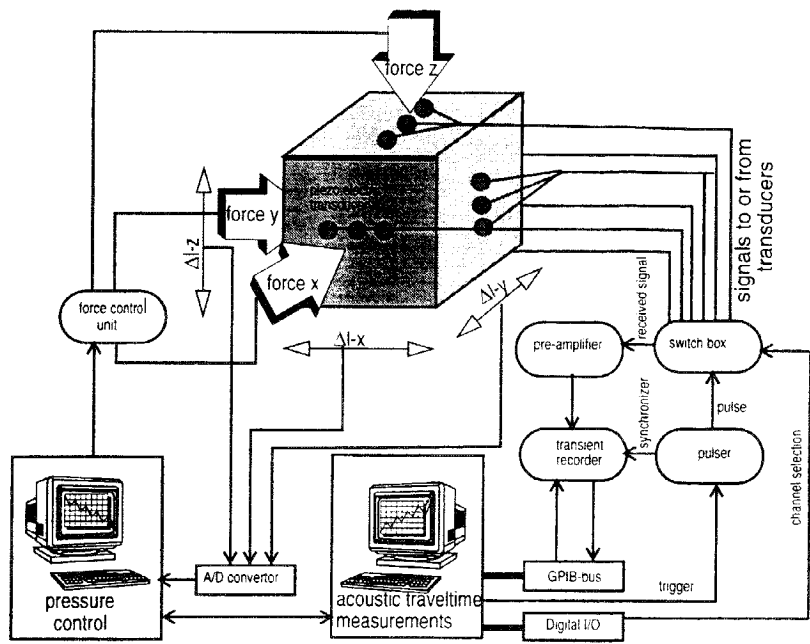


Figure 4.1: *Schematic lay-out of the ultrasonic triaxial stress experiment.*

4.2 Boundary conditions

In many published experiments (e.g. Stuart (1992)) a coupling platen is present between the piezo-electric transducer and the rock sample. In Groenenboom (1995) the following consequences for the ultrasonic signal are listed:

- loss of energy,
- creation of reverberations between the faces of the coupling platen resulting in notches in the spectrum of the signal,
- creation of mode-conversions,

which all cause a loss of resolution, making it more difficult to e.g. pick first arrivals. In the same report several coupling configurations were tested.

By placing the transducers directly against the sample a high amplitude localized P-wave arrival is obtained, with a clearly separated S-wave arrival, without the strong reverberations associated with a coupling plate. Also a smooth and stable high-frequency band is obtained. In Groenenboom (1998) experiments are described of acoustic monitoring of hydraulic fracture growth using this transducer coupling configuration.

To accomplish direct contact of the transducer faces with the sandstone three holes were drilled through the platen. Through these holes the transducers are pressed, with the aid of a spring, with a constant force of 900 N on the sample. Shear-wave couplant was applied to the transducer faces to improve signal quality. To study the relationship between the stress and the ultrasonic recordings we need an uniform and known stress distribution within the sample. However the experimental design causes stress gradients within the sample. In van Dam and de Pater (1995) the influence of the following factors is investigated:

- non-total coverage of the sample by the platens leaving stress-free strips at the edges of the sample,
- friction-dependent shear-stress between platen and sample caused by the different elastic moduli of the platen and the sample,
- stress-free transducer holes in the platens,
- imperfect working of the tri-axial pressure machine.

Below I use the data and conclusions from van Dam and de Pater (1995) to assess the implications for the experiments described in this thesis. Non-total coverage of the sample by the platens causes a lower normal stress in the center of the sample than the applied stress at the faces of the sample. The expected normal stress in the center of the sample, τ^{ex} , is defined as the ratio of the end platen surface, A^{pl} , and the sample surface, A^{sa} , multiplied with the applied normal stress, τ^{ap} , expressed as

$$\tau^{\text{ex}} = \frac{A^{\text{pl}}}{A^{\text{sa}}} \tau^{\text{ap}}. \quad (4.1)$$

Finite difference calculations indicate that the expected normal stress is a good approximation of the calculated average normal stress along a line parallel to an axis direction, from one side to the other side, through the center

of the sample. When there is a frictional restraint the shear-stress along the end platen-sample interface also causes a decrease of the normal-stress inside the sample. This shear stress is not constant, due to the inhomogeneous lateral differential displacement of the platen and the sample. In the middle of the interface the differential displacement is zero and increases towards the edges (Al-Chalabi and Huang (1974); van Dam and de Pater (1995)). Given the configuration of an aluminium end platen, vaseline, 0.1 mm Teflon (polytetrafluorethyleen) and a cement sample, a friction coefficient between 0.001 and 0.01 was measured under a confining stress of 10-20 MPa. A normal stress decrease of 0.3 MPa for a friction coefficient of 0.005 was calculated. The friction coefficient decreases after several hours because the vaseline film thickness gradually decreases. For the experiments described in this thesis we used the same configuration, except that instead of cement samples we used sandstone samples, and vaseline was also smeared between the Teflon layer and the sample surface. The cement surface is much smoother than the sandstone surface but because the friction between the end platen and the Teflon is lower than between the Teflon and the sample, movement will mainly take place between the former surfaces. The transducer holes in the pressure plate create a circular stress free region. Axisymmetric finite difference simulations with a stress-free hole at the center yield a normal stress deviation of 0.82 % at the center of the stress free hole and a deviation of 0.22 % at a distance of 7.5 cm from the center. Large shear-stress near the hole causes permanent deformation of the sandstone. Inspection of the samples after a maximum imposed normal stress of 82 MPa shows only minor visual deformation damage. Concluding, the most significant factor which diminishes the normal stress inside the sample is the use of end platens with dimensions smaller than the side of the block.

4.3 Transducers

Three ceramic piezo-electric broad-band transducers with a central frequency of 1 MHz were mounted in each pressure plate. The central transducer is a compressional-wave (also called P-wave for primary wave) transducer (Panametrics V-103) and the two outer transducers are shear-wave (also called S-wave for secondary wave) transducers (Panametrics V-153). The two shear-wave transducers have perpendicular polarizations, each aligned along an axis direction. For the shear-wave splitting experiments the P-

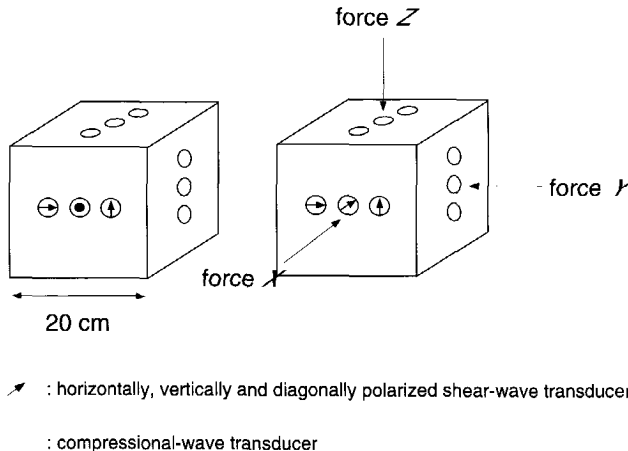


Figure 4.2: *Transducer configuration.*

wave transducer is exchanged for a diagonally polarized S-wave transducer (Figure 4.2). Transducers with corresponding polarizations are positioned on opposite sides of the sample. The sample frequency is set at 10 MHz. The record length is 2048, 16 bits, samples. It is possible to measure all transmitting-receiving transducer combinations, giving a data volume of $18 \times 18 \times 2048 \times 16 = 1.0610^6$ bits per scan. A high-pass filter of 10 kHz and a low-pass filter with a cut-off frequency of 2 MHz were used. To minimize trigger effects a post trigger delay was applied.

The transducers are in direct contact with the sample and pressed, with the aid of a spring, with a constant force on the block. Shear-wave couplant was applied to the transducer faces to improve signal quality. Using the above described transducer-sample coupling configuration, a high signal quality was obtained (Groenenboom (1995, 1998)).

4.4 Sandstone samples

4.4.1 Colton sandstone

The first ultrasonic experiments, described in this thesis, performed by H.M.A. Cruts and described in (Cruts (1995); Cruts et al. (1995); Dillen et al. (1999)), were done on a cubic block of Colton sandstone. The Colton formation is

a eocene fluvial deposit from North central Utah, at the south side of the Uinta basin, in the U.S.A. The clastic material is deposited at the during the Eocene. The sample is taken from a channel facies and consists of lithic quartz and feldspar. It is fairly homogeneous and has a porosity of about 13 % and an unconfined compressive strength of 47 MPa.

4.4.2 Flechtinger sandstone

The second series of experiments (den Boer (1996); den Boer et al. (1996); den Boer and Fokkema (1996)) were conducted with a Flechtinger sandstone which is an aeolian Upper Rotliegend Permian sandstone, obtained from the Sventesius Quarry near Magdeburg in Germany. The quarry is located south of the Flechtinger Hills at the southern edge of the Southern Permian Basin (Fig. (4.3)). The Flechtinger sandstone formation consists of massive cross-bedded aeolian dune sandstone (Fig. (4.4)) of medium grain size of 0.25-0.5 mm. Thicknesses vary, depending on the erosion of the top sequences, between 18-45 m. North of the location, documented by wells, it can reach thicknesses of more than 100 m (Weber (1998)). As shown in Fig. (4.5) the dune sandstone overlies a sequence with conglomerate alluvial fan deposits. Fig. (4.6) shows a detail of the tangential contact of the crossbedding at the bottom-set. Three intact rock samples were sawn from a larger piece with its long axis parallel to the cross-bedding. In spite of the different geological history of the Flechtinger hills, which were uplifted in the Upper Cretaceous and the Tertiary, the reservoir quality of the Flechtinger sandstone is still comparable to the Rotliegend dune sandstone buried to a depth of 3,000-6,000m. Laboratory measurements show a porosity of 10.7 %, a permeability of 3.44 mD, and a rock density of 2.65 g/cm³ (Weber (1998)). Measurements at the Dietz Laboratory resulted in a porosity of 9% and no measurable permeability. The unconfined compressive strength, measured in the laboratory of Rock Mechanics on three cylinders of 7 cm length and 3 cm diameter, is 75 MPa. The samples we acquired are, as the name suggests, red colored. The reddening occurs post-depositionally when ferrous ions in the groundwater were oxidized to the ferric state. Beneath the surface of modern deserts a diagenetic environment conducive to reddening is commonly present below the water table. Reddening is probably mostly an early diagenetic event (Glenie (1990a)). From thin sections digital images were made using the Leica Quantimet. The characteristic color of the Rotliegend is visible as a thin coating around the grains (Fig. (4.7)). The name of this type of sandstone

is an arkose. The category of roundness of the quartz grains is surrounded. The mineralogy consists of ca. 60% quartz, 20% feldspar, and 20% rock fragments cemented with calcite (Fig. (4.8) and (4.9)). From the thin section pressure solution of quartz grains is observed, indicating the high level of compaction. The porosity deduced from the thin sections is between 3 and 5 %, lower than the porosities measured in the laboratory.

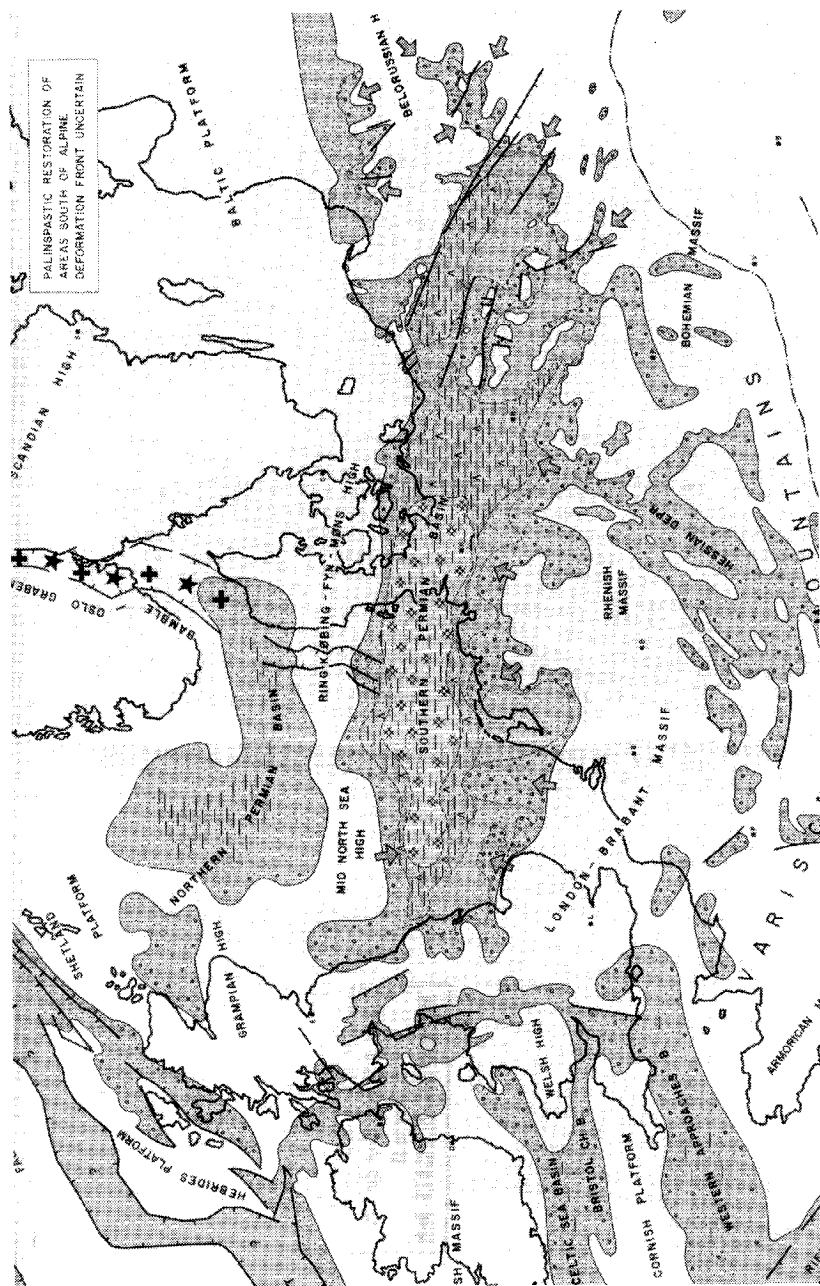


Figure 4.3: Location of the Southern Permian Basin (Ziegler (1981)).

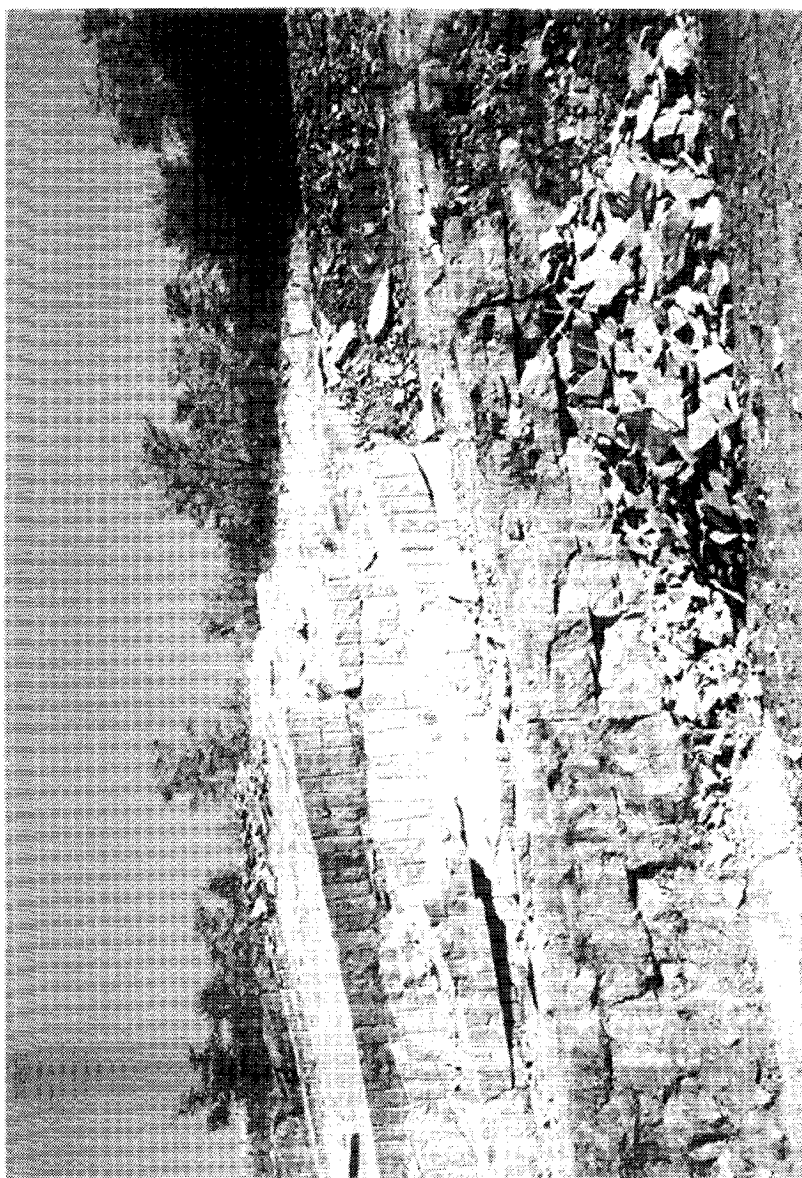


Figure 4.4: *Overview of the Sventesius Quarry. The basement consists of fluvial deposits overlying massive cross-bedded dune sandstones. The tangential contact at the bottom of the cross-bedded set can be clearly seen.*



Figure 4.5: Aeolian cross-bedding overlying conglomerate alluvial fan deposits.

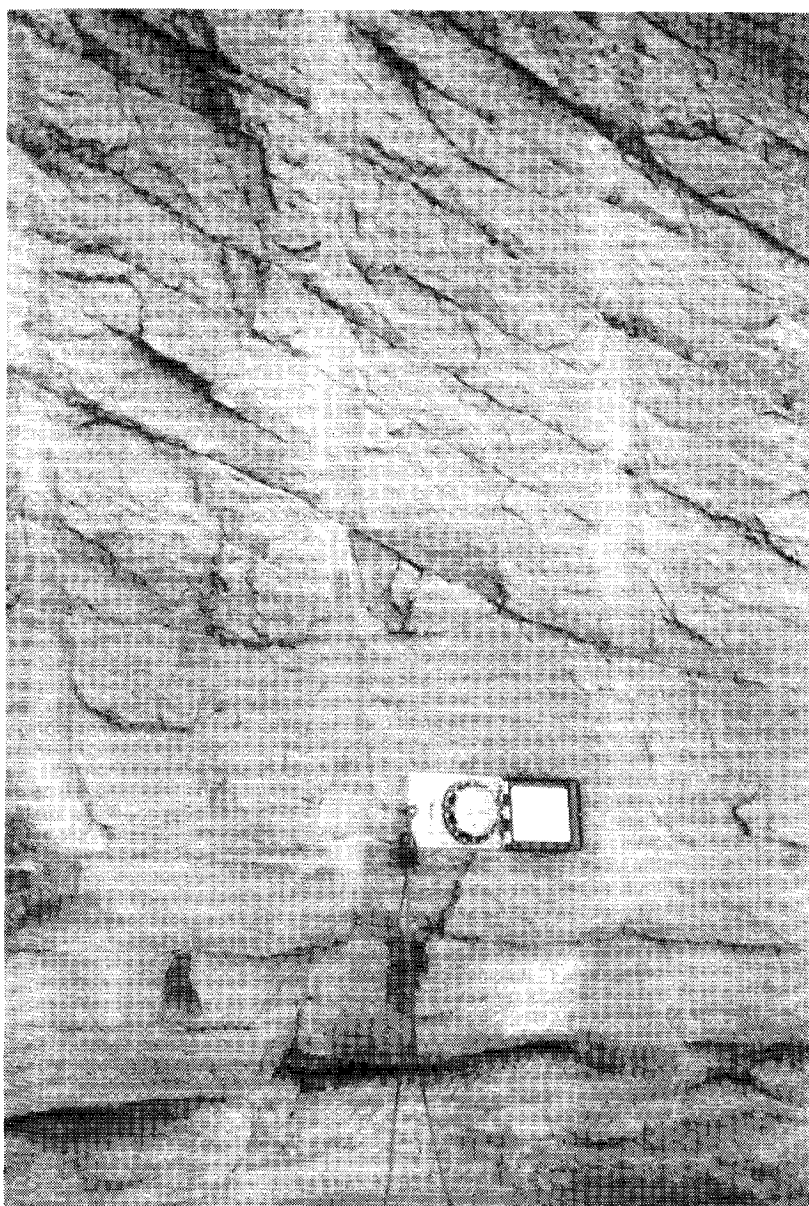


Figure 4.6: *Detail of a crossbedding showing steep foreset in upper half of the figure and tangential bottomset in lower half.*

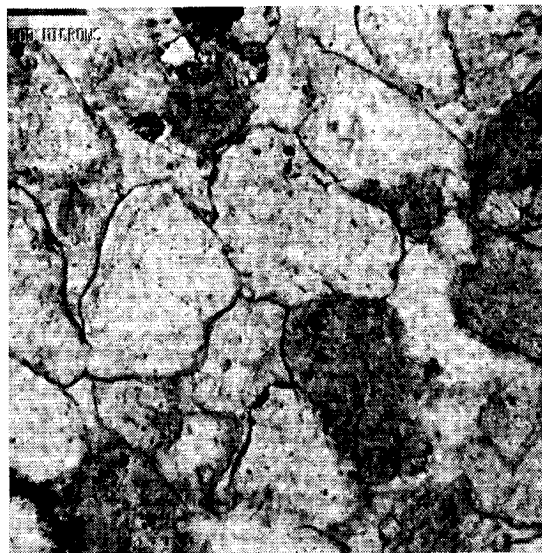


Figure 4.7: Thin section of the Flechtinger Rotliegend sandstone using unpolarized light. The characteristic color of the Rotliegend is visible as a thin coating around the grains.



Figure 4.8: Thin section of the Flechtinger Rotliegend sandstone using polarized light, showing subrounded grains.



Figure 4.9: Thin section of the Flechtinger Rotliegend sandstone using polarized light. Mineralogy: feldspar (weathered), rock fragments, multi-grain quartz, metamorphic (originally part of e.g. gneiss), quartz, calcite cement, highly compacted, visible pressure solution of the quartz grains.

4.4.3 Niederhausen sandstone

The Niederhausen sandstone, used for the third series of experiments, described in Swinnen (1997), is a Rotliegend sandstone from an outcrop near Niederhausen in the Saar-Nahe area in Germany. The samples were acquired from a quarry run by Fa. Naturstein Faller in Niederhausen am Nahe. A thin section is shown in Fig. (4.10). The rock is poorly sorted and consists



Figure 4.10: *Thin section of the Niederhausen Rotliegend sandstone using polarized light. Orientation of the section is perpendicular to the layering.*

mainly of quartz. Several of these grains are grown together, which reduces the permeability of the rock. According to Schutjens (1996) a permeability of 2.6 mD is noted. Some of the quartz minerals are replaced by calcite. Under polarized light the quartz minerals show 'unduleus uitdoven', which is caused by the stress-induced deformation of the quartz crystal lattice. The thin section also shows feldspars (plagioclase), most of which are converted into clay and iron-hydroxides. The Niederhausen Rotliegend has a yellow-brownish color because some of the ferric iron-hydroxides have dissolved in reducing ground waters and precipitated again later (Glennie (1990b)). The porosity is difficult to deduce from the thin sections. Probably there is some micro-porosity around the quartz grains. The porosity, measuring 19.3%, and the bulk density, measuring 2.69 g/cm³, were determined with a picnometer. The

layering is visible through the orientation of the mica minerals. The oriented mica minerals are visible in Fig. (4.10), whereas these same orientations do not show up in Fig. (4.11), which is oriented parallel to the layering. Fig.



Figure 4.11: Thin section of the Niederhausen Rotliegend sandstone using polarized light. Orientation of the section is parallel to the layering.

(4.12) shows polysynthetic twins which are caused by weathering of plagioclase to mica. In Fig. (4.13) we observe sericite which is composed of fine muscovite layers weathered from plagioclase.

4.4.4 Bad Dürckheim sandstone

The Bad Dürckheim sandstone was also used in the third series of experiments. This sandstone is a Bunter sandstone of Lower Triassic age. Like the Niederhausen sandstone it was quarried from an outcrop in the Saar-Nahe area in Germany. The sandstone samples were obtained at the Fa. Zeidler & Wimmel located in Bad Dürckheim-Leistadt, Baden-Württemberg Germany. From the thin section image using polarized light in Fig. (4.14) we can see that the dominant mineral of the rock is quartz. Some of the grains are coated with iron-hydroxides which is apparent in Fig. (4.15) in which unpolarized light was used. The Bunter Sandstone Formation is known to consist



Figure 4.12: *Thin section of the Niederhausen Rotliegend sandstone using polarized light. Orientation of the section is perpendicular to the layering. Shown are polysynthetic twins which are caused by weathering of plagioclase to mica.*

of red beds. Glennie (1990b) refers to Walker et al. (1978) and Turner (1980) for the hypothesis that the red coloration is caused by the post-depositional degradation of ferro-magnesium minerals, supplemented by detrital ferric hydroxides, which form haematite pigment. The red color of the Bad Dürckheim sandstones has disappeared. A few light-reddish concentrations can still be seen on the samples. The picnometer test resulted in an average porosity of 20.2%, and a bulk density of 2.66 g/cm^3 . According to Schutjens (1996) a permeability is measured of 953 mD, a much higher value than measured with the Niederhausen sandstone. This stems from the fact that the quartz minerals in the Bad Dürckheim sandstone are not grown together by pressure solution.



Figure 4.13: *Thin section of the Niederhausen Rotliegend sandstone using polarized light. Orientation of the section is perpendicular to the layering. Shown is sericite which is composed of fine muscovite layers weathered from plagioclase.*



Figure 4.14: *Thin section of the Bad Dürckheim Bunter sandstone using polarized light. Pores filled by black epoxy.*

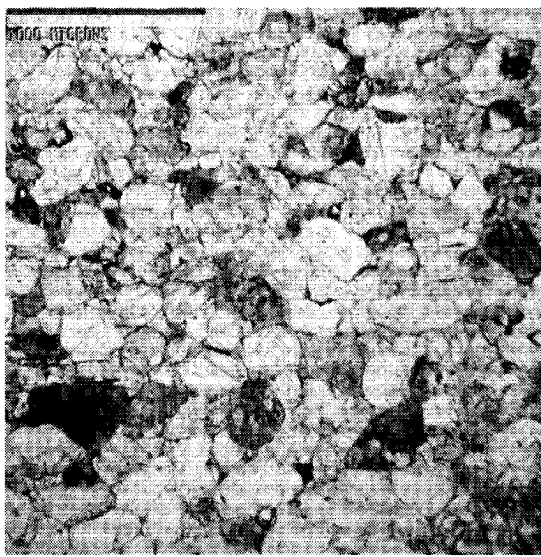


Figure 4.15: *Thin section of the Bad Dürckheim Bunter sandstone using unpolarized light. Observe iron-hydroxide coating.*

4.5 Stress experiments on cylindrical cores

In this chapter quasi-static stress experiments conducted on cylindrical cores are described. The main reason for doing these experiments is to establish the strength of the particular sandstone sample, before it is subjected to high stresses in the triaxial pressure machine, because failure of the sample during an experiment might damage the end platens. The strength of the samples is quantified by the unconfined compressive strength (u.c.s.), which is the maximum axial stress $\sigma^{(3)}$, under unconfined conditions ($\sigma^{(1)} = \sigma^{(2)} = 0$), sustained by the sample before failure. For the Colton and the Flechtinger sandstones only the u.c.s. parameter was determined. More elaborate experiments were performed on the Niederhausen and Bad Dürckheim sandstones, to establish the full nonlinear stress-strain behaviour, under unconfined and confined conditions. The added value of these experiments, compared to the experiments on the triaxial pressure machine, is that the elastic behaviour as a function of applied stress, can be studied up to and beyond failure. Also, because in Rock Mechanics many stress experiments are standardized to experiments on small cylindrical cores, the experiments in this chapter can be compared with experiments described in the literature.

4.5.1 Unconfined experiments

The Niederhausen and Bad Dürckheim sandstones were cored perpendicular and parallel to the layering of the samples. The height and the diameter of the cores are approximately 80 and 40 mm, respectively. The pressure machine is displacement controlled. The axial displacement rate is set at 4 $\mu\text{m/s}$. Two LVDT's measure the axial displacement, from which the average value is used to calculate the axial strain, and one LVDT measures the circumferential displacement, from which the radial strain is obtained. The cores are loaded until some seconds after failure. To obtain elastic behaviour, i.e. no permanent plastic deformation component, two secondary loading loops are incorporated. In Fig. (4.16) the axial strain versus axial stress curve is shown for the Niederhausen sandstone sample, drilled perpendicular to the layering. The loading path is divided into 7 subsequent parts, denoted by part 'a' to part 'g'. Part 'a' denotes loading until the first loop, parts 'b' and 'c' are unloading and loading parts of the first loop, respectively, part 'd' is further loading until the second loop, parts 'e' and 'f' are unloading and loading parts of the second loop, respectively, and part 'g' is

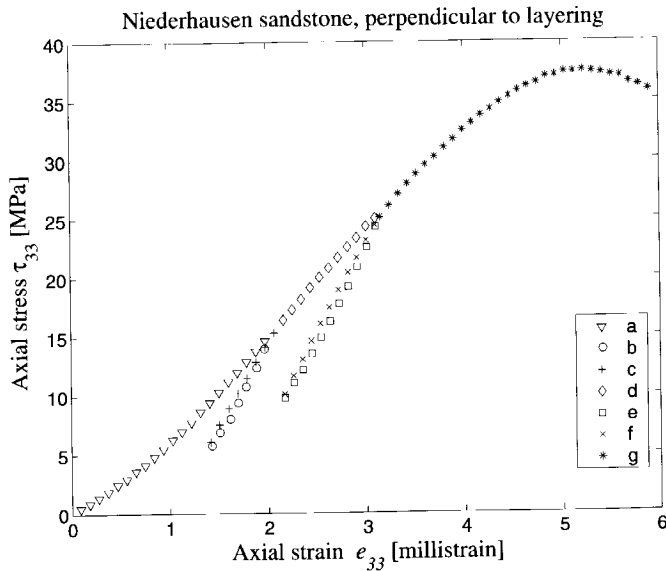


Figure 4.16: Axial strain versus axial stress applied to a cylindrical core of the Niederhausen sandstone. Core drilled perpendicular to the layering. Subsequent loading parts 'a', 'd' and 'g' denote main loading curve. Parts 'b' and 'c' denote unloading and loading parts of the first loop, whereas parts 'e' and 'f' signify the respective unloading and loading parts of the second loop.

further loading until and beyond failure. The following experiments follow this loading path, however not exactly, because the onset of a loop had to be initiated manually. In Figs. (4.19) to (4.22) we refer to this subdivision.

In Fig. (4.17) the stress-strain curves are shown, using the loading path described in Fig. (4.16), for cores of the Niederhausen sandstone, drilled perpendicular (top figure) and parallel (bottom figure) to the layering. Both radial, the negative strain curve, and axial, the positive strain curve, strain are plotted as a function of axial stress. No confinement pressure in the radial direction was applied. We observe from Fig. (4.17) that the stress increments per unit strain increase are larger during the loops than during the main loading curve, indicating that the rock reacts stiffer during the loop parts. The maximum stress or u.c.s. perpendicular to the layering is 37.5 MPa, which is larger than the u.c.s parallel to the layering, which measures 32.2 MPa. Hence, the Niederhausen sandstone is anisotropic with respect to

Sandstone	u.c.s [MPa]
Colton	47
Flechtinger	75
Niederhausen \parallel	32.2
Niederhausen \perp	37.5
Bad Dürckheim \parallel	32.1
Bad Dürckheim \perp	58.1

Table 4.1: Failure stresses under unconfined conditions for the Colton, Flechtinger, Niederhausen and Bad Dürckheim sandstones. For the latter two sandstones u.c.s values are shown for cores parallel (\parallel) and perpendicular (\perp) to the layering.

its strength, possibly caused by the layering. The axial stress-strain curve parallel to the layering appears to be more linear than the perpendicular curve.

In Fig. (4.18) the stress-strain curves are shown for the Bad Dürckheim sandstone obtained using the loading path described in Fig. (4.16). Comparing Fig. (4.18) with Fig. (4.17) we observe that the Bad Dürckheim sandstone is more anisotropic than the Niederhausen sandstone. The u.c.s. of the former sandstone measures 58.1 MPa perpendicular to the layering, whereas its u.c.s. parallel to the layering is 32.1 MPa. It is also apparent from Fig. (4.18) that the stress-strain curve parallel to the layering is generally less steep than the curve from the core drilled perpendicular to the layering, indicating that the Bad Dürckheim sandstone reacts more compliant to a normal stress parallel to the layering than to a normal stress perpendicular to the layering. In Fig. (4.18) the first loop of both the perpendicular and parallel to the layering cored samples unloads until zero axial stress. The associated axial and radial strain values quantify the anelastic permanent deformation, which is larger parallel to the layering than perpendicular.

In Table (4.1) the unconfined compressive strength parameters are summarized as these were measured for the four sandstones used in the experiments. The highest u.c.s. value is found for the Flechtinger Rotliegend, which may be attributed to its high quartz content and deep burial depth, causing large compaction, evidenced by pressure solution (Fig. (4.9)) of some of the quartz minerals, and relative tight packing and low porosity. The chemical weathering of the feldspar minerals is small, typical of an arkose sandstone,

and also attributing to its relatively high strength. No thin sections are available for the Colton sandstone, so its lower u.c.s. value, as compared to the Flechtinger sandstone, can only be explained by its higher porosity. The other Rotliegend, the Niederhausen sandstone, has much smaller u.c.s values than the one obtained for the Flechtinger Rotliegend. This may be explained by the higher porosity of the Niederhausen, the smaller compaction, the poorer sorting and the more abundant chemical weathering of the feldspar minerals (plagioclase) to clay. Some plagioclase weathering to mica (muscovite) is shown in Figs. (4.12) and (4.13). The higher u.c.s. value of the Bad Dürckheim Bunter sandstone as compared to the Niederhausen, both measured perpendicular to the layering, is due to the higher quartz content of the former sandstone and less apparent feldspar weathering (relatively high permeability). The Bad Dürckheim sandstone experienced a smaller compaction, e.g. no pressure solution of quartz, than the Niederhausen sandstone, which does show quartz pressure solution and 'unduleus uitdoven'. This may explain the differences between the u.c.s. values parallel to the layering between the Niederhausen and Bad Dürckheim sandstones. The layers of the Niederhausen are "fused" together due to the compaction and therefore a higher strength is obtained, under an axial stress parallel to the layering, than for the Bad Dürckheim sandstone which may experience more pronounced longitudinal splitting (separation of individual layers or layer aggregates), which is the dominant mode of failure under unconfined stress.

To quantify the elasticity of the samples we calculate Young's modulus, given by

$$E = \frac{\tau_{33}}{e_{33}}, \quad (4.2)$$

which is the ratio of the axial stress to the axial strain. This measure is a unique measure for a rock's elasticity if it has a linear stress-strain behaviour. In general, rocks have a nonlinear elasticity which is evident from Figs. (4.17) and (4.18), and the discussion in Chapter 3. Assuming that for sufficiently small stress increments a linear approximation is valid the following elasticity measure is introduced

$$E^t (\tau_{33}) = \frac{d\tau_{33}}{de_{33}}, \quad (4.3)$$

which is the tangent to the stress-strain curve. The elasticity modulus E^t , the superscript $.^t$ signifying 'tangent', is taken as a function of the axial stress

τ_{33} . To calculate E^t from the data of Figs. (4.17) and (4.18), each part 'a' to 'g' of Fig. (4.16) is separately, and subsequently, interpolated and smoothed with a Gaussian function. Then E^t is approximated using finite differences.

The results for the Niederhausen and Bad Dürckheim sandstones, using the annotation of Fig. (4.16), are shown in Figs. (4.19) and (4.20). From Fig. (4.19) one can see that the E^t modulus is larger in the two loops than in the main loading curve. This is partly caused by the additional permanent anelastic deformation during the main loading curve, which is absent during the loops, which involve secondary elastic loading. The main loading curve, parts 'a', 'd' and 'g', in the top figure of Fig. (4.19), shows first an increase in E^t , then a constant part or linear elastic part, followed by a decreasing part until E^t approaches zero at failure. By comparison, the curve parallel to the layering shows a more linear behaviour from the onset of the loading until 25 MPa. The unloading parts 'b' and 'e', in the top and bottom figures of Fig. (4.19) show a decrease, whereas the loading parts 'c' and 'f', show an increase, forming a x-shape. These different behaviours are caused by the elastic hysteresis. During these hysteresis loops the largest E^t values are obtained at the onset of unloading. This observation complies with Walsh (1965b) who suggests that these values give the best estimate of the true modulus of the rock matrix without cracks.

The anisotropic stress-strain behaviour of the Bad Dürckheim sandstone is readily identified in Fig. (4.20) by the anisotropy of the E^t modulus. Comparing the first loading curve 'a' with the second loading curve 'c', in both perpendicular and parallel cored samples, one can see that the modulus for the second loading over this range is larger, while the total change is smaller than during the first loading, because anelastic effects are minimal. In Fig. (4.20) we recognize the x-shapes, outlining the two loop cycles, as in Fig. (4.19).

Poisson's ratio ν , for a linear elastic solid, is given as the ratio of the negative radial strain to the positive axial strain. To acknowledge the non-linear elastic behaviour observed in the experiments we introduce the tangent Poisson's ratio as

$$\nu^t(\tau_{33}) = -\frac{de_{11}}{de_{33}}. \quad (4.4)$$

Subsequently, interpolating, smoothing of the data of Figs. (4.17) and (4.18), and calculating the tangent Poisson's ratio ν^t , using a finite difference approximation, we obtain Figs. (4.21) and (4.22). In these figures we use the same

annotation of subdivision into parts as in Fig. (4.16). From the Niederhausen samples, cored perpendicular and parallel to the layering, depicted in Fig. (4.21), we observe that ν^t increases with increasing axial stress during the main loading curve. For increasing stress, radial strain increments increase more than axial strain increments, per unit stress increment. According to linear elastic theory, Poisson's ratio has the value 1/2 as an upper limit, either representative for an incompressible solid, i.e. $\kappa = 0$ and $\mu = E/3$, or representative for a compressible fluid, i.e. $E = 0$ and $\mu = 0$ (Jaeger and Cook (1979)). In Figs. (4.21) and (4.22) ν^t increases with axial stress beyond the value 1/2. This happens, especially for samples cored parallel to the layering, before failure and before the tangent Young's modulus becomes zero (see Figs. (4.19) and (4.20)). One reason might be that an unconfined axial stress experiment causes longitudinal splitting in the axis direction which gives excessive radial displacements and loss of structural integrity due to separation of the individual split parts. The longitudinal splitting is facilitated when the layering is directed in the axial direction. The axial strains are less affected and hence Young's modulus is non-vanishing before failure. The top figure in Fig. (4.21) shows a fairly constant ν^t during the two hysteresis loops, as compared to the main loop. This can partly be explained by the observation in Fig. (4.17) that the ratio of anelastic to elastic strain is larger in the radial direction than in the axial direction. Hence, during the loops, where the anelastic strain is negligible, a unit stress change causes a relatively small radial strain change, such that ν^t changes less accordingly. The x-shapes of the loop cycles can also be discerned in Figs. (4.21) and (4.22). The ν^t values are least variable during the unloading parts 'b' and 'e'. The smallest values of these parts are attained during the onset of unloading, which may be best representative for the true Poisson's ratio of the intact rock.

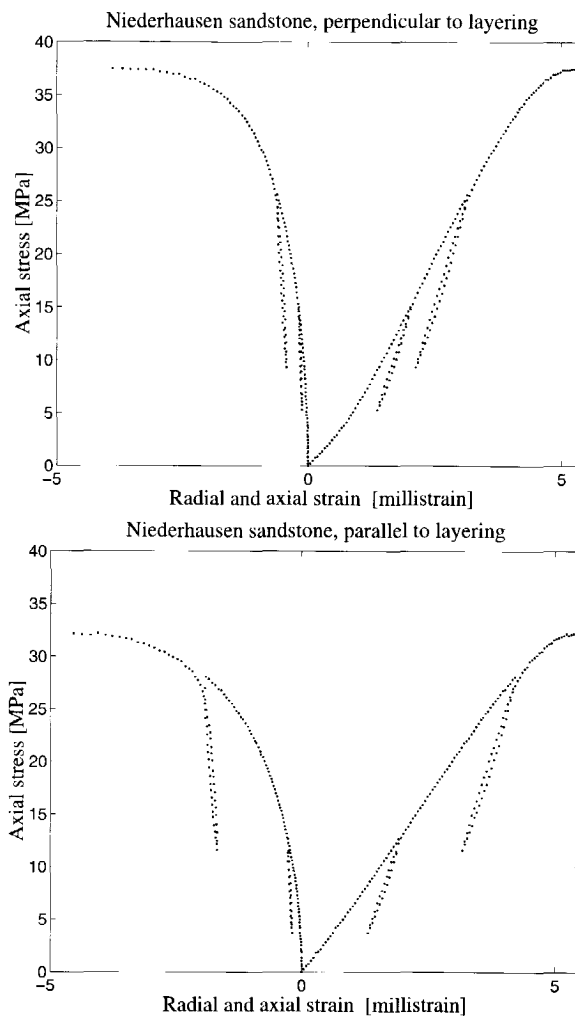


Figure 4.17: Radial (negative strains) and axial (positive strains) strain versus axial stress applied to a cylindrical core of the Niederhausen sandstone. Core drilled perpendicular (top figure) and parallel (bottom figure) to the layering.

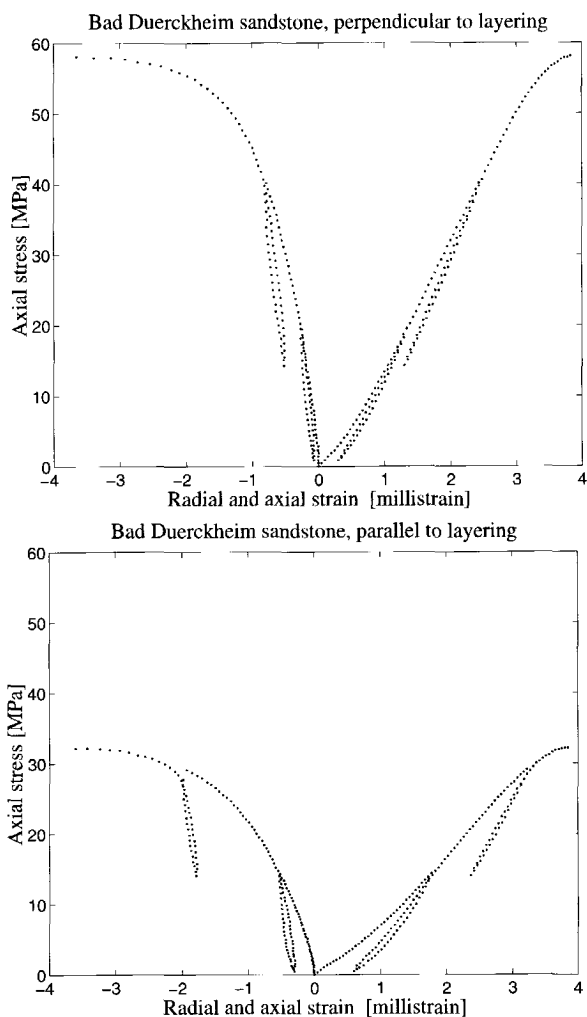


Figure 4.18: Radial (negative strains) and axial (positive strains) strain versus axial stress applied to a cylindrical core of the Bad Dürckheim sandstone. Core drilled perpendicular (top figure) and parallel (bottom figure) to the layering.

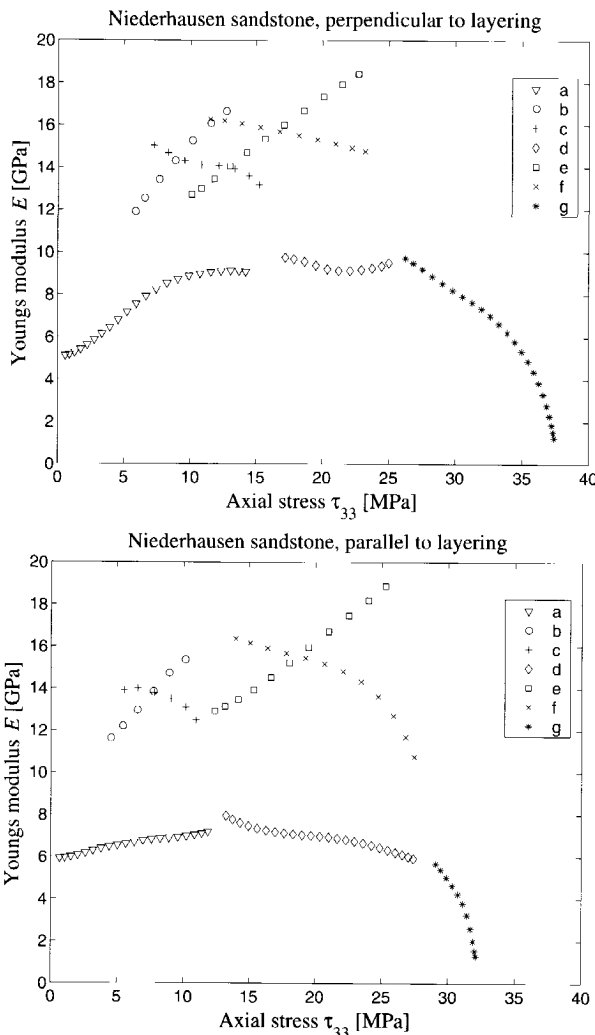


Figure 4.19: Tangent Young's modulus versus axial stress applied to a cylindrical core of the Niederhausen sandstone. Core drilled perpendicular (top figure) and parallel (bottom figure) to the layering. See Fig. (4.16) for the loading parts legend.

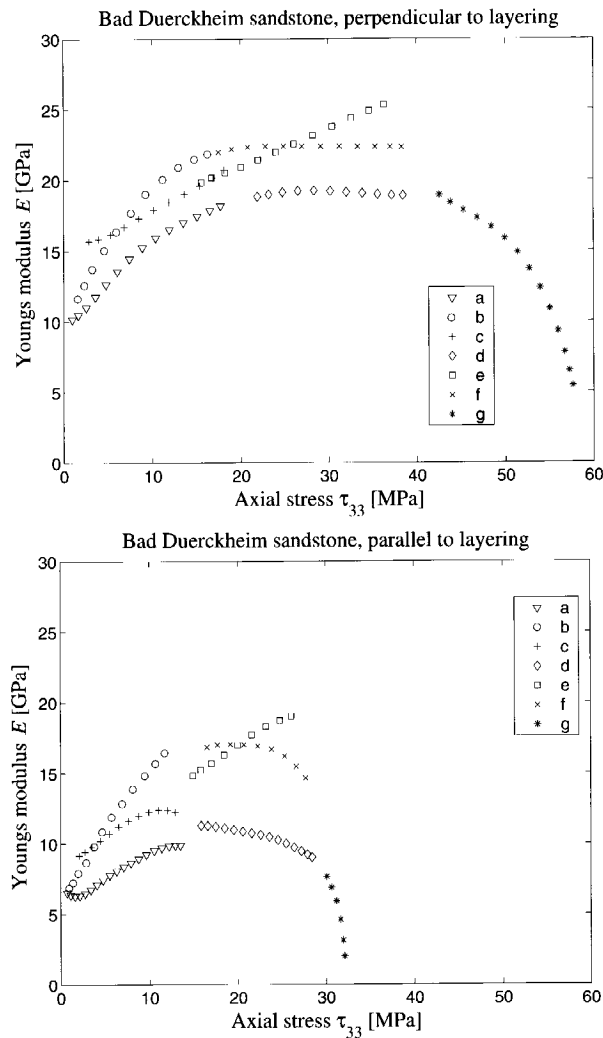


Figure 4.20: Tangent Young's modulus versus axial stress applied to a cylindrical core of the Bad Dürckheim sandstone. Core drilled perpendicular (top figure) and parallel (bottom figure) to the layering. See Fig. (4.16) for the loading parts legend.

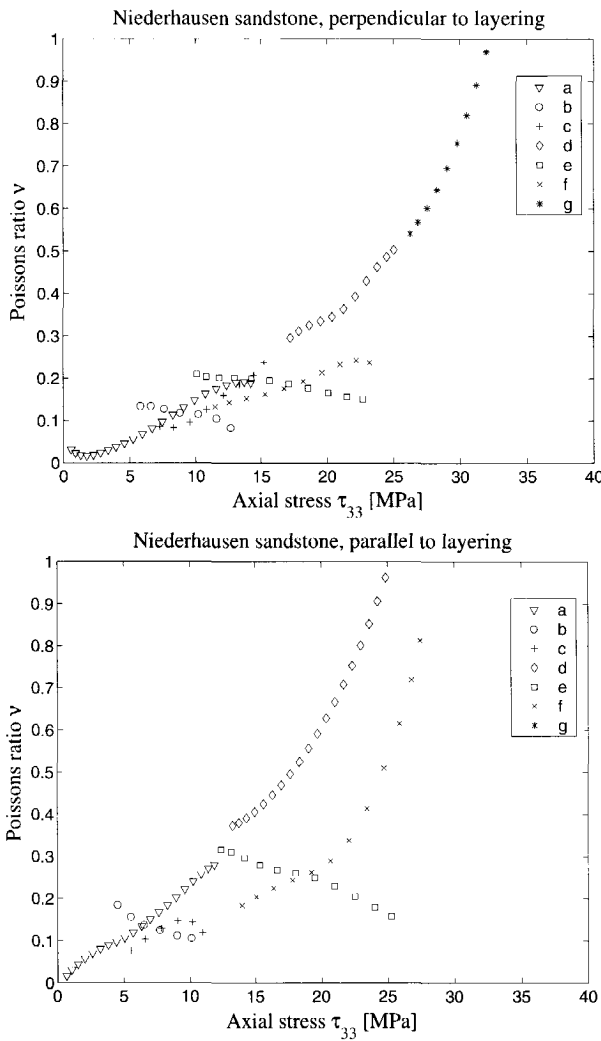


Figure 4.21: Poisson's ratio versus axial stress applied to a cylindrical core of the Niederhausen sandstone. Core drilled perpendicular (top figure) and parallel (bottom figure) to the layering. See Fig. (4.16) for the loading parts legend.

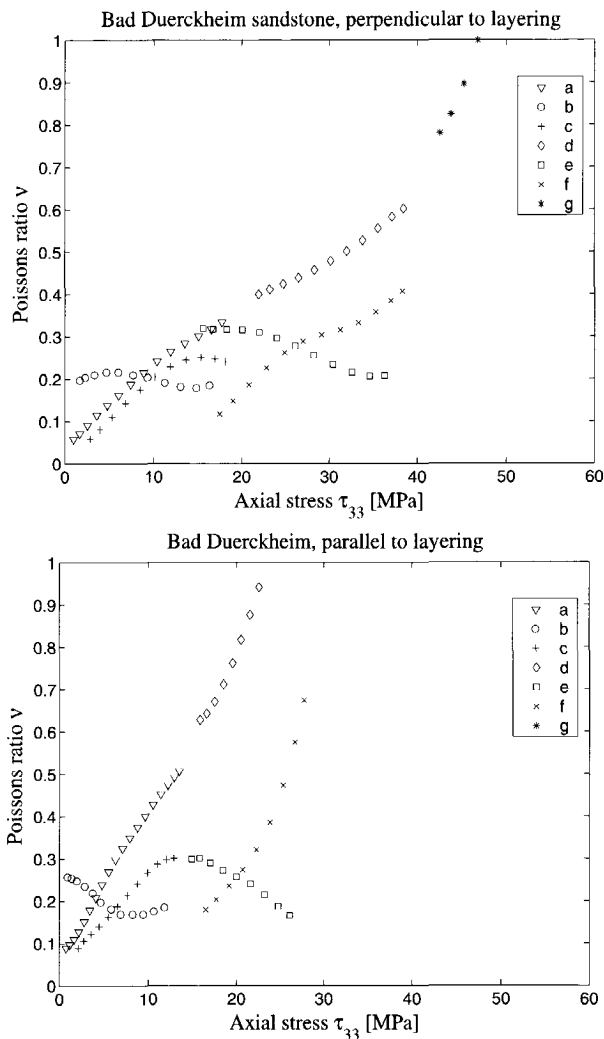


Figure 4.22: Poisson's ratio versus axial stress applied to a cylindrical core of the Bad Dürckheim sandstone. Core drilled perpendicular (top figure) and parallel (bottom figure) to the layering. See Fig. (4.16) for the loading parts legend.

4.5.2 Confined experiments

To establish the elastic behaviour of the Niederhausen and Bad Dürckheim sandstones, under conditions for which $\sigma^{(1)} = \sigma^{(2)} \neq 0$, uniaxial stress experiments were conducted under a constant confining pressure. The cores for these experiments, having a height and diameter of approximately 60 mm and 30 mm, respectively, are wrapped in an impermeable sleeve and placed in a cylindrical holder filled with oil, which is used to apply the confinement pressure. Axially, two steel cylinders are put between the pressure plates and the samples. First, the axial stress and the confining pressure are increased equally to the desired confining pressure. Then, the axial stress is increased while the recording starts, at which moment the strain is set to zero. Loading, at a rate of 7 $\mu\text{m/s}$, is continued until a few seconds after failure. The measured axial displacement is composed of the displacement of the core as well as the displacement of the total steel column, which has an effective length of 422 mm and an E modulus of 200 GPa. The axial strain of the core is obtained by subtracting the steel strain from the total strain. Consequently, at the beginning of the experiment, the stress-strain curves do not start at the confinement pressure for zero strain.

In Fig. (4.23) the stress-strain curves are shown from confined axial stress experiments for the Niederhausen sandstone, cored parallel to the layering, and the Bad Dürckheim sandstone, cored perpendicular to the layering. From the top figure we observe, for increasing confinement pressure, an increasing failure stress. Also, from the same figure it is evident that the rock shows a transition from brittle to increasingly ductile behaviour with increasing confinement pressure. The Bad Dürckheim sample, depicted in the bottom figure, shows higher failure stresses than the Niederhausen sample, and only brittle behaviour, even for the highest confinement pressure. The different behaviours between the two samples may be attributed to the orientation of the layering with respect to the axial direction, and the different mineralogies, with the Bad Dürckheim having a higher quartz content and less apparent feldspar weathering. The failure stresses are summarized in Table (4.2).

In Fig. (4.24) the tangent Young's modulus of Eq. (4.3) is shown, calculated from the pre-failure data of Fig. (4.23) in much the same way as described for the unconfined experiments. The E^t moduli for the Bad Dürckheim sample are more than twice as high as the ones for the Niederhausen sample. All E^t curves increase with increasing axial stress to a maximum value after which these curves decrease to zero at failure.

Confinement pressure [MPa]	Failure stress Niederhausen [MPa]	Failure stress Bad Dürckheim [MPa]
9	82	116
13	97	140
21	128	173

Table 4.2: *Failure stresses at different confinement pressures for the Niederhausen sandstone, cored parallel to the layering, and the Bad Dürckheim sandstone, cored perpendicular to the layering.*

	Shear strength or cohesion [MPa]	Angle of internal friction [degrees]
Niederhausen	12	37
Bad Dürckheim	16.5	41

Table 4.3: *Shear strength and angle of internal friction for the Niederhausen sandstone, cored parallel to the layering, and the Bad Dürckheim sandstone, cored perpendicular to the layering.*

Using the failure stresses from Table (4.2) one can construct the linear Coulomb criterion of Eq. (3.3) from the tangent of the Mohr circles (Chapter 2), as depicted in Fig. (3.2). The calculated Coulomb criterion is shown in Fig. (4.25) for both sandstone samples. The associated cohesion or shear strength τ^0 , and the angle of internal friction ψ , for both samples, are shown in Table (4.3).

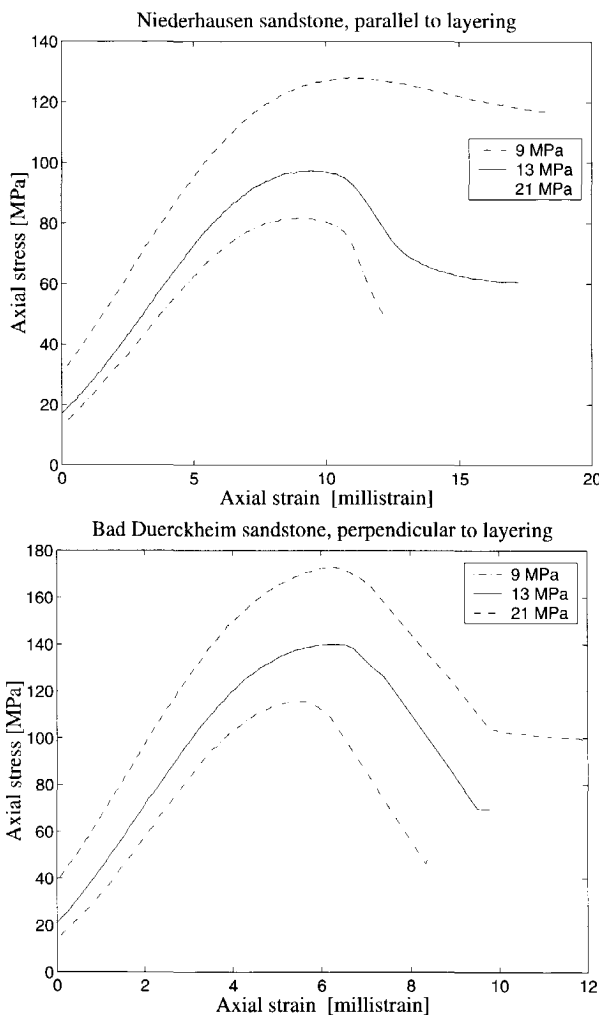


Figure 4.23: Axial strain versus axial stress under 9, 13 and 21 MPa confinement pressure. Top figure: Niederhausen sandstone drilled parallel to the layering. Bottom figure: Bad Dürckheim sandstone drilled perpendicular to the layering.

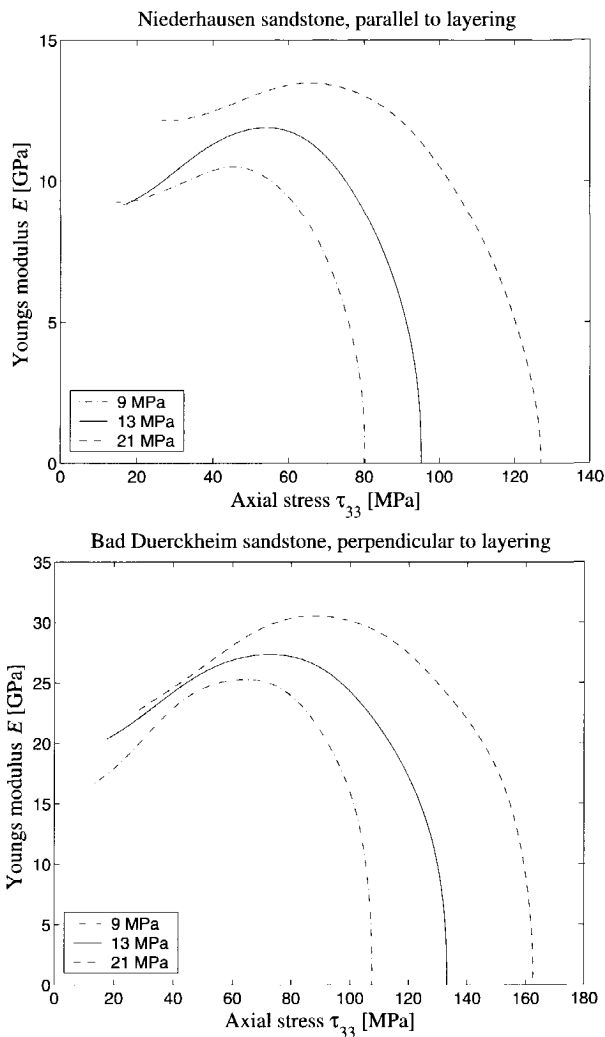


Figure 4.24: Tangent Young's modulus versus axial stress under 9, 13 and 21 MPa confinement pressure. Top figure: Niederhausen sandstone drilled parallel to the layering. Bottom figure: Bad Dürckheim sandstone drilled perpendicular to the layering.

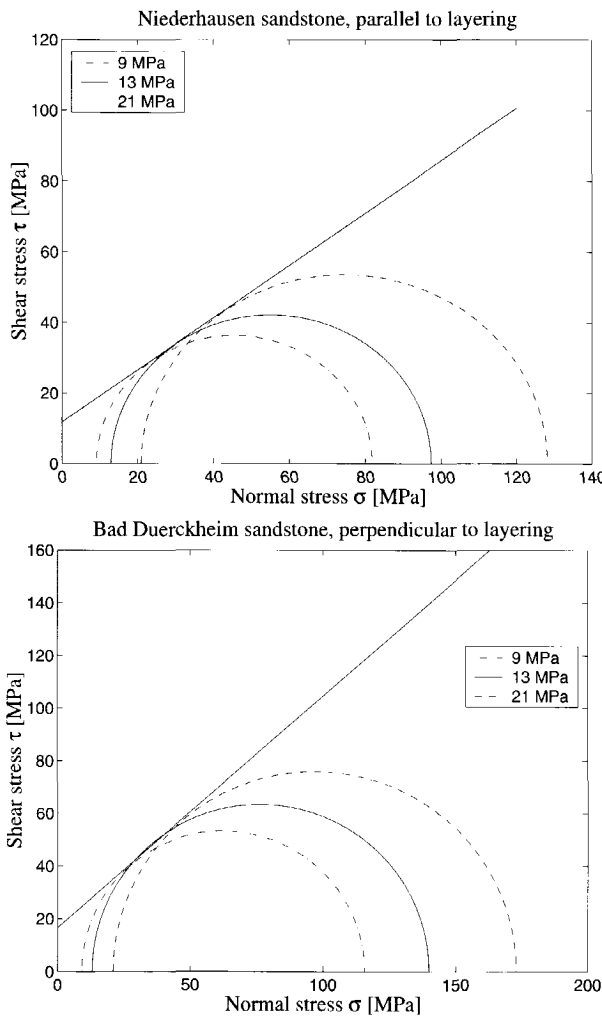


Figure 4.25: Mohr's circles for 9, 13 and 21 MPa confinement pressure. Top figure: Niederhausen sandstone drilled parallel to the layering. Bottom figure: Bad Dürckheim sandstone drilled perpendicular to the layering.

Chapter 5

Experimental results

5.1 Introduction

The fact that propagation of elastic waves in rocks can be sensitive to the effective stress has been verified in numerous laboratory experiments (Wyllie et al. (1956); Nur and Simmons (1969); Tao and King (1990)). In a controlled laboratory experiment the effective stress can be manipulated by changing the pore pressure or, in drained conditions, by changing the applied external stress (Wyllie et al. (1958); Rai and Hanson (1988)). Because the pressure machine we used for the experiments can not apply a pore pressure we changed the external stress under dry conditions. A common observation from ultrasonic stress experiments is that induced velocity changes in the stress direction become progressively smaller as stress increases, until an asymptotic value is reached (Wyllie et al. (1956); Nur and Simmons (1969); Lo et al. (1986)). Stress-induced velocity changes can be explained by structural models based on crack geometry and crack density which assume that cracks open or close in directions depending on the stress state (Nur (1971); Hudson (1980); Crampin (1982)). In this chapter we relate the stress tensor to ultrasonic velocities in a phenomenological way and show how the stress imprint can be recognized from its associated velocity pattern. The data shows the velocity change of nine combinations of compressional- and shear-waves (three propagation and three polarization directions) during a true tri-axial stress path. The comparatively large size of the sample and the transducer-sample coupling in our experiments are different from those previously published experiments. Although part of the results in this chapter

are not new we believe that the experiments produce a unique exposition of data which clarifies the sensitivity of elastodynamic waves to stress.

5.2 Experiments on the Colton sandstone

The ultrasonic experiments on a dry Colton sandstone were conducted by H.M.A Cruts, and are described in Cruts (1995); Cruts et al. (1995); Dillen et al. (2000).

5.2.1 Introduction

Ultrasonic experiments on a dry Colton sandstone placed in a tri-axial pressure machine, show that effective stress changes lead to distinct anisotropic velocity changes in compressional-waves and shear-waves. The stress imprint can be recognized from the associated velocity pattern by relating the velocities to the three normal stress directions. The ultrasonic velocities indicate that the sensitivity of the different waves to stress predominantly depends on stresses applied in the polarization and propagation directions of the particular wave mode. Also, stress-induced changes in shear-wave splitting are observed.

5.2.2 Experimental design

The ultrasonic experiments (Cruts (1995)) were carried out on a cubic block of Colton sandstone (Section 4.4). After grinding and polishing, the dimensions of the block are $0.205 \times 0.205 \times 0.205$ m³. The tri-axial pressure machine, its schematics shown in Fig. (4.1), and the transducer arrangement, shown in Fig. (4.2), are described in Section 4.3.

At zero pressure the measured P-wave velocities in the X- and Z-directions are approximately equal and differed by 5 % from the velocity in the Y-direction. Therefore we assume that the Colton sandstone has an intrinsic transversely isotropic symmetry, with the symmetry axis aligned in the direction of the Y-axis of the tri-axial pressure machine. Equal confining stresses in the X- and Z-directions will therefore preserve the transverse isotropy of the sample and arbitrary stress patterns will induce an orthorhombic symmetry (Nur (1971)). Fig. (5.1) shows the load cycle ABCD as a function of experiment time. The entire ABCD-stress path has equal normal stresses in

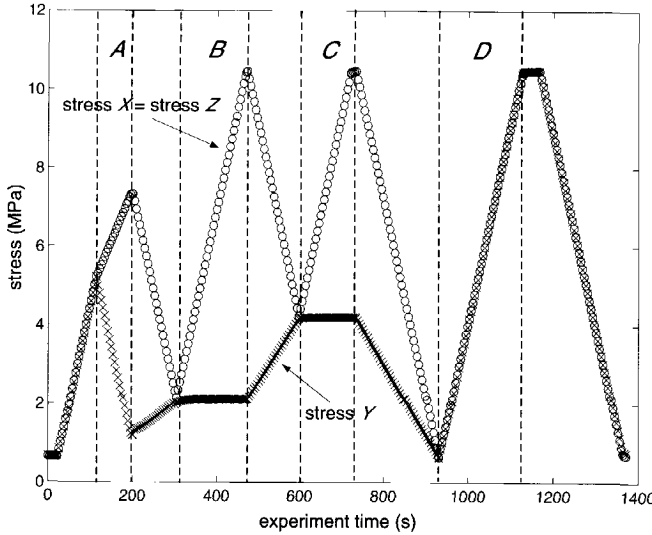


Figure 5.1: *Loading cycle ABCD of the tri-axial pressure machine. To preserve the intrinsic transverse isotropy of the sample, the stress in the X-direction is equal to the stress in the Z-direction.*

the X - and Z -directions. During parts A , B , C , and D , the X -force and the Z -force increase. Part A shows a decrease of the stress in the Y -direction, whereas during parts B and C the stress in the Y -direction was kept constant at 2 MPa and 4 MPa, respectively. Finally part D simulates increasing hydrostatic stress conditions up to 10 MPa.

5.2.3 Experimental results

Fig. (5.2) shows the full waveform signals of compressional-waves as functions of experiment time (top horizontal axis) and transmission travel time (vertical axis). The bottom horizontal axis indicates the segments A , B , C , and D similar to those in Fig. (5.1). The source and receiver are both P-wave transducers aligned in the X -direction. The transducer-sample coupling, described in the previous section, produces clean traces with easily discernible first arrivals and amplitudes. To visualize shear-wave splitting, shear-wave transducers were aligned in the X -direction and polarized in the YZ -plane in a direction of 45 degrees to the symmetry axis. Fig. (5.3) displays the

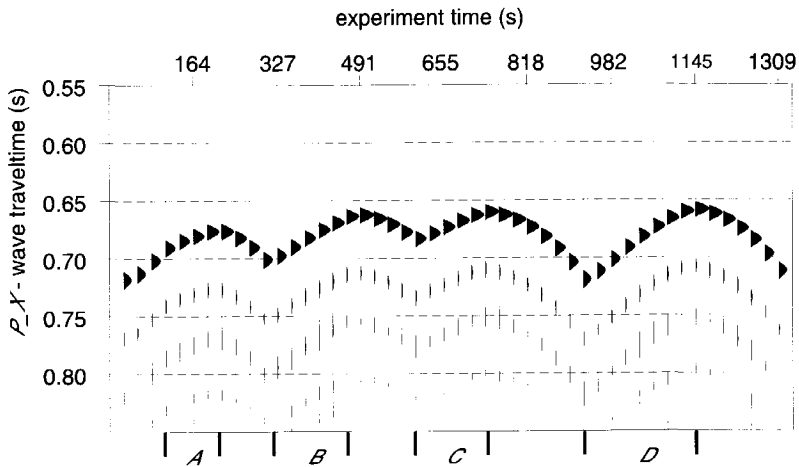


Figure 5.2: Ultrasonic recordings of a compressional-wave in the X -direction during load-cycle ABCD.

waveforms recorded at time intervals during stress pattern ABCD. Around the peak stresses of A , B , and C , two distinct waveforms appear and again disappear as experiment time progresses. These two distinct waveforms are split shear-waves traveling in the same X -direction. Shear-wave splitting becomes visible at those parts of the loading cycle where the stress-induced transverse isotropy is most pronounced. Comparing data from the diagonally polarized transducers with those from transducers polarized in the axis directions, we can determine that the first arriving shear-wave is polarized in the Z -direction and the second arriving shear-wave is polarized in the Y -direction.

From the recordings of P-wave transducer pairs first arrivals were hand-picked, converted to velocities and displayed in Fig. (5.4). We observe that the P_X - and P_Z -wave velocities (subscript denotes propagation direction) are almost equal and higher than the P_Y -wave velocity during the entire load cycle, reflecting the intrinsic and stress-induced anisotropy of the rock. For part A where the stresses in the X - and Z -directions increase and the stress in the Y -direction decreases, we can see in Fig. (5.4) that the P_X -wave and the P_Z -wave velocities increase and the P_Y -wave velocity decreases. We observe from parts B and C a larger increase of the velocity in the X - and Z -directions than in the Y -direction. In Fig. (5.5), six combinations of shear-

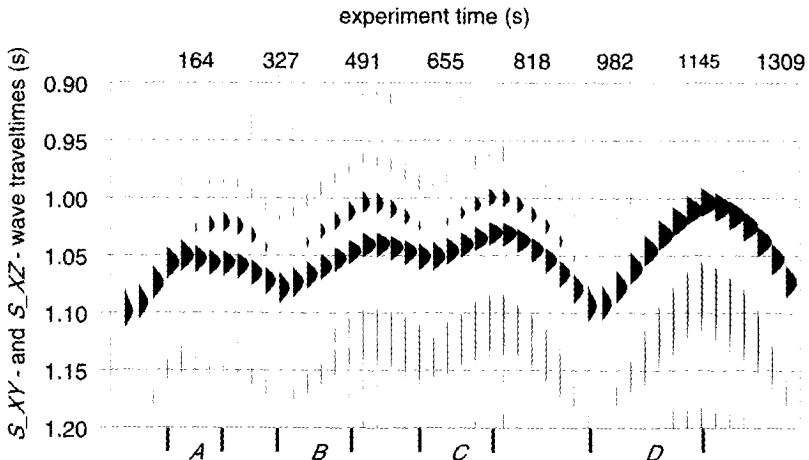


Figure 5.3: Shear-wave splitting in the X -direction during load-cycle ABCD. Transmitting and receiving transducers are positioned diagonally in the YZ -plane.

waves are shown. The S_{XZ} and S_{ZX} shear-waves (first subscript denotes propagation direction and second subscript denotes polarization direction) which neither polarize nor propagate in the Y -direction show an overall faster and different velocity behavior than the other four shear-waves, S_{XY} , S_{ZY} , S_{YX} , and S_{YZ} , which either polarize or propagate in the Y -direction.

Fig. (5.6) shows the P_X -wave velocity versus stress. The velocity lines show an approximately linear increase of velocity with stress. The slopes of the lines do not differ much because the stress change in the X - and Z -directions is similar for all four lines. The P_X -wave velocity does not show a clear dependence upon the stress changes in the Y -direction. The P_Y -wave stress-velocity pattern in Fig. (5.7) shows a strong dependence upon the stress in the Y -direction. P -waves are therefore predominantly affected by the normal component of the stress tensor that lies in the direction of propagation. The two-dimensional sensitivity of S -waves becomes clear when we look at the S -wave stress-velocity plots. The S_{XZ} -wave velocity plotted in Fig. (5.8) shows no appreciable dependence on the stress change in the Y -direction because of the almost uniform slopes of the velocity lines. We observe that, apart from a scaling factor, the stress-velocity pattern of Fig. (5.8) matches almost exactly the stress-velocity pattern in Fig. (5.6) because the P_X -wave and the S_{XZ} -wave experience equal stress changes in their

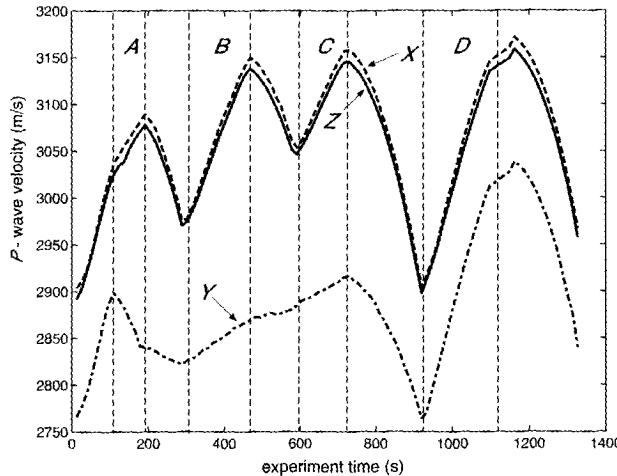


Figure 5.4: *Velocities of compressional-waves propagating in the X-, Y-, and Z-directions during load cycle ABCD.*

propagation and polarization directions. The S_{XY} -wave velocity in Fig.(5.9) shows a stronger dependence on the stress in the Y -direction. However the correlation with the stress in the Y -direction is less pronounced compared to the stress-velocity pattern observed in Fig. (5.7) for the P_Y -case.

5.2.4 Conclusions

The experiments on the Colton sandstone described in this section show how certain changes in a triaxial stress state cause changes in the velocities and anisotropy of compressional- and shear-waves. We observe that for all applied stress patterns compressional- and shear-waves are most sensitive to those normal stresses that lie in the propagation or polarization directions of the wave. Consequently, compressional-waves are predominantly sensitive to one direction of the prevailing stress state, whereas shear-waves show a two-dimensional sensitivity to stress. A split shear-wave pair is sensitive to all components of the stress tensor. The sensitivity analysis shows how experiments must be designed in order to acquire sufficient data, in terms of polarization and propagation directions, for stress inference purposes.

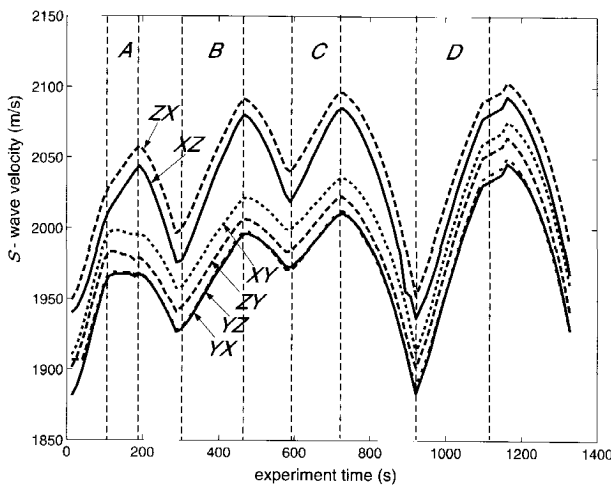


Figure 5.5: Velocities of shear-waves with propagations (first letter) and polarizations (second letter) in the X -, Y -, and Z -directions during load cycle ABCD.

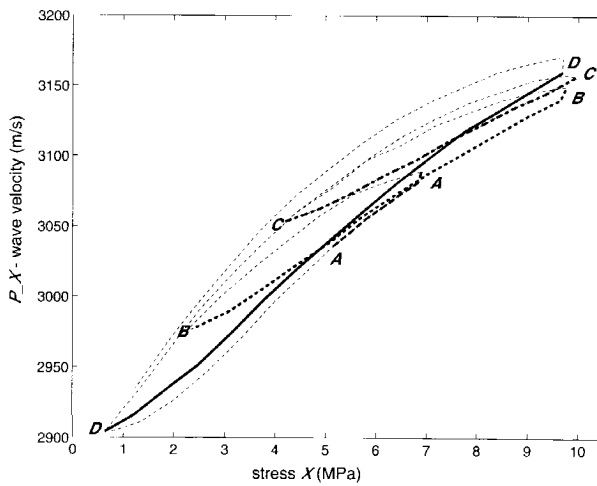


Figure 5.6: Velocity of a compressional-wave propagating in the X -direction versus the normal stress in the X -direction during load cycle ABCD.

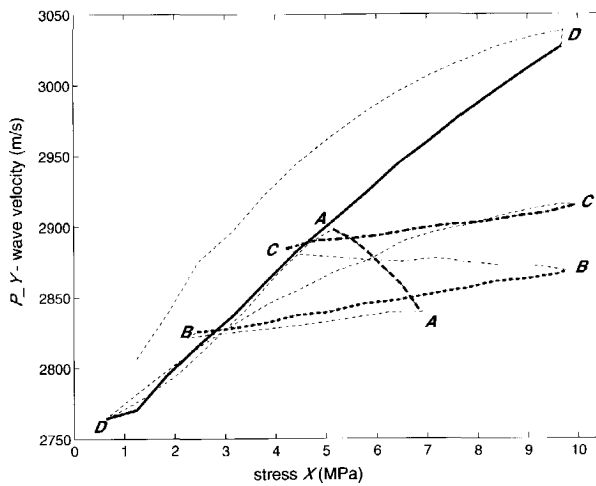


Figure 5.7: Velocity of a compressional-wave propagating in the Y-direction versus the normal stress in the X-direction during load cycle ABCD.

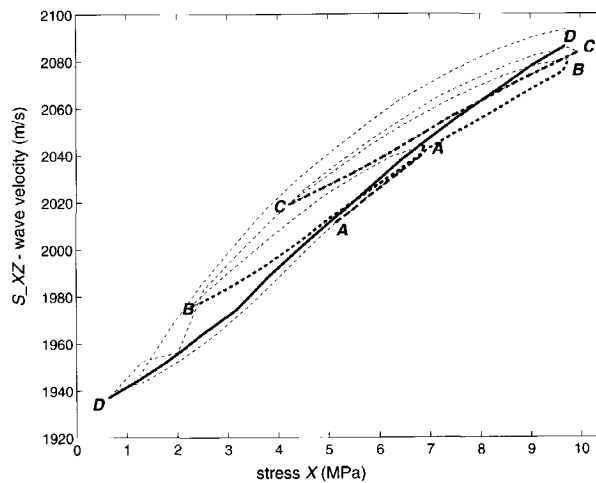


Figure 5.8: Velocity of a shear-wave with propagation in the X-direction and polarization in the Z-direction versus the normal stress in the X-direction during load cycle ABCD.

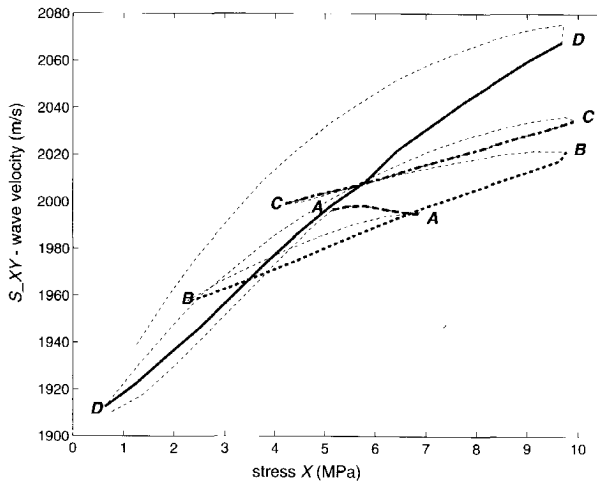


Figure 5.9: Velocity of a shear-wave with propagation in the X -direction and polarization in the Y -direction versus the normal stress in the X -direction during load cycle ABCD.

5.3 Experiments on the Flechtinger sandstone

The second series of experiments, conducted on the Flechtinger sandstone, are described in den Boer (1996); den Boer et al. (1996); den Boer and Fokkema (1996).

5.3.1 Introduction

A second series of experiments was initiated for the following reasons. The stress range up to 10 MPa to which the Colton sandstone was subjected, as described in the previous section, is too low to encompass in-situ stresses which occur in a hydrocarbon reservoir, except for overpressured reservoirs, showing anomalous high pore fluid pressures, resulting in correspondingly low effective stresses. Therefore, the second series of experiments were conducted at stresses from 0 to 82 MPa. The experiments were primarily designed to simulate in-situ conditions of small gas reservoirs in the north of the Netherlands. The gas bearing sandstones of these reservoirs are part of the Rotliegend formations, hence the need for a Rotliegend sandstone sample. The outcrop Flechtinger Rotliegend sandstone was taken as a close representative of the in-situ reservoir Rotliegend sandstone.

After grinding and polishing the dimensions of the Flechtinger sandstone samples are $204 \times 204 \times 204 \text{ mm}^3 \pm 0.03 \text{ mm}$, parallel within 0.01 mm. The results shown in this chapter are after multiple loading cycles such that the anelastic effects, most prominent at the first loading, are largely excluded.

5.3.2 Quasi-static experiments

The triaxial stress ranges of the following experiments are shown in Fig (5.10). Two loading cycles, denoted by 'a' and 'b', respectively, are depicted. One for which all axial stresses are equal, i.e. $\tau_{11} = \tau_{22} = \tau_{33}$, and one, for which only the transverse axial stresses are equal, i.e. $\tau_{11} = \tau_{22} \neq \tau_{33}$. Both cycles, 'a' and 'b', contain an up loading and a down loading part. A loading rate of 5 kN/s (= 0.12 MPa/s) was used. In Fig. (5.11) the stress-strain curves in the three axis directions are shown. Except for a small deviation of the strains in the x_2 -direction, all directions show a similar strain response. The up and down loading curves show hysteresis due to nonlinear effects discussed in Section 3.3. No permanent deformation is visible at the end of the down loading part.

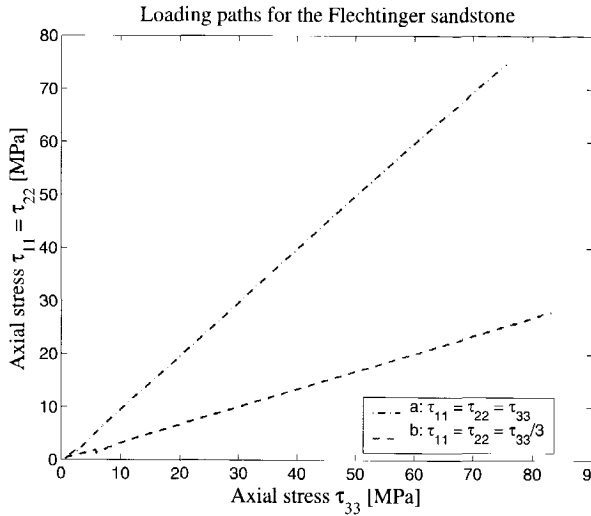


Figure 5.10: Axial stress τ_{33} versus axial stress $\tau_{11} = \tau_{22}$. Two experiments for a cube of the Flechtinger sandstone: loading cycle 'a', for which all axial stresses are equal, i.e. $\tau_{11} = \tau_{22} = \tau_{33}$, and loading cycle 'b', for which only the transverse axial stresses are equal, i.e. $\tau_{11} = \tau_{22} \neq \tau_{33}$.

By first smoothing the data of Fig. (5.11) with a Gaussian function we can calculate the tangent modulus E^t of Eq. (4.3) using finite differences. The modulus in the x_3 -direction, denoted by E_3^t , is shown in Fig. (5.12) as a function of the axial stress τ_{33} . During up loading we observe that E_3^t increases in two, approximately, linear stages, with a transition stress at 27 MPa. The first stage, from 13 to 37 GPa, shows a steeper ascent than the second stage, from 37 to 45 GPa. During down loading a similar division into two stages is observed, with the same transition stress of 27 MPa, but less pronounced. Also, the first stage of the up loading curve almost coincides with the down loading curve, whereas the second stage diverges from it. The different stress-strain behaviour during up loading and down loading is caused by the hysteresis effect, as described in Section 3.3, which can be explained by the process of frictional sliding of crack faces. The above evidence suggests that, according to this crack model, before the transition stress of 27 MPa, either frictional sliding does not occur, so only crack closure and opening causes the change in E_3^t , or this process is the same, but directionally reversed, during up loading and down loading. The E_3^t -modulus

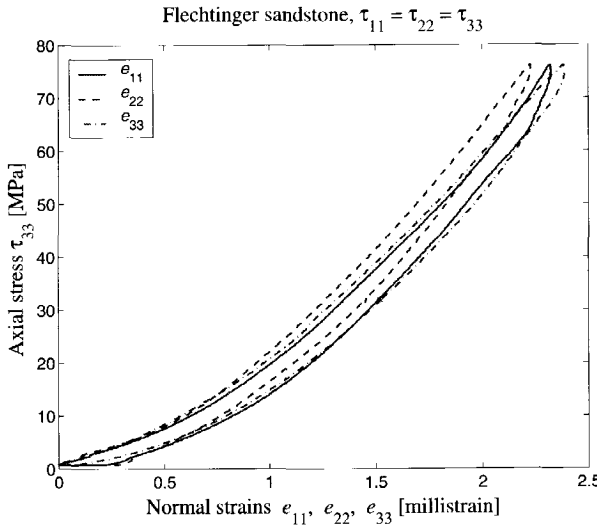


Figure 5.11: Axial strains e_{11} , e_{22} and e_{33} versus axial stress τ_{33} applied to a cube of the Flechtinger sandstone. Loading cycle 'a', all axial stresses equal: $\tau_{11} = \tau_{22} = \tau_{33}$.

reaches its highest value, at approximately 90 GPa, just after the onset of down loading. This observation is in agreement with Walsh (1965b), who suggests that the initial tangent Young's modulus upon unloading is larger because cracks which have undergone sliding do not immediately slide back. According to Walsh (1965b) this E^t maximum is the best estimate of the true modulus of the rock matrix without cracks. The initial unloading modulus is quite difficult to obtain accurately, because of the stick-slip behaviour of the LVDT's and the sensitivity of the tangent to the local irregular stress-strain data.

Within the linear elastic theory, using Eq. (2.33), we have for vanishing pore pressure

$$K = \frac{P}{e_{mm}}, \quad (5.1)$$

in which the compression modulus K is the inverse of the compressibility κ , e_{mm} is the volumetric strain and P is the confining pressure. We introduce

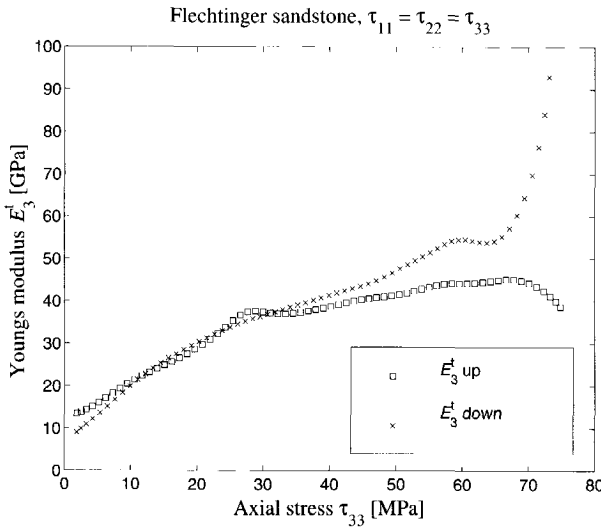


Figure 5.12: Axial stress τ_{33} versus Young's modulus in the three axis directions for a cube of the Flechtinger sandstone. Loading cycle 'a', all axial stresses equal: $\tau_{11} = \tau_{22} = \tau_{33}$.

the tangent compression modulus as,

$$K^t(P) = \frac{dP}{de_{mm}}. \quad (5.2)$$

The K^t -modulus is taken as a function of the confining pressure P . In Fig. (5.13) the K^t -modulus, calculated in a similar manner as E^t above, is depicted as a function of the confining pressure P . It ranges from 4 to 16 GPa during up loading, and from 32 to 4 GPa during down loading. A similar behaviour is observed as with the E^t in Fig. (5.12). The values of K^t are about a third of the values of E^t .

In Fig. (5.14) the stress-strain curves are shown for the loading path 'b', see Fig. (5.10), for which the transverse axial stresses are equal, and one-third, of the longitudinal axial stress. Observe that the transverse strains are much smaller than the longitudinal strains. Comparing the strains for this deviatoric stress state with the strains depicted in Fig. (5.11), for which all three applied axial stresses are equal, we observe that for the deviatoric case the transverse strains are smaller and that the longitudinal strain is larger.

The tangential Young's modulus E_3^t of Eq. (4.3) obtained from the data

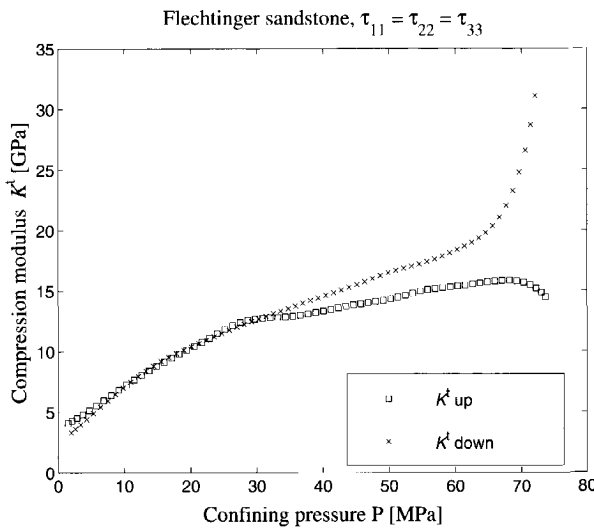


Figure 5.13: Confining stress P versus compression modulus for a cube of the Flechtinger sandstone. Loading cycle 'a', all axial stresses equal: $\tau_{11} = \tau_{22} = \tau_{33}$.

depicted in Fig. (5.14) is shown in Fig. (5.15). In this last figure lower values for E_3^t are observed than in Fig. (5.12). Also, in Fig. (5.15) the difference between up and down loading behaviour is smaller than in Fig. (5.12), perhaps because the deviatoric stress state facilitates frictional sliding along the crack faces.

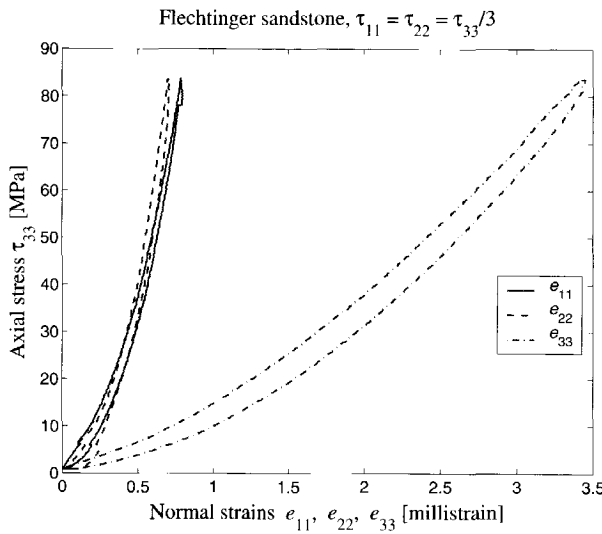


Figure 5.14: Axial strains e_{11} , e_{22} and e_{33} versus axial stress τ_{33} applied to a cube of the Flechtinger sandstone. Loading cycle 'b', transverse axial stresses equal: $\tau_{11} = \tau_{22} = \tau_{33}/3$.

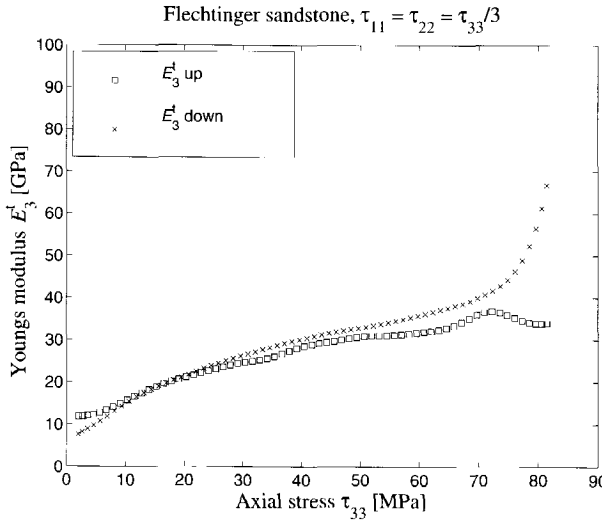


Figure 5.15: Axial stress versus Young's modulus in the three axis directions to a cube of the Flechtinger sandstone. Loading cycle 'b', transverse axial stresses equal: $\tau_{11} = \tau_{22} = \tau_{33}/3$.

5.3.3 Dynamic experiments

Using the same experimental set-up and transducer arrangement, as described in Section 5.2, and shown in Figs. (4.1) and (4.2), ultrasonic measurements were conducted during loading paths 'a' and 'b', depicted in Fig. (5.10). In Fig. (5.16) compressional-wave transmission recordings are shown during loading path 'a', from waves travelling in the x_3 -direction, as a function of the axial stress τ_{33} (horizontal axis) and transmission travel time (vertical axis). The wave form shows that the first arrival time decreases

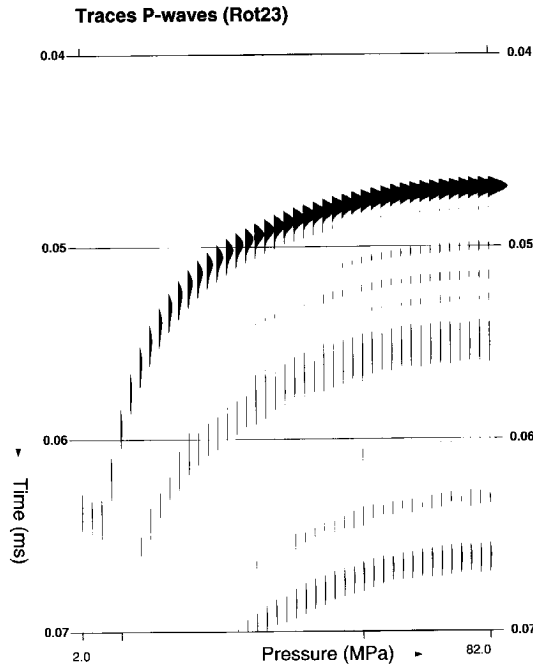


Figure 5.16: Compressional-wave transmission versus axial stress applied to a cube of the Flechtinger sandstone. All axial stresses equal: $\tau_{11} = \tau_{22} = \tau_{33}$.

with increasing stress towards an apparently asymptotic value. This observation has been described in numerous published experiments. The asymptotic behaviour is explained using the crack model by postulating that near the asymptote all cracks are closed and that the response to elastodynamic waves is close to the response that would be registered for the uncracked or intact rock. Another observation that we can make from Fig. (5.16) is that the peak amplitude of the transmitted wavelet increases with increasing stress.

Regarding the entire wavelet from low stress to high stress we measure a shortening of the time span it covers. The combined effect of the change in first arrival time and compression of the wave form can be represented by a scaling of the time axis, such that a recording obtained at one stress level can be transformed to a recording at another stress level (den Boer and Fokkema (1996)).

In Fig. (5.17) shear-wave transmissions in the x_3 -direction are shown using the same display as in Fig. (5.16). The same phenomena, of first arrival increase, peak amplitude increase and wave form compression, with increasing stress are observed for the shear-waves as these were observed for the compressional-waves.

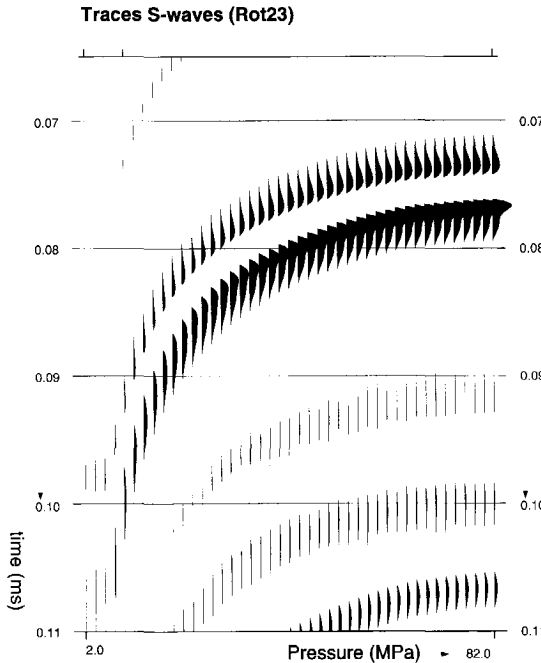


Figure 5.17: Shear-wave transmission versus axial stress applied to a cube of the Flechtinger sandstone. All axial stresses equal: $\tau_{11} = \tau_{22} = \tau_{33}$.

After picking the arrival times of the first arriving wave forms wave velocities are calculated by dividing the distance between the transmitting and receiving transducers by these travel times. The obtained velocities for the P-waves travelling in the x_1 , x_2 and x_3 -directions are shown in Fig. (5.18)

as a function of the axial stress τ_{33} . The stress-velocity curves show with

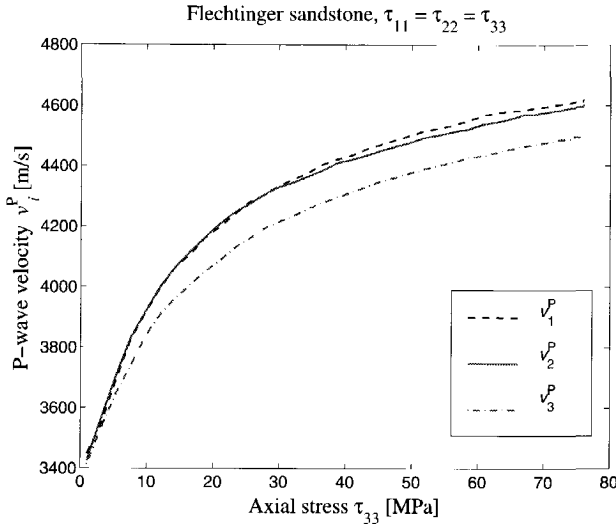


Figure 5.18: Axial stress in the x_3 -direction versus v_1^P , v_2^P and v_3^P wave velocities, applied to a cube of the Flechtinger sandstone. All axial stresses equal: $\tau_{11} = \tau_{22} = \tau_{33}$.

increasing stress a decreasing increment in the P-wave velocity per unit axial stress increase. Hence, the sensitivity of the P-wave velocity to stress is greatest at the low stress regime. The P-wave velocity in the x_3 -direction appear to be smaller than those in the other two transverse directions, which are approximately equal. The Rotliegend sample has been mounted such that its layering is perpendicular to the x_3 -direction. The measured anisotropy in P-wave velocity may therefore be caused by the layering of the sandstone. In Fig. (5.19) the following P-wave velocity anisotropy measure

$$a_{ij}^P = 2 \frac{v_i^P - v_j^P}{v_i^P + v_j^P}, \quad (5.3)$$

is depicted for two cases as function of the longitudinal stress. Both a_{13}^P and a_{23}^P increase fast from 0 to 10 MPa, then rise more slowly until 20 MPa after which these stay more or less constant at approximately 2.5 %. The phenomenon that the anisotropy reaches a constant value after the application of sufficient axial stresses may be explained by the presence of randomly

oriented defects or cracks which mask the layer-induced anisotropy. Progressive closure of these cracks during loading with equal axial stresses causes the layer-induced anisotropy to emerge. Both Figs. (5.18) and (5.19) show that the Rotliegend is slightly anisotropic with respect to the transverse direction. Hence, the anisotropy of this sandstone shows that it has orthorhombic or lower symmetry but that transverse isotropic symmetry is a good approximation.

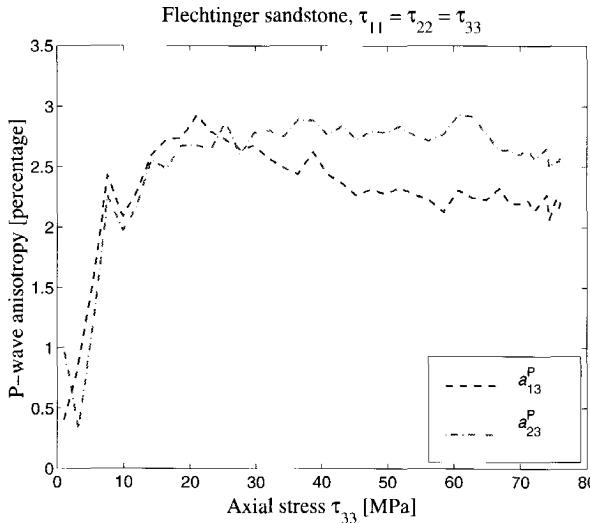


Figure 5.19: Axial stress in the x_3 -direction versus compressional-wave velocity anisotropy, between v_3^P and v_1^P , and v_3^P and v_2^P , applied to a cube of the Flechtinger sandstone. All axial stresses equal: $\tau_{11} = \tau_{22} = \tau_{33}$.

n

Fig. (5.20) shows six shear-wave velocities, two calculated from first arrival time picks in each axis direction (first subscript), from which each pair has two mutually perpendicular polarizations (second subscript). The S-wave curves have the same form as the P-wave curves in Fig. (5.18). The six curves lie close together but some differences are noticeable. The velocities v_{12}^S and v_{21}^S , from waves which either propagate or are polarized in the transverse direction, are larger than the other four velocities, from waves which either propagate or are polarized in the longitudinal direction. This observation can also be attributed to the layering of the sample. Introducing the

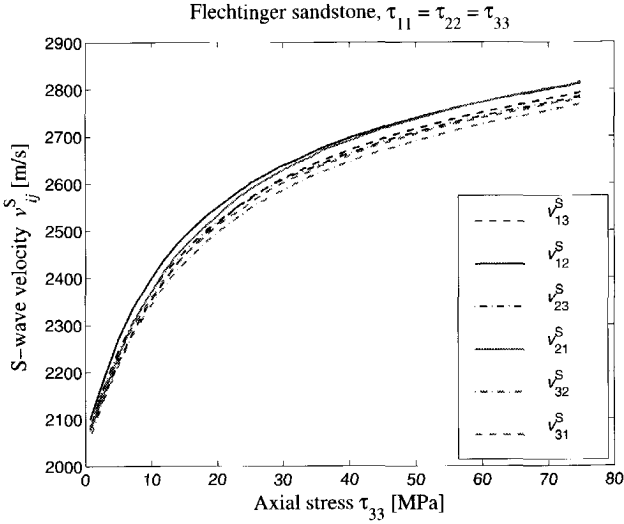


Figure 5.20: Axial stress in the x_3 -direction versus v_{13}^S , v_{12}^S , v_{23}^S , v_{21}^S , v_{32}^S , and v_{31}^S wave velocities, applied to a cube of the Flechtinger sandstone. All axial stresses equal: $\tau_{11} = \tau_{22} = \tau_{33}$.

following shear-wave anisotropy

$$a_{ijkl}^S = 2 \frac{v_{ij}^S - v_{kl}^S}{v_{ij}^S + v_{kl}^S}, \quad (5.4)$$

two combinations, a_{1231}^S and a_{1232}^S are depicted in Fig. (5.21). We observe a somewhat different behaviour than with the P-wave anisotropy depicted in Fig. (5.19). First a rapid rise after which the curves slowly decline. The average shear-wave anisotropy is approximately 1.5 % for the second slowly declining part which is a percentage point lower than for the P-wave anisotropy. The lower S-wave than P-wave anisotropy might be explained by the fact that a_{ijkl}^S must have at least one double subscript, e.g. a_{1231}^S and a_{1232}^S in Fig. (5.21), such that at least one of the S-waves of the S-wave pair is influenced by both the transverse and longitudinal directions through either its propagation or polarization direction.

Assuming that during the loading path 'a' in Fig. (5.10) the sample is approximately isotropic we may calculate the dynamic compression modulus

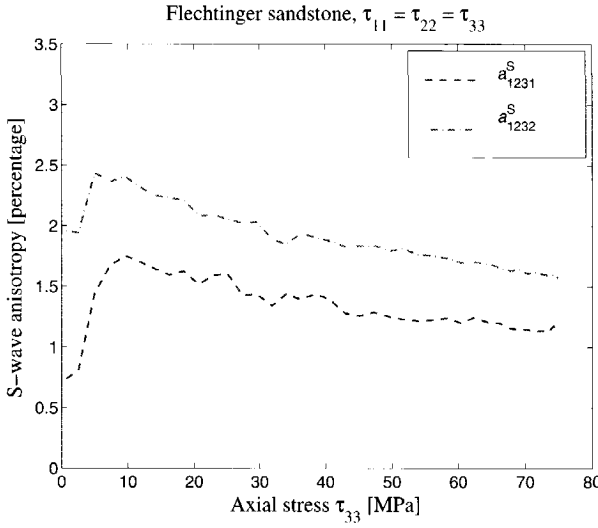


Figure 5.21: Axial stress in the x_3 -direction versus shear-wave velocity anisotropy, between v_{12}^S and v_{31}^S , and v_{12}^S and v_{32}^S , applied to a cube of the Flechtinger sandstone. All axial stresses equal: $\tau_{11} = \tau_{22} = \tau_{33}$.

from

$$K^{\text{dyn}} = \rho \left[(v^P)^2 - \frac{4}{3} (v^S)^2 \right]. \quad (5.5)$$

In Fig. (5.22) the dynamic compression modulus K^{dyn} is shown as a function of the confining stress P , using v_3^P and v_{31}^S , together with the quasi-static tangent compression modulus of Fig. (5.13). From this figure we see that the dynamic compression modulus is larger than the static compression modulus by approximately 10 to 12 GPa over the entire stress range of 0 to 80 MPa. Hence the sample reacts stiffer to dynamic strains than to quasi-static strains. The shape of both curves is more or less the same, showing a similar kind of behaviour with stress.

The following figures were made using loading path 'b' of Fig. (5.10), where the transverse axial stresses are one third of the longitudinal axial stress. Fig. (5.23) shows the P-wave velocities v_i^P as a function of the axial stress τ_{33} . In this figure the P-wave velocity in the longitudinal direction is larger than the other two velocities in the transverse directions, the latter two being approximately equal. This is in contrast with the curves shown in

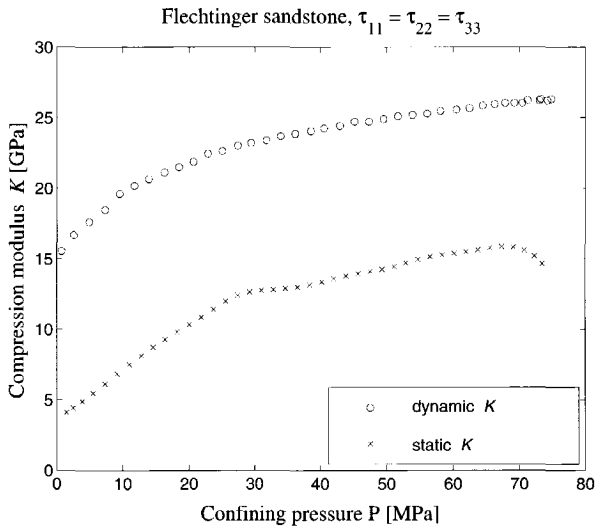


Figure 5.22: Axial stress in the x_3 -direction versus dynamic and static compression modulus, applied to a cube of the Flechtinger sandstone. All axial stresses equal: $\tau_{11} = \tau_{22} = \tau_{33}$.

Fig. (5.18) where the velocity in the longitudinal direction is smaller than in the transverse directions. This is explained by postulating that the P-wave anisotropy of Fig. (5.23) is stress-induced as well as layer-induced, whereas the anisotropy observed in Fig. (5.18) is probably only layer-induced. In Fig. (5.24) the P-wave anisotropies a_{31}^P and a_{32}^P are shown as a function of τ_{33} . Both anisotropies increase steeply until 10 MPa, after which these increase less rapidly per unit stress increase, and then decrease somewhat with increasing stress. The average P-wave anisotropy after 20 MPa is approximately 5 %. The stress-induced P-wave anisotropy for this stress region is this last value of 5%, representing the total anisotropy, minus the layer- or texture-induced anisotropy of -2.5 %, which can be obtained from Fig. (5.19), giving a value of approximately 7.5 %. The near constancy of the anisotropy after 20 MPa is reflected by the invariant layering and stress ratio's.

In Fig. (5.25) the same combination of S-waves is shown as in Fig. (5.20) but now for loading path 'b'. One observes that the S-wave velocities of waves which propagate and are polarized in the transverse directions, v_{12}^S and v_{21}^S , are slower than the other waves which either propagate or are polarized in the longitudinal direction. This observed anisotropy is stress-induced and re-

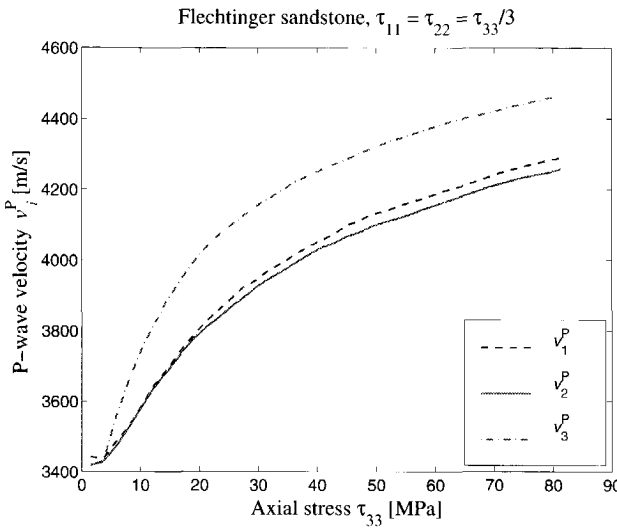


Figure 5.23: Axial stress in the x_3 -direction versus v_1^P , v_2^P and v_3^P wave velocities, applied to a cube of the Flechtinger sandstone. Transverse axial stresses equal: $\tau_{11} = \tau_{22} \neq \tau_{33}$.

versed to the layer- or texture-induced anisotropy in Fig. (5.20) for which the transverse velocities are the largest. Using Eq. (5.4) the S-wave anisotropy measures a_{3112}^S and a_{3212}^S are depicted in Fig. (5.26). Both anisotropies increase rapidly from negative to positive values over the stress range of 0 to 10 MPa. Subsequently, these increase more slowly from 10 to 20 MPa, after which we see a levelling off to sustained values of approximately 2%. The stress-induced S-wave anisotropy is this total anisotropy of 2% minus the layer-induced anisotropy of -1.5%, shown in Fig. (5.21), giving a value of approximately 3.5 % for the 20 to 80 MPa stress range.

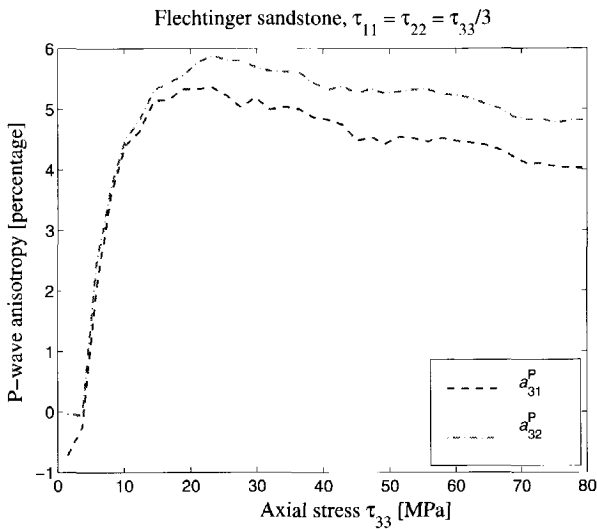


Figure 5.24: Axial stress in the x_3 -direction versus compressional-wave velocity anisotropy, between v_3^P and v_1^P , and v_3^P and v_2^P , applied to a cube of the Flechtinger sandstone. Transverse axial stresses equal: $\tau_{11} = \tau_{22} \neq \tau_{33}$.

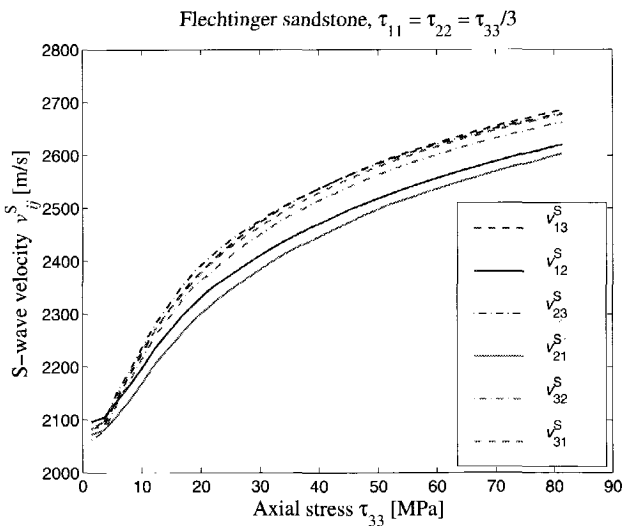


Figure 5.25: Axial stress in the x_3 -direction versus v_{13}^S , v_{12}^S , v_{23}^S , v_{21}^S , v_{32}^S , and v_{31}^S wave velocities, applied to a cube of the Flechtinger sandstone. Transverse axial stresses equal: $\tau_{11} = \tau_{22} = \tau_{33}/3$.

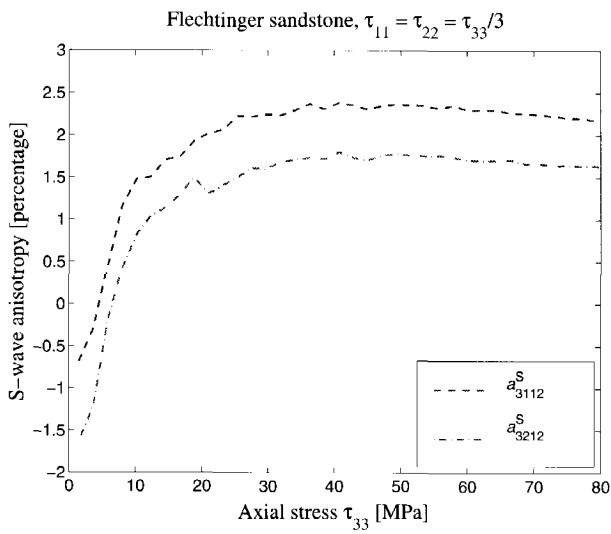


Figure 5.26: Axial stress in the x_3 -direction versus shear-wave velocity anisotropy, between v_{31}^S and v_{12}^S , and v_{32}^S and v_{12}^S , applied to a cube of the Flechtinger sandstone. Transverse axial stresses equal: $\tau_{11} = \tau_{22} = \tau_{33}/3$.

5.3.4 Sensitivity of wave velocities to stress

In Section 5.2 the sensitivity of ultrasonic elastodynamic waves to stress is investigated for the Colton sandstone. A number of loading paths were applied up to 10 MPa. In order to measure this stress sensitivity for a more extensive coverage of the stress space, and to have it tested for a Rotliegend sandstone, the loading sequence depicted in Fig (5.27) was devised. Using

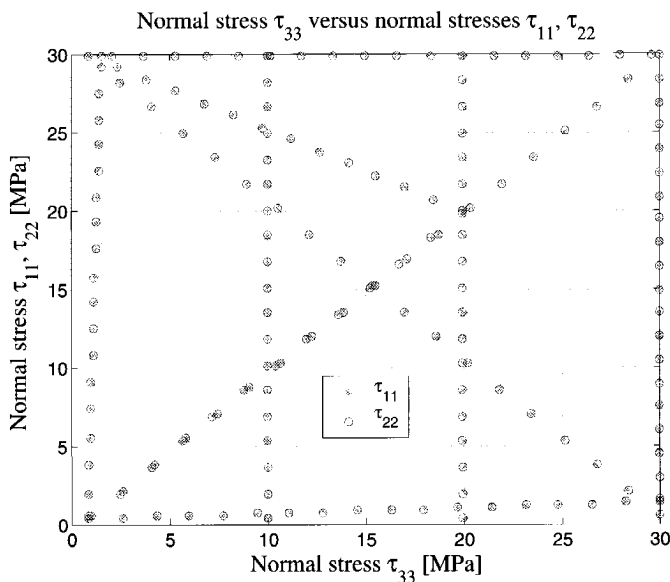


Figure 5.27: Loading sequence which covers the three-dimensional normal stress space from 0 to 30 MPa. Transverse axial stresses equal: $\tau_{11} = \tau_{22} \neq \tau_{33}$.

the transducer configuration described in Section 4.3 and shown in Fig. (4.2) the first arrival travel times of the following waves are converted to velocities:

- P-wave in the x_1 -direction,
- S-wave propagating in the x_1 -direction and polarized in the x_2 -direction,
- P-wave in the x_3 -direction,
- S-wave propagating in the x_3 -direction and polarized in the x_1 -direction,

- quasi P-wave travelling diagonally from one transducer of the transducer pair that is aligned in the x_1 -direction to one transducer of the transducer pair that is aligned in the x_3 -direction.

The associated velocities, v_1^P , v_{12}^S , v_3^P , v_{31}^S and v_{13}^{qP} , are shown in Figs. (5.28), (5.29), (5.30), (5.31) and (5.32), respectively, as a function of the transverse stresses τ_{11} and τ_{22} , with $\tau_{11} = \tau_{22}$, and the longitudinal stress τ_{33} . The loading sequence preserves the approximate transverse isotropic symmetry of the Rotliegend sample. From Fig. (5.28) we observe that v_1^P is relatively insensitive to changes in the axial stress τ_{33} , whereas it is relatively sensitive to changes in the transverse axial stresses, τ_{11} and τ_{22} . The sensitivity for the transverse axial stresses decreases with increasing transverse axial stresses. The shape of the surface in Fig. (5.28) confirms the experimental findings in Section 5.2 which state that a pure P-wave is most sensitive to that normal stress which acts in its propagation-polarization direction.

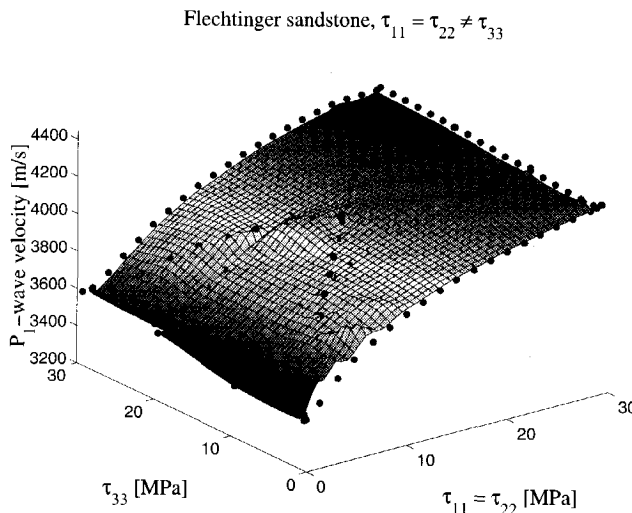


Figure 5.28: Transversely isotropic stress, 0-30 MPa, versus v_1^P

The velocity v_{12}^S in Fig. (5.29) shows, qualitatively, the same sensitivity to the transverse stress directions as v_1^P in Fig. (5.28). This is explained by the propagation and polarization directions of v_{12}^S which are both oriented in the transverse direction.

Flechtinger sandstone, $\tau_{11} = \tau_{22} \neq \tau_{33}$

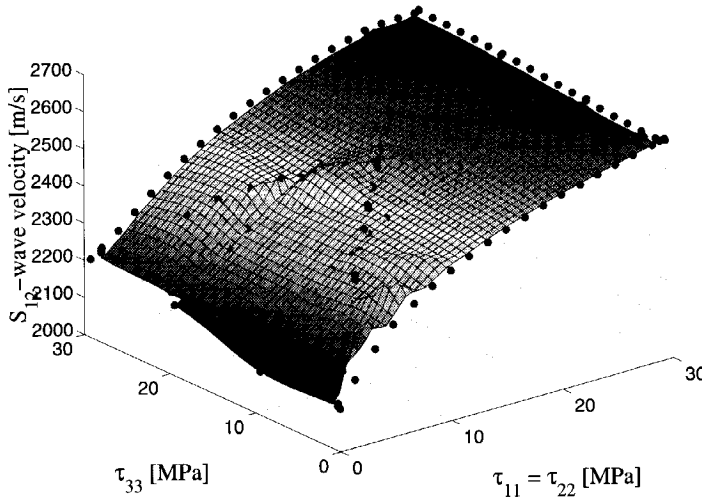


Figure 5.29: Transversely isotropic stress, 0-30 MPa, versus v_{12}^S

In Fig. (5.30) the velocity v_3^P shows a higher sensitivity to the longitudinal axial stress than to the transverse axial stresses because its propagation-polarization direction is aligned in the longitudinal direction.

From Fig. (5.31) we observe an approximately equal sensitivity of v_{31}^S to the stress in the transverse directions as to the stress in the longitudinal direction. Because the shear-wave associated with the velocity v_{31}^S propagates in the longitudinal direction and is polarized in the transverse direction it experiences both longitudinal and transverse stress changes. The velocity v_{31}^S at zero longitudinal stress and 30 MPa transverse stress is approximately 2400 m/s. At 30 MPa longitudinal stress and 0 MPa transverse stress this velocity measures approximately 2350 m/s. Hence, the velocity change as a function of transverse stress is somewhat larger than the velocity change as a function of the longitudinal stress. Therefore, the sensitivity of this shear-wave to stress changes seems larger with respect to the polarization direction than with respect to the propagation direction. However this reasoning assumes that the polarization and propagation are perpendicular and directed along the pressure machine's axis directions, which is the case for exact transverse isotropy with symmetry axis along the x_3 -direction. But we already concluded from the P- and S-wave velocity anisotropies that the

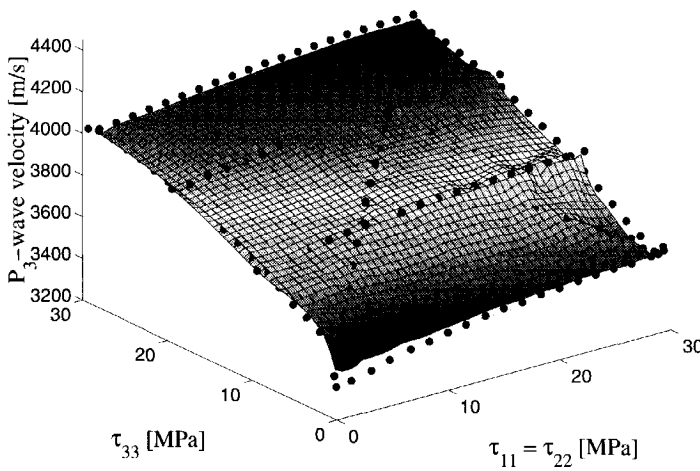


Figure 5.30: Transversely isotropic stress, 0-30 MPa, versus v_3^P

Rotliegend samples deviates somewhat from this symmetry. Hence, the velocity difference from which the conclusion is drawn with respect to the relative sensitivity of the propagation and polarization directions to stress may be attributed to the non-conformance of the sample to ideal transverse isotropic symmetry.

In Fig. (5.32) the velocity v_{13}^{qP} of a quasi P-wave is shown as a function of transverse and longitudinal axial stresses. The prefix quasi is added because the wave travels at an inclination of 45 degrees with respect to the principal axes of the presumed transversely isotropic sample. One can show that in such a direction the propagation and polarization directions of the P-wave are not aligned but diverge somewhat depending on orientation with the principal axes. The quasi P-wave associated with the velocity v_{13}^{qP} travels from a x_1 is constant to a x_3 is constant plane. Propagating and polarized in the (x_1, x_3) -plane the wave shows, in Fig. (5.32), approximately equal sensitivity to the longitudinal and the transverse stresses. Observe that the velocity v_{13}^{qP} of this quasi P-wave shows qualitatively the same kind of sensitivity as the velocity v_{31}^S of the S-wave of Fig. (5.31).

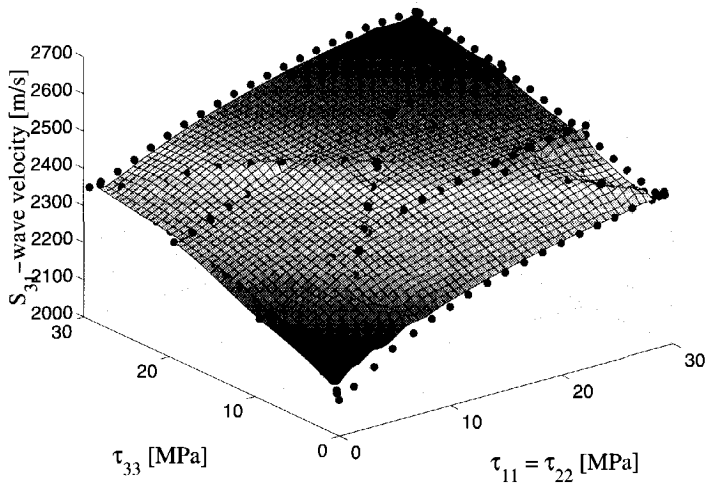


Figure 5.31: Transversely isotropic stress, 0-30 MPa, versus v_{31}^S

5.3.5 Conclusions

The quasi-static E_3^t shows that the Rotliegend sample has a nonlinear stress-strain behaviour by increasing with increasing stress and decreasing with decreasing stress. Its highest value of approximately 90 GPa is obtained just after down loading, which agrees well with Walsh (1965b), who suggests that the initial Young's modulus upon unloading is larger because cracks which have undergone sliding do not immediately slide back. The deviation of the up loading from the down loading E_3^t increases with increasing applied stress after a transition stress of 27 MPa. This may be caused by the fact that the sample has undergone deviatoric pre-stresses up to about 30 MPa, which may have altered frictional processes. The same qualitative observations are found for the tangent compression modulus K^t as a function of the confining stress, having values of approximately one-third of the tangent Young's modulus E^t . For deviatoric stresses, i.e. for $\tau_{11} = \tau_{22} = \tau_{33}/3$, E_3^t exhibits a smaller deviation of the up loading curve from the down loading curve, compared with the non deviatoric case for which $\tau_{11} = \tau_{22} = \tau_{33}$, probably because the deviatoric stress state facilitates frictional sliding along crack faces.

The dynamic data, identified with an oscillatory stress state superposed

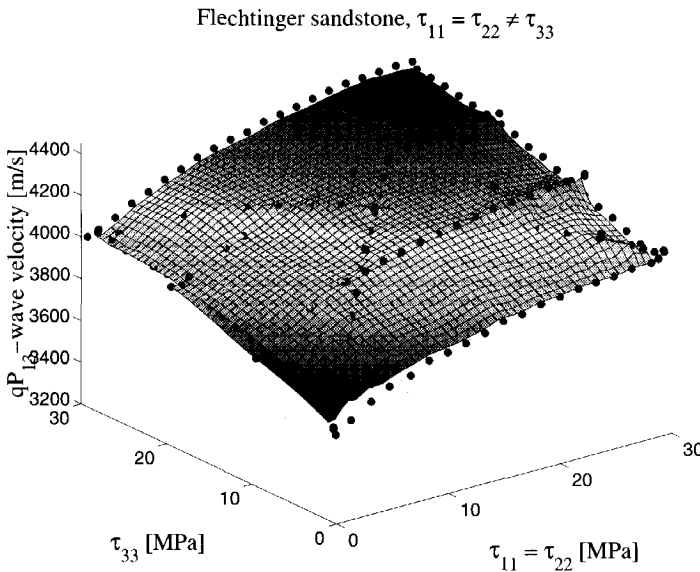


Figure 5.32: Transversely isotropic stress, 0-30 MPa, versus v_{13}^{qP}

on ambient applied stress, associated with relatively small strains as compared to the quasi-static experiments, is quantified in terms of wave velocity and stress. For equal axial stresses one observes an increasing P- and S-wave velocity with increasing stress. The velocity increase per unit stress increment decreases with increasing stress. Hence, the sensitivity of elastodynamic response to a changing ambient stress state is greatest for small stresses. We also observe that the peak amplitude of the wave form increases with increasing stress while the wave form itself compresses with respect to recording time. The cross-bedding of the aeolian sandstone appears through the velocity anisotropy of P- and S-waves. Waves which propagate or are polarized in the direction perpendicular to the layering are slower than the other waves. Application of the deviatoric stress state, $\tau_{11} = \tau_{22} = \tau_{33}/3$, shows stress-induced velocity anisotropy. The measured anisotropy is the sum of both intrinsic (layer-induced) and stress-induced anisotropies. In order to infer the change in a stress state from a measured changing anisotropy one must know the intrinsic anisotropy, which is static, to obtain the stress-induced component. The data in this section on the Rotliegend sandstone, obtained for axial stresses in the 0 to 30 MPa range, agrees with the conclusion from the data in section 5.2 on the Colton sandstone, for a few loading

paths from 0 to 10 MPa, i.e. that compressional- and shear-waves are most sensitive to those normal stresses that lie in the propagation or polarization directions of the wave. The respective sensitivities can easily be deduced from the orientations of the surfaces in the wave velocity versus longitudinal stress versus transverse stress graphs.

The dynamic modulus, calculated from P- and S-wave velocities, assuming isotropy under equally applied axial stresses, is an approximately 10 to 12 GPa larger as the quasi-static tangent compression modulus, obtained from strain measurements, over the stress range of 0 to 80 MPa during uploading. Hence, the sample reacts stiffer when subject to higher (oscillatory) stress rates. The approximate constant difference between the dynamic and quasi-static moduli over the entire stress range suggests a relation between the two which depends on the intrinsic properties of the Rotliegend. This would enable to infer a change in a quasi-static modulus from a change in the wave velocities given the knowledge of some intrinsic property of the sandstone.

5.4 Experiments on the Niederhausen and Bad Dürckheim sandstones

The third series of experiments, conducted on the Niederhausen and Bad Dürckheim sandstones, are described in Swinnen (1997).

5.4.1 Introduction

The Flechtinger Rotliegend sandstone is, due to its deep burial history, and consequent compaction, with the associated changes to its mineralogy (Section 4.4), a so-called tight sandstone with a relative low porosity of approximately 9 percent. The Rotliegend sandstone formations, forming gas reservoirs in the North of the Netherlands, show porosities of 20 percent and higher, and are less compacted than the Flechtinger formation. Because porosity and stress history are factors which influence the elasticity of a rock the Niederhausen and Bad Dürckheim sandstone samples were acquired to better match the reservoir sandstone. The sample descriptions and the location of the quarries were provided by Schutjens (1996). The results on the Flechtinger sandstone in the previous section were acquired after multiple loading such that anelastic effects are eliminated. In this section first loading experiments are described which investigate hysteresis and anelastic deformation.

5.4.2 Quasi-static experiments

In Fig. (5.33) the loading cycles of the experiments, on the Niederhausen and Bad Dürckheim sandstone samples, described in this section are shown. Two experiments are shown, which attempt to simulate possible in-situ conditions, one, denoted by loading cycle 'a', for which the horizontal axial stresses are one-half of the vertical axial stress, i.e. $\tau_{11} = \tau_{22} = \frac{1}{2} \tau_{33}$, and another, denoted by loading cycle 'b', for which the horizontal axial stresses are one-third of the vertical axial stress, i.e. $\tau_{11} = \tau_{22} = \frac{1}{3} \tau_{33}$. Both cycles ('main loops') contain during up loading a single loop ('lower loop') at lower stresses, a double loop at intermediate stresses ('intermediate loops'), and again a single loop at higher stresses ('upper loop'). In Figs. (5.34) and (5.35) the three axial strains, e_{11} , e_{22} and e_{33} versus the axial stress τ_{33} are shown, for the Niederhausen and Bad Dürckheim sandstones, respectively.

The top figures in Figs. (5.34) and (5.35) depict the results for loading cycle 'a', whereas, the bottom figures show the loading cycle 'b' results. We observe in Figs. (5.34) and (5.35) for loading cycle 'a', in the top figures, a smaller deviation between the two horizontal strains and the vertical strain, than for loading cycle 'b', in the bottom figures, for which the deviatoric stress are higher. Also, for both cycles, in Figs. (5.34) and (5.35), the e_{22} strain is smaller than the e_{11} strain, while $\tau_{11} = \tau_{22}$, which indicates a lower symmetry than the initially assumed layer-induced transverse isotropic symmetry with respect to the vertical x_3 -axis. The four inner loops, superposed on the main loop, display smaller strain changes per unit stress change than the main loop, showing that during the inner loops both rocks react stiffer than during the main loop. After unloading both the Niederhausen as well as the Bad Dürckheim sandstone show a substantial permanent deformation. The strains and the permanent deformation associated with the Niederhausen sandstone are approximately twice as large as the one measured for the Bad Dürckheim sandstone, which is confirmed by the core experiments described in Section 4.5, and explained on the basis of the mineralogies of both sandstones.

By first smoothing the data of Figs. (5.34) and (5.35) with a Gaussian function we can calculate the tangent modulus E^t of Eq. (4.3) using finite differences. This modulus, calculated in the x_3 -direction, is shown in Figs. (5.36) and (5.37) as a function of the axial stress τ_{33} . From these figures we discern, apart from an interrupted main up-loading curve and a main down-loading curve, the x-shapes associated with the four inner loops, similar to the ones observed for the core experiments of Section 4.5. The E^t values during the inner loops are, for a given axial stress τ_{33} , higher than at the main loop, while the main down-loading E^t values are higher than the main up-loading ones. The largest values are reached at the onset of down-loading of an inner loop.

The difference between the up- and down-loading main loop is also seen, after multiple loading excluding anelastic effects, in Fig. (5.15), for the Flechtinger sandstone, for which the loading path, $\tau_{11} = \tau_{22} = \tau_{33}/3$, is the same as in the bottom figures of Figs. (5.36) and (5.37). Comparing, observe that the difference between up- and down-loading Young's moduli is largest in the bottom figure of Fig. (5.36), and smallest for Fig. (5.15). The magnitude of this same difference in the bottom figure of Fig. (5.37) is in between that of the former two figures. This may be explained by the softer mineralogy of the Niederhausen with respect to the Bad Dürckheim, and the

difference between first loading, in Figs. (5.36) and (5.37), and the result of loading after multiple loading in Fig. (5.15).

The x-shapes of the inner loops reflect the hysteresis effect. Approximately half-way the stress interval of an inner loop, the down- and up-loading moduli are the same. During the first half of an inner loop stress interval the down-loading modulus is smaller than the up-loading modulus, whereas, during the second half of the stress interval the down-loading modulus exceeds the up-loading modulus, beyond the up-loading modulus maximum. This small inner loop behaviour is different from the main loop, in Figs. (5.36) and (5.37), with regard to the observation that during the main loop the up-loading modulus never exceeds the down-loading modulus. However, in Fig. (5.15) we do recognize a 'flattened' x-shape with a point of intersection between the up- and down-loading curves at approximately 15 MPa. This similarity is possibly caused by the fact that both the loading cycle in Fig. (5.15) and the inner loops in Figs. (5.36) and (5.37) are associated with elastic deformation.

The tangent Young's modulus is somewhat higher during loading cycle 'a' than during loading cycle 'b', other than that, there is not much difference between these two loading cycles. Observe that the two intermediate loops in Figs. (5.36) and (5.37), representing secondary and tertiary loading, almost coincide, indicating that after first loading anelastic effects are, for the most part, eliminated.

5.4.3 Dynamic experiments

Using the same experimental set-up and transducer arrangement, as described in Section 5.2, and shown in Figs. (4.1) and (4.2), ultrasonic measurements were conducted during loading paths 'a' and 'b', depicted in Fig. (5.33). In Figs. (5.38) and (5.39), P- and S-wave transmissions (top and bottom figure, respectively) are shown, as function of experiment time and wave travel time, during loading cycle 'b' ($\tau_{11} = \tau_{22} = \tau_{33}/3$), for the Niederausen and Bad Dürckheim, respectively. The geometry of the main loading loop with its four inner loop, as displayed in Fig. (5.33) is easily recognizable from these figures.

After picking the arrival times of the first arriving wave forms wave velocities are calculated by dividing the distance between the transmitting and receiving transducers by these travel times. The obtained velocities for the P-waves travelling in the x_1 , x_2 and x_3 -directions, during loading cycle 'a'

and 'b', are shown in Figs. (5.40) and (5.41), as a function of the experiment time, for the Niederhausen and Bad Dürckheim sandstones, respectively. We observe that in all four figures the P-wave velocities change per unit experiment time is highest at low stress levels, i.e. at the beginning and end of the loading cycles. The permanent deformation at the end of both loading cycles, as is observed from Figs. (5.34) and (5.35), is apparent in Figs. (5.40) and (5.41), from the higher velocity at the end of a particular cycle, compared to the velocity at the beginning of a cycle. This effect is much larger for the Niederhausen sandstone than for the Bad Dürckheim sandstone, confirming the results from Figs. (5.34) and (5.35). The P-wave anisotropy between the horizontal P-wave velocities v_1^P , v_2^P and the vertical P-wave velocity v_3^P , in all four figures, is larger for loading cycle 'b' than for loading cycle 'a', the former having the largest deviatoric stresses. In Fig. (5.40) the anisotropy between v_1^P and v_2^P is quite small, as compared to Fig. (5.41), which shows a large anisotropy between these two velocities. Because the horizontal axial stresses are the same this horizontal P-wave anisotropy reflects an intrinsic anisotropy, attributed to texture or layering of the Bad Dürckheim sandstone. In order to obtain the stress-induced anisotropy one has to discern the intrinsic anisotropy from the total anisotropy, which in time-lapse measurements is facilitated by the fact that the intrinsic anisotropy is constant over time, excluding small stress effects.

In Figs. (5.42) and (5.43) the six shear-wave velocities, v_{13}^S , v_{12}^S , v_{23}^S , v_{21}^S , v_{32}^S , and v_{31}^S , are shown, in which the first and second subscripts designate propagation and polarization directions, respectively, using loading cycles 'a' and 'b' on the Niederhausen and Bad Dürckheim sandstones. Considering all four figures we discern, roughly, three groups of two shear-waves, $\{v_{13}^S, v_{31}^S\}$, $\{v_{32}^S, v_{23}^S\}$ and $\{v_{12}^S, v_{21}^S\}$, in order of velocity magnitude. Hence, the x_3 -direction has precedence over the x_1 - and x_2 -directions, reflecting stress-induced effects, and the x_1 -direction causes larger velocities than the x_2 -direction, explained by the intrinsic anisotropy, particularly for the Bad Dürckheim sandstone. Analogously to the observations from the Colton and Flechtinger sandstones in previous sections of this Chapter, the respective shear-wave is sensitive to those axial stresses which lie in its polarization or propagation direction.

In Figs. (5.44) and (5.45) the P-wave velocities in the three axis directions are depicted as a function of the axial stress τ_{33} , during loading cycle 'a', top figures, and loading cycle 'b', bottom figures, for the Niederhausen and Bad Dürckheim sandstones, respectively. As in Fig. (5.18) for the Flechtinger

sandstone the stress-velocity curves show with increasing stress a decreasing increment in the P-wave velocity per unit axial stress increase. The difference with Fig. (5.18) is that anelastic effects are included, especially during first loading, and the unloading curve is also shown, together with the four inner loops. In Fig. (5.44) the Niederhausen shows a larger difference in P-wave velocity between the up-loading and the down-loading curves, compared with the Bad Dürckheim of Fig. (5.45). This may be explained by the mineralogy of both sandstones (the Niederhausen contains less quartz and more weathered feldspar), causing anelastic effect to be more pronounced for the Niederhausen. The inner loops in Fig. (5.44) show a smaller velocity change per unit stress change than the main loops. In Fig. (5.45) their is no discernible difference between the inner and main loop velocity change per unit stress change. This latter observation may also be attributed to the 'harder' mineralogy of the Bad Dürckheim causing smaller anelastic effect. The observed P-wave velocity anisotropy in Figs. (5.44) and (5.45) has already been discussed with regard to Figs. (5.40) and (5.41).

Figs. (5.46) and (5.47) depict the axial stress versus the shear-wave velocities v_{21}^S and v_{31}^S for the Niederhausen and Bad Dürckheim sandstones, respectively. Qualitatively, the same observation can be made in these figures as in Figs. (5.44) and (5.45).

In Eq. (5.5) the dynamic compression modulus is calculated for the Flechtinger sandstone, assuming isotropy during loading path 'a' of Fig. (5.10). The loading cycles of Fig. (5.33) induce a transverse isotropy, superposed on the intrinsic anisotropy of the samples, hence isotropic dynamic elasticity moduli can not be calculated. Therefore the following dynamic elasticity modulus is introduced

$$M^{\text{dyn}} = \rho (v_3^P)^2, \quad (5.6)$$

in which v_3^P is the P-wave velocity in the x_3 -direction, and compared with the static tangent Young's modulus E^t of Eq. (4.3), evaluated in the x_3 -direction. In Figs. (5.48) and (5.49) the static tangent Young's moduli, of Figs. (5.36) and (5.37), are reproduced and superposed on the dynamic elastic moduli of Eq. (5.6), for the Niederhausen and Bad Dürckheim sandstones, respectively. Both E^t and M^{dyn} are calculated from stresses and strains in the x_3 -direction. We observe in Figs. (5.48) and (5.49) that the dynamic modulus is larger than the static modulus of the main loop, except for values just after the beginning of down-loading. The dynamic modulus curves are more or less parallel to

the main up-loading curve, which agrees with Fig. (5.22). Comparing the dynamic modulus with the static values in the inner loops we can see that the dynamic modulus is larger, or intersects, the up-loading inner loop curves, and intersects the down-loading curve. Hence, the dynamic modulus equals some small loop static modulus after some time instant after the onset of down-loading.

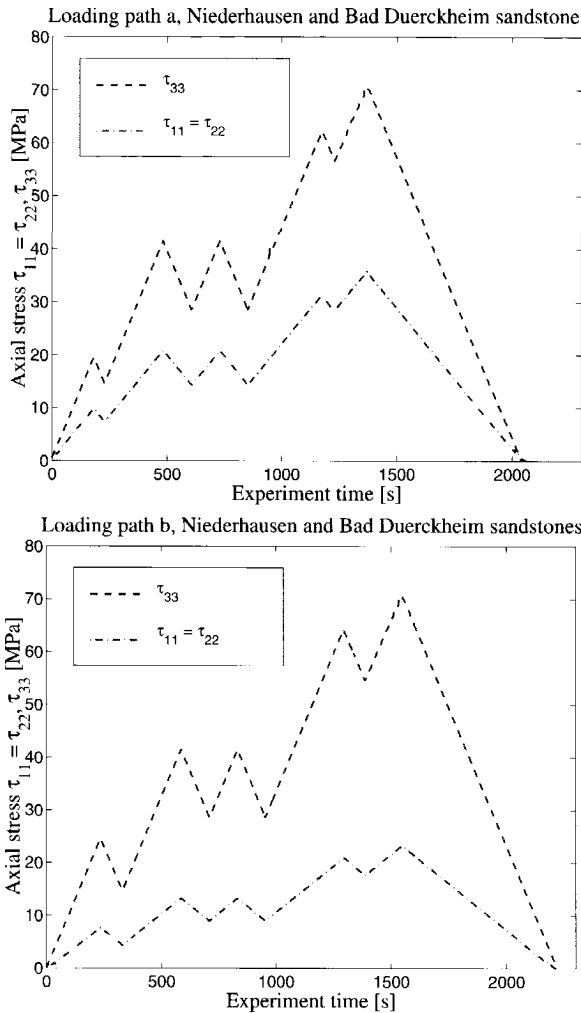


Figure 5.33: Axial stress τ_{33} versus axial stress $\tau_{11} = \tau_{22}$. Two experiments for cubes of Niederhausen and Bad Dürckheim sandstones: loading cycle 'a', for which the horizontal axial stresses are one-half of the vertical axial stress, i.e. $\tau_{11} = \tau_{22} = \frac{1}{2} \tau_{33}$ (top figure), and loading cycle 'b', for which the horizontal axial stresses are one-third of the vertical axial stress, i.e. $\tau_{11} = \tau_{22} = \frac{1}{3} \tau_{33}$ (bottom figure).

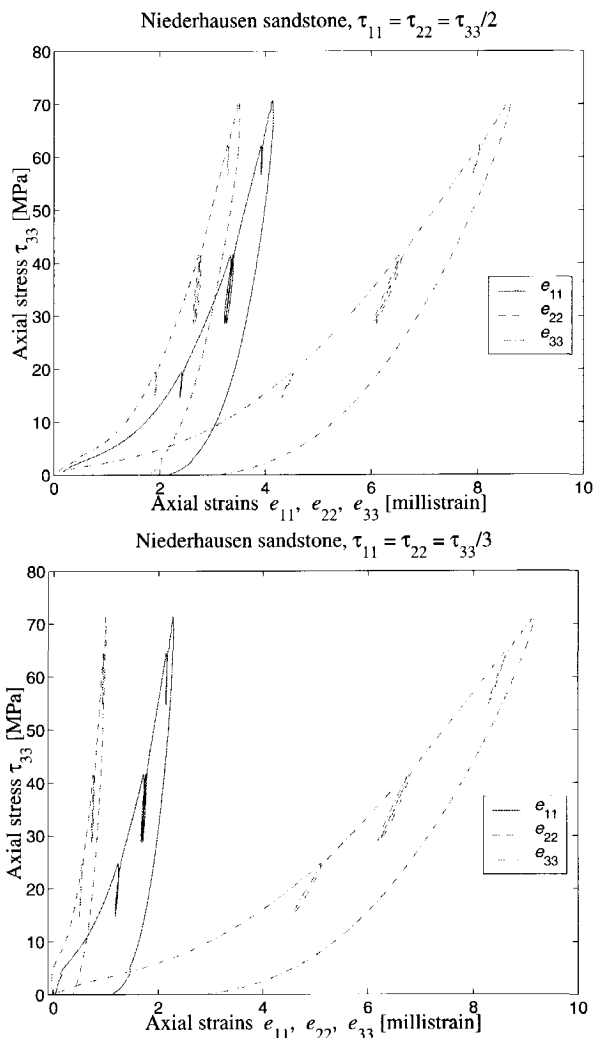


Figure 5.34: Axial strains e_{11} , e_{22} and e_{33} versus axial stress τ_{33} applied to a cube of the Niederhausen sandstone. Loading cycle 'a' (top figure), loading cycle 'b' (bottom figure).

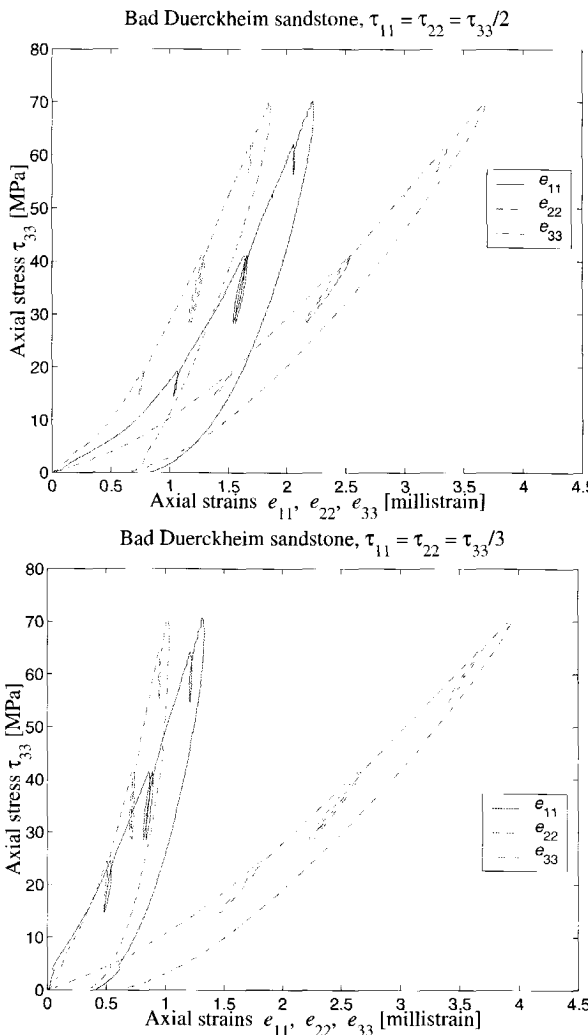


Figure 5.35: Axial strains e_{11} , e_{22} and e_{33} versus axial stress τ_{33} applied to a cube of the Bad Dürckheim sandstone. Loading cycle 'a' (top figure), loading cycle 'b' (bottom figure).

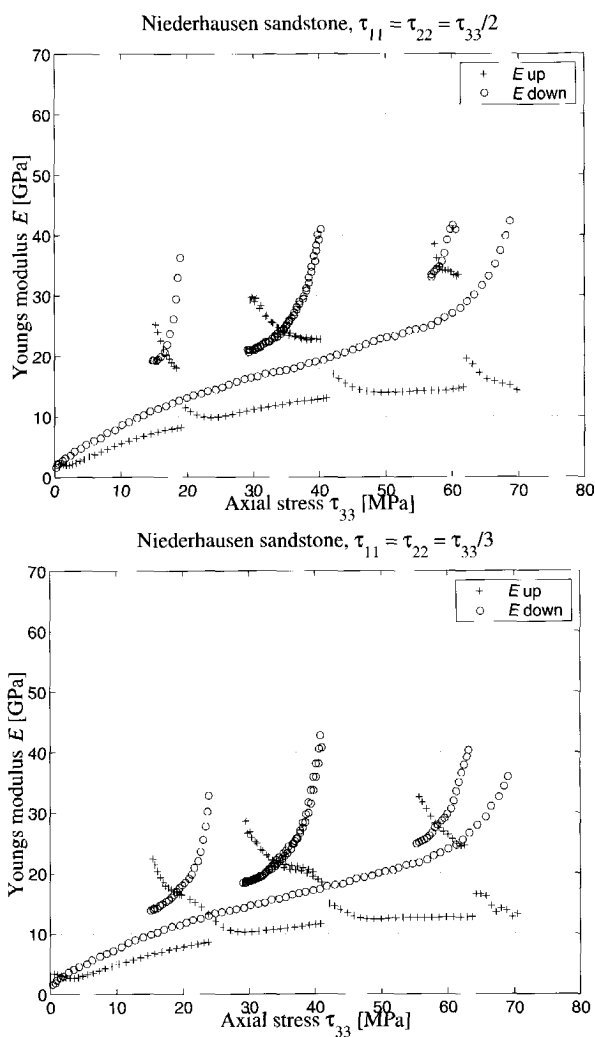


Figure 5.36: Axial stress τ_{33} versus tangential Young's modulus E_3^t applied to a cube of the Niederhausen sandstone. Loading cycle 'a' (top figure), loading cycle 'b' (bottom figure).

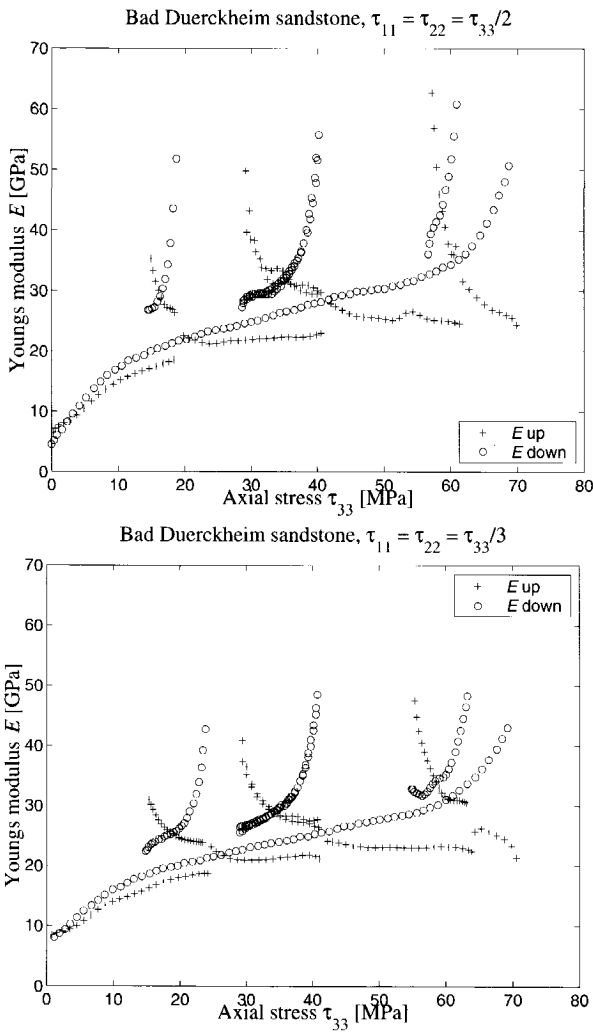


Figure 5.37: Axial stress τ_{33} versus tangential Young's modulus E_3^t applied to a cube of the Bad Dürckheim sandstone. Loading cycle 'a' (top figure), loading cycle 'b' (bottom figure).

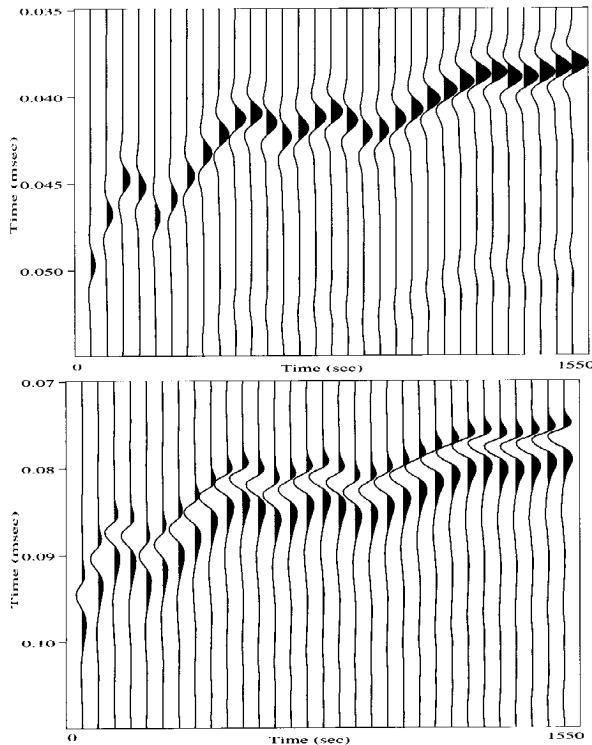


Figure 5.38: Compressional-wave (top figure) and shear-wave (bottom figure) transmissions through a cube of the Niederhausen sandstone. Horizontal and vertical axes display experiment time versus transmission travel time, respectively. Loading cycle 'b': $\tau_{11} = \tau_{22} = \tau_{33}/3$.

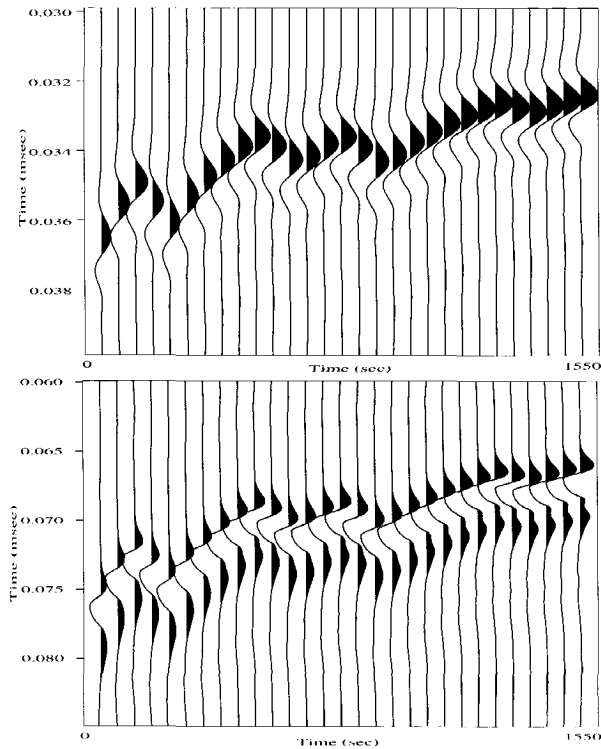


Figure 5.39: Compressional-wave (top figure) and shear-wave (bottom figure) transmissions through a cube of the Bad Dürckheim sandstone. Horizontal and vertical axes display experiment time versus transmission travel time, respectively. Loading cycle 'b': $\tau_{11} = \tau_{22} = \tau_{33}/3$.

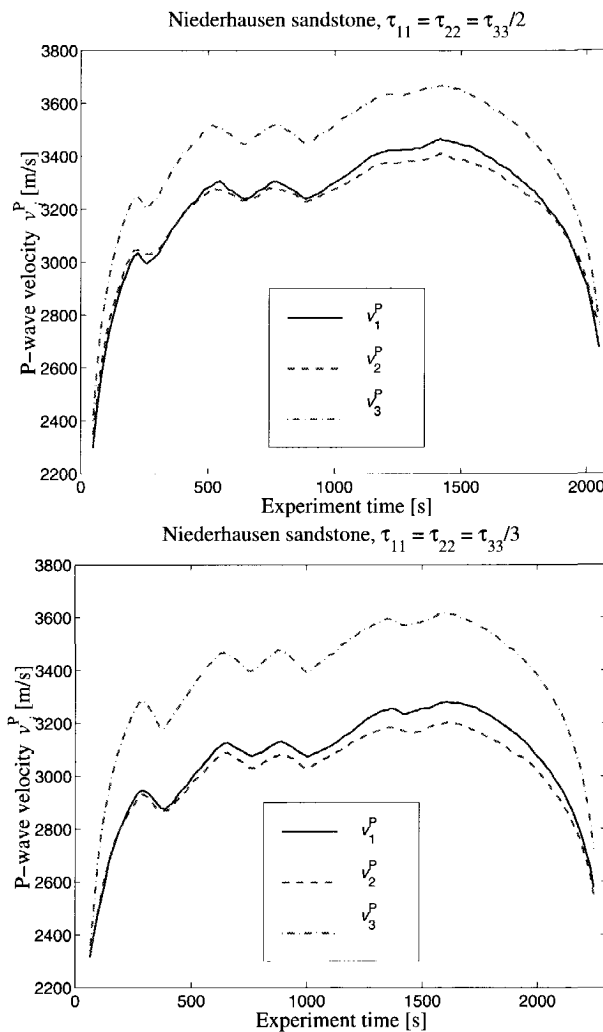


Figure 5.40: Experiment time during loading cycles 'a' (top figure) and 'b' (bottom figure), versus v_1^P , v_2^P and v_3^P wave velocities of a cube of Niederhausen sandstone.

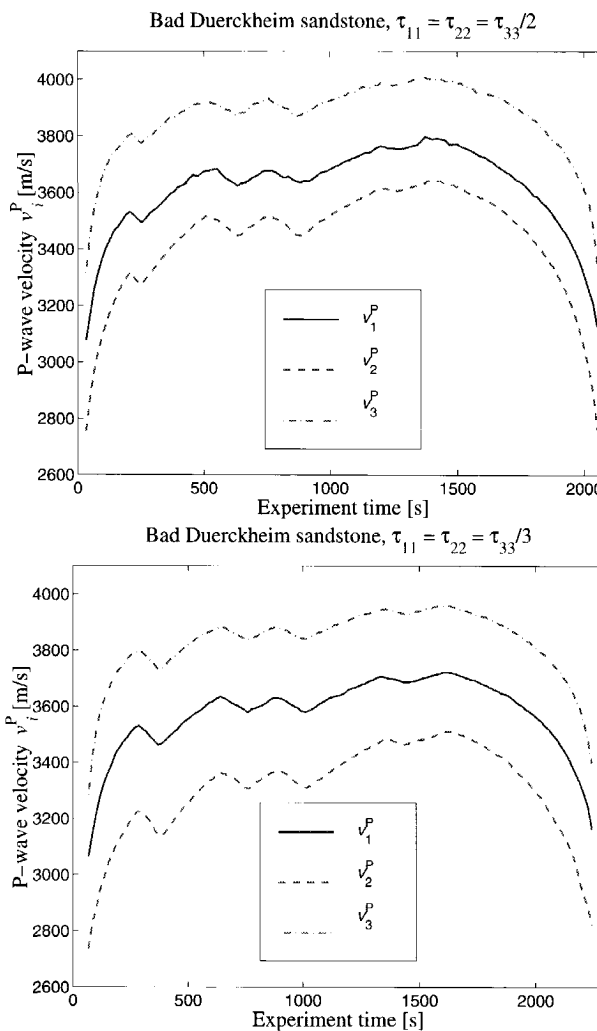


Figure 5.41: Experiment time during loading cycles 'a' (top figure) and 'b' (bottom figure), versus v_1^P , v_2^P and v_3^P wave velocities of a cube of Bad Dürckheim sandstone.

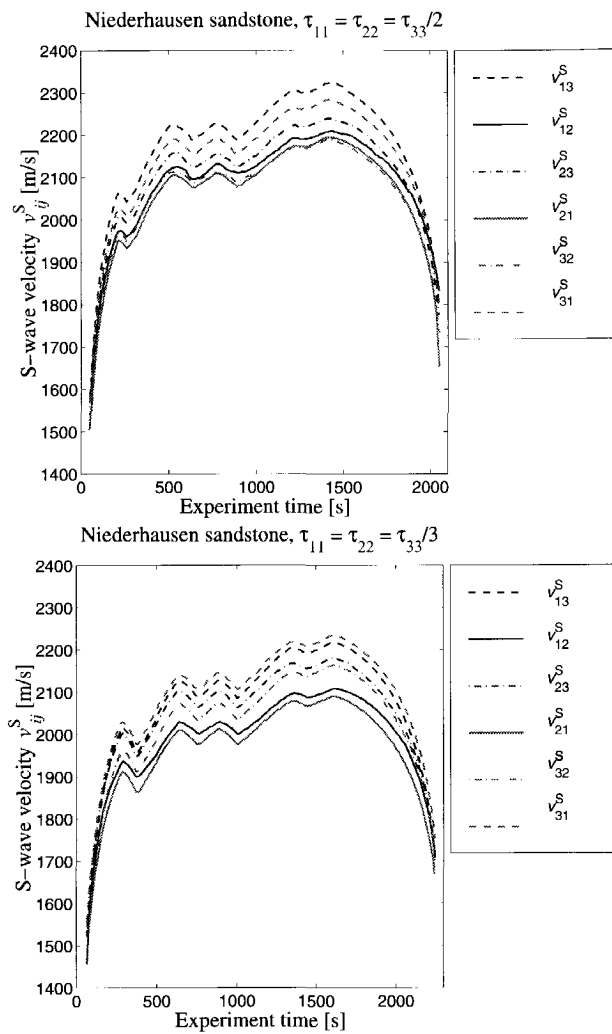


Figure 5.42: Experiment time during loading cycles 'a' (top figure) and 'b' (bottom figure), versus v_{13}^S , v_{12}^S , v_{23}^S , v_{21}^S , v_{32}^S , and v_{31}^S wave velocities of a cube of Niederhausen sandstone.

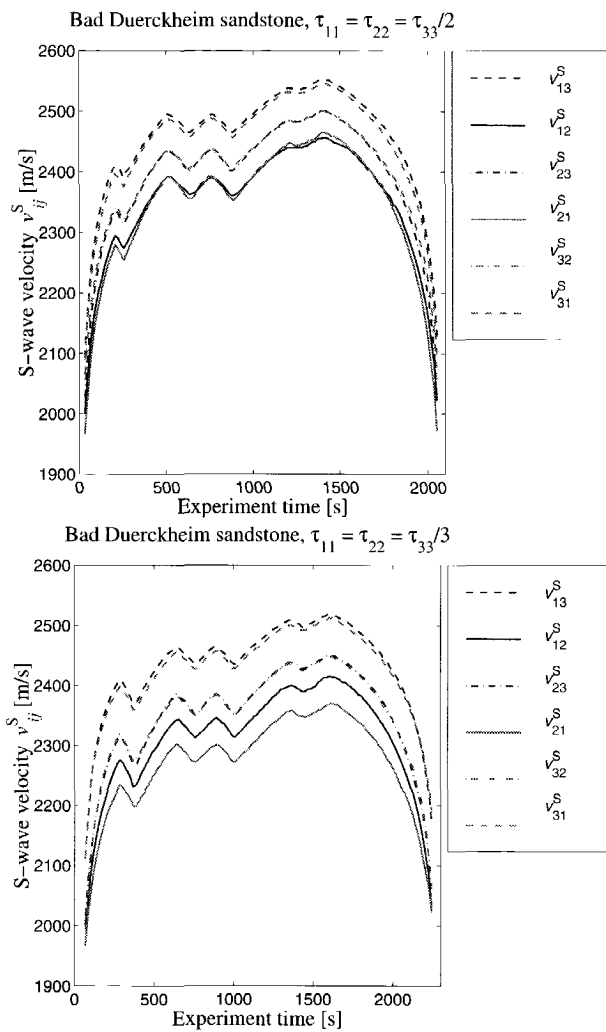


Figure 5.43: Experiment time during loading cycles 'a' (top figure) and 'b' (bottom figure), versus v_{13}^S , v_{12}^S , v_{23}^S , v_{21}^S , v_{32}^S , and v_{31}^S wave velocities of a cube of Bad Dürckheim sandstone.

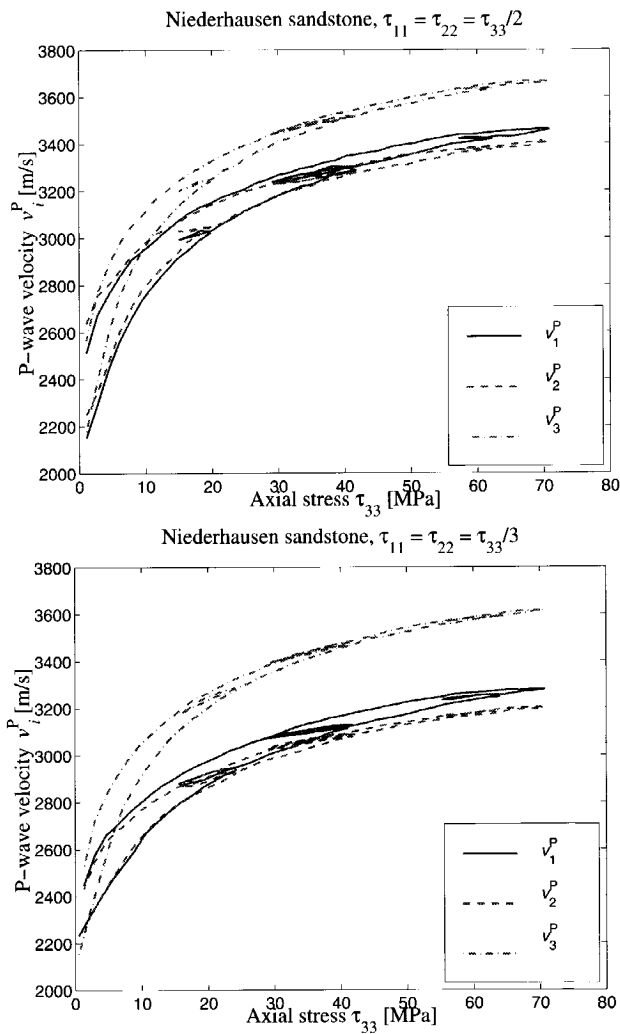


Figure 5.44: Axial stress τ_{33} during loading cycles 'a' (top figure) and 'b' (bottom figure), versus v_1^P , v_2^P and v_3^P wave velocities of a cube of Niederhausen sandstone.

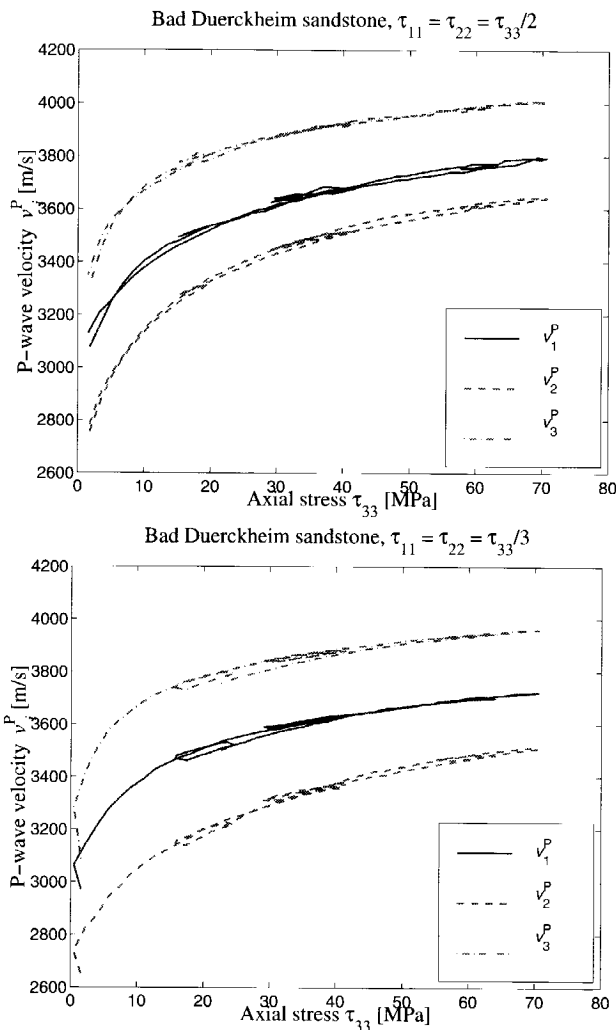


Figure 5.45: Axial stress τ_{33} during loading cycles 'a' (top figure) and 'b' (bottom figure), versus v_1^P , v_2^P and v_3^P wave velocities of a cube of Bad Dürckheim sandstone.

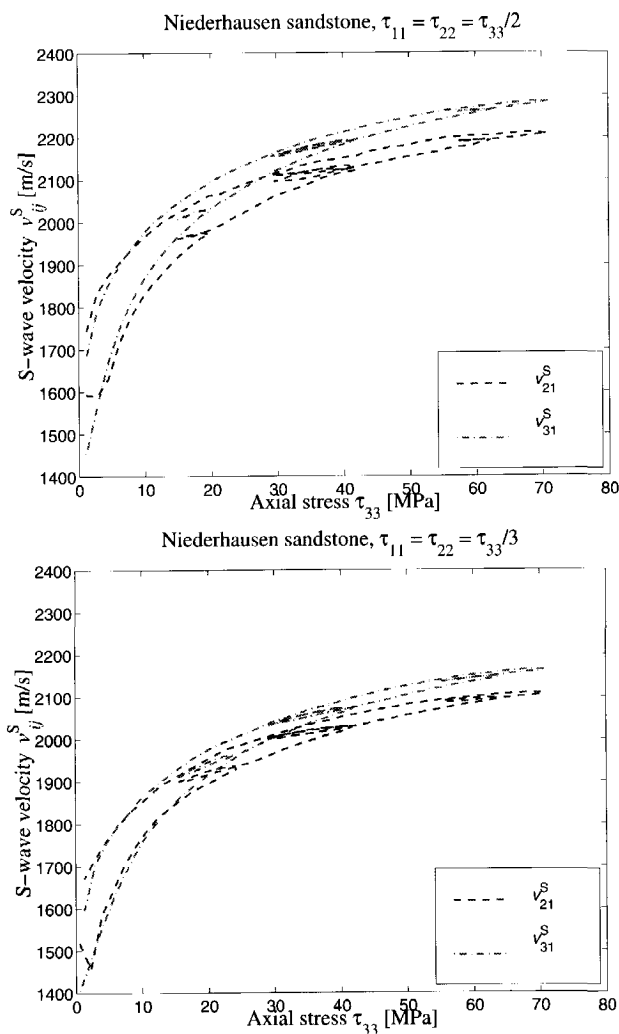


Figure 5.46: Axial stress τ_{33} during loading cycles 'a' (top figure) and 'b' (bottom figure), versus v_{21}^S and v_{31}^S wave velocities of a cube of Niederhausen sandstone.

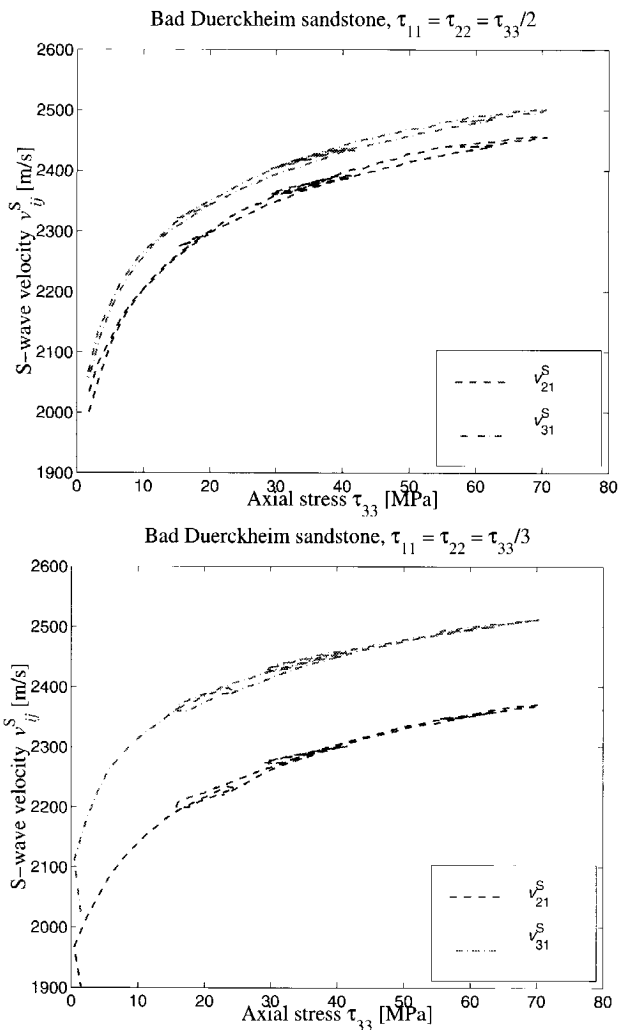


Figure 5.47: Axial stress τ_{33} during loading cycles 'a' (top figure) and 'b' (bottom figure), versus v_{21}^S and v_{31}^S wave velocities of a cube of Bad Dürckheim sandstone.

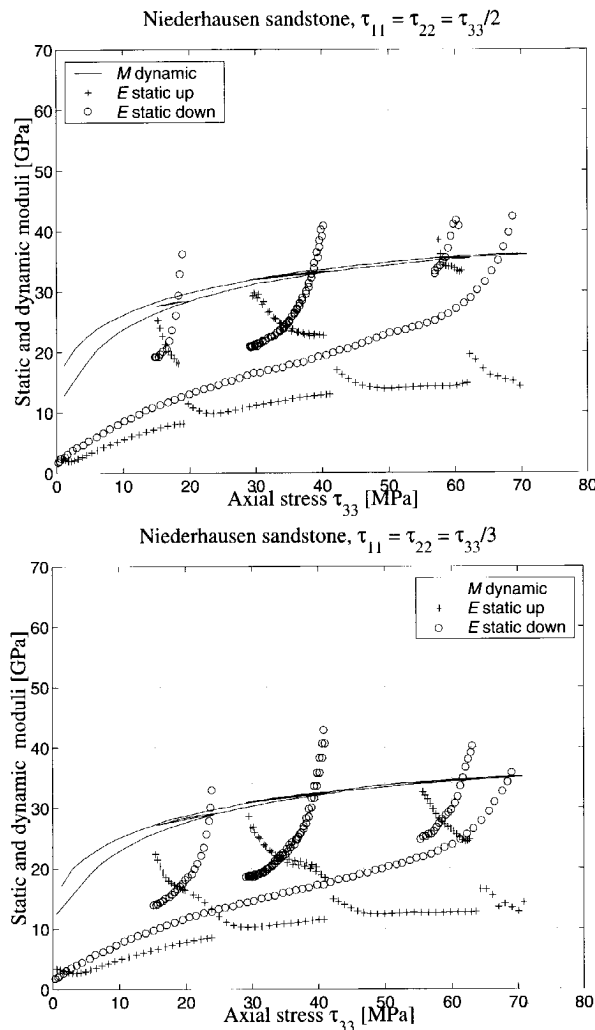


Figure 5.48: Axial stress τ_{33} during loading cycles 'a' (top figure) and 'b' (bottom figure) versus the static tangent Young's moduli of Eq. (4.3), in Figs. (5.36) and (5.37), reproduced and superposed on the dynamic elastic modulus M^{dyn} , of Eq. (5.6), for the Niederhausen sandstone.

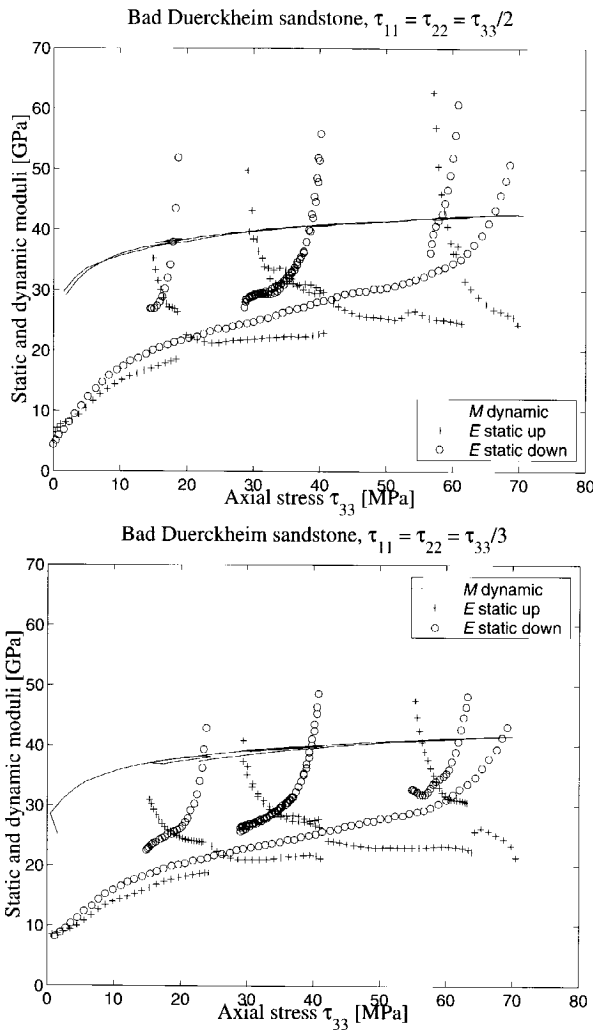


Figure 5.49: Axial stress τ_{33} during loading cycles 'a' (top figure) and 'b' (bottom figure) versus the static tangent Young's moduli of Eq. (4.3), in Figs. (5.36) and (5.37), reproduced and superposed on the dynamic elastic modulus M^{dyn} , of Eq. (5.6), for the Bad Dürckheim sandstone.

5.4.4 Conclusions

The third series of experiments investigates additionally, as compared to the second series, the phenomena associated with anelasticity, as these are observed at first loading. Also, the elasticity and wave velocities during small loading cycles superposed on the main up-loading path is investigated. The conclusions that can be drawn are listed below.

- The strains and the permanent deformation associated with the Niederhausen sandstone are approximately twice as large as the one measured for the Bad Dürckheim sandstone, which is confirmed by the core experiments described in Section 4.5, and explained on the basis of the mineralogies of both sandstones.
- The tangent Young's modulus E^t in Figs. (5.36) and (5.37) is higher during down-loading of the main loading cycle than during up-loading.
- The largest values for the tangent Young's modulus E^t are obtained at the onset of down-loading of an inner loop, which is confirmed by the core experiments described in Section 4.5.
- Approximately half-way the stress interval of an inner loop the down- and up-loading moduli are the same. During the first half of a inner loop stress interval, the down-loading modulus is smaller than the up-loading modulus, whereas, during the second half of the stress interval, the down-loading modulus exceeds the up-loading modulus. This phenomenon is the hysteresis effect.
- The two intermediate loops representing secondary and tertiary loading, almost coincide, indicating that after first loading anelastic effects are apparently eliminated.
- The permanent deformation at the end of both loading cycles, as is observed from Figs. (5.34) and (5.35), is apparent in Figs. (5.40) and (5.41), from the higher velocity at the end of a particular cycle, compared to the velocity at the beginning of a cycle. This effect is larger for the Niederhausen sandstone than for the Bad Dürckheim sandstone.

- Analogously to the observations from the Colton and Flechtinger sandstones in previous sections of this Chapter, compressional- and shear-waves are sensitive to those axial stresses which lie in the polarization and/or propagation direction.
- Anisotropy between the horizontal P-wave velocities v_1^P , v_2^P and the vertical P-wave velocity v_3^P , is larger for loading cycle 'b' than for loading cycle 'a', the former having the largest deviatoric stresses.
- The horizontal P-wave anisotropy of the Bad Dürckheim sandstone reflects an intrinsic anisotropy, attributed to texture or layering.
- The Niederhausen shows a larger difference in P-wave velocity between the up-loading and the down-loading curves, compared with the Bad Dürckheim. This may be explained by the mineralogy of both sandstones (the Niederhausen contains less quartz and more weathered feldspar), causing anelastic effect to be more pronounced for the Niederhausen.
- The dynamic elastic modulus of Eq. (5.6), at a certain stress τ_{33} , equals the static elastic modulus of Eq. (4.3), evaluated after some instant after the onset of down-loading during some small loop cycle around the stress τ_{33} .

5.5 Discussion

The determination of the applicability of the results in this section to seismic experiments is not straightforward. It requires the translation of the wave velocity dependence on stress from the ultrasonic scale (hundreds of kHz) to the seismic scale (tens of Hz). The possibility of this transformation is suggested by the self-similar or fractal nature of the dynamic scaling laws observed in deformation (finite strain) and in wave propagation (infinitesimal strain). This will be argued below.

The sensitivity of ultrasonic waves to stress can be explained by micro-crack mechanisms as micro-crack closure, nucleation, and growth, and micro-seismicity. According to Main (1996) these mechanical deformation phenomena have spatio-temporal scaling properties. Following this argument one can imagine that some spatio-temporal scaling law might explain a transformation of a small loop stress-strain curve to the main loop curve in Figs.

(5.34) and (5.35). According to Plona and Cook (1995) the elastic modulus determined from a small loop will approach the dynamic elastic modulus as the size of the small loop is decreased. In Figs. (5.48) and (5.49) one observes, in accordance with Plona and Cook (1995), that the small loop moduli are closer to the dynamic moduli than the main loop moduli.

In the limit from quasi-static to dynamic strain inertial effects will become significant enough to generate wave propagation. In the spatio-temporal domain associated with wave propagation we also observe scaling laws. In Fig. (5.50) the traces of Fig. (5.16) are superposed on one time axis. We observe a clear scaling behaviour of the wavelet, with respect to time and amplitude, as a function of the triaxial stress. The stress increases from right to left in Fig. (5.50). The spatio-temporal scaling property of crack deformation is visible as a scaling of the transmitted wave. The scaling

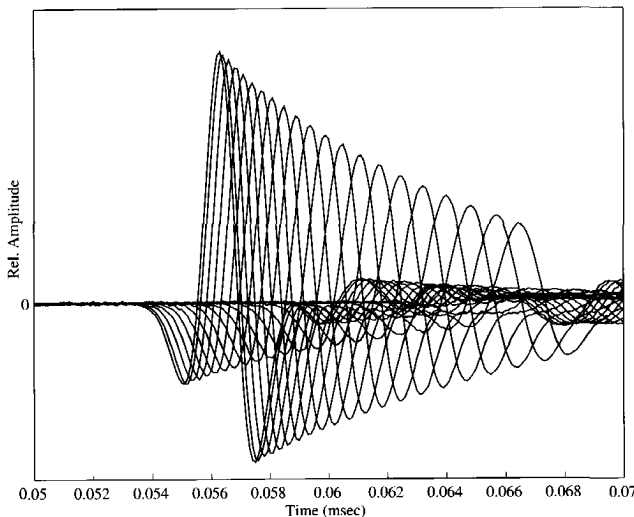


Figure 5.50: *Superposition on one time axis of compressional-wave transmissions through the Flechtinger sandstone for stresses from 2 to 20 MPa. The stress increases from right to left. All axial stresses are equal: $\tau_{11} = \tau_{22} = \tau_{33}$.*

operations, with respect to time and amplitude, is further detailed in Fig. (5.51). In this figure the solid and the double dashed lines represent P-wave recordings at 8.7 and 20 MPa, respectively. The dashed line is computed from the 20 MPa recording by a scaling of the time and amplitude axis (den Boer and Fokkema (1996)). Observe that the recorded and the computed

lines are similar for the first cycle part, validating the existence of a dynamic scaling law.

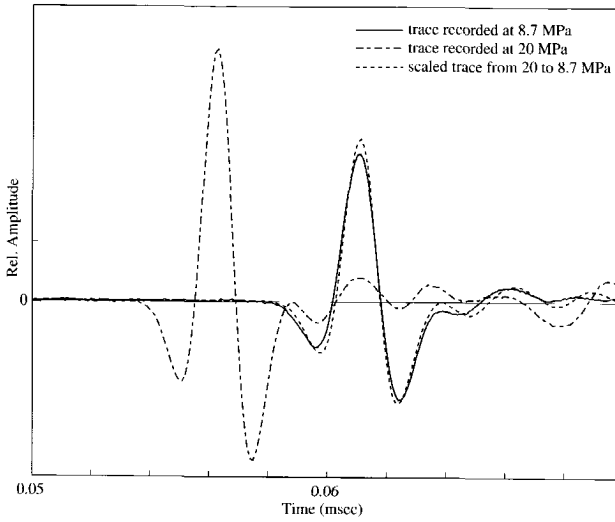


Figure 5.51: *Detail of Fig. (5.50). The solid and the double dashed lines represent P-wave transmissions through the Flechtinger sandstone at, respectively, 8.7 and 20 MPa. The dashed line is computed from the 20 MPa recording by a scaling of the time axis and the amplitude axis.*

Using the observed self-similar nature in well-log measurements of geological strata (Walden and Hosken (1985); Todoeschuck and Jensen (1989); Saucier and Muller (1993); Herrmann (1997)), one can envisage some renormalization technique (Lesne (1998)), which transforms the ultrasonic results to the seismic scale through a so-called coarse-graining procedure. Given the above indication of scaling laws governing the medium and the dynamics of deformation and wave propagation one could conceive that the transformation from the ultrasonic to the seismic scale involves a scaling law which relates the two spatio-temporal observation domains in a correct way. Herrmann (1997) suggests that one has to include scale dynamics in wave theory involving derivatives with respect to scale. Given the complexity of the ultrasonic-seismic scale problem no attempt is made in this thesis to up-scale the ultrasonic results to the seismic scale. Of course it is an intriguing problem that must be addressed when working with down-scaled experiments, that are supposed to be relevant for the seismic scale.

Experiments have shown that the wave-velocity dispersion (a measure for the velocity change over a frequency band, e.g. from seismic to sonic) in case of dry- or gas-saturated porous media is quite small (Spencer (1981); Winkler (1985)). The small dispersion can be explained according to Fermat's shortest path principle, meaning that higher frequency waves show higher velocities than low frequency waves, because on a small scale a wave is more 'manoeuvrable' to pass through the higher velocity parts. Moos and Zoback (1983) and Murphy III (1984) argue that the observed velocity dispersion is primarily due to the sample size rather than the frequency. Ultrasonic measurements, as in this thesis, are conducted on intact samples, whereas field measurements from the sonic to the seismic scale involve the in-situ rock containing cracks and fractures on a range of scales. According to the simple model of Walsh (1965a) in Eq. (3.2) the average crack length appears to the third power. Hence, the compressibility and wave-velocity are strongly affected by a few relatively long cracks making a comparison between laboratory and in-situ measurements difficult.

The wave-velocity dispersion in fluid-saturated rock is known to be significantly larger than in dry rock (Winkler (1985)). Therefore, the translation of the room-dry ultrasonic results reported in this thesis to the saturated seismic scale must be done carefully. The reason for this is that additional loss mechanisms come into play. Winkler (1985) and Wang and Nur (1990) discuss dispersion mechanisms as the viscous interaction between fluid and solid, described by Biot's theory (Biot (1956a,b)). Further they identify local flow mechanisms, which take into account that some parts of the pore space are more compliant than others (e.g. squirt mechanisms in Mavko and Nur (1975)). Winkler (1985) suggests that, assuming that velocities in dry rock are independent of frequency, seismic velocities in fluid-saturated rock can be computed from ultrasonic measurements on dry rock, using the low-frequency limit of Biot's theory (equivalent to the static limit theory of Gassmann (1951)).

For stress inference wave-velocity anisotropy is important. In Mukerji and Mavko (1994) a local-flow theory is derived which predicts the high- and low-frequency saturated velocities in anisotropic rocks in terms of dry-rock properties measured e.g. in the laboratory. At low frequencies the predicted velocities are equivalent to the ones computed from the fluid substitution theory of Brown and Korringa (1975), which is an anisotropic extension of Gassmann (1951). The data displayed in Figs. (5.28) to (5.32) can be used to compute the dry-rock elastic moduli assuming transverse isotropy (Cruts

(1995); Cruts et al. (1995); den Boer (1996)). Using Mukerji and Mavko (1994) one can compute from these ultrasonic measurements the seismic velocities for a fluid saturated transversely isotropic rock.

The number of parameters involved in theories on wave propagation in porous media is often quite large. These parameters must be specified in order to compute wave velocities at one scale from those at another scale. The scaling laws observed from experiments on porous media are, however, simple relations.

My view is that we must adhere to this experimental simplicity and find scaling laws involving a minimum number of parameters, corresponding to good scientific practice. The derivation of a transformation law between the ultrasonic and seismic scale is not pursued in this thesis.

In Part II of this thesis a processing scheme is derived which produces an image of temporal contrasts in terms of the kernel of a difference reflection operator. This reflection operator depends on the acoustic velocities and densities of the reference and monitor media. To yield the change in the stress state these velocities must be inverted using stress-velocity relations obtained from ultrasonic laboratory or field experiments. This inversion has not been implemented but appears high on the future research agenda.

Part II

Time-lapse seismic monitoring

Chapter 6

Time-lapse contrast formalism

The following chapters are partly based on the work reported in the M.Sc. theses van Spaendonck (1996), Beishuizen (1997), and de Brouwere (1998). Chapter 6 is adapted after Dillen et al. (1999).

6.1 Introduction

By calculating a time-convolution type interaction integral, evaluated at a certain depth, involving two sets of time-lapse acoustic wave fields, one obtains a representation of a difference wave field at the recording level. This difference wave field appears as difference reflections originating from temporal contrast sources located below the interaction depth. Temporal contrasts above the interaction depth do not produce difference reflections in this difference wave field. The equivalence of the time-convolution type interaction integral with a difference wave field is derived by introducing a temporal contrast source formalism, similar to the spatial contrast source formalism in scattering theory. In this respect the difference wave field takes the role of the scattered wave field. Calculating the interaction integral progressively with depth one obtains an elimination procedure of difference reflections above the interaction depth, which is illustrated by some finite difference examples in this chapter. These vanishing difference reflections can be used in a minimization scheme which attempts to infer the temporal contrast parameters above the interaction depth. Numerical examples show that the arrival time of the difference wave field, generated by the interaction integral, appears to be governed by a medium which is some average of the two media, each rep-

representative for a time-lapse state. In Chapter 10 the difference reflections are derived as functions of temporal contrasts in the admittance operator. By applying a symplectic eigenvalue decomposition in Chapter 10 the interaction integral is set in terms of a single eigenvalue operator for both time-lapse states, which is a function of the two admittance operators, each representative for a time-lapse state above the interaction depth. Hence, the absence of difference reflections in this domain. The arrival time is shown in to be governed by an up-going and a down-going wave field extrapolation operator, the former identified with the reference state, whereas the latter is identified with the monitor state. Using the aforementioned extrapolation operators an image of the temporal contrasts is obtained from the consecutive interaction integrals.

In the following sections, first a temporal contrast source formalism is derived in terms of the wave field equations of the difference wave field. Subsequently, the difference wave field is decomposed, at a particular depth, into a down-going and an up-going wave field. Application of the acoustic reciprocity theorem yields a boundary integral representation involving the reference and monitor wave fields. This interaction integral, evaluated at the decomposition depth, is shown to be equivalent to the up-going component of the difference wave field, which is causally related to the temporal contrast sources below the decomposition (interaction) depth.

6.2 The acoustic wave field equations

We consider two sets of time-lapse acoustic wave fields. One set of wave fields is denoted by the term *reference* wave fields, whereas the other set of wave fields is identified as *monitor* wave fields. Reference and monitor wave fields are denoted by the superscripts $^{(1)}$ and $^{(2)}$, respectively. The space and time Cartesian reference frames used are introduced in Appendix A. We define a global time scale t' . With respect to this time scale, and for a certain shot position, the onset of a reference wave field is at the time instant $t' = t^{(1)}$, whereas the onset of a monitor wave field is at the time instant $t' = t^{(2)}$, with $t^{(2)} > t^{(1)}$. Local time scales are obtained as $t' - t^{(1)}$ and $t' - t^{(2)}$, and are both denoted by the symbol t . Between the time instants $t' = t^{(1)}$ and $t' = t^{(2)}$, changes in the medium parameters may have occurred. We assume that the duration of the seismic experiments is much smaller than the time-lapse interval $t^{(2)} - t^{(1)}$, such that during either seismic experiment the medium

parameters ρ and κ may be approximated by constant functions of time. The reference state is governed by the medium parameters $\{\rho^{(1)}, \kappa^{(1)}\}$, whereas the medium of the monitor state is governed by the parameters $\{\rho^{(2)}, \kappa^{(2)}\}$ (see Chapter 7 for an introduction of the acoustic wave field quantities and equations). Consider the Laplace domain (see Appendix B) acoustic reference wave field equations,

$$\partial_k \hat{p}^{(1)}(\mathbf{x}; \mathbf{x}^S, s) + s\rho^{(1)}(\mathbf{x}) \hat{v}_k^{(1)}(\mathbf{x}; \mathbf{x}^S, s) = \hat{f}_k^{(1)}(s) \delta(\mathbf{x} - \mathbf{x}^S), \quad (6.1)$$

$$\partial_k \hat{v}_k^{(1)}(\mathbf{x}; \mathbf{x}^S, s) + s\kappa^{(1)}(\mathbf{x}) \hat{p}^{(1)}(\mathbf{x}; \mathbf{x}^S, s) = \hat{q}^{(1)}(s) \delta(\mathbf{x} - \mathbf{x}^S), \quad (6.2)$$

and the Laplace domain acoustic monitor wave field equations,

$$\partial_k \hat{p}^{(2)}(\mathbf{x}; \mathbf{x}^S, s) + s\rho^{(2)}(\mathbf{x}) \hat{v}_k^{(2)}(\mathbf{x}; \mathbf{x}^S, s) = \hat{f}_k^{(2)}(s) \delta(\mathbf{x} - \mathbf{x}^S), \quad (6.3)$$

$$\partial_k \hat{v}_k^{(2)}(\mathbf{x}; \mathbf{x}^S, s) + s\kappa^{(2)}(\mathbf{x}) \hat{p}^{(2)}(\mathbf{x}; \mathbf{x}^S, s) = \hat{q}^{(2)}(s) \delta(\mathbf{x} - \mathbf{x}^S), \quad (6.4)$$

in which $\mathbf{x} \in \mathbb{R}^3$ and s is the Laplace transform parameter. The space \mathbb{R}^3

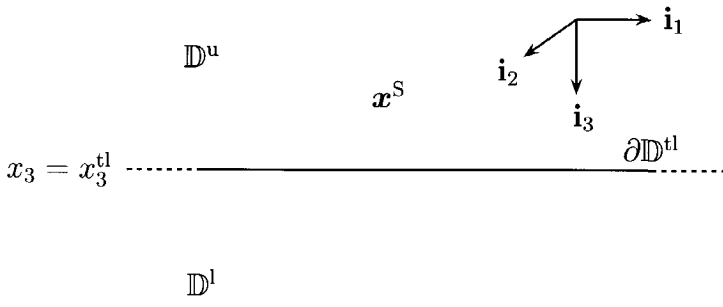


Figure 6.1: Time-lapse configuration with source position.

is divided by the planar surface $\partial\mathbb{D}^{\text{tl}} = \{(\mathbf{x}_T, x_3) | \mathbf{x}_T \in \mathbb{R}^2, x_3 = x_3^{\text{tl}}\}$ into an upper half-space \mathbb{D}^u , for which $x_3 < x_3^{\text{tl}}$, and a lower half-space \mathbb{D}^l , for which $x_3 > x_3^{\text{tl}}$ (Fig. 6.1). The transverse coordinate \mathbf{x}_T equals (x_1, x_2) . For this configuration the longitudinal coordinate x_3 is pointing downwards. The source distributions with source functions, $\{\hat{q}^{(1)}, \hat{f}_k^{(1)}\}$ and $\{\hat{q}^{(2)}, \hat{f}_k^{(2)}\}$, in Eqs. (6.1) to (6.4), are located at $\mathbf{x}^S \in \mathbb{D}^u$. Rewriting Eqs. (6.3) and (6.4) yields

$$\partial_k \hat{p}^{(2)} + s\rho^{(1)} \hat{v}_k^{(2)} = -s\Delta^{\text{tl}} \rho \hat{v}_k^{(2)} + \hat{f}_k^{(2)} \delta(\mathbf{x} - \mathbf{x}^S), \quad (6.5)$$

$$\partial_k \hat{v}_k^{(2)} + s\kappa^{(1)} \hat{p}^{(2)} = -s\Delta^{\text{tl}} \kappa \hat{p}^{(2)} + \hat{q}^{(2)} \delta(\mathbf{x} - \mathbf{x}^S), \quad (6.6)$$

with temporal contrast functions given by

$$\Delta^{\text{tl}}\rho = \rho^{(2)} - \rho^{(1)} \quad \text{and} \quad \Delta^{\text{tl}}\kappa = \kappa^{(2)} - \kappa^{(1)}. \quad (6.7)$$

By subtracting Eqs. (6.1) and (6.2) from Eqs. (6.5) and (6.6) we construct the following difference wave field equations

$$\partial_k \hat{p}^{\text{dif}} + s\rho^{(1)} \hat{v}_k^{\text{dif}} = \hat{f}_k^{\text{dif}}, \quad \text{in } \mathbb{R}^3, \quad (6.8)$$

$$\partial_k \hat{v}_k^{\text{dif}} + s\kappa^{(1)} \hat{p}^{\text{dif}} = \hat{q}^{\text{dif}}, \quad \text{in } \mathbb{R}^3, \quad (6.9)$$

in which the difference wave field quantities are given by

$$\hat{p}^{\text{dif}} = \hat{p}^{(2)} - \hat{p}^{(1)} \quad \text{and} \quad \hat{v}_k^{\text{dif}} = \hat{v}_k^{(2)} - \hat{v}_k^{(1)}. \quad (6.10)$$

The difference source quantities in Eqs. (6.8) and (6.9) are obtained as

$$\hat{f}_k^{\text{dif}} = -s\Delta^{\text{tl}}\rho \hat{v}_k^{(2)} + \Delta^{\text{tl}}\hat{f}_k, \quad (6.11)$$

$$\hat{q}^{\text{dif}} = -s\Delta^{\text{tl}}\kappa \hat{p}^{(2)} + \Delta^{\text{tl}}\hat{q}, \quad (6.12)$$

in which

$$\Delta^{\text{tl}}\hat{f}_k = \left(\hat{f}_k^{(2)} - \hat{f}_k^{(1)} \right) \delta(\mathbf{x} - \mathbf{x}^S), \quad (6.13)$$

$$\Delta^{\text{tl}}\hat{q} = \left(\hat{q}^{(2)} - \hat{q}^{(1)} \right) \delta(\mathbf{x} - \mathbf{x}^S). \quad (6.14)$$

6.3 Wave field decomposition

Next, we assume the following decomposition of the difference wave field quantities

$$\hat{p}^{\text{dif}} = \hat{p}^{\text{dif},\text{d}} + \hat{p}^{\text{dif},\text{u}}, \quad \text{in } \mathbb{R}^3, \quad (6.15)$$

$$\hat{v}_k^{\text{dif}} = \hat{v}_k^{\text{dif},\text{d}} + \hat{v}_k^{\text{dif},\text{u}}, \quad \text{in } \mathbb{R}^3. \quad (6.16)$$

The wave field components $\{\hat{p}^{\text{dif},\text{d}}, \hat{v}_k^{\text{dif},\text{d}}\}$ are governed by the wave field equations

$$\partial_k \hat{p}^{\text{dif},\text{d}} + s\rho^{(1)} \hat{v}_k^{\text{dif},\text{d}} = \hat{f}_k^{\text{dif},\text{d}}, \quad \text{in } \mathbb{R}^3, \quad (6.17)$$

$$\partial_k \hat{v}_k^{\text{dif},\text{d}} + s\kappa^{(1)} \hat{p}^{\text{dif},\text{d}} = \hat{q}^{\text{dif},\text{d}}, \quad \text{in } \mathbb{R}^3, \quad (6.18)$$

with source quantities

$$\{\hat{f}_k^{\text{dif},\text{d}}, \hat{q}^{\text{dif},\text{d}}\} = \{\hat{f}_k^{\text{dif}}, \hat{q}^{\text{dif}}\}, \quad \text{in } \mathbb{D}^{\text{u}}, \quad (6.19)$$

$$\{\hat{f}_k^{\text{dif},\text{d}}, \hat{q}^{\text{dif},\text{d}}\} = \{0, 0\}, \quad \text{in } \mathbb{D}^{\text{l}}. \quad (6.20)$$

The wave field equations of the wave field components $\{\hat{p}^{\text{dif},\text{u}}, \hat{v}_k^{\text{dif},\text{u}}\}$ are given by

$$\partial_k \hat{p}^{\text{dif},\text{u}} + s\rho^{(1)} \hat{v}_k^{\text{dif},\text{u}} = \hat{f}_k^{\text{dif},\text{u}}, \quad \text{in } \mathbb{R}^3, \quad (6.21)$$

$$\partial_k \hat{v}_k^{\text{dif},\text{u}} + s\kappa^{(1)} \hat{p}^{\text{dif},\text{u}} = \hat{q}^{\text{dif},\text{u}}, \quad \text{in } \mathbb{R}^3, \quad (6.22)$$

with source quantities

$$\{\hat{f}_k^{\text{dif},\text{u}}, \hat{q}^{\text{dif},\text{u}}\} = \{0, 0\}, \quad \text{in } \mathbb{D}^{\text{u}}, \quad (6.23)$$

$$\{\hat{f}_k^{\text{dif},\text{u}}, \hat{q}^{\text{dif},\text{u}}\} = \{\hat{f}_k^{\text{dif}}, \hat{q}^{\text{dif}}\}, \quad \text{in } \mathbb{D}^{\text{l}}. \quad (6.24)$$

Observe that in \mathbb{D}^{l}

$$\hat{f}_k^{\text{dif}} = -s\Delta^{\text{tl}} \rho \hat{v}_k^{(2)}, \quad \text{in } \mathbb{D}^{\text{l}}, \quad (6.25)$$

$$\hat{q}^{\text{dif}} = -s\Delta^{\text{tl}} \kappa \hat{p}^{(2)}, \quad \text{in } \mathbb{D}^{\text{l}}. \quad (6.26)$$

Hence the temporal contrast sources of $\{\hat{p}^{\text{dif},\text{u}}, \hat{v}_k^{\text{dif},\text{u}}\}$ in Eq. (6.24) only depend on the time-lapse differences of ρ and κ in \mathbb{D}^{l} , and are independent of the time-lapse changes in the source functions \hat{f}_k and \hat{q} . The decomposition of Eqs. (6.15) and (6.16) is invoked by choosing different supports for the temporal contrast functions of Eqs. (6.11) and (6.12). From the source domains given in Eqs. (6.19), (6.20), (6.23) and (6.24) one can show that $\{\hat{p}^{\text{dif},\text{d}}, \hat{v}_k^{\text{dif},\text{d}}\}$ is a down-going wave field at $\partial\mathbb{D}^{\text{tl}}$, whereas $\{\hat{p}^{\text{dif},\text{u}}, \hat{v}_k^{\text{dif},\text{u}}\}$ is an up-going wave field at $\partial\mathbb{D}^{\text{tl}}$. Observe that the difference wave fields defined by Eqs. (6.8), (6.9), (6.17), (6.18), (6.21) and (6.22) propagate in the reference medium.

6.4 Reciprocity theorem

In this section the acoustic reciprocity theorem of the time-convolution type is used (for a more elaborate discussion see Chapter 7). This theorem has its roots in Green's theorem for Laplace's equation and Helmholtz's extension to the wave equation. A reciprocity theorem interrelates the wave field

quantities of two admissible states, A and B , that occur in one and the same time-invariant domain $\mathbb{D} \subset \mathbb{R}^3$ (de Hoop (1995)). In forward/inverse source and scattering problems one state is identified with a physical wave field while the other state is identified with a computational or so called Green's wave field. In time-lapse problems both states are identified with physical wave fields. The respective wave field equations for State A and State B are given by

$$\partial_k \hat{p}^{A,B}(\mathbf{x}, s) + s \rho^{A,B}(\mathbf{x}) \hat{v}_k^{A,B}(\mathbf{x}, s) = \hat{f}_k^{A,B}(\mathbf{x}, s), \quad (6.27)$$

$$\partial_k \hat{v}_k^{A,B}(\mathbf{x}, s) + s \kappa^{A,B}(\mathbf{x}) \hat{p}^{A,B}(\mathbf{x}, s) = \hat{q}^{A,B}(\mathbf{x}, s). \quad (6.28)$$

The complex-frequency domain reciprocity theorem of the time-convolution type (in the time-domain the multiplications represent convolutions) is obtained as (Fokkema and van den Berg (1993); de Hoop (1995)),

$$\begin{aligned} & \int_{\mathbf{x} \in \partial\mathbb{D}} (\hat{v}_k^A \hat{p}^B - \hat{p}^A \hat{v}_k^B) \nu_k dA \\ & + \int_{\mathbf{x} \in \mathbb{D}} s [(\rho^B - \rho^A) \hat{v}_k^A \hat{v}_k^B - (\kappa^B - \kappa^A) \hat{p}^A \hat{p}^B] dV \\ & = \int_{\mathbf{x} \in \mathbb{D}} (\hat{f}_k^B \hat{v}_k^A - \hat{f}_k^A \hat{v}_k^B + \hat{q}^A \hat{p}^B - \hat{q}^B \hat{p}^A) dV, \end{aligned} \quad (6.29)$$

in which the normal ν is pointing outward \mathbb{D} . Using the reference and monitor wave fields of (6.1) to (6.4) as State A and State B , respectively, taking the source position of the reference wave field to be \mathbf{x}^R instead of \mathbf{x}^S , and using only \hat{q} sources, application of the reciprocity theorem yields, omitting s ,

$$\begin{aligned} & \int_{\mathbf{x} \in \partial\mathbb{D}} [\hat{v}_k^{(1)}(\mathbf{x}; \mathbf{x}^R) \hat{p}^{(2)}(\mathbf{x}; \mathbf{x}^S) - \hat{p}^{(1)}(\mathbf{x}; \mathbf{x}^R) \hat{v}_k^{(2)}(\mathbf{x}; \mathbf{x}^S)] \nu_k dA \\ & + \int_{\mathbf{x} \in \mathbb{D}} s [\Delta^{tl} \rho \hat{v}_k^{(1)}(\mathbf{x}; \mathbf{x}^R) \hat{v}_k^{(2)}(\mathbf{x}; \mathbf{x}^S) - \Delta^{tl} \kappa \hat{p}^{(1)}(\mathbf{x}; \mathbf{x}^R) \hat{p}^{(2)}(\mathbf{x}; \mathbf{x}^S)] dV \\ & = \hat{q}^{(1)} \hat{p}^{(2)}(\mathbf{x}^R; \mathbf{x}^S) - \hat{q}^{(2)} \hat{p}^{(1)}(\mathbf{x}^S; \mathbf{x}^R). \end{aligned} \quad (6.30)$$

Hence, the sum of a boundary integral and a volume integral containing temporal contrast sources is equivalent to a difference measurement.

6.5 Interaction integral

Taking the boundary integral of Eq. (6.30) we define the following interaction integral (for a more elaborate analysis see Chapter 10),

$$\hat{I}^{\text{conv}}(x_3^{\text{tl}}; \mathbf{x}^{\text{R}}, \mathbf{x}^{\text{S}}) \stackrel{\text{def}}{=} \int_{\mathbf{x}_T \in \mathbb{R}^2} \left[\hat{v}_3^{(1)}(\mathbf{x}_T, x_3^{\text{tl}}; \mathbf{x}^{\text{R}}) \hat{p}^{(2)}(\mathbf{x}_T, x_3^{\text{tl}}; \mathbf{x}^{\text{S}}) \right. \\ \left. - \hat{p}^{(1)}(\mathbf{x}_T, x_3^{\text{tl}}; \mathbf{x}^{\text{R}}) \hat{v}_3^{(2)}(\mathbf{x}_T, x_3^{\text{tl}}; \mathbf{x}^{\text{S}}) \right] d\mathbf{x}_T. \quad (6.31)$$

The integration is with respect to the transverse coordinate $\mathbf{x}_T = (x_1, x_2)$, at a depth x_3^{tl} . Consider the wave fields, $\{\hat{p}^{(1)}, \hat{v}_k^{(1)}\}(\mathbf{x}_T, x_3^{\text{tl}}; \mathbf{x}^{\text{R}})$ and $\{\hat{p}^{(1)}, \hat{v}_k^{(1)}\}(\mathbf{x}_T, x_3^{\text{tl}}; \mathbf{x}^{\text{S}})$, which differ with respect to their source positions. Applications of the reciprocity theorem of Eq. (6.29) to these wave fields, with respect to the domain \mathbb{D}^{l} , leads to

$$0 = \int_{\mathbf{x}_T \in \mathbb{R}^2} \left[\hat{v}_3^{(1)}(\mathbf{x}_T, x_3^{\text{tl}}; \mathbf{x}^{\text{R}}) \hat{p}^{(1)}(\mathbf{x}_T, x_3^{\text{tl}}; \mathbf{x}^{\text{S}}) \right. \\ \left. - \hat{p}^{(1)}(\mathbf{x}_T, x_3^{\text{tl}}; \mathbf{x}^{\text{R}}) \hat{v}_3^{(1)}(\mathbf{x}_T, x_3^{\text{tl}}; \mathbf{x}^{\text{S}}) \right] d\mathbf{x}_T. \quad (6.32)$$

In the derivation we have taken into account that contributions at $(x_1^2 + x_2^2) \rightarrow \infty$ and at $x_3 \rightarrow \infty$ vanish. Because there is no contrast in the medium parameters between the two states, and inside the domain of application \mathbb{D}^{l} both states have no sources, the two volume integrals of Eq. (6.29) also vanish in Eq. (6.32). Subtracting Eq. (6.32) from Eq. (6.31), using Eq. (6.10), yields

$$\hat{I}^{\text{conv}}(x_3^{\text{tl}}; \mathbf{x}^{\text{R}}, \mathbf{x}^{\text{S}}) = \int_{\mathbf{x}_T \in \mathbb{R}^2} \left[\hat{v}_3^{(1)}(\mathbf{x}_T, x_3^{\text{tl}}; \mathbf{x}^{\text{R}}) \hat{p}^{\text{dif}}(\mathbf{x}_T, x_3^{\text{tl}}; \mathbf{x}^{\text{S}}) \right. \\ \left. - \hat{p}^{(1)}(\mathbf{x}_T, x_3^{\text{tl}}; \mathbf{x}^{\text{R}}) \hat{v}_3^{\text{dif}}(\mathbf{x}_T, x_3^{\text{tl}}; \mathbf{x}^{\text{S}}) \right] d\mathbf{x}_T. \quad (6.33)$$

Next, consider the wave fields, $\{\hat{p}^{(1)}, \hat{v}_k^{(1)}\}(\mathbf{x}_T, x_3^{\text{tl}}; \mathbf{x}^{\text{R}})$ and $\{\hat{p}^{\text{dif,d}}, \hat{v}_k^{\text{dif,d}}\}(\mathbf{x}_T, x_3^{\text{tl}}; \mathbf{x}^{\text{S}})$, the latter wave field being governed by Eqs. (6.17) and (6.18). Applications of the reciprocity theorem of Eq. (6.29) to these wave fields, with respect to the domain \mathbb{D}^{l} , leads to

$$0 = \int_{\mathbf{x}_T \in \mathbb{R}^2} \left[\hat{v}_3^{(1)}(\mathbf{x}_T, x_3^{\text{tl}}; \mathbf{x}^{\text{R}}) \hat{p}^{\text{dif,d}}(\mathbf{x}_T, x_3^{\text{tl}}; \mathbf{x}^{\text{S}}) \right. \\ \left. - \hat{p}^{(1)}(\mathbf{x}_T, x_3^{\text{tl}}; \mathbf{x}^{\text{R}}) \hat{v}_3^{\text{dif,d}}(\mathbf{x}_T, x_3^{\text{tl}}; \mathbf{x}^{\text{S}}) \right] d\mathbf{x}_T. \quad (6.34)$$

Subtracting Eq. (6.34) from Eq. (6.33), using Eqs. (6.15) and (6.16), yields

$$\hat{I}^{\text{conv}}(x_3^{\text{tl}}; \mathbf{x}^{\text{R}}, \mathbf{x}^{\text{S}}) = \int_{\mathbf{x}_{\text{T}} \in \mathbb{R}^2} \left[\hat{v}_3^{(1)}(\mathbf{x}_{\text{T}}, x_3^{\text{tl}}; \mathbf{x}^{\text{R}}) \hat{p}^{\text{dif},\text{u}}(\mathbf{x}_{\text{T}}, x_3^{\text{tl}}; \mathbf{x}^{\text{S}}) \right. \\ \left. - \hat{p}^{(1)}(\mathbf{x}_{\text{T}}, x_3^{\text{tl}}; \mathbf{x}^{\text{R}}) \hat{v}_3^{\text{dif},\text{u}}(\mathbf{x}_{\text{T}}, x_3^{\text{tl}}; \mathbf{x}^{\text{S}}) \right] d\mathbf{x}_{\text{T}}. \quad (6.35)$$

Taking the wave fields, $\{\hat{p}^{(1)}, \hat{v}_k^{(1)}\}(\mathbf{x}_{\text{T}}, x_3^{\text{tl}}; \mathbf{x}^{\text{R}})$ and $\{\hat{p}^{\text{dif},\text{u}}, \hat{v}_k^{\text{dif},\text{u}}\}(\mathbf{x}_{\text{T}}, x_3^{\text{tl}}; \mathbf{x}^{\text{S}})$, the latter wave field being governed by Eqs. (6.21) and (6.22), and applying Eq. (6.29) to these wave fields, with respect to the domain \mathbb{D}^{u} , gives

$$\hat{q}^{(1)} \hat{p}^{\text{dif},\text{u}}(\mathbf{x}^{\text{R}}, \mathbf{x}^{\text{S}}) = \int_{\mathbf{x}_{\text{T}} \in \mathbb{R}^2} \left[\hat{v}_3^{(1)}(\mathbf{x}_{\text{T}}, x_3^{\text{tl}}; \mathbf{x}^{\text{R}}) \hat{p}^{\text{dif},\text{u}}(\mathbf{x}_{\text{T}}, x_3^{\text{tl}}; \mathbf{x}^{\text{S}}) \right. \\ \left. - \hat{p}^{(1)}(\mathbf{x}_{\text{T}}, x_3^{\text{tl}}; \mathbf{x}^{\text{R}}) \hat{v}_3^{\text{dif},\text{u}}(\mathbf{x}_{\text{T}}, x_3^{\text{tl}}; \mathbf{x}^{\text{S}}) \right] d\mathbf{x}_{\text{T}}. \quad (6.36)$$

Using Eqs. (6.35) and (6.36) the interaction quantity is expressed as

$$\hat{I}^{\text{conv}}(x_3^{\text{tl}}; \mathbf{x}^{\text{R}}, \mathbf{x}^{\text{S}}) = \hat{q}^{(1)} \hat{p}^{\text{dif},\text{u}}(\mathbf{x}^{\text{R}}, \mathbf{x}^{\text{S}}). \quad (6.37)$$

We arrived at a representation of \hat{I}^{conv} in terms of the difference wave field $\hat{p}^{\text{dif},\text{u}}$. According to Eqs. (6.21) and (6.22), this wave field has sources depending on the temporal contrasts inside \mathbb{D}^{l} . Temporal contrasts inside \mathbb{D}^{u} do not generate difference reflections in the difference gather $\hat{p}^{\text{dif},\text{u}}$, and hence in \hat{I}^{conv} , whereas these would occur in \hat{p}^{dif} . If \hat{I}^{conv} is calculated incorrectly residual difference reflection energy from temporal contrasts inside \mathbb{D}^{u} will appear. Minimizing this energy could be the basis for an inference scheme for the reference and monitor medium parameters inside \mathbb{D}^{u} . The reference and monitor two-way wave fields appearing in \hat{I}^{conv} can be calculated from data by applying a wave field decomposition into down-going and up-going one-way wave fields at the recording level (Fokkema et al. (1999)). In the next section \hat{I}^{conv} is calculated numerically, using Eq. (6.31), for several x_3^{tl} , using wave field simulation with finite differences. Also, \hat{I}^{conv} is calculated in case $\{\rho^{(1)}, \kappa^{(1)}\} = \{\rho^{(2)}, \kappa^{(2)}\}$ in \mathbb{D}^{u} , using the right-hand side of the following equation,

$$\hat{I}^{\text{conv}}(x_3^{\text{tl}}; \mathbf{x}^{\text{R}}, \mathbf{x}^{\text{S}}) \Big|_{\{\rho^{(1)}, \kappa^{(1)}\} = \{\rho^{(2)}, \kappa^{(2)}\} \text{ in } \mathbb{D}^{\text{u}}} \\ = \hat{q}^{(1)} \hat{p}^{(2)}(\mathbf{x}^{\text{R}}; \mathbf{x}^{\text{S}}) - \hat{q}^{(2)} \hat{p}^{(1)}(\mathbf{x}^{\text{R}}; \mathbf{x}^{\text{S}}). \quad (6.38)$$

We consider two cases: one for which, inside \mathbb{D}^u the reference material state is equalized to the monitor material state, and one, vice versa, for which the monitor material state is equalized to the reference material state. Both calculations of \hat{I}^{conv} , one using the boundary integral, and the other using the difference wave field on the right-hand side of Eq. (6.38), are compared.

6.6 Numerical example

We consider the two-dimensional model shown in Fig. (6.2), with coordinate vector $\mathbf{x} = (x_1, x_3)$, in which x_1 denotes the lateral position in terms of source-receiver offset, and x_3 denotes depth (no x_2 dependency). The wave fields are calculated and displayed in the time domain. The reference and monitor velocities and densities are given in Table (6.1). With a

	$c^{(1)}$ [m/s]	$\rho^{(1)}$ [kg/m ³]
background	1800	1500
diamond-shaped object	2500	2000
lower layer	2700	2300

	$c^{(2)}$ [m/s]	$\rho^{(2)}$ [kg/m ³]
background	1800	1500
diamond-shaped object	2700	2200
lower layer	2900	2400

Table 6.1: Reference and monitor velocities and densities, $c^{(1)}, \rho^{(1)}$ and $c^{(2)}$ and $\rho^{(2)}$.

two-dimensional finite difference code two acoustic time-lapse wave fields in (x_1, x_3) -space are simulated. The reference and monitor sources are placed at the top of the model at 0 m depth, at 0 m offset. The receivers for both experiments are placed at 0 m depth, at offsets covering the entire model. Fig. (6.2) shows a difference gather \hat{p}^{dif} (see Eqs. (6.8) and (6.9)), obtained by subtracting a single reference shot-gather from a single monitor shot-gather. The first reflection originates from the top sides of the diamond-shaped object. The reflection from the bottom sides merges with the reflection from the top side at larger offsets, and shows a triplication at small offsets. The

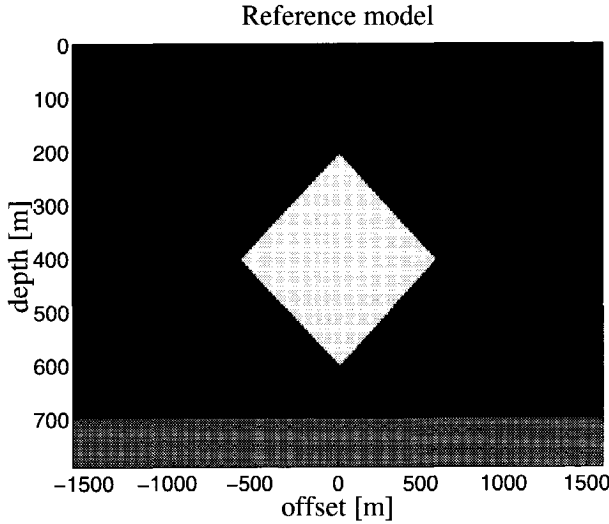


Figure 6.2: *Model containing a diamond-shaped object, embedded in a background medium, and a lower layer. Temporal contrast in diamond-shaped object and lower layer.*

reflection from the lower layer starts, at zero offset, just after 0.700 s, its complex shape determined by the diamond-shaped object.

The following finite difference modelling results were done to test the equivalence of the interaction integral of Eq. (6.31) with an up-going difference wave field, governed by Eqs. (6.21) and (6.22), as expressed by Eq. (6.37). First, we model the interaction integral at $x_3^{\text{tl}} = 400$ m and $x_3^{\text{tl}} = 650$ m, for $(x_1^S, x_3^S) = (0, 0)$ m, x_1^R ranging over the entire model and $x_3^R = 0$ m. From Eq. (6.31) we see that (x_1^R, x_3^R) is the source location of the reference wave field, whereas (x_1^S, x_3^S) is the source location of the monitor wave field. Hence, several reference shot-gathers are modelled for the aforementioned (x_1^R, x_3^R) -range, with the wave field measured at $x_3 = x_3^{\text{tl}}$. Also, a single monitor shot-gather with source position, $(x_1^S, x_3^S) = (0, 0)$, and also with receivers at $x_3 = x_3^{\text{tl}}$, is modelled. Using these shot-gathers we calculate the interaction integral of Eq. (6.31), in the time-domain, at $x_3^{\text{tl}} = 400$ m and $x_3^{\text{tl}} = 650$ m. The resulting $I^{\text{conv}}(x_3^{\text{tl}}; x_1^R, x_3^R, x_1^S, x_3^S)$ are shown in Figs. (6.4) and (6.5), respectively.

To test if I^{conv} is equivalent to an up-going difference measurement $\hat{p}^{\text{dif},u}$, according to Eq. (6.37), evaluated in the time domain, we should model this

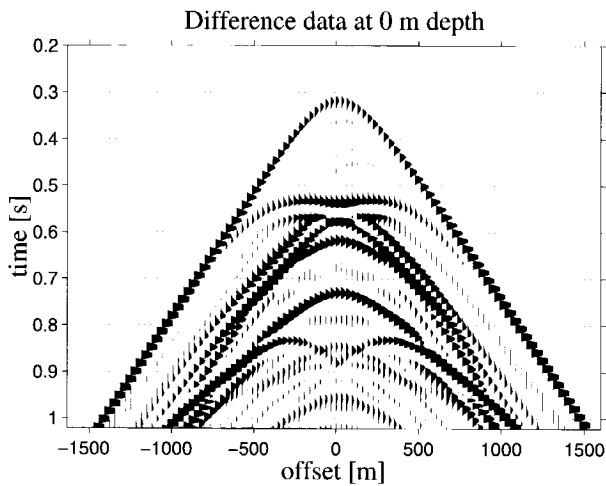


Figure 6.3: *Difference wave field evaluated at $x_3 = 0$ m depth for a range of offsets covering the model.*

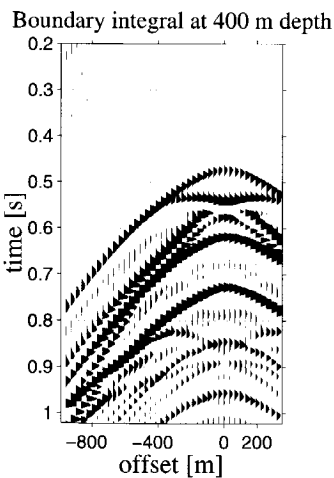


Figure 6.4: *interaction integral at $x_3^{\text{tl}} = 400$ m.*

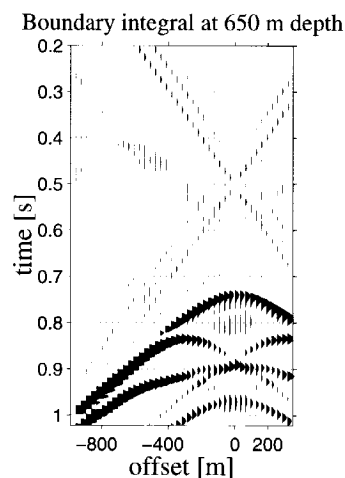


Figure 6.5: *Interaction integral at $x_3^{\text{tl}} = 650$ m.*

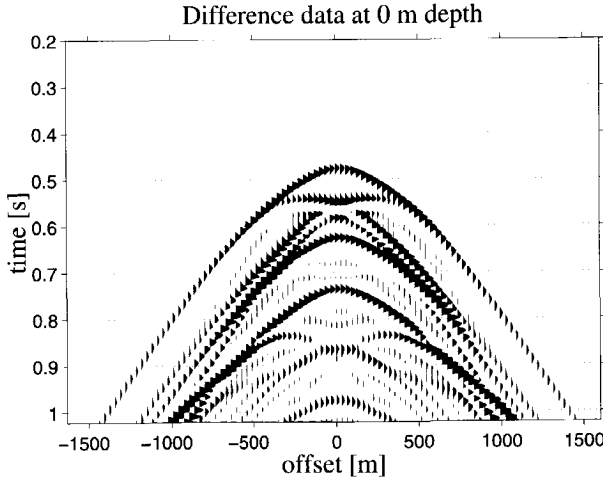


Figure 6.6: *Difference wave field at $x_3 = 0$ m, no temporal contrasts for $x_3 < 400$ m.*

wave field using the wave field equations of Eqs. (6.21) and (6.22). Given the source distribution of this wave field this is quite difficult to accomplish. Using the fact that $\hat{p}^{\text{dif},u}$ originates from contrast sources at $x_3 < x_3^{\text{tl}}$ we apply the following simpler procedure given in Eq. (6.38). The monitor model of Table (6.1) is changed such that it equals the reference model for $x_3 < 400$ m (halfway the diamond-shaped object), thereby eliminating the temporal contrasts for $x_3 < 400$ m and retaining the temporal contrasts for $x_3 > 400$ m. The resulting difference gather, using the same source/receiver parameters with which Fig. (6.3) is obtained, is shown in Fig. (6.6). One observes that Fig. (6.6) is very similar to Fig. (6.4), thereby indicating that the interaction integral is equivalent to a difference wave field which shows no temporal contrast above the interaction depth. We proceed by further altering the monitor model such that there is no temporal contrast in the diamond-shaped object. The only temporal contrast is in the lower layer. In Fig. (6.7) the difference gather is shown. The difference reflections associated with the temporal contrast in the diamond-shaped object, visible in Fig. (6.3) have disappeared. Note the similarity of Fig. (6.7) with Fig. (6.5).

In Fig. (6.7) the monitor model was changed such that it equalized the reference model for $x_3 < 650$ m. To examine the arrival times of the difference

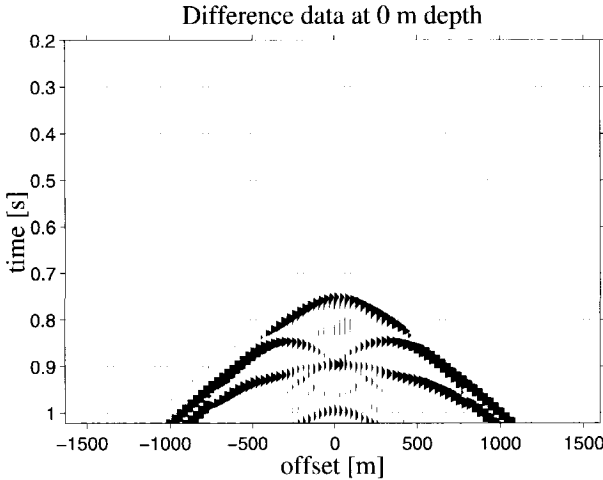


Figure 6.7: *Difference wave field at $x_3 = 0$ m, no temporal contrasts for $x_3 < 650$ m.*

reflections for this configuration, Fig. (6.7) is reproduced in Fig. (6.8) at a smaller scale. For comparison, in Fig. (6.9), a difference gather is shown obtained by changing the reference model to the monitor model for $x_3 < 650$ m. We observe that the maximum of the first arrival, at zero offset, in Fig. (6.8), is approximately at 0.73 s, whereas the same arrival, in Fig. (6.9), measures 0.71 s. The first reflection in the latter figure arrives earlier because, according to Table (6.1), the monitor velocity, $c^{(2)}$, is larger than the reference velocity, $c^{(1)}$. To examine the same arrival time in case of the interaction integral, calculated at $x_3 = 650$ m, as shown in Fig. (6.5), this last figure is also shown on a larger scale in Fig. (6.10). The arrival time of the maximum of the first reflection, at zero offset, is approximately 0.72 s, in between the aforementioned arrival times in Figs. (6.8) and (6.9). Because there are no apparent difference reflections present above the interaction depth of $x_3 = 650$ m in Fig. (6.10), we expect to be able to identify with the first reflection two media descriptions which do not generate difference reflections, as is possible in the Figs. (6.8) and (6.9). Because the wave field of Fig. (6.10) is constructed using the interaction integral of Eq. (6.31), these media descriptions will be some integral average of both the reference and monitor media, with respect to the lateral coordinates x_1 . This observation is quantified in Chapter 10 in terms of the reference and monitor scalar

density and admittance operators. The temporal contrast in the density is maintained, but the contrast in the admittance operator is eliminated through an eigenvalue decomposition (see Fig (10.1)). Because difference reflections only depend on temporal contrasts in the admittance operator, absence of this contrast eliminates these reflections.

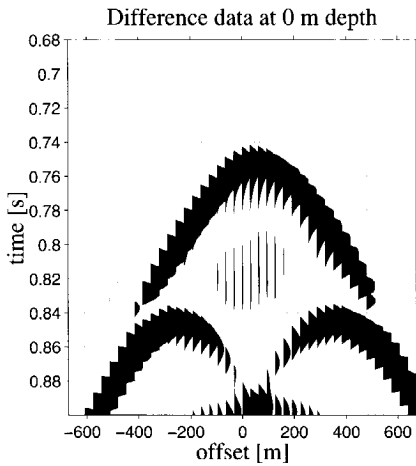


Figure 6.8: *Difference wave field at $x_3 = 0$ m, monitor model equalized to reference model for $x_3 < 650$ m.*

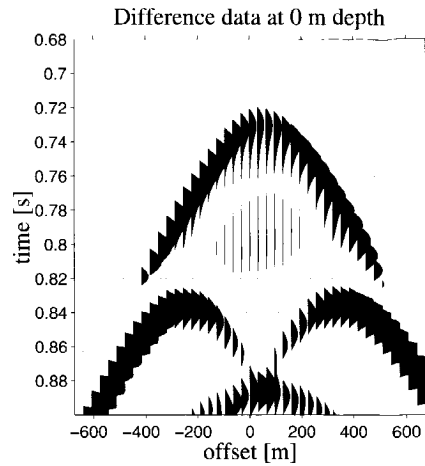


Figure 6.9: *Difference wave field at $x_3 = 0$ m, reference model equalized to monitor model for $x_3 < 650$ m.*

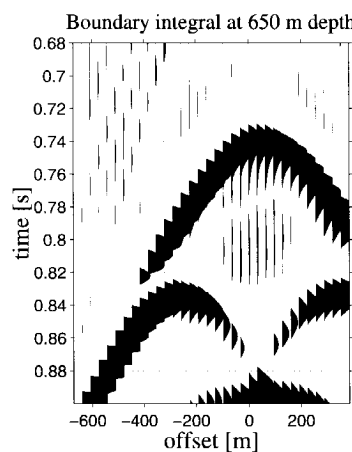


Figure 6.10: *Interaction integral at $x_3 = 650$ m.*

Chapter 7

Acoustic reciprocity theorems

7.1 Introduction

In this chapter the acoustic reciprocity theorems of the time-convolution and the time-correlation types are derived. The theorems have their roots in Green's theorem for Laplace's equation and Helmholtz's extension to the wave equation, the latter being introduced by Lord Rayleigh in his book *The theory of sound*. The acoustic reciprocity theorem, or Rayleigh's reciprocity theorem, has numerous applications, such as in

- transmitting/receiving properties of acoustic transducers,
- direct(forward) and inverse source problems,
- forward and inverse scattering problems,
- time-lapse problems (this thesis).

It also leads, as will be shown later, to a mathematical formulation of Huygens' principle. A reciprocity theorem interrelates the wave field quantities of two admissible states that occur in one and the same time-invariant domain $\mathbb{D} \subset \mathbb{R}^3$ (de Hoop (1995)). In forward/inverse source and scattering problems one state is identified with a physical wave field while the other state is identified with a computational or so called Green's wave field. In time-lapse problems both states are identified with physical wave fields. Application of the time-domain reciprocity theorem to these problems leads to an integral representation of the physical wave field in terms of its time-retarded state

(forward problems) or in terms of its time-advanced state (inverse problems). According to Brody (1993), Einstein already showed in 1909, with regard to Maxwell's equations, that as long as the domain of application is confined to a finite region, the time-retarded and the time-advanced representations are equivalent. Initial conditions in the form of the physical wave field's initial state are used in the time-retarded representation to calculate its final state. The time-advanced representation uses the physical wave field's final state as final conditions to confirm the initial state. Mixed boundary conditions are also possible as long as the domain is finite. Brody (1993) identifies this bi-directional determinism with finite and limited systems on the one hand and reversibility on the other. According to Brody (1993) infinite systems are associated with uni-directional determinism which can not be inverted. In this thesis the domain of application for a reciprocity theorem comprises a finite interval along the longitudinal coordinate and is infinite in the transverse directions. Contributions for which the transverse coordinates tend to infinity vanish (Fokkema and van den Berg (1993)). The time-retarded representation of a wave field in terms of contributions from two infinite surfaces can be reduced to one, using Sommerfeld radiation conditions (causality conditions in de Hoop's terminology) at infinity, yielding the mathematical formulation of Huygens' principle. The time-advanced representation, in which the state of the physical wave field depends on its future state, involves anti-causal Green's wave fields. These latter wave fields do not satisfy Sommerfeld radiation conditions at infinity, which excludes the possibility of representing the physical wave field in terms of contributions from a single infinite surface (Bojarski (1983)). Hence, the incompatibility of the time-retarded and time-advanced representations for a half-space configuration poses one example of an infinite system which does not allow bi-directionality. The philosophical implication of a system which is both infinite and bi-directional is that the concept of causality becomes meaningless because no distinction can be made between cause and effect (Brody (1993)).

7.2 The acoustic scalar wave field equations

The wave field equations of acoustics are given by the equation of motion,

$$\partial_k p(\mathbf{x}, t) + \dot{\Phi}_k(\mathbf{x}, t) = f_k(\mathbf{x}, t), \quad (7.1)$$

and the deformation equation,

$$\partial_k v_k(\mathbf{x}, t) - \dot{\theta}(\mathbf{x}, t) = q(\mathbf{x}, t) \quad (7.2)$$

(Fokkema and van den Berg (1993); de Hoop (1995)). In Eq. (7.1) p constitutes the pressure, $\dot{\Phi}_k$ represents a component of the mass flow density rate and f_k signifies a component of the volume source density of volume force. In Eq. (7.2) v_k constitutes a component of the particle velocity, $\dot{\theta}$ represents the cubic dilatation rate and q represents the volume source density of injection rate. For a fluid that is linear, time-invariant, instantaneously reacting, locally reacting, isotropic and lossless in its acoustic behaviour we use the following constitutive equations,

$$\dot{\Phi}_k(\mathbf{x}, t) = \rho(\mathbf{x}) D_t v_k(\mathbf{x}, t) \quad (7.3)$$

and

$$\dot{\theta}(\mathbf{x}, t) = -\kappa(\mathbf{x}) D_t p(\mathbf{x}, t), \quad (7.4)$$

with the co-moving time derivative, $D_t = \partial_t + v_k \partial_k$, which produces the rate of change with time that an observer registers when moving through the fluid with the particle velocity \mathbf{v} . We assume that inside the considered domain the constitutive quantities, the volume density of mass ρ and the compressibility κ , in Eqs. (7.3) and (7.4), are smooth, i.e. infinitely differentiable functions of position. The acoustic quantities are summarized in Table (7.1). The

Symbol	Name	Unit
p	pressure	Pa
\mathbf{v}	particle velocity	m s^{-1}
$\dot{\Phi}$	mass flow density rate	$\text{kg m}^{-2} \text{s}^{-2}$
$\dot{\theta}$	cubic dilatation rate	s^{-1}
ρ	volume density of mass	kg m^{-3}
κ	compressibility	Pa^{-1}
\mathbf{f}	volume source density of volume force	N m^{-3}
q	volume source density of volume injection rate	s^{-1}

Table 7.1: Acoustic quantities and their units

system of equations (7.1) to (7.4) is nonlinear in the particle velocity \mathbf{v} due

to the occurrence of \mathbf{v} in the co-moving time derivative D_t . Assuming that the dynamic pressure, associated with the acoustic wave motion, represents small amplitude variations on a static equilibrium distribution of pressure (e.g., seismic waves in the Earth superposed on a hydrostatic gravity background pressure), and assuming that the particle velocity is small with respect to the stream velocity of the fluid (e.g., sound waves in a stream of the exhaust of an internal combustion engine), the linearized acoustic wave field equations can be derived as

$$\partial_k p(\mathbf{x}, t) + \rho(\mathbf{x}) \partial_t v_k(\mathbf{x}, t) = f_k(\mathbf{x}, t), \quad (7.5)$$

and

$$\partial_k v_k(\mathbf{x}, t) + \kappa(\mathbf{x}) \partial_t p(\mathbf{x}, t) = q(\mathbf{x}, t), \quad (7.6)$$

(see de Hoop (1995)[p. 31-34]).

The *causal* wave field quantities, p and \mathbf{v} are subject to the following *initial* conditions

$$\begin{aligned} p(\mathbf{x}, t) &= 0 \quad \text{for } t < 0, \\ \mathbf{v}(\mathbf{x}, t) &= 0 \quad \text{for } t < 0. \end{aligned} \quad (7.7)$$

Application of the Laplace transform of Eq. (B.2), to the Eqs. (7.5) and (7.6) yields

$$\partial_k \hat{p}(\mathbf{x}, s) + s \rho(\mathbf{x}) \hat{v}_k(\mathbf{x}, s) = \rho(\mathbf{x}) v_k(\mathbf{x}, 0+) + \hat{f}_k(\mathbf{x}, s), \quad (7.8)$$

and

$$\partial_k \hat{v}_k(\mathbf{x}, s) + s \kappa(\mathbf{x}) \hat{p}(\mathbf{x}, s) = \kappa(\mathbf{x}) p(\mathbf{x}, 0+) + \hat{q}(\mathbf{x}, s), \quad (7.9)$$

where we used Eq. (B.21). Non-vanishing wave field quantities at $t = 0$ are handled by incorporating these in the source terms in the right-hand sides of Eqs. (7.8) and (7.9). Assuming that \mathbf{f} and \hat{q} incorporate the extended source definitions we can write

$$\partial_k \hat{p}(\mathbf{x}, s) + s \rho(\mathbf{x}) \hat{v}_k(\mathbf{x}, s) = \hat{f}_k(\mathbf{x}, s), \quad (7.10)$$

and

$$\partial_k \hat{v}_k(\mathbf{x}, s) + s \kappa(\mathbf{x}) \hat{p}(\mathbf{x}, s) = \hat{q}(\mathbf{x}, s). \quad (7.11)$$

Any causal Laplace transformed function in Eqs. (7.10) and (7.11), satisfying the initial conditions of Eqs. (7.7), satisfies the condition $\text{Re}(s) > 0$, which ensures regularity in the right half plane of the complex s -space. By reversing the time-axis, according to $\{p^a, v_3^a\}(\mathbf{x}, t) = \{p, v_3\}(\mathbf{x}, -t)$ (Eq. (B.14)), one can also consider the following *anti-causal* wave field equations,

$$\partial_k p^a(\mathbf{x}, t) - \rho(\mathbf{x}) \partial_t v_k^a(\mathbf{x}, t) = f_k^a(\mathbf{x}, t), \quad (7.12)$$

and

$$\partial_k v_k^a(\mathbf{x}, t) - \kappa(\mathbf{x}) \partial_t p^a(\mathbf{x}, t) = q^a(\mathbf{x}, t), \quad (7.13)$$

which are subject to the following *final* conditions

$$\begin{aligned} p^a(\mathbf{x}, t) &= 0 \quad \text{for } t > 0, \\ \mathbf{v}^a(\mathbf{x}, t) &= 0 \quad \text{for } t > 0. \end{aligned} \quad (7.14)$$

Taking the Laplace transform of Eqs. (7.12) and (7.13), using (B.10) and Eq (B.16), and incorporating non-vanishing wave field quantities at $t = 0$ in the source terms on the right-hand sides of these equations, yields

$$\partial_k \hat{p}(\mathbf{x}, -s^a) - s^a \rho(\mathbf{x}) \hat{v}_k(\mathbf{x}, -s^a) = \hat{f}_k(\mathbf{x}, -s^a), \quad (7.15)$$

and

$$\partial_k \hat{v}_k(\mathbf{x}, -s^a) - s^a \kappa(\mathbf{x}) \hat{p}(\mathbf{x}, -s^a) = \hat{q}(\mathbf{x}, -s^a), \quad (7.16)$$

in which the Laplace transform parameter s^a , in Eqs. (7.15) and (7.16), satisfies the condition $\text{Re}(s^a) < 0$. Hence, wave field equations which describe anti-causal wave fields are obtained by *time-reversal* in the time domain and taking $-s^a$ instead of s as the Laplace parameter in the transformed domain (Fokkema and van den Berg (1993) and de Hoop (1995)).

7.3 The acoustic vectorial wave field equation

Employing a Cartesian reference frame we regard the wave field quantities as a function of the transverse vector coordinate \mathbf{x}_T and the longitudinal scalar coordinate x_3 . The orientation of the Cartesian reference frame is fixed by choosing the longitudinal coordinate x_3 to coincide with the general wave

field direction. In surface seismic measurements the longitudinal direction is chosen to be vertical and measures depth, whereas e.g. in cross-well seismic measurements the longitudinal direction is horizontal, measuring inter-well distance. To accommodate such a directional decomposition the transverse particle velocity components \hat{v}_1 and \hat{v}_2 are eliminated from the wave field equations (7.10) and (7.11), obtaining a single differential vector equation in terms of wave field vectors.

We separate from the wave field equations, Eqs. (7.10) and (7.11),

$$\partial_k \hat{p} + s\rho \hat{v}_k = \hat{f}_k, \quad (7.17)$$

$$\partial_k \hat{v}_k + s\kappa \hat{p} = \hat{q}, \quad (7.18)$$

the transverse and longitudinal spatial derivatives,

$$\partial_\alpha \hat{p} + s\rho \hat{v}_\alpha = \hat{f}_\alpha, \quad (7.19)$$

$$\partial_3 \hat{p} + s\rho \hat{v}_3 = \hat{f}_3, \quad (7.20)$$

$$\partial_3 \hat{v}_3 + \partial_\alpha \hat{v}_\alpha + s\kappa \hat{p} = \hat{q}. \quad (7.21)$$

Extraction of \hat{v}_α from Eq. (7.19),

$$\hat{v}_\alpha = - (s\rho)^{-1} \partial_\alpha \hat{p} + (s\rho)^{-1} \hat{f}_\alpha, \quad (7.22)$$

and substitution of the result into Eq. (7.21) yields

$$\partial_3 \hat{v}_3 + (s\rho)^{-1} [\hat{\gamma}^2 - \rho \partial_\alpha (\rho^{-1} \partial_\alpha)] \hat{p} = \hat{q} - s^{-1} \partial_\alpha (\rho^{-1} \hat{f}_\alpha), \quad (7.23)$$

in which

$$\hat{\gamma} = \frac{s}{c}, \quad (7.24)$$

and the acoustic wave speed is given by

$$c = (\rho\kappa)^{-\frac{1}{2}}. \quad (7.25)$$

Combining Eq. (7.20) with Eq. (7.23) results in the following first-order ordinary differential equation with respect to x_3 (Wapenaar and Berkhouwt (1989); de Hoop (1992)),

$$\partial_3 \hat{\mathbf{F}} + \hat{\mathbf{A}} \hat{\mathbf{F}} = \hat{\mathbf{N}}, \quad (7.26)$$

with the wave field vector $\hat{\mathbf{F}}$, the acoustic system operator $\hat{\mathbf{A}}$ and the source vector $\hat{\mathbf{N}}$ given by

$$\hat{\mathbf{F}} = \begin{pmatrix} \hat{p} \\ \hat{v}_3 \end{pmatrix}, \quad \hat{\mathbf{A}} = \begin{pmatrix} 0 & s\rho \\ s\hat{\mathcal{K}} & 0 \end{pmatrix}, \quad \hat{\mathbf{N}} = \begin{pmatrix} \hat{f}_3 \\ \hat{q} - s^{-1}\partial_\alpha(\rho^{-1}\hat{f}_\alpha) \end{pmatrix}, \quad (7.27)$$

respectively. The operator $\hat{\mathcal{K}}$, given by

$$\hat{\mathcal{K}} = \kappa - s^{-2}\partial_\alpha(\rho^{-1}\partial_\alpha), \quad (7.28)$$

contains only spatial derivatives with respect to the transverse coordinates. Defining the so called Helmholtz operator as,

$$\hat{\mathcal{H}}_2 \stackrel{\text{def}}{=} \hat{\gamma}^2 - \rho\partial_\alpha(\rho^{-1}\partial_\alpha), \quad (7.29)$$

we have

$$\hat{\mathcal{K}} = s^{-2}\rho^{-1}\hat{\mathcal{H}}_2. \quad (7.30)$$

7.4 Acoustic states

We consider a time-invariant, open domain \mathbb{D} in \mathbb{R}^3 , bounded by the infinite surfaces $x_3 = x_3^u$ and $x_3 = x_3^l$ (the superscripts u and l stand for ‘upper’ and ‘lower’, respectively), with $x_3^l > x_3^u$ (geological configuration), in which two, possibly non-identical acoustic states can occur. The two states are denoted by the superscripts A and B . Both states are defined by:

- the wave field quantities $\{\hat{\mathbf{F}}^A, \hat{\mathbf{F}}^B\}$,
- the material matrix operators $\{\hat{\mathbf{A}}^A, \hat{\mathbf{A}}^B\}$,
- the source quantities $\{\hat{\mathbf{N}}^A, \hat{\mathbf{N}}^B\}$.

For both State A and State B , the relation between the wave field state, the material state and the source state is governed by the wave field vector equation (7.26). The two states are expressed as

$$A = \{\hat{\mathbf{F}}^A, \hat{\mathbf{A}}^A, \hat{\mathbf{N}}^A\} \quad \text{and} \quad B = \{\hat{\mathbf{F}}^B, \hat{\mathbf{A}}^B, \hat{\mathbf{N}}^B\}. \quad (7.31)$$

The respective wave field vector equations are given by

$$\partial_3 \hat{\mathbf{F}}^A + \hat{\mathbf{A}}^A \hat{\mathbf{F}}^A = \hat{\mathbf{N}}^A, \quad (7.32)$$

$$\partial_3 \hat{\mathbf{F}}^B + \hat{\mathbf{A}}^B \hat{\mathbf{F}}^B = \hat{\mathbf{N}}^B. \quad (7.33)$$

The two states and the domain of application of the reciprocity theorem are shown in Fig. (7.1). The wave field vector equations of Eqs. (7.32) and

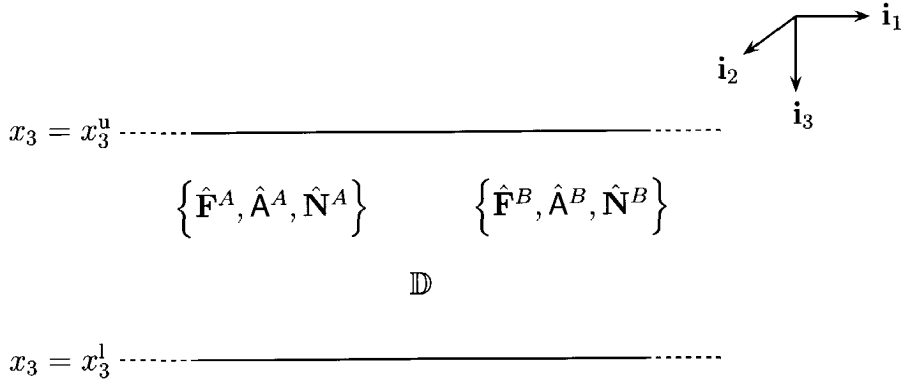


Figure 7.1: The two states, State $A = \{\hat{\mathbf{F}}^A, \hat{\mathbf{A}}^A, \hat{\mathbf{N}}^A\}$ and State $B = \{\hat{\mathbf{F}}^B, \hat{\mathbf{A}}^B, \hat{\mathbf{N}}^B\}$, and the domain of application \mathbb{D} of the reciprocity theorem.

(7.33) apply to those points in \mathbb{D} where the medium parameters κ and ρ are smooth, i.e. infinitely differentiable with respect to the spatial coordinate (\mathbf{x}_T, x_3) . At interfaces x_3 is constant, for which the medium parameters are discontinuous with respect to the longitudinal coordinate x_3 , the wave field vector equations of Eq. (7.32) must be supplemented with the following boundary conditions,

$$\{\hat{\mathbf{F}}^A, \hat{\mathbf{F}}^B\} \text{ is continuous across interface.} \quad (7.34)$$

In case of interfaces represented by hyper-surfaces, which coincide e.g. with geological contrasts, a reference frame with curvilinear coordinates would be more appropriate. In this thesis we confine ourselves to planar surfaces.

In de Hoop (1995) and Fokkema and van den Berg (1993) the wave field equations (7.10) and (7.11) are used to derive the Laplace domain reciprocity theorems. In this thesis we use instead the wave field vector equation (7.26) to accommodate the preferential longitudinal propagation direction of the wave fields.

7.5 Bilinear forms

Consider the following definition of a *bilinear form* \hat{f} ,

$$f(\mathbf{F}, \mathbf{G}) \stackrel{\text{def}}{=} \int_{\mathbf{x}_T \in \mathbb{R}^2} \mathbf{F}^t(\mathbf{x}_T) \mathbf{B} \mathbf{G}(\mathbf{x}_T) d\mathbf{x}_T, \quad (7.35)$$

which constitutes the mapping,

$$f : [L^2(\mathbb{R}^2)]^2 \times [L^2(\mathbb{R}^2)]^2 \rightarrow \mathbb{C}, \quad (7.36)$$

from the product of two Hilbert spaces into the complex plane \mathbb{C} . A Hilbert space $[L^2(\mathbb{R}^2)]^2$ is a set of square-integrable (L^2), vector-valued ($[\cdot]^2$) functions, $\mathbf{F}, \mathbf{G} \in [L^2(\mathbb{R}^2)]^2$, defined on the transverse coordinate space \mathbb{R}^2 . The superscript \cdot^t denotes transposition of the vector \mathbf{F} . The linear operator \mathbf{B} associated with f is given by the map,

$$\mathbf{B} : [L^2(\mathbb{R}^2)]^2 \rightarrow [L^2(\mathbb{R}^2)]^2. \quad (7.37)$$

Bilinearity means that (Lang (1993)), $\forall \mathbf{F}, \mathbf{F}_1, \mathbf{F}_2, \mathbf{G}, \mathbf{G}_1, \mathbf{G}_2 \in [L^2(\mathbb{R}^2)]^2$ and $\forall a, b \in \mathbb{C}$, we have linearity in the first variable

$$\begin{aligned} f(\mathbf{F}_1 + \mathbf{F}_2, \mathbf{G}) &= f(\mathbf{F}_1, \mathbf{G}) + f(\mathbf{F}_2, \mathbf{G}), \\ f(a\mathbf{F}, \mathbf{G}) &= af(\mathbf{F}, \mathbf{G}), \end{aligned} \quad (7.38)$$

and linearity in the second variable

$$\begin{aligned} f(\mathbf{F}, \mathbf{G}_1 + \mathbf{G}_2) &= f(\mathbf{F}, \mathbf{G}_1) + f(\mathbf{F}, \mathbf{G}_2), \\ f(\mathbf{F}, b\mathbf{G}) &= bf(\mathbf{F}, \mathbf{G}). \end{aligned} \quad (7.39)$$

We say that f is a *symmetric* bilinear form if

$$f(\mathbf{F}, \mathbf{G}) = f(\mathbf{G}, \mathbf{F}), \quad \forall \mathbf{F}, \mathbf{G} \in [L^2(\mathbb{R}^2)]^2. \quad (7.40)$$

A bilinear form f is called an *alternating* form if

$$f(\mathbf{F}, \mathbf{F}) = 0, \quad \forall \mathbf{F} \in [L^2(\mathbb{R}^2)]^2. \quad (7.41)$$

An alternating form has the following property,

$$f(\mathbf{F}, \mathbf{G}) = -f(\mathbf{G}, \mathbf{F}), \quad \forall \mathbf{F}, \mathbf{G} \in [L^2(\mathbb{R}^2)]^2, \quad (7.42)$$

as one can see by substituting $\mathbf{F} + \mathbf{G}$ in Eq. (7.41) and using the bilinearity property of Eqs. (7.38) and (7.39).

The bilinear form f associated with \mathbf{B} is symbolized as

$$f(\mathbf{F}, \mathbf{G}) = \langle \mathbf{F}, \mathbf{B}\mathbf{G} \rangle_b. \quad (7.43)$$

Given the linear operator \mathbf{B} and its associated bilinear form f there exists a unique linear map

$$\mathbf{B}^t : [L^2(\mathbb{R}^2)]^2 \rightarrow [L^2(\mathbb{R}^2)]^2, \quad (7.44)$$

such that

$$\langle \mathbf{F}, \mathbf{B}\mathbf{G} \rangle_b = \langle \mathbf{B}^t \mathbf{F}, \mathbf{G} \rangle_b, \quad \forall \mathbf{F}, \mathbf{G} \in [L^2(\mathbb{R}^2)]^2. \quad (7.45)$$

We call \mathbf{B}^t the *transpose* of \mathbf{B} with respect to f . For, $a \in \mathbb{C}$ and $\mathbf{B}, \mathbf{C} : [L^2(\mathbb{R}^2)]^2 \rightarrow [L^2(\mathbb{R}^2)]^2$, we deduce that (Lang (1993)),

$$(a\mathbf{B})^t = a\mathbf{B}^t, \quad (\mathbf{B} + \mathbf{C})^t = \mathbf{B}^t + \mathbf{C}^t, \quad (\mathbf{B}^t)^t = \mathbf{B}, \quad \text{and} \quad (\mathbf{BC})^t = \mathbf{C}^t \mathbf{B}^t. \quad (7.46)$$

In terms of scalar operators we have,

$$\mathbf{B} = \begin{pmatrix} \mathcal{B}_{11} & \mathcal{B}_{12} \\ \mathcal{B}_{21} & \mathcal{B}_{22} \end{pmatrix} \iff \mathbf{B}^t = \begin{pmatrix} \mathcal{B}_{11}^t & \mathcal{B}_{21}^t \\ \mathcal{B}_{12}^t & \mathcal{B}_{22}^t \end{pmatrix}, \quad (7.47)$$

in which the operators $\mathcal{B}_{\alpha\beta}$ constitute the maps $\mathcal{B}_{\alpha\beta} : [L^2(\mathbb{R}^2)]^1 \rightarrow [L^2(\mathbb{R}^2)]^1$, with $[L^2(\mathbb{R}^2)]^1$ being a Hilbert space of scalar-valued functions, and the

transposition operation is with respect to a bilinear form, $f : [L^2(\mathbb{R}^2)]^1 \times [L^2(\mathbb{R}^2)]^1 \rightarrow \mathbb{C}$, of scalar-valued functions.

If f is symmetric then, using Eqs. (7.35), (7.40) and (7.45),

$$\langle \mathbf{F}, \mathbf{B}\mathbf{G} \rangle_b = \langle \mathbf{G}, \mathbf{B}\mathbf{F} \rangle_b = \langle \mathbf{B}^t \mathbf{G}, \mathbf{F} \rangle_b = \langle \mathbf{F}, \mathbf{B}^t \mathbf{G} \rangle_b, \\ \forall \mathbf{F}, \mathbf{G} \in [L^2(\mathbb{R}^2)]^2. \quad (7.48)$$

Hence,

$$\mathbf{B} = \mathbf{B}^t. \quad (7.49)$$

The matrix operator \mathbf{B} is said to be *symmetric* with respect to f . If f is alternating then, using Eqs. (7.35), (7.42) and (7.45),

$$\langle \mathbf{F}, \mathbf{B}\mathbf{G} \rangle_b = -\langle \mathbf{G}, \mathbf{B}\mathbf{F} \rangle_b = -\langle \mathbf{B}^t \mathbf{G}, \mathbf{F} \rangle_b = \langle \mathbf{F}, -\mathbf{B}^t \mathbf{G} \rangle_b, \\ \forall \mathbf{F}, \mathbf{G} \in [L^2(\mathbb{R}^2)]^2. \quad (7.50)$$

Hence,

$$\mathbf{B} = -\mathbf{B}^t. \quad (7.51)$$

The matrix operator \mathbf{B} is said to be *skew-symmetric* or *alternating* with respect to f .

7.6 Time-convolution type reciprocity theorem

Consider the domain $\mathbb{D} = \{(\mathbf{x}_T, x_3) | \mathbf{x}_T \in \mathbb{R}^2, x_3^u < x_3 < x_3^l\}$ shown in Fig. (7.1). Following Wapenaar (1996b) and Haines and de Hoop (1996), in \mathbb{D} , an interaction quantity \hat{I}^{conv} between the two states, A and B , associated with the wave field vector Eqs. (7.32) and (7.33), is defined, according to,

$$\hat{I}^{\text{conv}} : [L^2(\mathbb{R}^2)]^2 \times [L^2(\mathbb{R}^2)]^2 \rightarrow \mathbb{C}. \quad (7.52)$$

and

$$\left[\hat{I}^{\text{conv}} \left(\hat{\mathbf{F}}^A, \hat{\mathbf{F}}^B \right) \right] (x_3, s) \\ \stackrel{\text{def}}{=} \int_{\mathbf{x}_T \in \mathbb{R}^2} \left(\hat{\mathbf{F}}^A \right)^t (\mathbf{x}_T, x_3, s) \mathbf{J} \hat{\mathbf{F}}^B (\mathbf{x}_T, x_3, s) d\mathbf{x}_T. \quad (7.53)$$

The interaction quantity \hat{I}^{conv} constitutes a bilinear form with the variables x_3 and s acting as parameters. The *standard alternating* matrix operator \mathbf{J} , associated with the bilinear form \hat{I}^{conv} , is given by

$$\mathbf{J} = \begin{pmatrix} \mathcal{O} & \mathcal{I} \\ -\mathcal{I} & \mathcal{O} \end{pmatrix}, \quad (7.54)$$

with \mathcal{O} and \mathcal{I} representing the scalar null and scalar identity operators, respectively. Using the notation of Eq. (7.43) the bilinear form \hat{I}^{conv} is symbolized as

$$\hat{I}^{\text{conv}} \left(\hat{\mathbf{F}}^A, \hat{\mathbf{F}}^B \right) = \left\langle \hat{\mathbf{F}}^A, \mathbf{J} \hat{\mathbf{F}}^B \right\rangle_b. \quad (7.55)$$

In accordance with the skew-symmetry of \mathbf{J} ,

$$\mathbf{J} = -\mathbf{J}^t, \quad (7.56)$$

the interaction quantity \hat{I}^{conv} is an alternating form. Hence, according to Eq. (7.41)

$$I^{\text{conv}} \left(\hat{\mathbf{F}}, \hat{\mathbf{F}} \right) = 0, \quad \forall \hat{\mathbf{F}} \in [L^2(\mathbb{R}^2)]^2, \quad (7.57)$$

and according to Eq. (7.42)

$$I^{\text{conv}} \left(\hat{\mathbf{F}}^A, \hat{\mathbf{F}}^B \right) = -I^{\text{conv}} \left(\hat{\mathbf{F}}^B, \hat{\mathbf{F}}^A \right), \quad \forall \hat{\mathbf{F}}^A, \hat{\mathbf{F}}^B \in [L^2(\mathbb{R}^2)]^2. \quad (7.58)$$

The *multiplication* of the Laplace transformed wave field quantities in Eq. (7.53) is equivalent to a *convolution* in the time domain, hence the denotation \hat{I}^{conv} .

Taking the derivative of Eq. (7.53) with respect to the longitudinal coordinate x_3 , omitting the Laplace transform parameter s from the argument lists, yields

$$\partial_3 \left\langle \hat{\mathbf{F}}^A, \mathbf{J} \hat{\mathbf{F}}^B \right\rangle_b (x_3) = \left\langle \partial_3 \hat{\mathbf{F}}^A, \mathbf{J} \hat{\mathbf{F}}^B \right\rangle_b (x_3) + \left\langle \hat{\mathbf{F}}^A, \mathbf{J} \partial_3 \hat{\mathbf{F}}^B \right\rangle_b (x_3). \quad (7.59)$$

Substitution of the wave field vector Eqs. (7.32) and (7.33) into the right-hand side of Eq. (7.59) leads to the *local* form of the reciprocity theorem of the time-convolution type,

$$\begin{aligned} \partial_3 \left\langle \hat{\mathbf{F}}^A, \mathbf{J} \hat{\mathbf{F}}^B \right\rangle_b (x_3) &= - \left\langle \hat{\mathbf{F}}^A, \left[\left(\hat{\mathbf{A}}^A \right)^t \mathbf{J} + \mathbf{J} \hat{\mathbf{A}}^B \right] \hat{\mathbf{F}}^B \right\rangle_b (x_3) \\ &\quad + \left\langle \hat{\mathbf{N}}^A, \mathbf{J} \hat{\mathbf{F}}^B \right\rangle_b (x_3) + \left\langle \hat{\mathbf{F}}^A, \mathbf{J} \hat{\mathbf{N}}^B \right\rangle_b (x_3), \end{aligned} \quad (7.60)$$

Eq. (7.60) is local with respect to the longitudinal coordinate x_3 . In this last equation $(\hat{\mathbf{A}}^A)^t$ denotes the transpose of the matrix operator $\hat{\mathbf{A}}^A$, as defined in Eq. (7.45). The contrast operator in the first integral on the right-hand side of Eq. (7.60) is derived as

$$(\hat{\mathbf{A}}^A)^t \mathbf{J} + \mathbf{J} \hat{\mathbf{A}}^B = \begin{pmatrix} s \left[\hat{\mathcal{K}}^B - (\hat{\mathcal{K}}^A)^t \right] & \mathcal{O} \\ \mathcal{O} & -s(\rho^B - \rho^A) \mathcal{I} \end{pmatrix}, \quad (7.61)$$

which constitutes a diagonal matrix operator. Taking identical states in Eq. (7.31),

$$A = B = \{\hat{\mathbf{F}}, \hat{\mathbf{A}}, \hat{\mathbf{N}}\}, \quad (7.62)$$

Eq. (7.60) becomes, using Eq. (7.41), the quadratic form

$$\left\langle \hat{\mathbf{F}}, (\hat{\mathbf{A}}^t \mathbf{J} + \mathbf{J} \hat{\mathbf{A}}) \hat{\mathbf{F}} \right\rangle_b (x_3) = 0, \quad (7.63)$$

with

$$\hat{\mathbf{A}}^t \mathbf{J} + \mathbf{J} \hat{\mathbf{A}} = \begin{pmatrix} s(\hat{\mathcal{K}} - \hat{\mathcal{K}}^t) & \mathcal{O} \\ \mathcal{O} & \mathcal{O} \end{pmatrix}. \quad (7.64)$$

Because Eq. (7.63) must hold for $\forall \mathbf{F} \in [L^2(\mathbb{R}^2)]^2$ we have that $\hat{\mathcal{K}}$ of Eq. (7.64) is symmetric with respect to its associated bilinear form,

$$\hat{\mathcal{K}} = \hat{\mathcal{K}}^t. \quad (7.65)$$

Hence, $\hat{\mathbf{A}}$ is symplectic, i.e.

$$\hat{\mathbf{A}}^t \mathbf{J} = -\mathbf{J} \hat{\mathbf{A}}. \quad (7.66)$$

We can now write

$$(\hat{\mathbf{A}}^A)^t \mathbf{J} + \mathbf{J} \hat{\mathbf{A}}^B = \mathbf{J} \Delta \hat{\mathbf{A}} = \begin{pmatrix} s \Delta \hat{\mathcal{K}} & \mathcal{O} \\ \mathcal{O} & -s \Delta \rho \mathcal{I} \end{pmatrix}, \quad (7.67)$$

with

$$\Delta \hat{\mathbf{A}} = \hat{\mathbf{A}}^B - \hat{\mathbf{A}}^A, \quad (7.68)$$

and

$$\Delta \hat{\mathcal{K}} = \hat{\mathcal{K}}^B - \hat{\mathcal{K}}^A \quad \text{and} \quad \Delta \rho = \rho^B - \rho^A. \quad (7.69)$$

Integration of Eq. (7.60) with respect to x_3 , from $x_3 = x_3^u$ to $x_3 = x_3^l$, with $x_3^l > x_3^u$ (Fig. (7.1)), yields the *global* form of the reciprocity theorem of the convolution type,

$$\begin{aligned} & \left\langle \hat{\mathbf{F}}^A, \mathbf{J} \hat{\mathbf{F}}^B \right\rangle_b (x_3^l) - \left\langle \hat{\mathbf{F}}^A, \mathbf{J} \hat{\mathbf{F}}^B \right\rangle_b (x_3^u) \\ &= - \int_{x_3=x_3^u}^{x_3^l} \left\langle \hat{\mathbf{F}}^A, \mathbf{J} \Delta \hat{\mathbf{A}} \hat{\mathbf{F}}^B \right\rangle_b (x_3) dx_3 \\ &+ \int_{x_3=x_3^u}^{x_3^l} \left[\left\langle \hat{\mathbf{N}}^A, \mathbf{J} \hat{\mathbf{F}}^B \right\rangle_b (x_3) + \left\langle \hat{\mathbf{F}}^A, \mathbf{J} \hat{\mathbf{N}}^B \right\rangle_b (x_3) \right] dx_3. \end{aligned} \quad (7.70)$$

In de Hoop (1995)[p. 164-166] and Fokkema and van den Berg (1993)[p. 95-97], the reciprocity theorem of the convolution type is derived in terms of the scalar wave field quantities \hat{p} and $\hat{\mathbf{v}}$. In case of equality of the material parameters of State A and State B Eq. (7.70) reduces to

$$\begin{aligned} & \left\langle \hat{\mathbf{F}}^A, \mathbf{J} \hat{\mathbf{F}}^B \right\rangle_b (x_3^l) - \left\langle \hat{\mathbf{F}}^A, \mathbf{J} \hat{\mathbf{F}}^B \right\rangle_b (x_3^u) \\ &= \int_{x_3=x_3^u}^{x_3^l} \left[\left\langle \hat{\mathbf{N}}^A, \mathbf{J} \hat{\mathbf{F}}^B \right\rangle_b (x_3) + \left\langle \hat{\mathbf{F}}^A, \mathbf{J} \hat{\mathbf{N}}^B \right\rangle_b (x_3) \right] dx_3. \end{aligned} \quad (7.71)$$

7.7 Sesquilinear forms

Consider the following definition of a *sesquilinear form* g ,

$$g(\mathbf{F}, \mathbf{G}) \stackrel{\text{def}}{=} \int_{\mathbf{x}_T \in \mathbb{R}^2} \mathbf{F}^\dagger(\mathbf{x}_T) \mathbf{B} \mathbf{G}(\mathbf{x}_T) d\mathbf{x}_T, \quad (7.72)$$

which constitutes the mapping,

$$g : [L^2(\mathbb{R}^2)]^2 \times [L^2(\mathbb{R}^2)]^2 \rightarrow \mathbb{C}, \quad (7.73)$$

from the product of two Hilbert spaces into the complex plane \mathbb{C} . The superscript \dagger denotes the product operation of transposition, signified by \cdot^t ,

and complex conjugation, signified by \cdot^* . The linear operator \mathbf{B} associated with g is given by the map,

$$\mathbf{B} : [L^2(\mathbb{R}^2)]^2 \rightarrow [L^2(\mathbb{R}^2)]^2. \quad (7.74)$$

Sesquilinearity means that (Lang (1993)), $\forall \mathbf{F}, \mathbf{F}_1, \mathbf{F}_2, \mathbf{G}, \mathbf{G}_1, \mathbf{G}_2 \in [L^2(\mathbb{R}^2)]^2$ and $\forall a, b \in \mathbb{C}$, we have *anti-linearity* in the first variable

$$\begin{aligned} g(\mathbf{F}_1 + \mathbf{F}_2, \mathbf{G}) &= g(\mathbf{F}_1, \mathbf{G}) + g(\mathbf{F}_2, \mathbf{G}), \\ g(a\mathbf{F}, \mathbf{G}) &= a^*g(\mathbf{F}, \mathbf{G}), \end{aligned} \quad (7.75)$$

and linearity in the second variable

$$\begin{aligned} g(\mathbf{F}, \mathbf{G}_1 + \mathbf{G}_2) &= g(\mathbf{F}, \mathbf{G}_1) + g(\mathbf{F}, \mathbf{G}_2), \\ g(\mathbf{F}, b\mathbf{G}) &= bg(\mathbf{F}, \mathbf{G}). \end{aligned} \quad (7.76)$$

A sesquilinear form g is called a *hermitian* form if

$$g(\mathbf{F}, \mathbf{G}) = g^*(\mathbf{G}, \mathbf{F}), \quad \forall \mathbf{F}, \mathbf{G} \in [L^2(\mathbb{R}^2)]^2. \quad (7.77)$$

The sesquilinear form g associated with \mathbf{B} is symbolized as

$$g(\mathbf{F}, \mathbf{G}) = \langle \mathbf{F}, \mathbf{B}\mathbf{G} \rangle_s, \quad (7.78)$$

The subscript $._s$ is used to distinguish it from a bilinear form, for which in Eq. (7.43) the subscript $._b$ is employed. Observe that a sesquilinear form can be expressed as a bilinear form according to

$$\langle \mathbf{F}, \mathbf{B}\mathbf{G} \rangle_s = \langle \mathbf{F}^*, \mathbf{B}\mathbf{G} \rangle_b. \quad (7.79)$$

Given the linear operator \mathbf{B} and its associated sesquilinear form g there exists a unique linear map

$$\mathbf{B}^\dagger : [L^2(\mathbb{R}^2)]^2 \rightarrow [L^2(\mathbb{R}^2)]^2, \quad (7.80)$$

such that

$$\langle \mathbf{F}, \mathbf{B}\mathbf{G} \rangle_s = \langle \mathbf{B}^\dagger \mathbf{F}, \mathbf{G} \rangle_s, \quad \forall \mathbf{F}, \mathbf{G} \in [L^2(\mathbb{R}^2)]^2. \quad (7.81)$$

We call \mathbf{B}^\dagger the *adjoint* of \mathbf{B} with respect to g . For, $a \in \mathbb{C}$ and $\mathbf{B}, \mathbf{C} : [L^2(\mathbb{R}^2)]^2 \rightarrow [L^2(\mathbb{R}^2)]^2$, we deduce that (Lang (1993)),

$$(a\mathbf{B})^\dagger = a^*\mathbf{B}^\dagger, \quad (\mathbf{B} + \mathbf{C})^\dagger = \mathbf{B}^\dagger + \mathbf{C}^\dagger, \quad (\mathbf{B}^\dagger)^\dagger = \mathbf{B}, \quad \text{and} \quad (\mathbf{BC})^\dagger = \mathbf{C}^\dagger \mathbf{B}^\dagger. \quad (7.82)$$

In terms of scalar operators we have,

$$\mathbf{B} = \begin{pmatrix} \mathcal{B}_{11} & \mathcal{B}_{12} \\ \mathcal{B}_{21} & \mathcal{B}_{22} \end{pmatrix} \iff \mathbf{B}^\dagger = \begin{pmatrix} \mathcal{B}_{11}^\dagger & \mathcal{B}_{21}^\dagger \\ \mathcal{B}_{12}^\dagger & \mathcal{B}_{22}^\dagger \end{pmatrix}, \quad (7.83)$$

in which the adjoint operation is with respect to a sesquilinear form, $g : [L^2(\mathbb{R}^2)]^1 \times [L^2(\mathbb{R}^2)]^1 \rightarrow \mathbb{C}$, of scalar-valued functions.

Consider the operator \mathbf{B} and its associated sesquilinear form g of Eq. (7.78). If g is hermitian then, using Eqs. (7.72), (7.77) and (7.81),

$$\langle \mathbf{F}, \mathbf{B}\mathbf{G} \rangle_s = \langle \mathbf{G}, \mathbf{B}\mathbf{F} \rangle_s^* = \langle \mathbf{B}^\dagger \mathbf{G}, \mathbf{F} \rangle_s^* = \langle \mathbf{F}, \mathbf{B}^\dagger \mathbf{G} \rangle_s, \\ \forall \mathbf{F}, \mathbf{G} \in [L^2(\mathbb{R}^2)]^2. \quad (7.84)$$

Hence,

$$\mathbf{B} = \mathbf{B}^\dagger. \quad (7.85)$$

The matrix operator \mathbf{B} is said to be *self-adjoint* or *hermitian* with respect to a sesquilinear form g . One can easily prove that (Lang (1993))

$$\mathbf{B} = \mathbf{B}^\dagger \iff \langle \mathbf{F}, \mathbf{B}\mathbf{F} \rangle_s \text{ is real, } \forall \mathbf{F} \in [L^2(\mathbb{R}^2)]^2. \quad (7.86)$$

7.8 Time-correlation type reciprocity theorem

Consider the limiting case in which the Laplace parameter $s \rightarrow j\omega$ via $\text{Re}(s) > 0$, i.e. we consider the wave field quantities in the Fourier domain, and express this, according to Eq. (B.6), with the symbol $\check{\cdot}$. Following Wapenaar (1996b) and Haines and de Hoop (1996), inside the domain $\mathbb{D} = \{(\mathbf{x}_T, x_3) | \mathbf{x}_T \in \mathbb{R}^2, x_3^u < x_3 < x_3^l\}$, shown in Fig. (7.1), an interaction quantity \check{I}^{corr} between two states, A and B , associated with the wave field vector Eqs. (7.32) and (7.33), is defined, according to,

$$\check{I}^{\text{corr}} : [L^2(\mathbb{R}^2)]^2 \times [L^2(\mathbb{R}^2)]^2 \rightarrow \mathbb{C}, \quad (7.87)$$

and

$$[\check{I}^{\text{corr}}(\check{\mathbf{F}}^A, \check{\mathbf{F}}^B)](x_3, \omega) \stackrel{\text{def}}{=} \int_{\mathbf{x}_T \in \mathbb{R}^2} (\check{\mathbf{F}}^A)^\dagger(\mathbf{x}_T, x_3, \omega) \mathbf{K} \check{\mathbf{F}}^B(\mathbf{x}_T, x_3, \omega) d\mathbf{x}_T, \quad (7.88)$$

The interaction quantity \check{I}^{corr} constitutes a *sesquilinear* form with the variables x_3 and ω acting as parameters. The matrix operator \mathbf{K} , associated with the sesquilinear form \check{I}^{corr} , is given by

$$\mathbf{K} = \begin{pmatrix} \mathcal{O} & \mathcal{I} \\ \mathcal{I} & \mathcal{O} \end{pmatrix}. \quad (7.89)$$

Using the notation of Eq. (7.78) the sesquilinear form \check{I}^{corr} is symbolized as

$$\check{I}^{\text{corr}}(\check{\mathbf{F}}^A, \check{\mathbf{F}}^B) = \langle \check{\mathbf{F}}^A, \mathbf{K} \check{\mathbf{F}}^B \rangle_s. \quad (7.90)$$

In accordance with the self-adjointness of \mathbf{K} ,

$$\mathbf{K} = \mathbf{K}^\dagger, \quad (7.91)$$

the interaction quantity \check{I}^{corr} is a hermitian form. Hence, according to Eq. (7.77)

$$\check{I}^{\text{corr}}(\check{\mathbf{F}}^A, \check{\mathbf{F}}^B) = [\check{I}^{\text{corr}}(\check{\mathbf{F}}^B, \check{\mathbf{F}}^A)]^*, \quad \forall \check{\mathbf{F}}^A, \check{\mathbf{F}}^B \in [L^2(\mathbb{R}^2)]^2. \quad (7.92)$$

Multiplication in the Fourier domain of a function with an other complex conjugate function, as in the interaction quantity of Eq. (7.88), is equivalent to a *correlation* of the pertaining functions in the time-domain, hence the denotation \hat{I}^{corr} .

Taking the derivative of Eq. (7.88) with respect to the longitudinal coordinate x_3 , omitting the Fourier parameter ω from the argument lists, yields

$$\partial_3 \langle \check{\mathbf{F}}^A, \mathbf{K} \check{\mathbf{F}}^B \rangle_s(x_3) = \langle \partial_3 \check{\mathbf{F}}^A, \mathbf{K} \check{\mathbf{F}}^B \rangle_s(x_3) + \langle \check{\mathbf{F}}^A, \mathbf{K} \partial_3 \check{\mathbf{F}}^B \rangle_s(x_3). \quad (7.93)$$

Substitution of the wave field vector Eqs. (7.32) and (7.33) into the right-hand side of (7.93) leads to the *local* form of the reciprocity theorem of the time-correlation type,

$$\begin{aligned} \partial_3 \langle \check{\mathbf{F}}^A, \mathbf{K} \check{\mathbf{F}}^B \rangle_s(x_3) &= - \left\langle \check{\mathbf{F}}^A, \left[(\check{\mathbf{A}}^A)^\dagger \mathbf{K} + \mathbf{K} \check{\mathbf{A}}^B \right] \check{\mathbf{F}}^B \right\rangle_s(x_3) \\ &\quad + \langle \check{\mathbf{N}}^A, \mathbf{K} \check{\mathbf{F}}^B \rangle_s(x_3) + \langle \check{\mathbf{F}}^A, \mathbf{K} \check{\mathbf{N}}^B \rangle_s(x_3), \end{aligned} \quad (7.94)$$

In this last equation $(\check{\mathbf{A}}^A)^\dagger$ denotes the adjoint of the matrix operator $\check{\mathbf{A}}^A$, as defined in Eq. (7.81). The contrast operator in the first integral on the right-hand side of Eq. (7.94) is derived as

$$(\check{\mathbf{A}}^A)^\dagger \mathbf{K} + \mathbf{K} \check{\mathbf{A}}^B = \begin{pmatrix} j\omega [\check{\mathcal{K}}^B - (\check{\mathcal{K}}^A)^\dagger] & \mathcal{O} \\ \mathcal{O} & j\omega (\rho^B - \rho^A) \mathcal{I} \end{pmatrix}, \quad (7.95)$$

which constitutes a diagonal matrix operator. Taking identical states in Eq. (7.31),

$$A = B = \{\hat{\mathbf{F}}, \hat{\mathbf{A}}, \hat{\mathbf{N}}\}, \quad (7.96)$$

Eq. (7.94) becomes, using Eq. (7.86),

$$\langle \check{\mathbf{F}}, (\check{\mathbf{A}}^\dagger \mathbf{K} + \mathbf{K} \check{\mathbf{A}}) \check{\mathbf{F}} \rangle_s (x_3) \text{ is real,} \quad (7.97)$$

with

$$\check{\mathbf{A}}^\dagger \mathbf{K} + \mathbf{K} \check{\mathbf{A}} = \begin{pmatrix} j\omega (\check{\mathcal{K}} - \check{\mathcal{K}}^\dagger) & \mathcal{O} \\ \mathcal{O} & \mathcal{O} \end{pmatrix}. \quad (7.98)$$

From Eqs. (7.97) and (7.98) we obtain the scalar form

$$\langle \check{p}, j\omega (\check{\mathcal{K}} - \check{\mathcal{K}}^\dagger) \check{p} \rangle_s (x_3) \text{ is real.} \quad (7.99)$$

We consider real frequencies, hence

$$\langle \check{p}, (\check{\mathcal{K}} - \check{\mathcal{K}}^\dagger) \check{p} \rangle_s (x_3) \text{ is purely imaginary.} \quad (7.100)$$

Because this last equation must hold for $\forall \check{p} \in [L^2(\mathbb{R}^2)]^1$, we must have that, using the fact that for lossless media $\check{\mathcal{K}}$ of Eq. (7.28) is a real operator, $\check{\mathcal{K}}$ is self-adjoint with respect to its associated sesquilinear form, expressed as

$$\hat{\mathcal{K}} = \hat{\mathcal{K}}^\dagger. \quad (7.101)$$

In Wapenaar (1996b) it is shown that $\check{\mathcal{K}}$ is a self-adjoint operator assuming certain boundary conditions. We obtain the following property for $\hat{\mathbf{A}}$

$$\hat{\mathbf{A}}^\dagger \mathbf{K} = -\mathbf{K} \hat{\mathbf{A}}. \quad (7.102)$$

We can now write

$$(\check{\mathbf{A}}^A)^\dagger \mathbf{K} + \mathbf{K} \check{\mathbf{A}}^B = \mathbf{K} \Delta \check{\mathbf{A}} = \begin{pmatrix} j\omega \Delta \check{\mathcal{K}} & \mathcal{O} \\ \mathcal{O} & j\omega \Delta \rho \mathcal{I} \end{pmatrix}, \quad (7.103)$$

in which the difference quantities are given in Eqs. (7.68) and (7.69). Integration of Eq. (7.94) with respect to x_3 , from $x_3 = x_3^u$ to $x_3 = x_3^l$, yields the

global form of the reciprocity theorem of the correlation type,

$$\begin{aligned}
 \langle \check{\mathbf{F}}^A, \mathbf{K} \check{\mathbf{F}}^B \rangle_s (x_3^1) - \langle \check{\mathbf{F}}^A, \mathbf{K} \check{\mathbf{F}}^B \rangle_s (x_3^u) \\
 = - \int_{x_3=x_3^u}^{x_3^1} \langle \check{\mathbf{F}}^A, \mathbf{K} \Delta \check{\mathbf{A}} \check{\mathbf{F}}^B \rangle_s (x_3) dx_3 \\
 + \int_{x_3=x_3^u}^{x_3^1} [\langle \check{\mathbf{N}}^A, \mathbf{K} \check{\mathbf{F}}^B \rangle_s (x_3) + \langle \check{\mathbf{F}}^A, \mathbf{K} \check{\mathbf{N}}^B \rangle_s (x_3)] dx_3, \quad (7.104)
 \end{aligned}$$

In de Hoop (1995)[p. 169-171] and Fokkema and van den Berg (1993)[p. 101-102], the reciprocity theorem of the correlation type is derived in terms of the scalar wave field quantities \check{p} and $\check{\mathbf{v}}$. Equality of the material states entails,

$$\begin{aligned}
 \langle \check{\mathbf{F}}^A, \mathbf{K} \check{\mathbf{F}}^B \rangle_s (x_3^1) - \langle \check{\mathbf{F}}^A, \mathbf{K} \check{\mathbf{F}}^B \rangle_s (x_3^u) \\
 = \int_{x_3=x_3^u}^{x_3^1} [\langle \check{\mathbf{N}}^A, \mathbf{K} \check{\mathbf{F}}^B \rangle_s (x_3) + \langle \check{\mathbf{F}}^A, \mathbf{K} \check{\mathbf{N}}^B \rangle_s (x_3)] dx_3. \quad (7.105)
 \end{aligned}$$

The reciprocity theorems of the time-convolution and time-correlation types, derived in this chapter, are used in the subsequent chapters to derive wave field representations, and symmetry and adjointness relations.

Chapter 8

Wave field decomposition

8.1 Introduction

By defining a background medium and an associated laterally infinite scattering surface, acting as a bounding surface of a scattering domain, a wave field decomposition is introduced. The wave field components are the incident wave field, propagating with respect to the background medium and originating from the actual source, and the scattered wave field, which also propagates through the background medium, but originates from contrast sources located inside the scattering domain. Both the incident and scattered wave fields are, obeying down- and up-going wave field conditions, respectively, with respect to the background medium, one-way wave fields, which can be propagated into the medium using operators derived in the Chapter 9. This enables a recursive approach, where a sub-domain is progressively enlarged, reflecting an increasing state of knowledge, until the entire domain of application is covered. This approach is especially suited to time-lapse states, in which the interactions (e.g. quantified by phase differences) are cumulative in the main wave field directions.

Integral representations are derived for the first component of the wave field vectors of the incident, scattered and total wave fields. Taking the limit towards the scattering surface these representation are used to derive Dirichlet-to-Neumann (D-t-N) operators, which transform, at the scattering surface, the first component of the wave field vectors to the second component. Decomposition, reflection and transmission operators are derived and expressed in terms of D-t-N operators. The aforementioned operators

characterize the medium and will be used to quantify temporal changes that might occur within two media realizations.

8.2 Wave field equations

Consider the surface $\partial\mathbb{D}^{\text{sct}}$, given by $x_3 = x_3^{\text{sct}}$, which divides \mathbb{R}^3 into two half spaces: the open scattering domain, \mathbb{D}^{sct} , and the open domain $\mathbb{D}^{\text{sct}'}$, which is the complement of $\mathbb{D}^{\text{sct}} \cup \partial\mathbb{D}^{\text{sct}}$ in \mathbb{R}^3 (Fig. (8.1)). Consider the acoustic wave field vector $\hat{\mathbf{F}}$ governed by the following wave field vector equation (see Eq. (7.26)) inside \mathbb{R}^3 ,

$$\partial_3 \hat{\mathbf{F}}(\mathbf{x}; \mathbf{x}^S, s) + \hat{\mathbf{A}} \hat{\mathbf{F}}(\mathbf{x}; \mathbf{x}^S, s) = \hat{\mathbf{N}}(\mathbf{x}; \mathbf{x}^S, s), \quad \mathbf{x} \in \mathbb{R}^3, \mathbf{x}^S \in \mathbb{D}^{\text{sct}'} \quad (8.1)$$

with source vector

$$\hat{\mathbf{N}}(\mathbf{x}; \mathbf{x}^S, s) = \begin{pmatrix} 0 \\ \hat{q}(s) \delta(\mathbf{x} - \mathbf{x}^S) \end{pmatrix}. \quad (8.2)$$

The source vector $\hat{\mathbf{N}}$ has a zero first component, and a second component given by the volume density of volume injection rate \hat{q} , represented by a Dirac distribution with support at $\mathbf{x} = \mathbf{x}^S$, indicated in the argument lists of $\hat{\mathbf{F}}$ and $\hat{\mathbf{N}}$. The medium system matrix operator $\hat{\mathbf{A}}$ is determined by the medium parameters $\{\rho, \kappa\}$, from now on also called *actual* medium parameters, according to Eq. (7.27). In \mathbb{R}^3 the *background* medium parameters, $\{\rho^b, \kappa^b\}$, characterizing the background medium and an associated background medium system matrix $\hat{\mathbf{A}}^b$, are defined, and set with respect to the actual medium parameters according to

$$\{\rho, \kappa\} = \{\rho^b, \kappa^b\}, \quad \text{in } \mathbb{D}^{\text{sct}'}, \quad (8.3)$$

$$\{\rho, \kappa\} = \{\rho^b, \kappa^b\} + \{\Delta\rho, \Delta\kappa\}, \quad \text{in } \mathbb{D}^{\text{sct}}. \quad (8.4)$$

Inside $\mathbb{D}^{\text{sct}'}$ the actual medium parameters equal the background medium parameters, whereas inside \mathbb{D}^{sct} , the actual medium parameters are the sum of the background medium parameters and the perturbations $\{\Delta\rho, \Delta\kappa\}$ (Fig. (8.1)). Accordingly, the actual wave field vector $\hat{\mathbf{F}}$, also denoted as the *total* wave field vector, is decomposed into an *incident* wave field vector $\hat{\mathbf{F}}^{\text{inc}}$, and a *scattered* wave field vector $\hat{\mathbf{F}}^{\text{sct}}$, as

$$\hat{\mathbf{F}} = \hat{\mathbf{F}}^{\text{inc}} + \hat{\mathbf{F}}^{\text{sct}}, \quad \text{in } \mathbb{R}^3. \quad (8.5)$$

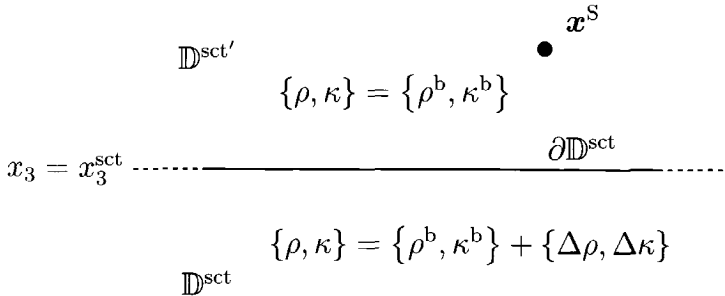


Figure 8.1: Scattering configuration with actual medium parameters in terms of background medium parameters and a perturbation. Actual source position \mathbf{x}^S inside $\mathbb{D}^{\text{sct}'}$.

The incident wave field is governed by the background medium, expressed by the incident wave field vector equation as

$$\partial_3 \hat{\mathbf{F}}^{\text{inc}} (\mathbf{x}; \mathbf{x}^S, s) + \hat{\mathbf{A}}^b \hat{\mathbf{F}}^{\text{inc}} (\mathbf{x}; \mathbf{x}^S, s) = \hat{\mathbf{N}} (\mathbf{x}; \mathbf{x}^S, s), \quad \mathbf{x} \in \mathbb{R}^3, \mathbf{x}^S \in \mathbb{D}^{\text{sct}'}, \quad (8.6)$$

with the same source vector $\hat{\mathbf{N}}$ as with the total wave field, which is given in Eq. (8.2). Inside \mathbb{D}^{sct} the incident wave field has no sources expressed as

$$\partial_3 \hat{\mathbf{F}}^{\text{inc}} + \hat{\mathbf{A}}^b \hat{\mathbf{F}}^{\text{inc}} = \mathbf{O}, \quad \text{in } \mathbb{D}^{\text{sct}}, \quad (8.7)$$

with \mathbf{O} representing the null vector. Inside \mathbb{D}^{sct} the total wave field vector equation of Eq. (8.1) is rewritten to

$$\partial_3 \hat{\mathbf{F}} + \hat{\mathbf{A}}^b \hat{\mathbf{F}} = - \left(\hat{\mathbf{A}} - \hat{\mathbf{A}}^b \right) \hat{\mathbf{F}}, \quad \text{in } \mathbb{D}^{\text{sct}}. \quad (8.8)$$

Subtracting Eq. (8.7) from Eq. (8.8), using the decomposition of Eq. (8.5), we obtain the wave field vector equation of the scattered wave field in \mathbb{D}^{sct} , as

$$\partial_3 \hat{\mathbf{F}}^{\text{sct}} + \hat{\mathbf{A}}^b \hat{\mathbf{F}}^{\text{sct}} = - \left(\hat{\mathbf{A}} - \hat{\mathbf{A}}^b \right) \hat{\mathbf{F}}, \quad \text{in } \mathbb{D}^{\text{sct}}. \quad (8.9)$$

Because the incident and total wave fields have identical source distributions inside $\mathbb{D}^{\text{sct}'}$ it follows that the scattered wave field is source-free inside this domain,

$$\partial_3 \hat{\mathbf{F}}^{\text{sct}} + \hat{\mathbf{A}}^b \hat{\mathbf{F}}^{\text{sct}} = \mathbf{0}, \quad \text{in } \mathbb{D}^{\text{sct}'}. \quad (8.10)$$

Combining Eqs. (8.9) and (8.10) yields the wave field vector equation for the scattered wave field in \mathbb{R}^3 ,

$$\partial_3 \hat{\mathbf{F}}^{\text{sct}} (\mathbf{x}; \mathbf{x}^S, s) + \hat{\mathbf{A}}^b \hat{\mathbf{F}}^{\text{sct}} (\mathbf{x}; \mathbf{x}^S, s) = \hat{\mathbf{N}}^{\text{sct}} (\mathbf{x}; \mathbf{x}^S, s), \\ \mathbf{x} \in \mathbb{R}^3, \mathbf{x}^S \in \mathbb{D}^{\text{sct}'}, \quad (8.11)$$

with source vector

$$\hat{\mathbf{N}}^{\text{sct}} (\mathbf{x}; \mathbf{x}^S, s) = \begin{cases} \mathbf{0} & \mathbf{x} \in \mathbb{D}^{\text{sct}'} \\ -(\hat{\mathbf{A}} - \hat{\mathbf{A}}^b) \hat{\mathbf{F}} (\mathbf{x}; \mathbf{x}^S, s), & \mathbf{x} \in \mathbb{D}^{\text{sct}}, \end{cases} \quad (8.12)$$

(Fokkema and van den Berg (1993)[p. 140-144]).

8.3 Integral representations

8.3.1 Incident wave field

Following Fokkema and van den Berg (1993)[p. 129-131], we introduce the volume-injection Green's state vector

$$\hat{\mathbf{F}}^{q,b} = \begin{pmatrix} \hat{p}^{q,b} \\ \hat{v}_3^{q,b} \end{pmatrix}, \quad (8.13)$$

governed by

$$\partial_3 \hat{\mathbf{F}}^{q,b} (\mathbf{x}; \mathbf{x}', s) + \hat{\mathbf{A}}^b \hat{\mathbf{F}}^{q,b} (\mathbf{x}; \mathbf{x}', s) = \hat{\mathbf{N}}^q (\mathbf{x}; \mathbf{x}', s), \quad \mathbf{x}, \mathbf{x}' \in \mathbb{R}^3, \quad (8.14)$$

with source vector

$$\hat{\mathbf{N}}^q (\mathbf{x}; \mathbf{x}', s) = \begin{pmatrix} 0 \\ \hat{q}(s) \delta(\mathbf{x} - \mathbf{x}') \end{pmatrix}. \quad (8.15)$$

The wave field vector $\hat{\mathbf{F}}^{q,b}$ is governed by the background medium parameters and is causally related to a Dirac distribution with support at $\mathbf{x} = \mathbf{x}'$. The

source position is indicated in the argument list of $\hat{\mathbf{F}}^{q,b}$. Observe that, using Eqs. (8.6) and (8.14),

$$\hat{\mathbf{F}}^{\text{inc}}(\mathbf{x}; \mathbf{x}^S, s) = \hat{\mathbf{F}}^{q,b}(\mathbf{x}; \mathbf{x}^S, s). \quad (8.16)$$

Because $\hat{p}^{q,b}$ and $\hat{v}_3^{q,b}$ are linearly related to \hat{q} , we may define the monopole Green's state $\hat{G}^{q,b}$

$$\hat{p}^{q,b}(\mathbf{x}; \mathbf{x}', s) \stackrel{\text{def}}{=} \hat{q}(s) \hat{G}^{q,b}(\mathbf{x}'; \mathbf{x}, s), \quad (8.17)$$

and the dipole Green's state $\hat{\Gamma}_3^{q,b}$

$$\hat{v}_3^{q,b}(\mathbf{x}; \mathbf{x}', s) \stackrel{\text{def}}{=} -\hat{q}(s) \hat{\Gamma}_3^{q,b}(\mathbf{x}'; \mathbf{x}, s). \quad (8.18)$$

The reciprocity theorem of the convolution type is applied to the domain $\mathbb{D} = \{(\mathbf{x}_T, x_3) | \mathbf{x}_T \in \mathbb{R}^2, x'_3 < x_3 < x_3^1\}$, with $x'_3 > x_3^S$ (Fig. (8.2)). We take for State *A* the volume-injection Green's wave field of Eq. (8.14), with source at $\mathbf{x} \in \mathbb{R}^3$, and for State *B* the incident wave field of Eq. (8.6), with source at $\mathbf{x}^S \in \mathbb{D}^{\text{sct}'}$. We have in \mathbb{D}

$$A = \left\{ \hat{\mathbf{F}}^{q,b}, \hat{\mathbf{A}}^b, \hat{\mathbf{N}}^q \right\} \quad \text{and} \quad B = \left\{ \hat{\mathbf{F}}^{\text{inc}}, \hat{\mathbf{A}}^b, \mathbf{O} \right\}, \quad \text{in } \mathbb{D}. \quad (8.19)$$

Because both these states are determined by the background medium we apply the reciprocity theorem of the convolution type of Eq. (7.71), yielding

$$\begin{aligned} \left\langle \hat{\mathbf{F}}^{q,b}, \mathbf{J}\hat{\mathbf{F}}^{\text{inc}} \right\rangle_b (x_3^1; \mathbf{x}, \mathbf{x}^S) - \left\langle \hat{\mathbf{F}}^{q,b}, \mathbf{J}\hat{\mathbf{F}}^{\text{inc}} \right\rangle_b (x'_3; \mathbf{x}, \mathbf{x}^S) \\ = \int_{x''_3=x'_3}^{x'_3} \left\langle \hat{\mathbf{N}}^q, \mathbf{J}\hat{\mathbf{F}}^{\text{inc}} \right\rangle_b (x''_3; \mathbf{x}, \mathbf{x}^S) dx''_3. \end{aligned} \quad (8.20)$$

in which the sources of $\hat{\mathbf{F}}^{q,b}$ and $\hat{\mathbf{F}}^{\text{inc}}$ are indicated in the argument list of the bilinear forms. Because the source of the incident wave field has no support inside \mathbb{D} , the second term in the integrand on the right-hand side of Eq. (7.71) vanishes in Eq. (8.20). The first term in the integrand on the left-hand of the representation of Eq. (8.20) vanishes because in the limit, $x'_3 \rightarrow \infty$, Sommerfeld radiation conditions are applicable. In terms of scalar wave field values we can derive the following integral representation for the

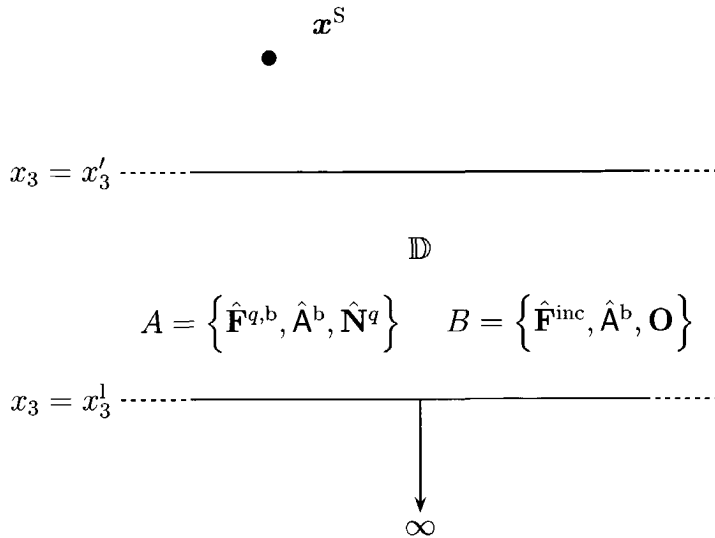


Figure 8.2: The incident wave field representation: the two states and the domain of application of the reciprocity theorem

incident wave field

$$\begin{aligned}
 \chi_{\mathbb{D}}(\mathbf{x}_T, x_3) \hat{q} \hat{p}^{\text{inc}}(\mathbf{x}_T, x_3; \mathbf{x}_T^S, x_3^S) \\
 = \int_{\mathbf{x}'_T \in \mathbb{R}^2} \left[\hat{p}^{q,b}(\mathbf{x}'_T, x'_3; \mathbf{x}_T, x_3) \hat{v}_3^{\text{inc}}(\mathbf{x}'_T, x'_3; \mathbf{x}_T^S, x_3^S) \right. \\
 \left. - \hat{v}_3^{q,b}(\mathbf{x}'_T, x'_3; \mathbf{x}_T, x_3) \hat{p}^{\text{inc}}(\mathbf{x}'_T, x'_3; \mathbf{x}_T^S, x_3^S) \right] d\mathbf{x}'_T, \\
 (\mathbf{x}_T, x_3) \in \mathbb{R}^3, x'_3 > x_3^S, \quad (8.21)
 \end{aligned}$$

(see Fokkema and van den Berg (1993)[p. 152]), in which the characteristic function $\chi_{\mathbb{D}}$ is given by

$$\chi_{\mathbb{D}}(\mathbf{x}_T, x_3) = \begin{cases} 1, & (\mathbf{x}_T, x_3) \in \mathbb{D} \\ \frac{1}{2}, & (\mathbf{x}_T, x_3) \in \partial\mathbb{D} \\ 0, & (\mathbf{x}_T, x_3) \in \mathbb{D}', \end{cases} \quad (8.22)$$

and $\mathbb{D} = \{(\mathbf{x}_T, x_3) | \mathbf{x}_T \in \mathbb{R}^2, x_3 > x'_3\}$. The open domain, $\mathbb{D}' = \mathbb{R}^3 \setminus \bar{\mathbb{D}}$, is the complement of the closure of \mathbb{D} , signified by $\bar{\mathbb{D}}$, with respect to \mathbb{R}^3 .

The integral in Eq. (8.21), at the limiting value $\partial\mathbb{D}$, is a Cauchy principal value integral, in which the integration is over the pertaining boundary with the symmetric exclusion of the singular point (Colton and Kress (1983)). Implementing the Green's states of Eqs. (8.17) and (8.18) we arrive at

$$\begin{aligned} \chi_{\mathbb{D}}(\mathbf{x}_T, x_3) \hat{p}^{\text{inc}}(\mathbf{x}_T, x_3; \mathbf{x}_T^S, x_3^S) \\ = \int_{\mathbf{x}'_T \in \mathbb{R}^2} \left[\hat{G}^{q,b}(\mathbf{x}_T, x_3; \mathbf{x}'_T, x'_3) \hat{v}_3^{\text{inc}}(\mathbf{x}'_T, x'_3; \mathbf{x}_T^S, x_3^S) \right. \\ \left. + \hat{\Gamma}_3^{q,b}(\mathbf{x}_T, x_3; \mathbf{x}'_T, x'_3) \hat{p}^{\text{inc}}(\mathbf{x}'_T, x'_3; \mathbf{x}_T^S, x_3^S) \right] d\mathbf{x}'_T, \\ (\mathbf{x}_T, x_3) \in \mathbb{R}^3, x'_3 > x_3^S. \quad (8.23) \end{aligned}$$

In terms of a bilinear form of scalar-valued functions we can express this last equation more compactly as

$$\begin{aligned} \chi_{\mathbb{D}}(\mathbf{x}) \hat{p}^{\text{inc}}(\mathbf{x}; \mathbf{x}^S) = \left\langle \hat{G}^{q,b}, \hat{v}_3^{\text{inc}} \right\rangle_b(x'_3; \mathbf{x}, \mathbf{x}^S) + \left\langle \hat{\Gamma}_3^{q,b}, \hat{p}^{\text{inc}} \right\rangle_b(x'_3; \mathbf{x}, \mathbf{x}^S), \\ \mathbf{x} \in \mathbb{R}^3, x'_3 > x_3^S. \quad (8.24) \end{aligned}$$

8.3.2 Scattered wave field

In order to derive an integral representation for the scattered wave field we take for the domain of application of the reciprocity theorem, $\mathbb{D} = \{(\mathbf{x}_T, x_3) | \mathbf{x}_T \in \mathbb{R}^2, x_3^u < x_3 < x'_3\}$, with $x'_3 \leq x_3^{\text{sct}}$ (Fig. (8.3)). We take for State *A* the volume-injection Green's wave field of Eq. (8.14), with source at $\mathbf{x} \in \mathbb{R}^3$, and for State *B* the scattered wave field of Eq. (8.11), associated with the actual source at $\mathbf{x}^S \in \mathbb{D}^{\text{sct}'}$. We have

$$A = \left\{ \hat{\mathbf{F}}^{q,b}, \hat{\mathbf{A}}^b, \hat{\mathbf{N}}^q \right\} \quad \text{and} \quad B = \left\{ \hat{\mathbf{F}}^{\text{sct}}, \hat{\mathbf{A}}^b, \mathbf{O} \right\} \quad \text{in } \mathbb{D}. \quad (8.25)$$

Because both these states are determined by the background medium we apply the reciprocity theorem of the convolution type of Eq. (7.71) yielding,

$$\begin{aligned} \left\langle \hat{\mathbf{F}}^{q,b}, \mathbf{J} \hat{\mathbf{F}}^{\text{sct}} \right\rangle_b(x'_3; \mathbf{x}, \mathbf{x}^S) - \left\langle \hat{\mathbf{F}}^{q,b}, \mathbf{J} \hat{\mathbf{F}}^{\text{sct}} \right\rangle_b(x_3^u; \mathbf{x}, \mathbf{x}^S) \\ = \int_{x''_3=x_3^u}^{x'_3} \left\langle \hat{\mathbf{N}}^q, \mathbf{J} \hat{\mathbf{F}}^{\text{sct}} \right\rangle_b(x''_3; \mathbf{x}, \mathbf{x}^S) dx''_3. \quad (8.26) \end{aligned}$$

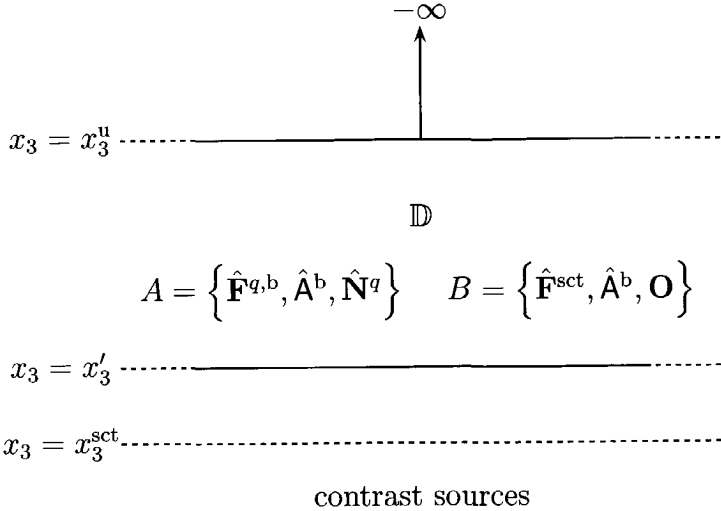


Figure 8.3: The scattered wave field representation: the two states and the domain of application of the reciprocity theorem

Because the contrast sources of the scattered wave field have no support inside \mathbb{D} , the second term in the integrand on the right-hand side of Eq. (7.71) vanishes in Eq. (8.26). The second term in the integrand on the left-hand of the representation of Eq. (8.26) vanishes because in the limit, $x_3^u \rightarrow -\infty$, Sommerfeld radiation conditions are applicable. In terms of scalar wave field values we can derive the following integral representation for the scattered wave field

$$\begin{aligned}
 & \chi_{\mathbb{D}}(\mathbf{x}_T, x_3) \hat{q} \hat{p}^{sct}(\mathbf{x}_T, x_3; \mathbf{x}_T^S, x_3^S) \\
 &= \int_{\mathbf{x}'_T \in \mathbb{R}^2} \left[-\hat{p}^{q,b}(\mathbf{x}'_T, x'_3; \mathbf{x}_T, x_3) \hat{v}_3^{sct}(\mathbf{x}'_T, x'_3; \mathbf{x}_T^S, x_3^S) \right. \\
 & \quad \left. + \hat{v}_3^{q,b}(\mathbf{x}'_T, x'_3; \mathbf{x}_T, x_3) \hat{p}^{sct}(\mathbf{x}'_T, x'_3; \mathbf{x}_T^S, x_3^S) \right] d\mathbf{x}'_T, \\
 & \quad (\mathbf{x}_T, x_3) \in \mathbb{R}^3, x'_3 \leq x_3^{sct}, \quad (8.27)
 \end{aligned}$$

in which the characteristic function $\chi_{\mathbb{D}'}$ is given by

$$\chi_{\mathbb{D}'}(\mathbf{x}_T, x_3) = \begin{cases} 1, & (\mathbf{x}_T, x_3) \in \mathbb{D}' \\ \frac{1}{2}, & (\mathbf{x}_T, x_3) \in \partial\mathbb{D} \\ 0, & (\mathbf{x}_T, x_3) \in \mathbb{D}, \end{cases} \quad (8.28)$$

and $\mathbb{D} = \{(\mathbf{x}_T, x_3) | \mathbf{x}_T \in \mathbb{R}^2, x_3 < x'_3\}$. The integral in Eq. (8.27) is, when evaluated at $\partial\mathbb{D}$, a Cauchy principal value integral, in which the integration is over the pertaining boundary with the symmetric exclusion of the singular point. Implementing the Green's states of Eqs. (8.17) and (8.18) we arrive at

$$\begin{aligned} \chi_{\mathbb{D}'}(\mathbf{x}_T, x_3) \hat{p}^{\text{sct}}(\mathbf{x}_T, x_3; \mathbf{x}_T^S, x_3^S) \\ = - \int_{\mathbf{x}'_T \in \mathbb{R}^2} \left[\hat{G}^{q,b}(\mathbf{x}_T, x_3; \mathbf{x}'_T, x'_3) \hat{v}_3^{\text{sct}}(\mathbf{x}'_T, x'_3; \mathbf{x}_T^S, x_3^S) \right. \\ \left. + \hat{\Gamma}_3^{q,b}(\mathbf{x}_T, x_3; \mathbf{x}'_T, x'_3) \hat{p}^{\text{sct}}(\mathbf{x}'_T, x'_3; \mathbf{x}_T^S, x_3^S) \right] d\mathbf{x}'_T, \\ (\mathbf{x}_T, x_3) \in \mathbb{R}^3, x'_3 \leq x_3^{\text{sct}} \quad (8.29) \end{aligned}$$

(see Fokkema and van den Berg (1993)[p. 151]). In terms of a bilinear form of scalar-valued functions we can express this last equation more compactly as

$$\begin{aligned} \chi_{\mathbb{D}'}(\mathbf{x}) \hat{p}^{\text{sct}}(\mathbf{x}; \mathbf{x}^S) \\ = - \left\langle \hat{G}^{q,b}, \hat{v}_3^{\text{sct}} \right\rangle_b(x'_3; \mathbf{x}, \mathbf{x}^S) - \left\langle \hat{\Gamma}_3^{q,b}, \hat{p}^{\text{sct}} \right\rangle_b(x'_3; \mathbf{x}, \mathbf{x}^S), \\ \mathbf{x} \in \mathbb{R}^3, x'_3 \leq x_3^{\text{sct}}. \quad (8.30) \end{aligned}$$

8.3.3 Total wave field

Following Fokkema and van den Berg (1993)[p. 129-131], we introduce the volume-injection Green's state vector

$$\hat{\mathbf{F}}^q = \begin{pmatrix} \hat{p}^q \\ \hat{v}_3^q \end{pmatrix}, \quad (8.31)$$

governed by

$$\partial_3 \hat{\mathbf{F}}^q(\mathbf{x}; \mathbf{x}', s) + \hat{\mathbf{A}} \hat{\mathbf{F}}^q(\mathbf{x}; \mathbf{x}', s) = \hat{\mathbf{N}}^q(\mathbf{x}; \mathbf{x}', s), \quad \mathbf{x}, \mathbf{x}' \in \mathbb{R}^3, \quad (8.32)$$

with source vector

$$\hat{\mathbf{N}}^q(\mathbf{x}; \mathbf{x}', s) = \begin{pmatrix} 0 \\ \hat{q}(s) \delta(\mathbf{x} - \mathbf{x}') \end{pmatrix}. \quad (8.33)$$

The wave field vector $\hat{\mathbf{F}}^q$ is governed by the actual medium parameters, whereas $\hat{\mathbf{F}}^{q,b}$ of Eq. (8.14) is determined by the background medium parameters. $\hat{\mathbf{F}}^q$ is causally related to a Dirac distribution with support at $\mathbf{x} = \mathbf{x}'$. Because \hat{p}^q and \hat{v}_3^q are linearly related to \hat{q} , we may define the monopole Green's state \hat{G}^q

$$\hat{p}^q(\mathbf{x}; \mathbf{x}', s) \stackrel{\text{def}}{=} \hat{q}(s) \hat{G}^q(\mathbf{x}'; \mathbf{x}, s), \quad (8.34)$$

and the dipole Green's state $\hat{\Gamma}_3^q$

$$\hat{v}_3^q(\mathbf{x}; \mathbf{x}', s) \stackrel{\text{def}}{=} -\hat{q}(s) \hat{\Gamma}_3^q(\mathbf{x}'; \mathbf{x}, s). \quad (8.35)$$

The reciprocity theorem of the convolution type is applied to the domain $\mathbb{D} = \{(\mathbf{x}_T, x_3) | \mathbf{x}_T \in \mathbb{R}^2, x'_3 < x_3 < x^l_3\}$, with $x'_3 > x^S_3$ (Fig. (8.4)). We take for State *A* the volume-injection Green's wave field of Eq. (8.32), with source at $\mathbf{x} \in \mathbb{R}^3$, and for State *B* the transmitted wave field governed by the total wave field vector equation of Eq. (8.1), with source at $\mathbf{x}^S \in \mathbb{D}^{\text{sct}'}$. We have

$$A = \left\{ \hat{\mathbf{F}}^q, \hat{\mathbf{A}}, \hat{\mathbf{N}}^q \right\} \quad \text{and} \quad B = \left\{ \hat{\mathbf{F}}, \hat{\mathbf{A}}, \mathbf{O} \right\}, \quad \text{in } \mathbb{D}. \quad (8.36)$$

Because both these states are determined by the actual medium we apply the reciprocity theorem of the convolution type of Eq. (7.71), yielding

$$\begin{aligned} \left\langle \hat{\mathbf{F}}^q, \mathbf{J}\hat{\mathbf{F}} \right\rangle_b (x^l_3; \mathbf{x}, \mathbf{x}^S) - \left\langle \hat{\mathbf{F}}^q, \mathbf{J}\hat{\mathbf{F}} \right\rangle_b (x'_3; \mathbf{x}, \mathbf{x}^S) \\ = \int_{x''_3=x'_3}^{x^l_3} \left\langle \hat{\mathbf{N}}^q, \mathbf{J}\hat{\mathbf{F}} \right\rangle_b (x''_3; \mathbf{x}, \mathbf{x}^S) dx''_3. \end{aligned} \quad (8.37)$$

Because the source of the total wave field has no support inside \mathbb{D} , the second term in the integrand on the right-hand side of Eq. (7.71) vanishes in Eq. (8.37). The first term in the integrand on the left-hand of the representation of Eq. (8.37) vanishes because in the limit, $x^l_3 \rightarrow \infty$, Sommerfeld radiation conditions are applicable. In terms of scalar wave field values we can derive

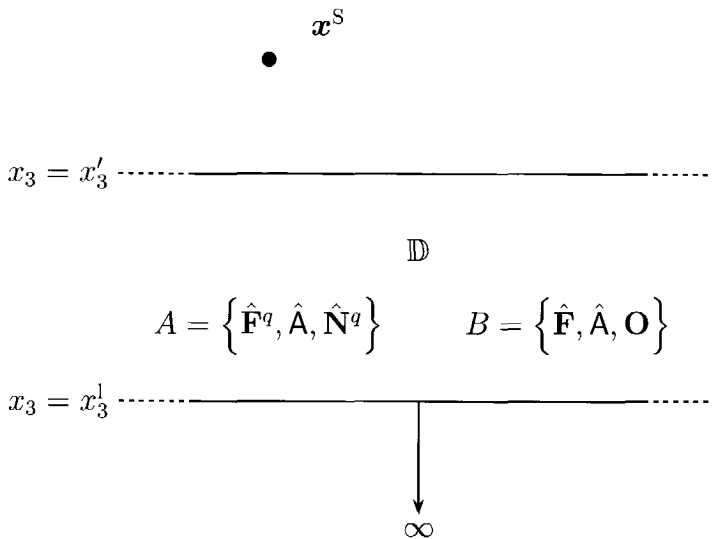


Figure 8.4: The total wave field representation: the two states and the domain of application of the reciprocity theorem

the following integral representation for the total wave field

$$\begin{aligned}
 & \chi_{\mathbb{D}}(\mathbf{x}_T, x_3) \hat{q} \hat{p}(\mathbf{x}_T, x_3; \mathbf{x}_T^S, x_3^S) \\
 &= \int_{\mathbf{x}'_T \in \mathbb{R}^2} [\hat{p}^q(\mathbf{x}'_T, x'_3; \mathbf{x}_T, x_3) \hat{v}_3(\mathbf{x}'_T, x'_3; \mathbf{x}_T^S, x_3^S) \\
 &\quad - \hat{v}_3^q(\mathbf{x}'_T, x'_3; \mathbf{x}_T, x_3) \hat{p}(\mathbf{x}'_T, x'_3; \mathbf{x}_T^S, x_3^S)] d\mathbf{x}'_T, \\
 & \quad (\mathbf{x}_T, x_3) \in \mathbb{R}^3, x'_3 > x_3^S \quad (8.38)
 \end{aligned}$$

(see Fokkema and van den Berg (1993)[p. 153]), in which the characteristic function $\chi_{\mathbb{D}}$ is given by Eq. (8.22). The integral in Eq. (8.38) is, when evaluated at $\partial\mathbb{D}$, a Cauchy principal value integral, in which the integration is over the pertaining boundary with the symmetric exclusion of the singular point. Implementing the Green's states of Eqs. (8.34) and (8.35) we arrive

at

$$\begin{aligned}
& \chi_{\mathbb{D}}(\mathbf{x}_T, x_3) \hat{p}(\mathbf{x}_T, x_3; \mathbf{x}_T^S, x_3^S) \\
&= \int_{\mathbf{x}'_T \in \mathbb{R}^2} \left[\hat{G}^q(\mathbf{x}_T, x_3; \mathbf{x}'_T, x'_3) \hat{v}_3(\mathbf{x}'_T, x'_3; \mathbf{x}_T^S, x_3^S) \right. \\
&\quad \left. + \hat{\Gamma}_3^q(\mathbf{x}_T, x_3; \mathbf{x}'_T, x'_3) \hat{p}(\mathbf{x}'_T, x'_3; \mathbf{x}_T^S, x_3^S) \right] d\mathbf{x}'_T, \\
& (\mathbf{x}_T, x_3) \in \mathbb{R}^3, x'_3 > x_3^S. \quad (8.39)
\end{aligned}$$

In terms of a bilinear form of scalar-valued functions we can express this last equation more compactly as

$$\begin{aligned}
& \chi_{\mathbb{D}}(\mathbf{x}) \hat{p}(\mathbf{x}; \mathbf{x}^S) = \left\langle \hat{G}^q, \hat{v}_3 \right\rangle_b(x'_3; \mathbf{x}, \mathbf{x}^S) + \left\langle \hat{\Gamma}_3^q, \hat{p} \right\rangle_b(x'_3; \mathbf{x}, \mathbf{x}^S), \\
& \mathbf{x} \in \mathbb{R}^3, x'_3 > x_3^S. \quad (8.40)
\end{aligned}$$

8.4 Dirichlet-to-Neumann operators

We proceed by defining, inside \mathbb{D} , the following *single-layer potential* boundary integral operator

$$\hat{\mathcal{S}}^b f(\mathbf{x}_T, x_3) \stackrel{\text{def}}{=} 2 \int_{\mathbf{x}'_T \in \mathbb{R}^2} \hat{G}^{q,b}(\mathbf{x}_T, x_3; \mathbf{x}'_T, x_3) f(\mathbf{x}'_T, x_3) d\mathbf{x}'_T, \quad (8.41)$$

and the *double-layer potential* boundary integral operator

$$\hat{\mathcal{D}}^b g(\mathbf{x}_T, x_3) \stackrel{\text{def}}{=} 2 \int_{\mathbf{x}'_T \in \mathbb{R}^2} \hat{\Gamma}_3^{q,b}(\mathbf{x}_T, x_3; \mathbf{x}'_T, x_3) g(\mathbf{x}'_T, x_3) d\mathbf{x}'_T, \quad (8.42)$$

(Colton and Kress (1983); Sabatier (1990)), in which $f, g \in [L^2(\mathbb{R}^2)]^1$. The integral symbol in these last two definitions signifies that the integrals are Cauchy principal value integrals. Consider the incident wave field representation of Eq. (8.23) for $x'_3 > x_3^S$. Evaluating this representation at $(\mathbf{x}_T, x_3) = (\mathbf{x}_T, x'_3)$, $\forall x'_3 > x_3^S$, using the singular boundary integral operators, yields the *down-going wave field condition* for $\{\hat{p}^{\text{inc}}, \hat{v}_3^{\text{inc}}\}(\mathbf{x}_T, x_3; \mathbf{x}_T^S, x_3^S)$,

$$(\mathcal{I} - \hat{\mathcal{D}}^b) \hat{p}^{\text{inc}} - \hat{\mathcal{S}}^b \hat{v}_3^{\text{inc}} = 0, \quad \text{at} \quad x_3 > x_3^S, \quad (8.43)$$

with respect to the background medium. One should keep in mind that the directionality is relative with respect to the choice of a medium. For example, the incident wave field in Eq. (8.43) is not necessarily down-going in the usual sense, i.e. with respect to a homogeneous medium. Next, consider the scattered wave field representation of Eq. (8.29) for $x'_3 \leq x_3^{\text{sct}}$. Evaluating this representation at $(x_T, x_3) = (x_T, x'_3)$, $\forall x'_3 \leq x_3^{\text{sct}}$, using the singular boundary integral operators, yields the *up-going wave field condition* for $\{\hat{p}^{\text{sct}}, \hat{v}_3^{\text{sct}}\}(\mathbf{x}_T, x_3; \mathbf{x}_T^S, x_3^S)$,

$$\left(\mathcal{I} + \hat{\mathcal{D}}^b \right) \hat{p}^{\text{sct}} + \hat{\mathcal{S}}^b \hat{v}_3^{\text{sct}} = 0, \quad \text{at } x_3 \leq x_3^{\text{sct}}, \quad (8.44)$$

with respect to the background medium (Weston (1988)). Assuming the existence of the inverse of $\hat{\mathcal{S}}^b$, we arrive at the following operators, at any level surface in \mathbb{D} , for the incident and scattered wave fields,

$$\hat{v}_3^{\text{inc}} = \hat{\mathcal{Y}}^d \hat{p}^{\text{inc}}, \quad \text{at } x_3 > x_3^S, \quad (8.45)$$

$$\hat{v}_3^{\text{sct}} = \hat{\mathcal{Y}}^u \hat{p}^{\text{sct}}, \quad \text{at } x_3 \leq x_3^{\text{sct}}, \quad (8.46)$$

with

$$\hat{\mathcal{Y}}^d = \left(\hat{\mathcal{S}}^b \right)^{-1} \left(\mathcal{I} - \hat{\mathcal{D}}^b \right), \quad (8.47)$$

$$\hat{\mathcal{Y}}^u = - \left(\hat{\mathcal{S}}^b \right)^{-1} \left(\mathcal{I} + \hat{\mathcal{D}}^b \right). \quad (8.48)$$

The operators $\hat{\mathcal{Y}}^d$ and $\hat{\mathcal{Y}}^u$ are *Dirichlet-to-Neumann* operators which map the first component of $\hat{\mathbf{F}}^{\text{inc}}$ and $\hat{\mathbf{F}}^{\text{sct}}$ to the second component of these wave field vectors, respectively. I.e., these operators map the pressure functions \hat{p}^{inc} and \hat{p}^{sct} to the longitudinal component of the particle velocity vector functions, \hat{v}_3^{inc} and \hat{v}_3^{sct} , respectively.

8.5 Decomposition operator

We designate the domain $\mathbb{D} = \{(\mathbf{x}_T, x_3) | \mathbf{x}_T \in \mathbb{R}^2, x_3^S < x_3 \leq x_3^{\text{sct}}\}$. Eqs. (8.5), (8.45) and (8.46) yield the following *wave field composition* operation

$$\hat{\mathbf{F}} = \hat{\mathbf{T}}^b \hat{\mathbf{P}}^b, \quad \text{in } \mathbb{D}, \quad (8.49)$$

with the wave field components vector,

$$\hat{\mathbf{P}}^b = \begin{pmatrix} \hat{p}^{inc} \\ \hat{p}^{sct} \end{pmatrix}, \quad (8.50)$$

and with the wave field composition matrix of operators,

$$\hat{\mathbf{T}}^b = \begin{pmatrix} \mathcal{I} & \mathcal{I} \\ \hat{\mathcal{Y}}^d & \hat{\mathcal{Y}}^u \end{pmatrix}. \quad (8.51)$$

The inverse operation, *wave field decomposition*, is given by

$$\hat{\mathbf{L}}^b = \frac{1}{2} \hat{\mathcal{S}}^b \begin{pmatrix} -\hat{\mathcal{Y}}^u & \mathcal{I} \\ \hat{\mathcal{Y}}^d & -\mathcal{I} \end{pmatrix}, \quad \text{in } \mathbb{D}, \quad (8.52)$$

in which we used

$$\hat{\mathcal{Y}}^d - \hat{\mathcal{Y}}^u = 2 \left(\hat{\mathcal{S}}^b \right)^{-1}. \quad (8.53)$$

In Haines and de Hoop (1996) a similar decomposition is implemented, in terms of curvilinear coordinates, for the case of internal wave fields, i.e. wave fields that are represented by two bounding surfaces, and originating outside the enclosed domain. Eq. (8.52) can also be written as

$$\hat{\mathbf{L}}^b = \frac{1}{2} \begin{pmatrix} \mathcal{I} + \hat{\mathcal{D}}^b & \hat{\mathcal{S}}^b \\ \mathcal{I} - \hat{\mathcal{D}}^b & -\hat{\mathcal{S}}^b \end{pmatrix}, \quad (8.54)$$

(see Weston (1988)). Hence, we obtain the converse of Eqs. (8.43) and (8.44)

$$(\mathcal{I} - \hat{\mathcal{D}}^b) \hat{p} - \hat{\mathcal{S}}^b \hat{v}_3 = 0 \implies \hat{p} = \hat{p}^{inc}, \quad (8.55)$$

$$(\mathcal{I} + \hat{\mathcal{D}}^b) \hat{p} + \hat{\mathcal{S}}^b \hat{v}_3 = 0 \implies \hat{p} = \hat{p}^{sct}, \quad (8.56)$$

respectively.

8.6 Reflection and transmission operators

We define the following single-layer potential boundary integral operator

$$\hat{\mathcal{S}}f(\mathbf{x}_T, x_3) \stackrel{\text{def}}{=} 2 \int_{\mathbf{x}'_T \in \mathbb{R}^2} \hat{G}^q(\mathbf{x}_T, x_3; \mathbf{x}'_T, x_3) f(\mathbf{x}'_T, x_3) d\mathbf{x}'_T, \quad (8.57)$$

and the double-layer potential boundary integral operator

$$\hat{\mathcal{D}}g(\mathbf{x}_T, x_3) \stackrel{\text{def}}{=} 2 \int_{\mathbf{x}'_T \in \mathbb{R}^2} \hat{\Gamma}_3^q(\mathbf{x}_T, x_3; \mathbf{x}'_T, x_3) g(\mathbf{x}'_T, x_3) d\mathbf{x}'_T, \quad (8.58)$$

(Colton and Kress (1983); Sabatier (1990)), in which $f, g \in [L^2(\mathbb{R}^2)]^1$. These last singular integral operators are defined with respect to the actual medium in contradistinction to the operators of Eqs. (8.41) and (8.42), which are defined with respect to the background medium. Consider the total wave field representation of Eq. (8.39) for $x'_3 > x_3^S$. Evaluating this representation at $(x_T, x_3) = (x_T, x'_3)$, $\forall x'_3 > x_3^S$, using the integral operators of Eqs. (8.57) and (8.58), yields the down-going wave field condition for $\{\hat{p}, \hat{v}_3\}(\mathbf{x}_T, x_3; \mathbf{x}_T^S, x_3^S)$,

$$(\mathcal{I} - \hat{\mathcal{D}}) \hat{p} - \hat{\mathcal{S}} \hat{v}_3 = 0, \quad \text{at } x_3 > x_3^S, \quad (8.59)$$

with respect to the actual medium. Assuming the existence of the inverse of $\hat{\mathcal{S}}$, we obtain

$$\hat{v}_3 = \hat{\mathcal{Y}} \hat{p}, \quad \text{at } x_3 > x_3^S, \quad (8.60)$$

with

$$\hat{\mathcal{Y}} = \hat{\mathcal{S}}^{-1} (\mathcal{I} - \hat{\mathcal{D}}). \quad (8.61)$$

The operator $\hat{\mathcal{Y}}$ constitutes the Dirichlet-to-Neumann map of the total wave field. Consider the domain $\mathbb{D} = \{(\mathbf{x}_T, x_3) | \mathbf{x}_T \in \mathbb{R}^2, x_3^S < x_3 \leq x_3^{\text{sct}}\}$. Combining the down-going wave field condition of the incident wave field in Eq. (8.43), with the up-going wave field condition of the scattered wave field of Eq. (8.44), together with the wave field composition of Eq. (8.5), yields

$$(\mathcal{I} + \hat{\mathcal{D}}^b) \hat{p} + \hat{\mathcal{S}}^b \hat{v}_3 = 2\hat{p}^{\text{inc}}, \quad \text{in } \mathbb{D}. \quad (8.62)$$

Using this last equation and Eq. (8.59), and using the boundary condition of Eq. (7.34), we obtain

$$\hat{\mathbf{L}} \hat{\mathbf{F}} = \hat{\mathbf{P}}^{\text{inc}}, \quad \text{in } \mathbb{D}, \quad (8.63)$$

with

$$\hat{\mathbf{P}}^{\text{inc}} = \begin{pmatrix} \hat{p}^{\text{inc}} \\ 0 \end{pmatrix}, \quad (8.64)$$

and

$$\hat{L} = \frac{1}{2} \begin{pmatrix} \mathcal{I} + \hat{\mathcal{D}}^b & \hat{\mathcal{S}}^b \\ \mathcal{I} - \hat{\mathcal{D}} & -\hat{\mathcal{S}} \end{pmatrix}, \quad (8.65)$$

(see Weston (1988) and compare with Eq. (8.54)). The inverse operation is given by

$$\hat{\mathbf{F}} = \hat{\mathbf{T}} \hat{\mathbf{P}}^{\text{inc}}, \quad \text{in } \mathbb{D}, \quad (8.66)$$

with

$$\hat{\mathbf{T}} = \begin{pmatrix} \hat{\mathcal{T}}^d & \hat{\mathcal{T}}^u \\ \hat{\mathcal{Y}} \hat{\mathcal{T}}^d & \hat{\mathcal{Y}}^u \hat{\mathcal{T}}^u \end{pmatrix}, \quad (8.67)$$

(compare with Eq. (8.51)), in which the transmission operators are given by

$$\hat{\mathcal{T}}^d = 2 \left(\hat{\mathcal{Y}} - \hat{\mathcal{Y}}^u \right)^{-1} \left(\hat{\mathcal{S}}^b \right)^{-1}, \quad (8.68)$$

$$\hat{\mathcal{T}}^u = 2 \left(\hat{\mathcal{Y}} - \hat{\mathcal{Y}}^u \right)^{-1} \hat{\mathcal{S}}^{-1}. \quad (8.69)$$

From Eq. (8.66) we obtain

$$\hat{p} = \hat{\mathcal{T}}^d \hat{p}^{\text{inc}}, \quad \text{in } \mathbb{D}. \quad (8.70)$$

The *reflection operator* $\hat{\mathcal{R}}^d$ is defined by

$$\hat{p}^{\text{sct}} \stackrel{\text{def}}{=} \hat{\mathcal{R}}^d \hat{p}^{\text{inc}}, \quad \text{in } \mathbb{D}, \quad (8.71)$$

From the wave field composition of Eq. (8.5) we obtain

$$\hat{\mathcal{R}}^d = \hat{\mathcal{T}}^d - \mathcal{I}. \quad (8.72)$$

Hence,

$$\hat{\mathcal{R}}^d = \left(\hat{\mathcal{Y}} - \hat{\mathcal{Y}}^u \right)^{-1} \left(\hat{\mathcal{Y}}^d - \hat{\mathcal{Y}} \right). \quad (8.73)$$

The reflection operator $\hat{\mathcal{R}}^d$ quantifies the spatial contrasts between the background medium and the actual medium, in terms of the D-t-N operators of the incident, scattered and total wave fields. Therefore, it is a global operator encompassing all contrasts for $x_3 > x_3^{\text{sct}}$.

8.7 Symmetry of the D-t-N operators

8.7.1 Symmetry of $\hat{\mathcal{Y}}^d$

Consider the application of the reciprocity theorem of the time-convolution type. We take for State A the incident wave field of Eq. (8.6), denoted by $\hat{\mathbf{F}}^{inc,A} = (\hat{p}^{inc,A}, \hat{v}_3^{inc,A})^t$, with source vector,

$$\hat{\mathbf{N}}^A(\mathbf{x}, s) = \begin{pmatrix} 0 \\ \hat{q}(s) \delta(\mathbf{x} - \mathbf{x}^R) \end{pmatrix}, \quad \mathbf{x}^R \in \mathbb{D}^{sct'}. \quad (8.74)$$

For State B we also take the incident wave field of Eq. (8.6), and denote it by $\hat{\mathbf{F}}^{inc,B} = (\hat{p}^{inc,B}, \hat{v}_3^{inc,B})^t$, with source vector,

$$\hat{\mathbf{N}}^B(\mathbf{x}, s) = \begin{pmatrix} 0 \\ \hat{q}(s) \delta(\mathbf{x} - \mathbf{x}^S) \end{pmatrix}, \quad \mathbf{x}^S \in \mathbb{D}^{sct'}, \quad (8.75)$$

(see Fig. (8.1)). Thus, the two states differ in the positioning of their sources. The reciprocity theorem is applied to the domain $\mathbb{D} = \{(\mathbf{x}_T, x_3) | \mathbf{x}_T \in \mathbb{R}^2, x'_3 < x_3 < x^R_3\}$, with $x'_3 > x^R_3 = x^S_3$ (Fig. (8.5)). We have in \mathbb{D}

$$A = \left\{ \hat{\mathbf{F}}^{inc,A}, \hat{\mathbf{A}}^b, \mathbf{O} \right\} \quad \text{and} \quad B = \left\{ \hat{\mathbf{F}}^{inc,B}, \hat{\mathbf{A}}^b, \mathbf{O} \right\}. \quad (8.76)$$

Because both states are governed by the same material state we apply the reciprocity theorem of Eq. (7.71). Taking into account that both states are source-free inside \mathbb{D} we obtain

$$\left\langle \hat{\mathbf{F}}^{inc,A}, \mathbf{J} \hat{\mathbf{F}}^{inc,B} \right\rangle_b (x^R_3; \mathbf{x}^R, \mathbf{x}^S) - \left\langle \hat{\mathbf{F}}^{inc,A}, \mathbf{J} \hat{\mathbf{F}}^{inc,B} \right\rangle_b (x'_3; \mathbf{x}^R, \mathbf{x}^S) = 0. \quad (8.77)$$

Taking the limit $x^R_3 \rightarrow \infty$ and applying Sommerfeld's radiation conditions, this last equation is expressed, in terms of a bilinear form of scalar-valued functions, as

$$\left\langle \hat{p}^{inc,A}, \hat{v}_3^{inc,B} \right\rangle_b (x'_3; \mathbf{x}^R, \mathbf{x}^S) = \left\langle \hat{v}_3^{inc,A}, \hat{p}^{inc,B} \right\rangle_b (x'_3; \mathbf{x}^R, \mathbf{x}^S), \quad x'_3 > x^S_3. \quad (8.78)$$

Substitution of the Dirichlet-to-Neumann operator of the incident wave field of Eq. (8.45), and using the property that $\hat{\mathcal{Y}}^d$ is independent of the source position of the wave field function it operates on, yields

$$\left\langle \hat{p}^{inc,A}, \hat{\mathcal{Y}}^d \hat{p}^{inc,B} \right\rangle_b = \left\langle \hat{\mathcal{Y}}^d \hat{p}^{inc,A}, \hat{p}^{inc,B} \right\rangle_b. \quad (8.79)$$

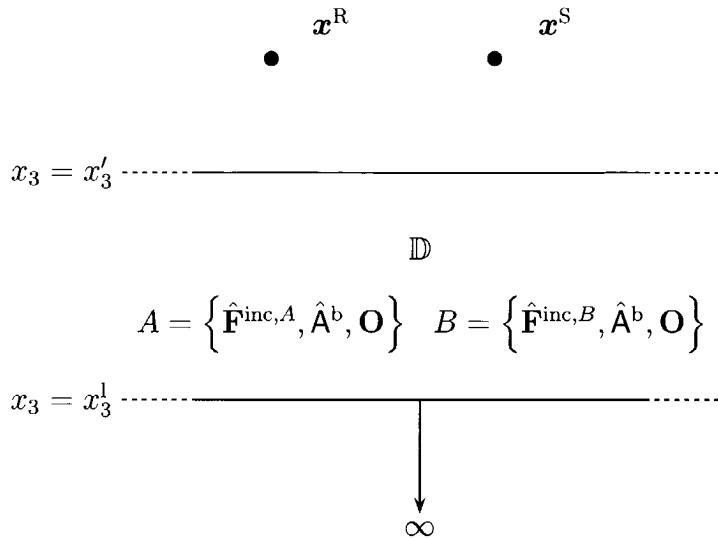


Figure 8.5: The interaction of two incident wave fields with different source positions: the two states and the domain of application of the reciprocity theorem.

Hence, the D-t-N operator $\hat{\mathcal{Y}}^d$ is, analogous to Eq. (7.48), a symmetric operator with respect to a bilinear form, expressed as

$$\hat{\mathcal{Y}}^d = \left(\hat{\mathcal{Y}}^d \right)^t, \quad \text{at all surfaces } x_3 = x'_3 > x^S_3. \quad (8.80)$$

8.7.2 Symmetry of $\hat{\mathcal{Y}}^u$

Consider the application of the reciprocity theorem of the convolution type to the domain $\mathbb{D} = \{(\mathbf{x}_T, x_3) | \mathbf{x}_T \in \mathbb{R}^2, x_3^u < x_3 < x'_3\}$, with $x'_3 \leq x_3^{sct}$. Take for State A the scattered wave field of Eq. (8.11), denoted by $\hat{\mathbf{F}}^{sct,A} = (\hat{p}^{sct,A}, \hat{v}_3^{sct,A})^t$, with source vector,

$$\hat{\mathbf{N}}^{sct,A} (\mathbf{x}; \mathbf{x}^R, s) = \begin{cases} \mathbf{0} & \mathbf{x} \in \mathbb{D}^{sct'}, \\ -(\hat{\mathbf{A}} - \hat{\mathbf{A}}^b) \hat{\mathbf{F}}^A (\mathbf{x}; \mathbf{x}^R, s), & \mathbf{x} \in \mathbb{D}^{sct}. \end{cases} \quad (8.81)$$

For State B we also take the scattered wave field of Eq. (8.11), denoted by $\hat{\mathbf{F}}^{\text{sct},B} = (\hat{p}^{\text{sct},B}, \hat{v}_3^{\text{sct},B})^t$, with source vector,

$$\hat{\mathbf{N}}^{\text{sct},B}(\mathbf{x}; \mathbf{x}^S, s) = \begin{cases} \mathbf{O} & \mathbf{x} \in \mathbb{D}^{\text{sct}'}, \\ -(\hat{\mathbf{A}} - \hat{\mathbf{A}}^b) \hat{\mathbf{F}}^B(\mathbf{x}; \mathbf{x}^S, s), & \mathbf{x} \in \mathbb{D}^{\text{sct}}, \end{cases} \quad (8.82)$$

(Fig. (8.6)). The wave field vectors $\hat{\mathbf{F}}^A$ and $\hat{\mathbf{F}}^B$, which appear in the source descriptions of the scattered wave fields of Eqs. (8.81) and (8.82), are governed by Eq. (8.1), and have respective source vectors given by Eqs. (8.74) and (8.75). Thus, the two states differ in the positioning of their actual sources. We have in \mathbb{D}

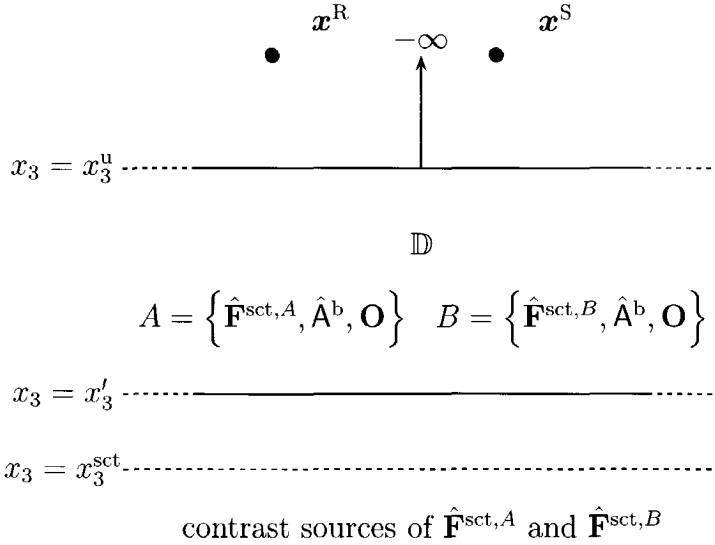


Figure 8.6: The interaction of two scattered wave fields with different source positions: the two states and the domain of application of the reciprocity theorem.

$$A = \{\hat{\mathbf{F}}^{\text{sct},A}, \hat{\mathbf{A}}^b, \mathbf{O}\} \quad \text{and} \quad B = \{\hat{\mathbf{F}}^{\text{sct},B}, \hat{\mathbf{A}}^b, \mathbf{O}\}. \quad (8.83)$$

Because both states are governed by the same material state we apply the reciprocity theorem of Eq. (7.71). Taking into account that both states are

source-free inside \mathbb{D} we obtain

$$\left\langle \hat{\mathbf{F}}^{\text{sct},A}, \mathbf{J}\hat{\mathbf{F}}^{\text{sct},B} \right\rangle_b (x'_3; \mathbf{x}^R, \mathbf{x}^S) - \left\langle \hat{\mathbf{F}}^{\text{sct},A}, \mathbf{J}\hat{\mathbf{F}}^{\text{sct},B} \right\rangle_b (x_3^u; \mathbf{x}^R, \mathbf{x}^S) = 0. \quad (8.84)$$

Taking the limit $x_3^u \rightarrow -\infty$ and applying Sommerfeld's radiation conditions, this last equation is expressed, in terms of a bilinear form of scalar-valued functions, as

$$\left\langle \hat{p}^{\text{sct},A}, \hat{v}_3^{\text{sct},B} \right\rangle_b (x'_3; \mathbf{x}^R, \mathbf{x}^S) = \left\langle \hat{v}_3^{\text{sct},A}, \hat{p}^{\text{sct},B} \right\rangle_b (x'_3; \mathbf{x}^R, \mathbf{x}^S), \\ x'_3 \leq x_3^{\text{sct}}. \quad (8.85)$$

Using the D-t-N operator of the scattered wave field of Eq. (8.46) yields

$$\left\langle \hat{p}^{\text{sct},A}, \hat{\mathcal{Y}}^u \hat{p}^{\text{sct},B} \right\rangle_b = \left\langle \hat{\mathcal{Y}}^u \hat{p}^{\text{sct},A}, \hat{p}^{\text{sct},B} \right\rangle_b. \quad (8.86)$$

Hence, the D-t-N operator in this last equation is a symmetric operator with respect to a bilinear form, expressed as

$$\hat{\mathcal{Y}}^u = \left(\hat{\mathcal{Y}}^u \right)^t, \quad \text{at all surfaces} \quad x_3 = x'_3 \leq x_3^{\text{sct}}. \quad (8.87)$$

The symmetries of $\hat{\mathcal{Y}}^d$ and $\hat{\mathcal{Y}}^u$ are a direct consequence of the validity of Sommerfeld radiation conditions towards infinity. Because of the latter two symmetries we have, using Eq. (8.53), and the fact that inverse and symmetry are interchangeable,

$$\hat{\mathcal{S}}^b = \left(\hat{\mathcal{S}}^b \right)^t, \quad \text{at all surfaces} \quad x_3 = x'_3, x_3^S < x'_3 \leq x_3^{\text{sct}}. \quad (8.88)$$

8.7.3 Symmetry of $\hat{\mathcal{Y}}$

Consider the application of the reciprocity theorem of the convolution type. We take for State A the total wave field of Eq. (8.1), denoted by $\hat{\mathbf{F}}^A = (\hat{p}^A, \hat{v}_3^A)^t$, with source vector $\hat{\mathbf{N}}^A$ given in Eq. (8.74). For State B we also take the total wave field of Eq. (8.1), and denote it by $\hat{\mathbf{F}}^B = (\hat{p}^B, \hat{v}_3^B)^t$, with source vector $\hat{\mathbf{N}}^B$ given in Eq. (8.75). Thus, the two states differ in the positioning of their sources. The reciprocity is applied to the domain $\mathbb{D} = \{(\mathbf{x}_T, x_3) | \mathbf{x}_T \in \mathbb{R}^2, x'_3 < x_3 < x_3^1\}$, with $x'_3 > x_3^R = x_3^S$ (Fig. (8.7)). We

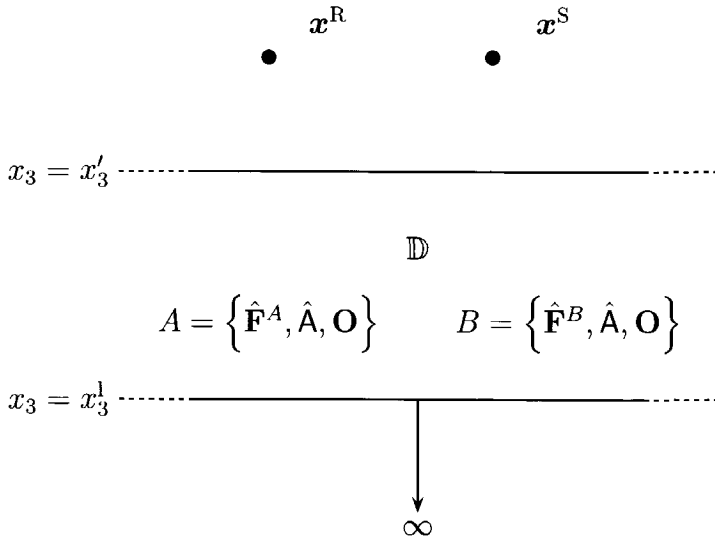


Figure 8.7: The interaction of two total wave fields with different source positions: the two states and the domain of application of the reciprocity theorem.

have in \mathbb{D}

$$A = \left\{ \hat{\mathbf{F}}^A, \hat{\mathbf{A}}, \mathbf{O} \right\} \quad \text{and} \quad B = \left\{ \hat{\mathbf{F}}^B, \hat{\mathbf{A}}, \mathbf{O} \right\}. \quad (8.89)$$

Because both states are governed by the same material state we apply the reciprocity theorem of Eq. (7.71). Taking into account that both states are source-free inside \mathbb{D} we obtain

$$\left\langle \hat{\mathbf{F}}^A, \mathbf{J} \hat{\mathbf{F}}^B \right\rangle_b (x_3^l; \mathbf{x}^R, \mathbf{x}^S) - \left\langle \hat{\mathbf{F}}^A, \mathbf{J} \hat{\mathbf{F}}^B \right\rangle_b (x'_3; \mathbf{x}^R, \mathbf{x}^S) = 0. \quad (8.90)$$

Taking the limit $x_3^l \rightarrow \infty$ and applying Sommerfeld's radiation conditions, this last equation is expressed, in terms of a bilinear form of scalar-valued functions, as

$$\left\langle \hat{p}^A, \hat{v}_3^B \right\rangle_b (x'_3; \mathbf{x}^R, \mathbf{x}^S) = \left\langle \hat{v}_3^A, \hat{p}^B \right\rangle_b (x'_3; \mathbf{x}^R, \mathbf{x}^S), \quad x'_3 > x_3^S. \quad (8.91)$$

Substitution of the Dirichlet-to-Neumann operator of the total wave field of Eq. (8.60), and using the property that $\hat{\mathcal{Y}}$ is independent of the source

position of the wave field function it operates on, yields

$$\left\langle \hat{p}^A, \hat{\mathcal{Y}}\hat{p}^B \right\rangle_b = \left\langle \hat{\mathcal{Y}}\hat{p}^A, \hat{p}^B \right\rangle_b. \quad (8.92)$$

Hence, the Dirichlet-to-Neumann operator $\hat{\mathcal{Y}}$ is a symmetric operator with respect to a bilinear form, expressed as

$$\hat{\mathcal{Y}} = \hat{\mathcal{Y}}^t, \quad \text{at all surfaces} \quad x_3 = x'_3 > x_3^s. \quad (8.93)$$

The symmetries of the D-t-N operators for the incident and scattered wave fields are used in the subsequent chapters to derive extrapolation operators which propagate a pressure wave field from one level surface to another.

Chapter 9

Wave field extrapolation

9.1 Introduction

In Chapter 6 the interaction integral of Eq. (6.31) is introduced, which integrand contains total wave fields. Using the decomposition introduced in the previous chapter one can construct these total wave fields from measurements, the latter being represented by the scattered wave fields. Because the wave fields in the interaction quantity are evaluated at a certain depth, one needs to express these in terms of wave fields at the recording level. To this end, extrapolation operators are derived, in this chapter, which exploit the fact that at the decomposition level the incident and the scattered wave fields obey down- and up-going wave field conditions, respectively. For the inverse formalism an inverse extrapolation operator is derived for the scattered wave field. Enforcing radiation conditions, equivalent to certain conditions on the D-t-N operators, one derives the necessary up-going wave field condition for a time-correlation type scattered wave field representation, analogous to the Sommerfeld radiation condition in case of the time-convolution type representation. The inverse extrapolation operation produces an approximate result for wave fields travelling in the transverse directions, e.g. refracted waves.

9.2 Incident wave field

The reciprocity theorem of the convolution type is applied to the domain $\mathbb{D} = \{(\mathbf{x}_T, x_3) | \mathbf{x}_T \in \mathbb{R}^2, x_3^u < x_3 < x_3^l\}$, with $x_3^u < x_3^S$ and $x_3^l > x_3^S$ (Fig.

(9.1)). We take for State A the volume-injection Green's wave field of Eq. (8.14), with source position $\mathbf{x} \in \mathbb{D}$ and for State B the incident wave field of Eq. (8.6), with source position, as stated above, $\mathbf{x}^S \in \mathbb{D}$. We have in \mathbb{D}

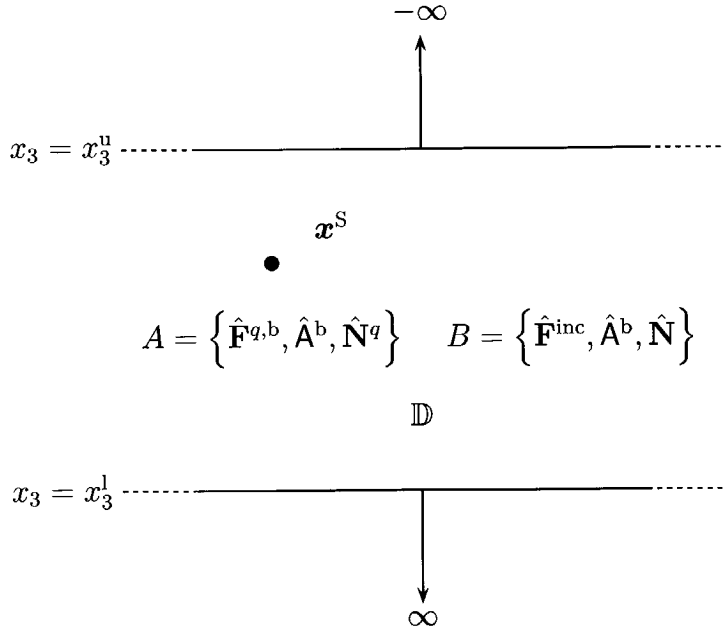


Figure 9.1: The incident wave field: the two states and the domain of application of the reciprocity theorem

$$A = \left\{ \hat{\mathbf{F}}^{q,b}, \hat{\mathbf{A}}^b, \hat{\mathbf{N}}^q \right\} \quad \text{and} \quad B = \left\{ \hat{\mathbf{F}}^{inc}, \hat{\mathbf{A}}^b, \hat{\mathbf{N}} \right\}, \quad \text{in } \mathbb{D}. \quad (9.1)$$

Application of the reciprocity theorem of the convolution type of Eq. (7.71) yields

$$\begin{aligned} & \left\langle \hat{\mathbf{F}}^{q,b}, \mathbf{J}\hat{\mathbf{F}}^{\text{inc}} \right\rangle_b (x_3^1; \mathbf{x}, \mathbf{x}^S) - \left\langle \hat{\mathbf{F}}^{q,b}, \mathbf{J}\hat{\mathbf{F}}^{\text{inc}} \right\rangle_b (x_3^u; \mathbf{x}, \mathbf{x}^S) \\ &= \int_{x_3' = x_3^u}^{x_3^1} \left[\left\langle \hat{\mathbf{N}}^q, \mathbf{J}\hat{\mathbf{F}}^{\text{inc}} \right\rangle_b (x_3'; \mathbf{x}, \mathbf{x}^S) + \left\langle \hat{\mathbf{F}}^{q,b}, \mathbf{J}\hat{\mathbf{N}} \right\rangle_b (x_3'; \mathbf{x}, \mathbf{x}^S) \right] dx_3'. \quad (9.2) \end{aligned}$$

By extending the domain \mathbb{D} to \mathbb{R}^3 , and applying Sommerfeld radiation conditions towards plus and minus infinity, the bilinear forms on the left-hand

side of this last equation vanish. Substituting the source distributions of both states into the integral of the right-hand side of Eq. (9.2) gives

$$\begin{aligned}\hat{p}^{\text{inc}}(\mathbf{x}_T, x_3; \mathbf{x}_T^S, x_3^S) &= \int_{x_3'=-\infty}^{+\infty} dx_3' \delta(x_3' - x_3^S) \\ &\times \int_{\mathbf{x}'_T \in \mathbb{R}^2} \hat{p}^{q,b}(\mathbf{x}'_T, x_3'; \mathbf{x}_T, x_3) \delta(\mathbf{x}'_T - \mathbf{x}_T^S) d\mathbf{x}'_T.\end{aligned}\quad (9.3)$$

Integration with respect to the longitudinal coordinate, and using the monopole Green's state of Eq. (8.17), leads to

$$\hat{p}^{\text{inc}}(\mathbf{x}_T, x_3; \mathbf{x}_T^S, x_3^S) = \hat{q} \int_{\mathbf{x}'_T \in \mathbb{R}^2} \hat{G}^{q,b}(\mathbf{x}_T, x_3; \mathbf{x}'_T, x_3^S) \delta(\mathbf{x}'_T - \mathbf{x}_T^S) d\mathbf{x}'_T.\quad (9.4)$$

Taking the limit $x_3 \downarrow x_3^S$, using the single-layer potential of Eq. (8.41), we obtain the following initial condition,

$$\hat{p}^{\text{inc}}(\mathbf{x}_T, x_3^S; \mathbf{x}_T^S, x_3^S) = \frac{1}{2} \hat{q} \hat{\mathcal{S}}^b \delta(\mathbf{x}_T - \mathbf{x}_T^S),\quad (9.5)$$

with

$$\hat{\mathcal{S}}^b \delta(\mathbf{x}_T - \mathbf{x}_T^S) = 2 \int_{\mathbf{x}'_T \in \mathbb{R}^2} \hat{G}^{q,b}(\mathbf{x}_T, x_3^S; \mathbf{x}'_T, x_3^S) \delta(\mathbf{x}'_T - \mathbf{x}_T^S) d\mathbf{x}'_T.\quad (9.6)$$

Substituting Eq. (9.5) into Eq. (9.4) gives

$$\begin{aligned}\hat{p}^{\text{inc}}(\mathbf{x}_T, x_3; \mathbf{x}_T^S, x_3^S) &= 2 \int_{\mathbf{x}'_T \in \mathbb{R}^2} \hat{G}^{q,b}(\mathbf{x}_T, x_3; \mathbf{x}'_T, x_3^S) \left(\hat{\mathcal{S}}^b\right)^{-1} \hat{p}^{\text{inc}}(\mathbf{x}'_T, x_3^S; \mathbf{x}_T^S, x_3^S) d\mathbf{x}'_T, \\ &\quad x_3 \geq x_3^S.\end{aligned}\quad (9.7)$$

We define the following two-parameter extrapolation operator $\hat{\mathcal{W}}^{q,b}$,

$$\begin{aligned}\hat{\mathcal{W}}^{q,b}(x_3, x_3') f(\mathbf{x}_T, x_3') &\stackrel{\text{def}}{=} 2 \int_{\mathbf{x}'_T \in \mathbb{R}^2} \hat{G}^{q,b}(\mathbf{x}_T, x_3; \mathbf{x}'_T, x_3') \left(\hat{\mathcal{S}}^b\right)^{-1} f(\mathbf{x}'_T, x_3') d\mathbf{x}'_T.\end{aligned}\quad (9.8)$$

In terms of a bilinear form we can write compactly,

$$\hat{\mathcal{W}}^{q,b}(x_3, x'_3) f(\mathbf{x}_T, x'_3) = 2 \left\langle \hat{G}^{q,b}, \left(\hat{\mathcal{S}}^b \right)^{-1} f \right\rangle_b (x'_3; \mathbf{x}), \quad (9.9)$$

with $f \in [L^2(\mathbb{R}^2)]^1$. Using Eq. (9.8), Eq. (9.7) is written as

$$\hat{p}^{inc}(\mathbf{x}_T, x_3; \mathbf{x}_T^S, x_3^S) = \hat{\mathcal{W}}^{q,b}(x_3, x_3^S) \hat{p}^{inc}(\mathbf{x}_T, x_3^S; \mathbf{x}_T^S, x_3^S), \quad x_3 \geq x_3^S, \quad (9.10)$$

in which $\hat{p}^{inc}(\mathbf{x}_T, x_3^S; \mathbf{x}_T^S, x_3^S)$ is given in Eq. (9.5).

Taking $x_3 > x'_3$ in Eq. (8.23) yields

$$\begin{aligned} \hat{p}^{inc}(\mathbf{x}_T, x_3; \mathbf{x}_T^S, x_3^S) \\ = \int_{\mathbf{x}'_T \in \mathbb{R}^2} \left[\hat{G}^{q,b}(\mathbf{x}_T, x_3; \mathbf{x}'_T, x'_3) \hat{v}_3^{inc}(\mathbf{x}'_T, x'_3; \mathbf{x}_T^S, x_3^S) \right. \\ \left. + \hat{\Gamma}_3^{q,b}(\mathbf{x}_T, x_3; \mathbf{x}'_T, x'_3) \hat{p}^{inc}(\mathbf{x}'_T, x'_3; \mathbf{x}_T^S, x_3^S) \right] d\mathbf{x}'_T, \quad x_3^S < x'_3 < x_3. \end{aligned} \quad (9.11)$$

Using the similarity between the Green's state vector $\hat{\mathbf{F}}^{q,b}$ and the incident wave field vector $\hat{\mathbf{F}}^{inc}$ expressed by Eq. (8.16), and using Eqs. (8.17), (8.18) and (8.45), one can show that for $\{\hat{G}^{q,b}, \hat{\Gamma}_3^{q,b}\}(\mathbf{x}_T, x_3; \mathbf{x}'_T, x'_3)$,

$$\hat{\Gamma}_3^{q,b} = -\hat{\mathcal{Y}}^d \hat{G}^{q,b}, \quad x_3 < x'_3, \quad (9.12)$$

and

$$\hat{\Gamma}_3^{q,b} = -\hat{\mathcal{Y}}^u \hat{G}^{q,b}, \quad x_3 > x'_3. \quad (9.13)$$

These last two equations express that the Green's state is an up-going or down-going wave field, respectively, depending on the source-receiver configuration. Implementing Eqs. (8.45) and (9.12), into Eq. (9.11), and using Eqs. (8.53) and (9.7), yields

$$\begin{aligned} \hat{p}^{inc}(\mathbf{x}_T, x_3; \mathbf{x}_T^S, x_3^S) \\ = 2 \int_{\mathbf{x}'_T \in \mathbb{R}^2} \hat{G}^{q,b}(\mathbf{x}_T, x_3; \mathbf{x}'_T, x'_3) \left(\hat{\mathcal{S}}^b \right)^{-1} \hat{p}^{inc}(\mathbf{x}'_T, x'_3; \mathbf{x}_T^S, x_3^S) d\mathbf{x}'_T, \\ x_3^S \leq x'_3 < x_3. \end{aligned} \quad (9.14)$$

This last equation and Eq. (9.8) yield

$$\hat{p}^{\text{inc}}(\mathbf{x}_T, x_3; \mathbf{x}_T^S, x_3^S) = \hat{\mathcal{W}}^{q,b}(x_3, x'_3) \hat{p}^{\text{inc}}(\mathbf{x}_T, x'_3; \mathbf{x}_T^S, x_3^S), \\ x_3^S \leq x'_3 < x_3. \quad (9.15)$$

Taking the limit $x_3 \downarrow x'_3$ in Eq. (9.8) we obtain for the extrapolation operator

$$\hat{\mathcal{W}}^{q,b}(x_3, x_3) f(\mathbf{x}_T, x_3) \\ = 2 \int_{\mathbf{x}'_T \in \mathbb{R}^2} \hat{G}^{q,b}(\mathbf{x}_T, x_3; \mathbf{x}'_T, x_3) \left(\hat{\mathcal{S}}^b \right)^{-1} f(\mathbf{x}'_T, x_3) d\mathbf{x}'_T. \quad (9.16)$$

Hence, using the single-layer potential of Eq. (8.41), it follows that the extrapolation operator becomes the identity operator

$$\hat{\mathcal{W}}^{q,b}(x_3, x_3) = \mathcal{I}. \quad (9.17)$$

Using Eq. (9.15) we can write

$$\hat{p}^{\text{inc}}(\mathbf{x}_T, x'_3; \mathbf{x}_T^S, x_3^S) = \hat{\mathcal{W}}^{q,b}(x'_3, x''_3) \hat{p}^{\text{inc}}(\mathbf{x}_T, x''_3; \mathbf{x}_T^S, x_3^S), \quad x''_3 \leq x'_3. \quad (9.18)$$

Substituting Eq. (9.18) into Eq. (9.15), yields the following transitivity property for $\hat{\mathcal{W}}^{q,b}$,

$$\hat{\mathcal{W}}^{q,b}(x_3, x''_3) = \hat{\mathcal{W}}^{q,b}(x_3, x'_3) \hat{\mathcal{W}}^{q,b}(x'_3, x''_3), \quad x''_3 \leq x'_3 \leq x_3. \quad (9.19)$$

Consider the two-parameter family of operators $\{\hat{\mathcal{W}}^{q,b}(x_3, x'_3) \mid x_3, x'_3 \in \mathcal{R}\}$. Because any operator $\hat{\mathcal{W}}^{q,b}$ satisfies Eqs. (9.19) and (9.17) this family of linear operators constitutes a semigroup (Pazy (1983); Goldstein (1985)).

9.3 Scattered wave field

Using Eq. (8.29), the scattered wave field representation at (\mathbf{x}_T, x_3) , with $x_3 < x'_3 \leq x_3^{\text{sct}}$, is given by

$$\hat{p}^{\text{sct}}(\mathbf{x}_T, x_3; \mathbf{x}_T^S, x_3^S) \\ = - \int_{\mathbf{x}'_T \in \mathbb{R}^2} \left[\hat{G}^{q,b}(\mathbf{x}_T, x_3; \mathbf{x}'_T, x'_3) \hat{v}_3^{\text{sct}}(\mathbf{x}'_T, x'_3; \mathbf{x}_T^S, x_3^S) \right. \\ \left. + \hat{\Gamma}_3^{q,b}(\mathbf{x}_T, x_3; \mathbf{x}'_T, x'_3) \hat{p}^{\text{sct}}(\mathbf{x}'_T, x'_3; \mathbf{x}_T^S, x_3^S) \right] d\mathbf{x}'_T, \quad x_3 < x'_3 \leq x_3^{\text{sct}}. \quad (9.20)$$

Substituting the D-t-N operations of Eqs. (8.46) and (9.12) into Eq. (9.20), yields

$$\begin{aligned} \hat{p}^{\text{sct}}(\mathbf{x}_T, x_3; \mathbf{x}_T^S, x_3^S) \\ = 2 \int_{\mathbf{x}'_T \in \mathbb{R}^2} \hat{G}^{q,b}(\mathbf{x}_T, x_3; \mathbf{x}'_T, x'_3) \left(\hat{\mathcal{S}}^b \right)^{-1} \hat{p}^{\text{sct}}(\mathbf{x}'_T, x'_3; \mathbf{x}_T^S, x_3^S) d\mathbf{x}'_T, \\ x_3 < x'_3 \leq x_3^{\text{sct}}. \end{aligned} \quad (9.21)$$

in which we used Eq. (8.53). Implementing the extrapolation operator of Eq. (9.8), and the identity property of Eq. (9.17), yields

$$\hat{p}^{\text{sct}}(\mathbf{x}_T, x_3; \mathbf{x}_T^S, x_3^S) = \hat{\mathcal{W}}^{q,b}(x_3, x'_3) \hat{p}^{\text{sct}}(\mathbf{x}_T, x'_3; \mathbf{x}_T^S, x_3^S), \quad x_3 \leq x'_3 \leq x_3^{\text{sct}}. \quad (9.22)$$

Using the reflection operator of Eq. (8.71), and using Eqs. (9.15), Eq. (9.22) can be expressed, in terms of the 'WRW-model' of Berkhout (1985), as

$$\begin{aligned} \hat{p}^{\text{sct}}(\mathbf{x}_T, x_3; \mathbf{x}_T^S, x_3^S) \\ = \hat{\mathcal{W}}^{q,b}(x_3, x'_3) \hat{\mathcal{R}}^d \hat{\mathcal{W}}^{q,b}(x'_3, x''_3) \hat{p}^{\text{inc}}(\mathbf{x}_T, x''_3; \mathbf{x}_T^S, x_3^S), \\ x_3, x''_3 \leq x'_3, \end{aligned} \quad (9.23)$$

except for the difference that the operator $\hat{\mathcal{R}}^d$ is a global operator with respect to the x_3 coordinate, whereas the reflection operator in the WRW model is local.

9.4 Reflection operator

In the following analysis I follow Fokkema (1993), except that I implement a scalar reflection operator with respect to a x_3 is constant surface, whereas Fokkema (1993) employs a matrix reflection operator for a curved surface. The results below can also be generalised to a curved surface, in terms of a scalar reflection coefficient, using curvilinear coordinates. Taking the limit $x_3 \uparrow x'_3$ in Eq. (9.21), the scattered wave field representation is given by the following Cauchy principal value integral,

$$\begin{aligned} \hat{p}^{\text{sct}}(\mathbf{x}_T, x_3; \mathbf{x}_T^S, x_3^S) \\ = 2 \int_{\mathbf{x}'_T \in \mathbb{R}^2} \hat{G}^{q,b}(\mathbf{x}_T, x_3; \mathbf{x}'_T, x_3) \left(\hat{\mathcal{S}}^b \right)^{-1} \hat{p}^{\text{sct}}(\mathbf{x}'_T, x_3; \mathbf{x}_T^S, x_3^S) d\mathbf{x}'_T, \\ x_3 \leq x_3^{\text{sct}} \end{aligned} \quad (9.24)$$

(Colton and Kress (1983)). According to Eq. (8.41) this last equation constitutes the identity operation. Using source-receiver reciprocity

$$\hat{p}^{\text{sct}}(\mathbf{x}_T, x_3; \mathbf{x}_T^S, x_3^S) = \hat{p}^{\text{sct}}(\mathbf{x}_T^S, x_3^S; \mathbf{x}_T, x_3), \quad (9.25)$$

we obtain

$$\begin{aligned} & \hat{p}^{\text{sct}}(\mathbf{x}_T, x_3; \mathbf{x}_T^S, x_3^S) \\ &= 2 \int_{\mathbf{x}'_T \in \mathbb{R}^2} \hat{G}^{q,b}(\mathbf{x}_T^S, x_3^S; \mathbf{x}'_T, x_3) \left(\hat{\mathcal{S}}^b \right)^{-1} \hat{p}^{\text{sct}}(\mathbf{x}'_T, x_3; \mathbf{x}_T, x_3) d\mathbf{x}'_T. \end{aligned} \quad (9.26)$$

Defining the monopole scattered state $\hat{G}^{q,\text{sct}}$,

$$\hat{p}^{\text{sct}}(\mathbf{x}_T, x_3; \mathbf{x}'_T, x_3') \stackrel{\text{def}}{=} \hat{q} \hat{G}^{q,\text{sct}}(\mathbf{x}'_T, x_3'; \mathbf{x}_T, x_3), \quad (9.27)$$

using Eqs. (8.17) and (8.16), yields

$$\begin{aligned} & \hat{p}^{\text{sct}}(\mathbf{x}_T, x_3; \mathbf{x}_T^S, x_3^S) \\ &= 2 \int_{\mathbf{x}'_T \in \mathbb{R}^2} \left(\hat{\mathcal{S}}^b \right)^{-1} \hat{G}^{q,\text{sct}}(\mathbf{x}_T, x_3; \mathbf{x}'_T, x_3) \hat{p}^{\text{inc}}(\mathbf{x}'_T, x_3; \mathbf{x}_T^S, x_3^S) d\mathbf{x}'_T, \\ & \quad x_3 \leq x_3^{\text{sct}}. \end{aligned} \quad (9.28)$$

Implementing the definition of the reflection operator of Eq. (8.71) yields for the reflection operator,

$$\begin{aligned} & \hat{\mathcal{R}}^d \hat{p}^{\text{inc}}(\mathbf{x}_T, x_3; \mathbf{x}_T^S, x_3^S) \\ &= \int_{\mathbf{x}'_T \in \mathbb{R}^2} \hat{R}^d(\mathbf{x}_T, x_3; \mathbf{x}'_T, x_3) \hat{p}^{\text{inc}}(\mathbf{x}'_T, x_3; \mathbf{x}_T^S, x_3^S) d\mathbf{x}'_T, \\ & \quad x_3 \leq x_3^{\text{sct}}, \end{aligned} \quad (9.29)$$

in which the kernel of $\hat{\mathcal{R}}^d$ is given by

$$\hat{R}^d(\mathbf{x}_T, x_3; \mathbf{x}'_T, x_3) = 2 \left(\hat{\mathcal{S}}^b \right)^{-1} \hat{G}^{q,\text{sct}}(\mathbf{x}_T, x_3; \mathbf{x}'_T, x_3). \quad (9.30)$$

In imaging one inverts for \hat{R}^d at $x_3 = x_3^{\text{sct}}$.

9.5 Inverse extrapolation

In the thissection the wave field quantities are considered in the Fourier domain and annotated according to Eq. (B.6). Application of the reciprocity theorem of the time-correlation type of Eq. (7.105) to the domain $\mathbb{D} = \{(\mathbf{x}_T, x_3) | \mathbf{x}_T \in \mathbb{R}^2, x_3^R < x_3 < x_3'\}, x_3' \leq x_3^{\text{sct}}$, with the states of Eq. (8.25), yields

$$\begin{aligned} & \langle \check{\mathbf{F}}^{q,b}, \mathbf{K} \check{\mathbf{F}}^{\text{sct}} \rangle_s (x_3'; \mathbf{x}, \mathbf{x}^S) - \langle \check{\mathbf{F}}^{q,b}, \mathbf{K} \check{\mathbf{F}}^{\text{sct}} \rangle_s (x_3^R; \mathbf{x}, \mathbf{x}^S) \\ &= \int_{x_3''=x_3^R}^{x_3'} \langle \check{\mathbf{N}}^q, \mathbf{K} \check{\mathbf{F}}^{\text{sct}} \rangle_s (x_3''; \mathbf{x}, \mathbf{x}^S) dx_3'', \quad x_3^R < x_3 < x_3'. \end{aligned} \quad (9.31)$$

In terms of scalar wave field values we can derive the following integral representation for the scattered wave field

$$\begin{aligned} & \check{q}^* \check{p}^{\text{sct}} (\mathbf{x}_T, x_3; \mathbf{x}_T^S, x_3^S) \\ &= \int_{\mathbf{x}'_T \in \mathbb{R}^2} \left[\check{p}^{q,b*} (\mathbf{x}'_T, x_3'; \mathbf{x}_T, x_3) \check{v}_3^{\text{sct}} (\mathbf{x}'_T, x_3'; \mathbf{x}_T^S, x_3^S) \right. \\ & \quad \left. + \check{v}_3^{q,b*} (\mathbf{x}'_T, x_3'; \mathbf{x}_T, x_3) \check{p}^{\text{sct}} (\mathbf{x}'_T, x_3'; \mathbf{x}_T^S, x_3^S) \right] d\mathbf{x}'_T \\ & - \int_{\mathbf{x}''_T \in \mathbb{R}^2} \left[\check{p}^{q,b*} (\mathbf{x}''_T, x_3^R; \mathbf{x}_T, x_3) \check{v}_3^{\text{sct}} (\mathbf{x}''_T, x_3^R; \mathbf{x}_T^S, x_3^S) \right. \\ & \quad \left. + \check{v}_3^{q,b*} (\mathbf{x}''_T, x_3^R; \mathbf{x}_T, x_3) \check{p}^{\text{sct}} (\mathbf{x}''_T, x_3^R; \mathbf{x}_T^S, x_3^S) \right] d\mathbf{x}''_T. \end{aligned} \quad (9.32)$$

Invoking a wave field decomposition and implementing the Green's states of Eqs. (8.17) and (8.18) we obtain

$$\check{p}^{\text{sct}} = \check{p}^{\text{sct},d} + \check{p}^{\text{sct},u} \quad \text{in } \mathbb{D}, \quad (9.33)$$

with

$$\begin{aligned} & \check{p}^{\text{sct},d} (\mathbf{x}_T, x_3; \mathbf{x}_T^S, x_3^S) \\ &= \int_{\mathbf{x}'_T \in \mathbb{R}^2} \left[\check{G}^{q,b*} (\mathbf{x}_T, x_3; \mathbf{x}'_T, x_3') \check{v}_3^{\text{sct}} (\mathbf{x}'_T, x_3'; \mathbf{x}_T^S, x_3^S) \right. \\ & \quad \left. - \check{\Gamma}_3^{q,b*} (\mathbf{x}_T, x_3; \mathbf{x}'_T, x_3') \check{p}^{\text{sct}} (\mathbf{x}'_T, x_3'; \mathbf{x}_T^S, x_3^S) \right] d\mathbf{x}'_T, \end{aligned} \quad (9.34)$$

and

$$\begin{aligned}
& \check{p}^{\text{sct},u}(\mathbf{x}_T, x_3; \mathbf{x}_T^S, x_3^S) \\
&= \int_{\mathbf{x}_T'' \in \mathbb{R}^2} \left[-\check{G}^{q,b}^*(\mathbf{x}_T, x_3; \mathbf{x}_T'', x_3^R) \check{v}_3^{\text{sct}}(\mathbf{x}_T'', x_3^R; \mathbf{x}_T^S, x_3^S) \right. \\
&\quad \left. + \check{\Gamma}_3^{q,b}^*(\mathbf{x}_T, x_3; \mathbf{x}_T'', x_3^R) \check{p}^{\text{sct}}(\mathbf{x}_T'', x_3^R; \mathbf{x}_T^S, x_3^S) \right] d\mathbf{x}_T''. \quad (9.35)
\end{aligned}$$

The symmetry of the D-t-N operators with respect to a bilinear form is derived in Section (8.7) using Sommerfeld radiation condition. Because Sommerfeld radiation condition does not apply to anti-causal wave fields we need other means to establish symmetry properties for the D-t-N operators with respect to a sesquilinear form. The following radiation condition is used as an ansatz,

$$\check{p}^{\text{sct},d} = 0, \quad \text{in } \mathbb{D}. \quad (9.36)$$

In terms of sesquilinear forms, $[L^2(\mathbb{R}^2)]^1 \times [L^2(\mathbb{R}^2)]^1 \rightarrow \mathbb{C}$, of scalar-valued functions Eq. (9.34) is rewritten as

$$\begin{aligned}
\check{p}^{\text{sct},d}(\mathbf{x}; \mathbf{x}^S) &= \langle \check{G}^{q,b}, \check{v}_3^{\text{sct}} \rangle_s(x'_3; \mathbf{x}, \mathbf{x}^S) - \langle \check{\Gamma}_3^{q,b}, \check{p}^{\text{sct}} \rangle_s(x'_3; \mathbf{x}, \mathbf{x}^S), \\
x_3 < x'_3 &\leq x_3^{\text{sct}}. \quad (9.37)
\end{aligned}$$

Invoking the radiation condition of Eq. (9.36), using Eqs. (8.46) and (9.12), yields

$$\begin{aligned}
\langle \check{G}^{q,b}, \check{\mathcal{Y}}^u \check{p}^{\text{sct}} \rangle_s(x'_3; \mathbf{x}, \mathbf{x}^S) &= \langle -\check{\mathcal{Y}}^d \check{G}^{q,b}, \check{p}^{\text{sct}} \rangle_s(x'_3; \mathbf{x}, \mathbf{x}^S), \\
x_3 < x'_3 &\leq x_3^{\text{sct}}. \quad (9.38)
\end{aligned}$$

One can show that starting from either Eq. (9.36) or Eq. (9.38) we have

$$\begin{aligned}
& \check{p}^{\text{sct},d} = 0 \quad \text{in } \mathbb{D} \\
\iff & \quad \check{\mathcal{Y}}^u \check{p}^{\text{sct}} = -\check{\mathcal{Y}}^d, \quad \text{at all surfaces} \quad x'_3 \in (x_3, x_3^{\text{sct}}]. \quad (9.39)
\end{aligned}$$

In order to find this last relation at $x_3 = x_3^R$ we substitute Eqs. (8.46) and (9.13) into Eq. (9.35), yielding

$$\begin{aligned} \check{p}^{\text{sct},u}(\mathbf{x}_T, x_3; \mathbf{x}_T^S, x_3^S) &= \int_{\mathbf{x}'_T \in \mathbb{R}^2} \left[-\check{G}^{q,b}^*(\mathbf{x}_T, x_3; \mathbf{x}'_T, x_3^R) \check{\mathcal{Y}}^u \check{p}^{\text{sct}}(\mathbf{x}'_T, x_3^R; \mathbf{x}_T^S, x_3^S) \right. \\ &\quad \left. - \check{\mathcal{Y}}^u \check{G}^{q,b}^*(\mathbf{x}_T, x_3; \mathbf{x}'_T, x_3^R) \check{p}^{\text{sct}}(\mathbf{x}'_T, x_3^R; \mathbf{x}_T^S, x_3^S) \right] d\mathbf{x}'_T \\ &\quad x_3^R < x_3. \end{aligned} \quad (9.40)$$

Assuming for the moment that the condition of Eq. (9.39) can be extended to

$$\check{p}^{\text{sct},d} = 0 \quad \text{in } \mathbb{D} \iff \check{\mathcal{Y}}^u \check{p}^{\text{sct},d} = -\check{\mathcal{Y}}^d, \quad \text{at the surface } x_3 = x_3^R. \quad (9.41)$$

Then, using $\check{p}^{\text{sct},d} = 0$ implies $\check{p}^{\text{sct},u} = \check{p}^{\text{sct}}$, Eq. (9.40) becomes

$$\begin{aligned} \check{p}^{\text{sct}}(\mathbf{x}_T, x_3; \mathbf{x}_T^S, x_3^S) &= 2 \int_{\mathbf{x}'_T \in \mathbb{R}^2} d\mathbf{x}'_T \\ &\quad \check{G}^{q,b}^*(\mathbf{x}_T, x_3; \mathbf{x}'_T, x_3^R) (\check{\mathcal{S}}^b)^{-1} \check{p}^{\text{sct}}(\mathbf{x}'_T, x_3^R; \mathbf{x}_T^S, x_3^S), \quad x_3^R < x_3. \end{aligned} \quad (9.42)$$

Taking the limit $x_3 \downarrow x_3^R$ in Eq. (9.42) yields (Colton and Kress (1983)),

$$\begin{aligned} \check{p}^{\text{sct}}(\mathbf{x}_T, x_3^R; \mathbf{x}_T^S, x_3^S) &= 2 \int_{\mathbf{x}'_T \in \mathbb{R}^2} d\mathbf{x}'_T \\ &\quad \check{G}^{q,b}^*(\mathbf{x}_T, x_3; \mathbf{x}'_T, x_3^R) (\check{\mathcal{S}}^b)^{-1} \check{p}^{\text{sct}}(\mathbf{x}'_T, x_3^R; \mathbf{x}_T^S, x_3^S), \end{aligned} \quad (9.43)$$

which, using Eq. (8.41), proves the consistency of Eq. (9.41). Combining Eqs. (9.39) and (9.41) gives, with $\mathbb{D} = \{(\mathbf{x}_T, x_3) | \mathbf{x}_T \in \mathbb{R}^2, x_3^R < x_3 < x_3^{\text{sct}}\}$, and its closure $\bar{\mathbb{D}} = \{(\mathbf{x}_T, x_3) | \mathbf{x}_T \in \mathbb{R}^2, x_3^R \leq x_3 \leq x_3^{\text{sct}}\}$,

$$\check{p}^{\text{sct},d} = 0 \quad \text{in } \mathbb{D} \iff \check{\mathcal{Y}}^u \check{p}^{\text{sct},d} = -\check{\mathcal{Y}}^d \quad \text{in } \bar{\mathbb{D}}. \quad (9.44)$$

Implementing equivalence (9.44) in Eq. (9.33) it follows that the correlation type representation of the scattered wave field is given by a single integral, enforcing uni-directionality with respect to the background medium. In general, the two contributions of Eq. (9.33) make it meaningless to assign a direction to the scattered wave field in \mathbb{D} , in case of correlation type

representations, due to the incompatibility of Sommerfeld radiation conditions to anti-causal wave fields (Bojarski (1983)). This means that Huygens' principle, which states that an infinitesimal change in a wave field can be constructed from infinitesimal contributions from secondary sources along a single surface, is not valid for these representations. The adjointness relation in (9.44) enables to use Huygens' principle such that extrapolation operators can be devised that, when regarded in the time domain, can propagate a wave field back in time. Wapenaar (1992) derives the same radiation condition of Eq. (9.36) for a homogeneous medium.

We have, using the adjoint relations in (9.44),

$$2(\check{\mathcal{S}}^b)^{-1} = \check{\mathcal{Y}}^d - \check{\mathcal{Y}}^u = -\check{\mathcal{Y}}^{u\dagger} + \check{\mathcal{Y}}^{d\dagger} = 2 \left[(\check{\mathcal{S}}^b)^{-1} \right]^\dagger, \quad (9.45)$$

i.e., $(\check{\mathcal{S}}^b)^{-1}$, and consequently $\check{\mathcal{S}}^b$, is self-adjoint. Using Eqs. (7.81), (9.8) and (9.45), Eq. (9.42) is written as

$$\check{p}^{sct}(\mathbf{x}_T, x_3; \mathbf{x}_T^S, x_3^S) = \check{\mathcal{W}}^{b\dagger}(x_3, x'_3) \check{p}^{sct}(\mathbf{x}_T, x'_3; \mathbf{x}_T^S, x_3^S), \quad x_3 > x'_3, \\ \text{if } \check{\mathcal{Y}}^{u\dagger} = -\check{\mathcal{Y}}^d. \quad (9.46)$$

In Berkhout (1985) this last equation is called the matched filter approach. Using a Laplace domain analysis Fokkema and van den Berg (1993) derive that inverse extrapolation is an exact operation without any additional symmetry requirement. Using Eqs. (9.22) and (9.46) we obtain

$$\check{\mathcal{W}}^{q,b\dagger}(x_3, x'_3) = [\check{\mathcal{W}}^{q,b}(x'_3, x_3)]^{-1}, \quad x_3 > x'_3, \quad \text{if } \check{\mathcal{Y}}^{u\dagger} = -\check{\mathcal{Y}}^d. \quad (9.47)$$

9.6 Fundamental solutions

Substituting the D-t-N operators in Eqs. (8.45) and (8.46) into Eqs. (8.6) and (8.11), see Eq. (7.20), yields the following evolution equations for $\hat{p}^{inc} = \hat{p}^{inc}(\mathbf{x}_T, x_3; \mathbf{x}_T^S, x_3^S)$ and $\hat{p}^{sct} = \hat{p}^{sct}(\mathbf{x}_T, x_3; \mathbf{x}_T^S, x_3^S)$,

$$\partial_3 \hat{p}^{inc} + s\rho \hat{\mathcal{Y}}^d \hat{p}^{inc} = 0, \quad \text{for } x_3 \in (x_3^S, x_3^{sct}], \quad (9.48)$$

$$\partial_3 \hat{p}^{sct} + s\rho \hat{\mathcal{Y}}^u \hat{p}^{sct} = 0, \quad \text{for } x_3 \in [x_3^S, x_3^{sct}), \quad (9.49)$$

with initial conditions (see Eqs. (9.5))

$$\hat{p}^{\text{inc}} = \hat{p}^{\text{inc}}(\mathbf{x}_T, x_3^S; \mathbf{x}_T^S, x_3^S), \quad (9.50)$$

$$\hat{p}^{\text{sct}} = \hat{p}^{\text{sct}}(\mathbf{x}_T, x_3^{\text{sct}}; \mathbf{x}_T^S, x_3^S). \quad (9.51)$$

One can show (Haines and de Hoop (1996)), by substitution in Eq. (7.20), that the D-t-N operators $\hat{\mathcal{Y}}^d$ and $\hat{\mathcal{Y}}^u$ in Eqs. (9.48) and (9.49), are solutions of the nonlinear Riccati equation,

$$\partial_3 \hat{\mathcal{Y}} - \hat{\mathcal{Y}} s\rho \hat{\mathcal{Y}} + \frac{1}{s\rho} \hat{\mathcal{H}}_2 = \mathcal{O}, \quad (9.52)$$

with initial conditions,

$$\hat{\mathcal{Y}}^d = \hat{\mathcal{Y}}^d \Big|_{x_3=x_3^{\text{sct}}}, \quad (9.53)$$

$$\hat{\mathcal{Y}}^u = \hat{\mathcal{Y}}^u \Big|_{x_3=x_3^S}, \quad (9.54)$$

and with $\hat{\mathcal{H}}_2$ given in Eq. (7.29). To solve Eqs. (9.48) to (9.51) we follow the fundamental solution approach (Pazy (1983); Krueger and Ochs (1989); Haines and de Hoop (1996); Wapenaar (1996a); Grimbergen et al. (1998)). In order to calculate $\hat{p}^{\text{inc}} = \hat{p}^{\text{inc}}(\mathbf{x}_T, x_3; \mathbf{x}_T^S, x_3^S)$, using Eq. (9.10), we need to obtain the kernel of $\hat{\mathcal{W}}^b(x_3, x_3^S)$ which, from Eq. (9.7), is given in terms of $\hat{G}^{q,b}(\mathbf{x}_T, x_3; \mathbf{x}'_T, x_3^S)$. Using the similarity between the Green's state vector $\hat{\mathbf{F}}^{q,b}$ of Eq. (8.14) and the incident wave field vector $\hat{\mathbf{F}}^{\text{inc}}$ of Eq. (8.6), expressed by Eq. (8.16), and using Eq. (9.13), yields the evolution equation for $\hat{G}^{q,b}(\mathbf{x}_T, x_3; \mathbf{x}'_T, x_3^S)$,

$$\partial_3 \hat{G}^{q,b} - s\rho \hat{\mathcal{Y}}^u \hat{G}^{q,b} = 0, \quad \text{for } x_3 \in (x_3^S, x_3^{\text{sct}}], \quad (9.55)$$

with initial condition, using Eq. (9.5),

$$\hat{G}^{q,b}(\mathbf{x}_T, x_3^S; \mathbf{x}'_T, x_3^S) = \frac{1}{2} \hat{\mathcal{S}}^b \delta(\mathbf{x}_T - \mathbf{x}'_T). \quad (9.56)$$

The D-t-N operator \mathcal{Y}^u in Eq. (9.55) is obtained by solving Eq. (9.52) with the initial condition of Eq. (9.54). Hence, $\hat{G}^{q,b}(\mathbf{x}_T, x_3; \mathbf{x}'_T, x_3^S)$ and \mathcal{Y}^u are solved downward from x_3^S . In order to calculate $\hat{p}^{\text{sct}} = \hat{p}^{\text{sct}}(\mathbf{x}_T, x_3; \mathbf{x}_T^S, x_3^S)$, using Eq. (9.22), we need to obtain the kernel of $\hat{\mathcal{W}}^b(x_3, x_3^{\text{sct}})$ which, from Eq.

(9.21), is given in terms of $\hat{G}^{q,b}(\mathbf{x}_T, x_3; \mathbf{x}'_T, x_3^{sct})$. Using (9.12) the evolution equation for $\hat{G}^{q,b}(\mathbf{x}_T, x_3; \mathbf{x}'_T, x_3^{sct})$ is given by,

$$\partial_3 \hat{G}^{q,b} - s\rho \hat{\mathcal{Y}}^d \hat{G}^{q,b} = 0, \quad \text{for } x_3 \in [x_3^S, x_3^{sct}), \quad (9.57)$$

with initial condition, using Eq. (9.5),

$$\hat{G}^{q,b}(\mathbf{x}_T, x_3^{sct}; \mathbf{x}'_T, x_3^{sct}) = \frac{1}{2} \hat{\mathcal{S}}^b \delta(\mathbf{x}_T - \mathbf{x}'_T). \quad (9.58)$$

The D-t-N operator \mathcal{Y}^d in Eq. (9.57) is obtained by solving Eq. (9.52) with the initial condition of Eq. (9.53). Hence, $\hat{G}^{q,b}(\mathbf{x}_T, x_3; \mathbf{x}'_T, x_3^{sct})$ and \mathcal{Y}^d are solved upward from x_3^{sct} .

9.7 Longitudinal invariance

Consider the subdomain $\mathbb{D}^i \subset \mathbb{D}$, with $\mathbb{D} = \{(\mathbf{x}_T, x_3) | \mathbf{x}_T \in \mathbb{R}^2, x_3^S < x_3 < x_3^{sct}\}$ and $\mathbb{D}^i = \{(\mathbf{x}_T, x_3) | \mathbf{x}_T \in \mathbb{R}^2, x_3^i < x_3 < x_3^{i+1}\}$. In \mathbb{D}^i the medium parameters are assumed to be invariant with respect to the longitudinal x_3 -coordinate. Then, implementing longitudinal-invariance into the Riccati equation (9.52) yields

$$\hat{\mathcal{Y}} s\rho \hat{\mathcal{Y}} - \frac{1}{s\rho} \hat{\mathcal{H}}_2 = 0, \quad \text{in } \mathbb{D}^i. \quad (9.59)$$

From this last equation we take the following solutions

$$\hat{\mathcal{Y}}^d = \hat{\mathcal{Y}}^i, \quad \text{in } \mathbb{D}^i, \quad (9.60)$$

$$\hat{\mathcal{Y}}^u = -\hat{\mathcal{Y}}^i, \quad \text{in } \mathbb{D}^i, \quad (9.61)$$

with

$$\hat{\mathcal{Y}}^i = (s\rho)^{-1} \hat{\mathcal{H}}_1, \quad (9.62)$$

in which the symmetric pseudo-differential operator $\hat{\mathcal{H}}_1$ ($\hat{\mathcal{Y}}^i$ is symmetric) is given by

$$\hat{\mathcal{H}}_2 = \hat{\mathcal{H}}_1 \hat{\mathcal{H}}_1, \quad \text{with} \quad \text{Re}(\lambda) > 0, \quad \forall \lambda \in \sigma(\hat{\mathcal{H}}_1), \quad (9.63)$$

in which $\sigma(\hat{\mathcal{H}}_1)$ designates the spectrum of $\hat{\mathcal{H}}_1$. It follows from Eqs. (8.47) and (8.48) that longitudinal-invariance implies $\hat{\mathcal{D}}^b = \mathcal{O}$, and therefore

$$\hat{\mathcal{Y}}^i = \left(\hat{\mathcal{S}}^b \right)^{-1}. \quad (9.64)$$

Implementing longitudinal-invariance the evolution equation (9.55) for $\hat{G}^{q,b} = \hat{G}^{q,b}(\mathbf{x}_T, x_3; \mathbf{x}'_T, x_3^i)$ becomes,

$$\partial_3 \hat{G}^{q,b} + \mathcal{H}_1 \hat{G}^{q,b} = 0, \quad \text{for } x_3 \in (x_3^i, x_3^{i+1}], \quad (9.65)$$

whereas, the evolution equation (9.57) for $\hat{G}^{q,b} = \hat{G}^{q,b}(\mathbf{x}_T, x_3; \mathbf{x}'_T, x_3^{i+1})$ becomes,

$$\partial_3 \hat{G}^{q,b} - \mathcal{H}_1 \hat{G}^{q,b} = 0, \quad \text{for } x_3 \in [x_3^i, x_3^{i+1}), \quad (9.66)$$

The respective initial conditions, using Eq. (9.16), are given by

$$\hat{G}^{q,b}(\mathbf{x}_T, x_3^i; \mathbf{x}'_T, x_3^i) = \left(2\hat{\mathcal{Y}}^i \right)^{-1} \delta(\mathbf{x}_T - \mathbf{x}'_T), \quad (9.67)$$

$$\hat{G}^{q,b}(\mathbf{x}_T, x_3^{i+1}; \mathbf{x}'_T, x_3^{i+1}) = \left(2\hat{\mathcal{Y}}^i \right)^{-1} \delta(\mathbf{x}_T - \mathbf{x}'_T). \quad (9.68)$$

For a x_3 -invariant medium the n th derivative of $\hat{G}^{q,b}$ of Eq. (9.65) with respect to the x_3 -coordinate is given by

$$\partial_3^{(n)} \hat{G}^{q,b} = (-1)^n \left(\hat{\mathcal{H}}_1 \right)^n \hat{G}^{q,b}. \quad (9.69)$$

A Taylor expansion gives

$$\begin{aligned} \hat{G}^{q,b}(\mathbf{x}_T, x_3; \mathbf{x}'_T, x_3^i) \\ = \sum_{k=0}^{\infty} (-1)^k \frac{(x_3 - x_3^i)^k}{k!} \left(\hat{\mathcal{H}}_1 \right)^k \left(2\hat{\mathcal{Y}}^i \right)^{-1} \delta(\mathbf{x}_T - \mathbf{x}'_T), \end{aligned} \quad (9.70)$$

which yields the following solution

$$\hat{G}^{q,b}(\mathbf{x}_T, x_3; \mathbf{x}'_T, x_3^i) = \exp \left[- (x_3 - x_3^i) \hat{\mathcal{H}}_1 \right] \left(2\hat{\mathcal{Y}}^i \right)^{-1} \delta(\mathbf{x}_T - \mathbf{x}'_T). \quad (9.71)$$

Analogously, one can show that

$$\hat{G}^{q,b}(\mathbf{x}_T, x_3; \mathbf{x}'_T, x_3^{i+1}) = \exp \left[- (x_3^{i+1} - x_3) \hat{\mathcal{H}}_1 \right] \left(2\hat{\mathcal{Y}}^i \right)^{-1} \delta(\mathbf{x}_T - \mathbf{x}'_T). \quad (9.72)$$

Substitution of Eq. (9.71) into Eq. (9.14), using Eq. (9.64), yields

$$\hat{\mathcal{W}}^{q,b}(x_3^i, x_3) = \exp \left[- (x_3 - x_3^i) \hat{\mathcal{H}}_1 \right], \quad x_3^i \leq x_3 \leq x_3^{i+1}. \quad (9.73)$$

Substitution of Eq. (9.72) into Eq. (9.21), using Eq. (9.64), gives

$$\hat{\mathcal{W}}^{q,b}(x_3, x_3^{i+1}) = \exp \left[- (x_3^{i+1} - x_3) \hat{\mathcal{H}}_1 \right]. \quad x_3^i \leq x_3 \leq x_3^{i+1}. \quad (9.74)$$

Eq. (7.29) shows that, by taking the limit $\text{Re}(s) \downarrow 0$, the partial differential operator $\hat{\mathcal{H}}_2$ is a real operator. Hence, the square-root operator $\check{\mathcal{H}}_1$ is, evaluated in the real-frequency domain, either real or purely imaginary. Eqs. (9.73) and (9.74) show that with imaginary $\check{\mathcal{H}}_1$ one associates propagating waves, whereas real $\check{\mathcal{H}}_1$ describes exponentially decaying waves, or so-called evanescent waves. The exponential decrease is ensured by $\text{Re}(\lambda) > 0, \forall \lambda \in \sigma(\hat{\mathcal{H}}_1)$. From Eqs. (9.74) it follows that the adjoint extrapolation operator is a stable operator, whereas the inverse extrapolation operator increases exponentially in the extrapolation direction, in the evanescent region. Hence, for x_3 -invariant media, the adjoint operator equals the inverse operator for the propagating wave field, whereas, as an inverse extrapolator its erroneous for the evanescent wave field. Substituting the D-t-N operators of Eqs. (9.60) and (9.61) for longitudinal invariant media, into the transmission and reflection operators of Eqs. (8.68) and (8.73), yields

$$\hat{\mathcal{T}}^d = 2 \left(\hat{\mathcal{Y}} + \hat{\mathcal{Y}}^i \right)^{-1} \hat{\mathcal{Y}}^i, \quad (9.75)$$

and

$$\hat{\mathcal{R}}^d = \left(\hat{\mathcal{Y}} + \hat{\mathcal{Y}}^i \right)^{-1} \left(\hat{\mathcal{Y}}^i - \hat{\mathcal{Y}} \right), \quad (9.76)$$

which represent the transmission and reflection operators, respectively, for depth-invariant media at either side of the scattering surface. .

Chapter 10

Acoustic time-lapse interaction

In this chapter the interaction integral of the convolution type \hat{I}^{conv} of Eq. (6.31) is investigated. Regarding it as a bilinear form, its associated matrix operator, in terms of D-t-N operators with respect to the reference and monitor background media, is first normalised to a symplectic operator. Assuming identical D-t-N operators for the two time-lapse cases, one obtains an alternating form for \hat{I}^{conv} , associated with a skew-symmetric or alternating operator. For a general time-lapse configuration, i.e. for contrasting D-t-N operators with respect to the background media, the symplectic matrix operator can be transformed to an alternating form, using a symplectic eigenvalue decomposition, yielding a symplectic eigenvalue operator, which parameterises both the reference and monitor background media. The resulting cancellation of the temporal contrast in D-t-N operators explains the absence of difference reflections in \hat{I}^{conv} of Figs. (6.4) and (6.5), above the interaction depth, as compared to the difference wave field of Fig. (6.3). The alternating form of \hat{I}^{conv} after the transformation, obtained from the symplectic eigenvalue decomposition of its operator, enables to introduce a difference reflection operator, which is used in an imaging scheme.

10.1 Interaction operator

Taking the same time-lapse configuration as described in Fig. (6.1) we consider the domains \mathbb{D}^u and \mathbb{D}^l , divided by the the surface $\partial\mathbb{D}^l$. In the following analysis, instead of the scalar wave field equations (6.1) to (6.4) used in Chapter 6, the wave field vector equation (see Eq. (7.26)) is used. The wave

field which acts as a reference wave field is governed by the wave field vector equation,

$$\partial_3 \hat{\mathbf{F}}^{(1)}(\mathbf{x}; \mathbf{x}^R, s) + \hat{\mathbf{A}}^{(1)} \hat{\mathbf{F}}^{(1)}(\mathbf{x}; \mathbf{x}^R, s) = \hat{\mathbf{N}}^{(1)}(\mathbf{x}; \mathbf{x}^R, s), \quad (10.1)$$

with source vector

$$\hat{\mathbf{N}}^{(1)}(\mathbf{x}; \mathbf{x}^R, s) = \begin{pmatrix} 0 \\ \hat{q}^{(1)}(s) \delta(\mathbf{x} - \mathbf{x}^R) \end{pmatrix}, \quad \mathbf{x} \in \mathbb{R}^3, \mathbf{x}^R \in \mathbb{D}^u. \quad (10.2)$$

The wave field of the monitor state is governed by the wave field vector equation

$$\partial_3 \hat{\mathbf{F}}^{(2)}(\mathbf{x}; \mathbf{x}^S, s) + \hat{\mathbf{A}}^{(2)} \hat{\mathbf{F}}^{(2)}(\mathbf{x}; \mathbf{x}^S, s) = \hat{\mathbf{N}}^{(2)}(\mathbf{x}; \mathbf{x}^S, s), \quad (10.3)$$

with source vector

$$\hat{\mathbf{N}}^{(2)}(\mathbf{x}; \mathbf{x}^S, s) = \begin{pmatrix} 0 \\ \hat{q}^{(2)}(s) \delta(\mathbf{x} - \mathbf{x}^S) \end{pmatrix}, \quad \mathbf{x} \in \mathbb{R}^3, \mathbf{x}^S \in \mathbb{D}^u. \quad (10.4)$$

Both the reference as well as the monitor source are located inside \mathbb{D}^u . In the further analysis, see Figs. (6.1) and (8.1), we take $x_3^{\text{sct}} = x_3^{\text{tl}}$, and hence, $\mathbb{D}^{\text{sct}'} = \mathbb{D}^u$ and $\mathbb{D}^{\text{sct}} = \mathbb{D}^l$. Consider the domain $\mathbb{D} = \{(\mathbf{x}_T, x_3) | \mathbf{x}_T \in \mathbb{R}^2, x_3^R = x_3^S < x_3 \leq x_3^{\text{tl}}\}$. We introduce, in \mathbb{D} , according to Eq. (8.49), the following decomposition operations,

$$\hat{\mathbf{F}}^{(1)} = \hat{\mathbf{T}}^{b,(1)} \hat{\mathbf{P}}^{b,(1)}, \quad \text{in } \mathbb{D}, \quad (10.5)$$

$$\hat{\mathbf{F}}^{(2)} = \hat{\mathbf{T}}^{b,(2)} \hat{\mathbf{P}}^{b,(2)}, \quad \text{in } \mathbb{D}, \quad (10.6)$$

with the wave field composition matrices of operators given by

$$\hat{\mathbf{T}}^{b,(1)} = \begin{pmatrix} \mathcal{I} & \mathcal{I} \\ \hat{\mathcal{Y}}^{d,(1)} & \hat{\mathcal{Y}}^{u,(1)} \end{pmatrix} \quad \text{and} \quad \hat{\mathbf{T}}^{b,(2)} = \begin{pmatrix} \mathcal{I} & \mathcal{I} \\ \hat{\mathcal{Y}}^{d,(2)} & \hat{\mathcal{Y}}^{u,(2)} \end{pmatrix}, \quad (10.7)$$

in which the D-t-N operators are given, according to Eqs. (8.47) and (8.48), in terms of single- and double-layer potential operators. Implementing the wave field decompositions, the interaction quantity of the convolution type \hat{I}^{conv} , which at $\partial\mathbb{D}^{\text{tl}}$ is given by Eq. (6.31), in \mathbb{D} , expressed as a bilinear form according to Eq. (7.53), yields

$$\left[\hat{I}^{\text{conv}} \left(\hat{\mathbf{F}}^{(1)}, \hat{\mathbf{F}}^{(2)} \right) \right] (x_3^{\text{tl}}; \mathbf{x}^R, \mathbf{x}^S) = \left\langle \hat{\mathbf{P}}^{b,(1)}, \hat{\mathbf{Y}}^{b,(1,2)} \hat{\mathbf{P}}^{b,(2)} \right\rangle_b (x_3; \mathbf{x}^R, \mathbf{x}^S), \quad \text{in } \mathbb{D} \quad (10.8)$$

with the interaction matrix of operators $\hat{Y}^{b,(1,2)}$ given by

$$\hat{Y}^{b,(1,2)} = \left(\hat{T}^{b,(1)} \right)^t J \hat{T}^{b,(2)} = \begin{pmatrix} \hat{Y}^{d,(2)} - \hat{Y}^{d,(1)} & \hat{Y}^{u,(2)} - \hat{Y}^{d,(1)} \\ \hat{Y}^{d,(2)} - \hat{Y}^{u,(1)} & \hat{Y}^{u,(2)} - \hat{Y}^{u,(1)} \end{pmatrix}. \quad (10.9)$$

In this last equation we used the symmetries of the pertaining Dirichlet-to-Neumann operators derived in Section 8.7. Next, consider the case

$$\left\{ \hat{Y}^{d,(1)}, \hat{Y}^{u,(1)} \right\} = \left\{ \hat{Y}^{d,(2)}, \hat{Y}^{u,(2)} \right\} = \left\{ \hat{Y}^d, \hat{Y}^u \right\} \quad \text{in } \mathbb{D}. \quad (10.10)$$

If there is absence of temporal contrasts in \mathbb{D} we obtain the stronger condition

$$\left\{ \rho^{(1)}, \kappa^{(1)} \right\} = \left\{ \rho^{(2)}, \kappa^{(2)} \right\} \quad \text{in } \mathbb{D}, \quad (10.11)$$

which implies the condition of Eq. (10.10). The weaker condition of Eq. (10.10) is exploited in the further analysis. Implementing the latter condition, using Eq. (8.53), $\hat{Y}^{b,(1,2)}$ of Eq. (10.9) becomes

$$\begin{aligned} \hat{Y}^{b,(1,2)} \Big|_{\left\{ \hat{Y}^{d,(1)}, \hat{Y}^{u,(1)} \right\} = \left\{ \hat{Y}^{d,(2)}, \hat{Y}^{u,(2)} \right\}} &= \hat{Y}^b \\ &= \left(\hat{T}^b \right)^t J \hat{T}^b = \begin{pmatrix} \mathcal{O} & -2 \left(\hat{\mathcal{S}}^b \right)^{-1} \\ 2 \left(\hat{\mathcal{S}}^b \right)^{-1} & \mathcal{O} \end{pmatrix}, \end{aligned} \quad (10.12)$$

in which we introduced the operator \hat{Y}^b , and \hat{T}^b is given in Eq. (8.51). We have according to Eqs. (6.7) and (6.30),

$$\begin{aligned} \left[\hat{I}^{\text{conv}} \left(\hat{\mathbf{F}}^{(1)}, \hat{\mathbf{F}}^{(2)} \right) \right] \left(x_3^{\text{tl}}, \mathbf{x}^R, \mathbf{x}^S \right) \Big|_{\left\{ \rho^{(1)}, \kappa^{(1)} \right\} = \left\{ \rho^{(2)}, \kappa^{(2)} \right\}} \\ = \hat{q}^{(1)} \hat{p}^{(2)} \left(\mathbf{x}^R; \mathbf{x}^S \right) - \hat{q}^{(2)} \hat{p}^{(1)} \left(\mathbf{x}^R; \mathbf{x}^S \right). \end{aligned} \quad (10.13)$$

Hence, given the strong condition of Eq. (10.11), which states that there are no temporal contrasts in the density and the compressibility above the interaction depth $\partial\mathbb{D}^{\text{tl}}$, \hat{I}^{conv} becomes, because Eq. (10.11) implies Eq. (10.10), an alternating form (Eq. (10.12)), equivalent to a difference wave field evaluated at the recording depth (Eq. (10.13)). In Chapter 6 we derived, according to Eq. (6.37), that, in general, \hat{I}^{conv} is equivalent to an up-going difference wave field which has no temporal contrast sources above the interaction depth (Eqs. (6.21) to (6.24)). However, according to Eq. (10.9), $\hat{Y}^{b,(1,2)}$ is, in

general, not alternating. The appearance of \hat{J}^{conv} in Fig. (6.10), as compared to the difference wave fields in Figs. (6.8) and (6.9), suggests that $\hat{Y}^{\text{b},(1,2)}$ can be expressed in alternating form, exploiting the weak condition of Eq. (10.10), using an symplectic eigenvalue decomposition (Abraham and Marsden (1978)). This decomposition requires that $\hat{Y}^{\text{b},(1,2)}$ is symplectic, which it is not, i.e.

$$\left(\hat{Y}^{\text{b},(1,2)}\right)^t J + J\hat{Y}^{\text{b},(1,2)} \neq 0. \quad (10.14)$$

In order to have $\hat{Y}^{\text{b},(1,2)}$ in symplectic form we use the ansatz

$$\left(\hat{D}^{\text{b}}\right)^t \hat{Y}^{\text{b}} \hat{D}^{\text{b}} = \hat{Y}^{\text{b}}. \quad (10.15)$$

This last equation represents a similarity transformation to \hat{Y}^{b} of Eq. (10.12), with \hat{D}^{b} given later. This transformation yields the following normalisation

$$\hat{Y}^{\text{b}} = \left(\hat{T}_n^{\text{b}}\right)^t J \hat{T}_n^{\text{b}} \quad \text{and} \quad \hat{T}_n^{\text{b}} = \hat{T}^{\text{b}} \hat{D}^{\text{b}}. \quad (10.16)$$

To obtain the normalised operators we write the wave field composition matrix operator \hat{T}^{b} of Eq. (8.51), using Eqs. (8.47) and (8.48), in terms of the single- and double-layer potential operators of Eqs. (8.41) and (8.42), as

$$\hat{T}^{\text{b}} = \begin{pmatrix} \mathcal{I} & \mathcal{I} \\ \left(\hat{S}^{\text{b}}\right)^{-1} \left(\mathcal{I} - \hat{D}^{\text{b}}\right) & -\left(\hat{S}^{\text{b}}\right)^{-1} \left(\mathcal{I} + \hat{D}^{\text{b}}\right) \end{pmatrix}. \quad (10.17)$$

Taking for the transformation matrix operator

$$\hat{D}^{\text{b}} = \begin{pmatrix} \mathcal{I} + \frac{1}{2} \hat{D}^{\text{b}} & \frac{1}{2} \hat{D}^{\text{b}} \\ -\frac{1}{2} \hat{D}^{\text{b}} & \mathcal{I} - \frac{1}{2} \hat{D}^{\text{b}} \end{pmatrix}, \quad (10.18)$$

the normalised composition operator is given by

$$\hat{T}_n^{\text{b}} = \begin{pmatrix} \mathcal{I} & \mathcal{I} \\ \left(\hat{S}^{\text{b}}\right)^{-1} & -\left(\hat{S}^{\text{b}}\right)^{-1} \end{pmatrix}. \quad (10.19)$$

Due to the symmetries of \hat{Y}^{d} and \hat{Y}^{u} , Eqs. (8.80) and (8.87), respectively, the difference of these operators, $(\hat{S}^{\text{b}})^{-1}$, is symmetric (Eq. (8.88)). Hence,

according to Eqs. (8.47) and (8.48), $(\hat{\mathcal{S}}^b)^{-1}\hat{\mathcal{D}}^b$, is also symmetric, which result is necessary for the transformation of Eq. (10.15) to be valid. Observe that $\hat{\mathbf{T}}_n^b$ does not contain the double-layer potential boundary integral operator $\hat{\mathcal{D}}^b$ of Eq. (8.42), whereas, $\hat{\mathbf{T}}^b$ of Eq. (10.17) does. In fact,

$$\hat{\mathbf{T}}_n^b = \hat{\mathbf{T}}^b \quad \text{when} \quad \hat{\mathcal{D}}^b = \mathcal{O}. \quad (10.20)$$

Observe that for longitudinal-invariance, for which Eqs. (9.60) and (9.61) are valid, we also have $\hat{\mathcal{D}}^b = \mathcal{O}$. Hence, the normalisation induces a symmetry with respect to the longitudinal direction. Defining,

$$\hat{\mathcal{Y}}^b \stackrel{\text{def}}{=} \left(\hat{\mathcal{S}}^b \right)^{-1}, \quad (10.21)$$

the interaction operator of Eq. (10.12), for which the background reference and monitor D-t-N operators are equal, is written as

$$\hat{\mathbf{Y}}^b = \begin{pmatrix} \mathcal{O} & -2\hat{\mathcal{Y}}^b \\ 2\hat{\mathcal{Y}}^b & \mathcal{O} \end{pmatrix}. \quad (10.22)$$

The normalised composition operator of Eq. (10.19) is written as

$$\hat{\mathbf{T}}_n^b = \begin{pmatrix} \mathcal{I} & \mathcal{I} \\ \hat{\mathcal{Y}}^b & -\hat{\mathcal{Y}}^b \end{pmatrix}. \quad (10.23)$$

Likewise, we define

$$\hat{\mathcal{Y}}^{b,(1)} \stackrel{\text{def}}{=} \left(\hat{\mathcal{S}}^{b,(1)} \right)^{-1}, \quad (10.24)$$

$$\hat{\mathcal{Y}}^{b,(2)} \stackrel{\text{def}}{=} \left(\hat{\mathcal{S}}^{b,(2)} \right)^{-1}. \quad (10.25)$$

Using the normalisation of Eq. (10.16), we obtain the following normalised wave field composition matrices

$$\hat{\mathbf{T}}_n^{b,(1)} = \begin{pmatrix} \mathcal{I} & \mathcal{I} \\ \hat{\mathcal{Y}}^{b,(1)} & -\hat{\mathcal{Y}}^{b,(1)} \end{pmatrix} \quad (10.26)$$

and

$$\hat{\mathbf{T}}_n^{b,(2)} = \begin{pmatrix} \mathcal{I} & \mathcal{I} \\ \hat{\mathcal{Y}}^{b,(2)} & -\hat{\mathcal{Y}}^{b,(2)} \end{pmatrix}. \quad (10.27)$$

In terms of these latter two matrices the wave field composition operations of Eqs. (10.5) and (10.6) transform to

$$\hat{\mathbf{F}}^{(1)} = \hat{\mathbf{T}}_n^{b,(1)} \hat{\mathbf{P}}_n^{b,(1)}, \quad \text{at} \quad \partial\mathbb{D}^{\text{tl}}, \quad (10.28)$$

$$\hat{\mathbf{F}}^{(2)} = \hat{\mathbf{T}}_n^{b,(2)} \hat{\mathbf{P}}_n^{b,(2)}, \quad \text{at} \quad \partial\mathbb{D}^{\text{tl}}, \quad (10.29)$$

in which $\hat{\mathbf{P}}_n^{b,(1)}$ and $\hat{\mathbf{P}}_n^{b,(2)}$ are the reference and monitor normalised wave fields components vectors. Implementation of the wave field composition matrices of Eqs. (10.26) and (10.27) into the interaction quantity of the time-convolution type \hat{I}^{conv} of Eq. (10.8), in \mathbb{D} , yields

$$\hat{I}^{\text{conv}} \left(\hat{\mathbf{F}}^{(1)}, \hat{\mathbf{F}}^{(2)} \right) = \left\langle \hat{\mathbf{P}}_n^{b,(1)}, \hat{Y}_n^{b,(1,2)} \hat{\mathbf{P}}_n^{b,(2)} \right\rangle_b \quad \text{in} \quad \mathbb{D}, \quad (10.30)$$

with the normalised interaction matrix of operators $\hat{Y}_n^{b,(1,2)}$ given by

$$\hat{Y}_n^{b,(1,2)} = \left(\hat{\mathbf{T}}_n^{b,(1)} \right)^t \mathbf{J} \hat{\mathbf{T}}_n^{b,(2)} = \begin{pmatrix} \hat{Y}^{b,(2)} - \hat{Y}^{b,(1)} & -\hat{Y}^{b,(2)} - \hat{Y}^{b,(1)} \\ \hat{Y}^{b,(2)} + \hat{Y}^{b,(1)} & -\hat{Y}^{b,(2)} + \hat{Y}^{b,(1)} \end{pmatrix}. \quad (10.31)$$

In contradistinction to $\hat{Y}_n^{b,(1,2)}$ of Eq. (10.9) the normalised operator $\hat{Y}_n^{b,(1,2)}$ has the desired symplectic property, i.e.

$$\left(\hat{Y}_n^{b,(1,2)} \right)^t \mathbf{J} + \mathbf{J} \hat{Y}_n^{b,(1,2)} = \mathbf{O}. \quad (10.32)$$

10.2 Symplectic eigenvalue decomposition

We investigate the eigenvalue decomposition of $\hat{Y}_n^{b,(1,2)}$ of Eq. (10.31). we consider the following eigenvector equations,

$$\hat{Y}_n^{b,(1,2)} \hat{\mathbf{Q}}_1 = 2j \hat{\mathbf{Q}}_1 \hat{\mathcal{Y}}^{\text{tl}}, \quad (10.33)$$

$$\hat{Y}_n^{b,(1,2)} \hat{\mathbf{Q}}_2 = -2j \hat{\mathbf{Q}}_2 \hat{\mathcal{Y}}^{\text{tl}}, \quad (10.34)$$

with eigenvalue operators $\pm 2j \hat{\mathcal{Y}}^{\text{tl}}$, and with eigenvectors

$$\hat{\mathbf{Q}}_1 = \begin{pmatrix} \hat{\mathcal{Q}}_{11} \\ \hat{\mathcal{Q}}_{21} \end{pmatrix} \quad \text{and} \quad \hat{\mathbf{Q}}_2 = \begin{pmatrix} \hat{\mathcal{Q}}_{12} \\ \hat{\mathcal{Q}}_{22} \end{pmatrix}. \quad (10.35)$$

Using Eq. (10.31), Eq. (10.33) is written as

$$\left(\hat{\mathcal{Y}}^{b,(2)} - \hat{\mathcal{Y}}^{b,(1)}\right)\hat{\mathcal{Q}}_{11} - \left(\hat{\mathcal{Y}}^{b,(2)} + \hat{\mathcal{Y}}^{b,(1)}\right)\hat{\mathcal{Q}}_{21} = 2j\hat{\mathcal{Q}}_{11}\hat{\mathcal{Y}}^{tl}, \quad (10.36)$$

$$\left(\hat{\mathcal{Y}}^{b,(2)} + \hat{\mathcal{Y}}^{b,(1)}\right)\hat{\mathcal{Q}}_{11} - \left(\hat{\mathcal{Y}}^{b,(2)} - \hat{\mathcal{Y}}^{b,(1)}\right)\hat{\mathcal{Q}}_{21} = 2j\hat{\mathcal{Q}}_{21}\hat{\mathcal{Y}}^{tl}. \quad (10.37)$$

Adding the last two equations gives

$$\hat{\mathcal{Y}}^{b,(2)}\left(\hat{\mathcal{Q}}_{11} - \hat{\mathcal{Q}}_{21}\right) = j\left(\hat{\mathcal{Q}}_{11} + \hat{\mathcal{Q}}_{21}\right)\hat{\mathcal{Y}}^{tl}. \quad (10.38)$$

Taking the normalisation

$$\hat{\mathcal{Q}}_{11} + \hat{\mathcal{Q}}_{21} = \mathcal{I}, \quad (10.39)$$

we obtain for the first eigenvector

$$\hat{\mathbf{Q}}_1 = \frac{1}{2} \begin{pmatrix} \mathcal{I} + j\left(\hat{\mathcal{Y}}^{b,(2)}\right)^{-1}\hat{\mathcal{Y}}^{tl} \\ \mathcal{I} - j\left(\hat{\mathcal{Y}}^{b,(2)}\right)^{-1}\hat{\mathcal{Y}}^{tl} \end{pmatrix}, \quad (10.40)$$

Alternatively, subtracting Eq. (10.37) from Eq. (10.36) and applying the normalisation of Eq. (10.39) yields

$$\hat{\mathbf{Q}}_1 = \frac{1}{2} \begin{pmatrix} \mathcal{I} + j\hat{\mathcal{Y}}^{b,(1)}\left(\hat{\mathcal{Y}}^{tl}\right)^{-1} \\ \mathcal{I} - j\hat{\mathcal{Y}}^{b,(1)}\left(\hat{\mathcal{Y}}^{tl}\right)^{-1} \end{pmatrix}. \quad (10.41)$$

Hence, we obtain

$$\left(\hat{\mathcal{Y}}^{b,(2)}\right)^{-1}\hat{\mathcal{Y}}^{tl} = \hat{\mathcal{Y}}^{b,(1)}\left(\hat{\mathcal{Y}}^{tl}\right)^{-1}. \quad (10.42)$$

This last result is needed later. This last equation also yields

$$\hat{\mathcal{Y}}^{tl}\hat{\mathcal{Y}}^{tl} = \hat{\mathcal{Y}}^{b,(2)}\hat{\mathcal{Y}}^{b,(1)}. \quad (10.43)$$

Hence, we obtain a square-root operator written as

$$\hat{\mathcal{Y}}^{tl} = \left(\hat{\mathcal{Y}}^{b,(2)}\hat{\mathcal{Y}}^{b,(1)}\right)^{\frac{1}{2}}. \quad (10.44)$$

Following the same procedure for Eq. (10.34), and taking the normalisation

$$\hat{Q}_{12} + \hat{Q}_{22} = \mathcal{I}, \quad (10.45)$$

yields for the second eigenvector

$$\hat{Q}_2 = \frac{1}{2} \begin{pmatrix} \mathcal{I} - j \left(\hat{\mathcal{Y}}^{b,(2)} \right)^{-1} \hat{\mathcal{Y}}^{tl} \\ \mathcal{I} + j \left(\hat{\mathcal{Y}}^{b,(2)} \right)^{-1} \hat{\mathcal{Y}}^{tl} \end{pmatrix}. \quad (10.46)$$

If, instead of the eigenvector Eq. (10.33) we use the following equation,

$$\hat{Y}_n^{b,(1,2)} \hat{Q}'_1 = 2j \hat{\mathcal{Y}}^{tl} \hat{Q}'_1. \quad (10.47)$$

Then, we obtain instead of Eq. (10.36) and (10.37),

$$\left(\hat{\mathcal{Y}}^{b,(2)} - \hat{\mathcal{Y}}^{b,(1)} \right) \hat{Q}'_{11} - \left(\hat{\mathcal{Y}}^{b,(2)} + \hat{\mathcal{Y}}^{b,(1)} \right) \hat{Q}'_{21} = 2j \hat{\mathcal{Y}}^{tl} \hat{Q}'_{11}, \quad (10.48)$$

$$\left(\hat{\mathcal{Y}}^{b,(2)} + \hat{\mathcal{Y}}^{b,(1)} \right) \hat{Q}'_{11} - \left(\hat{\mathcal{Y}}^{b,(2)} - \hat{\mathcal{Y}}^{b,(1)} \right) \hat{Q}'_{21} = 2j \hat{\mathcal{Y}}^{tl} \hat{Q}'_{21}. \quad (10.49)$$

Adding the last two equations gives

$$\hat{\mathcal{Y}}^{b,(2)} \left(\hat{Q}'_{11} - \hat{Q}'_{21} \right) = j \hat{\mathcal{Y}}^{tl} \left(\hat{Q}'_{11} + \hat{Q}'_{21} \right). \quad (10.50)$$

Application of the normalisation $\hat{Q}'_{11} + \hat{Q}'_{21} = \mathcal{I}$, similar to Eq. (10.39), yields

$$\hat{Q}'_1 = \begin{pmatrix} \hat{Q}'_{11} \\ \hat{Q}'_{21} \end{pmatrix} = \frac{1}{2} \begin{pmatrix} \mathcal{I} + j \left(\hat{\mathcal{Y}}^{b,(2)} \right)^{-1} \hat{\mathcal{Y}}^{tl} \\ \mathcal{I} - j \left(\hat{\mathcal{Y}}^{b,(2)} \right)^{-1} \hat{\mathcal{Y}}^{tl} \end{pmatrix}. \quad (10.51)$$

Hence, \hat{Q}'_1 equals \hat{Q}_1 of Eq. (10.40), yielding the commutation relation

$$\hat{\mathcal{Y}}^{tl} \left(\hat{\mathcal{Y}}^{b,(2)} \right)^{-1} = \left(\hat{\mathcal{Y}}^{b,(2)} \right)^{-1} \hat{\mathcal{Y}}^{tl}. \quad (10.52)$$

Also, subtracting Eq. (10.49) from Eq. (10.48), using the normalisation $\hat{Q}'_{11} + \hat{Q}'_{21} = \mathcal{I}$, and using the fact that \hat{Q}'_1 equals \hat{Q}_1 yields

$$\left(\hat{\mathcal{Y}}^{tl} \right)^{-1} \hat{\mathcal{Y}}^{b,(1)} = \hat{\mathcal{Y}}^{b,(1)} \left(\hat{\mathcal{Y}}^{tl} \right)^{-1}. \quad (10.53)$$

Using Eqs. (10.33), (10.34), (10.40) and (10.46) we obtain the following eigenvalue decomposition of $\hat{Y}_n^{b,(1,2)}$,

$$\hat{Y}_n^{b,(1,2)} \hat{Q} = \hat{Q} \hat{Y}. \quad (10.54)$$

The eigenvalue matrix \hat{Y} is given by

$$\hat{Y} = \begin{pmatrix} 2j\hat{\mathcal{Y}}^{tl} & \mathcal{O} \\ \mathcal{O} & -2j\hat{\mathcal{Y}}^{tl} \end{pmatrix}, \quad (10.55)$$

with the operator $\hat{\mathcal{Y}}^{tl}$ given in (10.44). The eigenvector matrix \hat{Q} is given by

$$\hat{Q} = \frac{1}{2} \begin{pmatrix} \mathcal{I} + j \left(\hat{\mathcal{Y}}^{b,(2)} \right)^{-1} \hat{\mathcal{Y}}^{tl} & \mathcal{I} - j \left(\hat{\mathcal{Y}}^{b,(2)} \right)^{-1} \hat{\mathcal{Y}}^{tl} \\ \mathcal{I} - j \left(\hat{\mathcal{Y}}^{b,(2)} \right)^{-1} \hat{\mathcal{Y}}^{tl} & \mathcal{I} + j \left(\hat{\mathcal{Y}}^{b,(2)} \right)^{-1} \hat{\mathcal{Y}}^{tl} \end{pmatrix}. \quad (10.56)$$

We have from Eq. (10.52) symmetry for the eigenvector matrix, expressed as

$$\hat{Q} = \hat{Q}^t. \quad (10.57)$$

In order to change the eigenvalue decomposition of Eq. (10.54) into a symplectic one we proceed, using a similar approach as in Abraham and Marsden (1978), as follows. The linear combinations of the eigenvectors \hat{Q}_1 and \hat{Q}_2 of Eqs. (10.40) and (10.46), respectively,

$$\hat{Q}_1 + j\hat{Q}_2 = \frac{1}{2} (1+j) \begin{pmatrix} \mathcal{I} + \left(\hat{\mathcal{Y}}^{b,(2)} \right)^{-1} \hat{\mathcal{Y}}^{tl} \\ \mathcal{I} - \left(\hat{\mathcal{Y}}^{b,(2)} \right)^{-1} \hat{\mathcal{Y}}^{tl} \end{pmatrix}, \quad (10.58)$$

$$j\hat{Q}_1 + \hat{Q}_2 = \frac{1}{2} (1+j) \begin{pmatrix} \mathcal{I} - \left(\hat{\mathcal{Y}}^{b,(2)} \right)^{-1} \hat{\mathcal{Y}}^{tl} \\ \mathcal{I} + \left(\hat{\mathcal{Y}}^{b,(2)} \right)^{-1} \hat{\mathcal{Y}}^{tl} \end{pmatrix}, \quad (10.59)$$

transform the eigenvector equations (10.33) and (10.34) to,

$$\hat{Y}_n^{b,(1,2)} (\hat{Q}_1 + j\hat{Q}_2) = 2 (j\hat{Q}_1 + \hat{Q}_2) \hat{\mathcal{Y}}^{tl}, \quad (10.60)$$

$$\hat{Y}_n^{b,(1,2)} (j\hat{Q}_1 + \hat{Q}_2) = -2 (\hat{Q}_1 + j\hat{Q}_2) \hat{\mathcal{Y}}^{tl}. \quad (10.61)$$

Using the last two equation the eigenvalue decomposition of Eq. (10.54) is transformed to a symplectic eigenvalue decomposition, written as

$$\hat{Y}_n^{b,(1,2)} \hat{Q}^{tl} = \hat{Q}^{tl} \hat{Y}^{tl}, \quad (10.62)$$

with the alternating matrix of symplectic eigenvalue operators,

$$\hat{Y}^{tl} = \begin{pmatrix} \mathcal{O} & -2\hat{Y}^{tl} \\ 2\hat{Y}^{tl} & \mathcal{O} \end{pmatrix}, \quad (10.63)$$

and with the symplectic eigenvector matrix given by

$$\hat{Q}^{tl} = \frac{1}{2} \begin{pmatrix} \mathcal{I} + (\hat{Y}^{b,(2)})^{-1} \hat{Y}^{tl} & \mathcal{I} - (\hat{Y}^{b,(2)})^{-1} \hat{Y}^{tl} \\ \mathcal{I} - (\hat{Y}^{b,(2)})^{-1} \hat{Y}^{tl} & \mathcal{I} + (\hat{Y}^{b,(2)})^{-1} \hat{Y}^{tl} \end{pmatrix}. \quad (10.64)$$

From the commutation relation of Eq. (10.52) it follows that, using the symmetry of $\hat{Y}^{b,(2)}$ and \hat{Y}^{tl} , this last matrix is symmetric,

$$\hat{Q}^{tl} = (\hat{Q}^{tl})^t. \quad (10.65)$$

Using the transformation , see Eq. (10.62),

$$\hat{Y}_n^{b,(1,2)} = \hat{Q}^{tl} \hat{Y}^{tl} (\hat{Q}^{tl})^{-1}, \quad (10.66)$$

we obtain an alternating interaction operator \hat{Y}^{tl} , which has the same form as \hat{Y}^b of Eqs. (10.12) and (10.22). The interaction operator \hat{Y}^b is valid if the background reference and monitor D-t-N operators, $\hat{Y}^{b,(1)}$ and $\hat{Y}^{b,(2)}$, are equal, i.e. when the condition Eq. (10.10) is satisfied. The operator \hat{Y}^{tl} is valid for any temporal contrast configuration. Substituting Eq. (10.66) into Eq. (10.30), using the symmetry of \hat{Q}^{tl} , yields

$$\hat{I}^{\text{conv}} \left(\hat{\mathbf{F}}^{(1)}, \hat{\mathbf{F}}^{(2)} \right) = \left\langle \hat{\mathbf{P}}^{tl,(1)}, \hat{Y}^{tl} \hat{\mathbf{P}}^{tl,(2)} \right\rangle_b \quad \text{in } \mathbb{D}, \quad (10.67)$$

in which

$$\hat{\mathbf{P}}^{tl,(1)} = \hat{Q}^{tl} \hat{\mathbf{P}}_n^{b,(1)}, \quad (10.68)$$

$$\hat{\mathbf{P}}^{tl,(2)} = (\hat{Q}^{tl})^{-1} \hat{\mathbf{P}}_n^{b,(2)}, \quad (10.69)$$

with

$$\left(\hat{Q}^{tl}\right)^{-1} = \frac{1}{2} \begin{pmatrix} \mathcal{I} + \left(\hat{\mathcal{Y}}^{tl}\right)^{-1} \hat{\mathcal{Y}}^{b,(2)} & \mathcal{I} - \left(\hat{\mathcal{Y}}^{tl}\right)^{-1} \hat{\mathcal{Y}}^{b,(2)} \\ \mathcal{I} - \left(\hat{\mathcal{Y}}^{tl}\right)^{-1} \hat{\mathcal{Y}}^{b,(2)} & \mathcal{I} + \left(\hat{\mathcal{Y}}^{tl}\right)^{-1} \hat{\mathcal{Y}}^{b,(2)} \end{pmatrix}. \quad (10.70)$$

From Eqs. (10.26), (10.27), (10.28) and (10.29) we obtain the following wave field decomposition operations

$$\hat{L}_n^{b,(1)} \hat{\mathbf{F}}^{(1)} = \hat{\mathbf{P}}_n^{b,(1)}, \quad (10.71)$$

$$\hat{L}_n^{b,(2)} \hat{\mathbf{F}}^{(2)} = \hat{\mathbf{P}}_n^{b,(2)}, \quad (10.72)$$

with

$$\hat{L}_n^{b,(1)} = \frac{1}{2} \begin{pmatrix} \mathcal{I} & \left(\hat{\mathcal{Y}}^{b,(1)}\right)^{-1} \\ \mathcal{I} & -\left(\hat{\mathcal{Y}}^{b,(1)}\right)^{-1} \end{pmatrix}, \quad (10.73)$$

and

$$\hat{L}_n^{b,(2)} = \frac{1}{2} \begin{pmatrix} \mathcal{I} & \left(\hat{\mathcal{Y}}^{b,(2)}\right)^{-1} \\ \mathcal{I} & -\left(\hat{\mathcal{Y}}^{b,(2)}\right)^{-1} \end{pmatrix}. \quad (10.74)$$

Substituting Eqs. (10.71) and (10.72) into Eqs. (10.68) and (10.69), respectively, yields

$$\hat{Q}^{tl} \hat{L}_n^{b,(1)} \hat{\mathbf{F}}^{(1)} = \hat{\mathbf{P}}^{tl,(1)}, \quad (10.75)$$

$$\left(\hat{Q}^{tl}\right)^{-1} \hat{L}_n^{b,(2)} \hat{\mathbf{F}}^{(2)} = \hat{\mathbf{P}}^{tl,(2)}. \quad (10.76)$$

Using Eqs. (10.42) and (10.64) for \hat{Q}^{tl} and Eq. (10.70) for $(\hat{Q}^{tl})^{-1}$, one can show that the last two wave field decomposition operators are identical, i.e.

$$\hat{Q}^{tl} \hat{L}_n^{b,(1)} = \left(\hat{Q}^{tl}\right)^{-1} \hat{L}_n^{b,(2)}. \quad (10.77)$$

Defining,

$$\hat{L}^{tl} \hat{\mathbf{F}}^{(1)} \stackrel{\text{def}}{=} \hat{\mathbf{P}}^{tl,(1)}, \quad (10.78)$$

$$\hat{L}^{tl} \hat{\mathbf{F}}^{(2)} \stackrel{\text{def}}{=} \hat{\mathbf{P}}^{tl,(2)}, \quad (10.79)$$

then Eqs. (10.75) and (10.76) and Eq. (10.77) yield

$$\hat{\mathbf{L}}^{\text{tl}} = \frac{1}{2} \begin{pmatrix} \mathcal{I} & \left(\hat{\mathcal{Y}}^{\text{tl}}\right)^{-1} \\ \mathcal{I} & -\left(\hat{\mathcal{Y}}^{\text{tl}}\right)^{-1} \end{pmatrix}. \quad (10.80)$$

The composition operations are given by

$$\hat{\mathbf{F}}^{(1)} = \hat{\mathbf{T}}^{\text{tl}} \hat{\mathbf{P}}^{\text{tl},(1)}, \quad (10.81)$$

$$\hat{\mathbf{F}}^{(2)} = \hat{\mathbf{T}}^{\text{tl}} \hat{\mathbf{P}}^{\text{tl},(2)}, \quad (10.82)$$

with

$$\hat{\mathbf{T}}^{\text{tl}} = \begin{pmatrix} \mathcal{I} & \mathcal{I} \\ \hat{\mathcal{Y}}^{\text{tl}} & -\hat{\mathcal{Y}}^{\text{tl}} \end{pmatrix}. \quad (10.83)$$

The symplectic eigenvalue decomposition of Eq. (10.66) yields one symplectic eigenoperator $\hat{\mathcal{Y}}^{\text{tl}}$ of Eq. (10.44), which is a square root function of the reference and monitor normalised background D-t-N operators of Eqs. (10.24) and (10.25). Defining the components of $\hat{\mathbf{P}}^{\text{tl},(1)}$ and $\hat{\mathbf{P}}^{\text{tl},(2)}$ of Eqs. (10.68) and (10.69), respectively, as

$$\hat{\mathbf{P}}^{\text{tl},(1)} \stackrel{\text{def}}{=} \begin{pmatrix} \hat{p}^{\text{d},(1)} \\ \hat{p}^{\text{u},(1)} \end{pmatrix} \quad \text{and} \quad \hat{\mathbf{P}}^{\text{tl},(2)} \stackrel{\text{def}}{=} \begin{pmatrix} \hat{p}^{\text{d},(2)} \\ \hat{p}^{\text{u},(2)} \end{pmatrix}, \quad (10.84)$$

Eq. (6.31) is, using Eq. (7.53), and Eqs. (10.81) and (10.82), written as

$$\hat{I}^{\text{conv}}(x_3^{\text{tl}}, \mathbf{x}^{\text{R}}, \mathbf{x}^{\text{S}}) = 2 \int_{\mathbf{x}_T \in \mathbb{R}^2} \left[\hat{p}^{\text{d},(1)}(\mathbf{x}_T, x_3^{\text{tl}}; \mathbf{x}^{\text{R}}) \hat{\mathcal{Y}}^{\text{tl}} \hat{p}^{\text{u},(2)}(\mathbf{x}_T, x_3^{\text{tl}}; \mathbf{x}^{\text{S}}) \right. \\ \left. - \hat{p}^{\text{u},(1)}(\mathbf{x}_T, x_3^{\text{tl}}; \mathbf{x}^{\text{R}}) \hat{\mathcal{Y}}^{\text{tl}} \hat{p}^{\text{d},(2)}(\mathbf{x}_T, x_3^{\text{tl}}; \mathbf{x}^{\text{S}}) \right] d\mathbf{x}_T. \quad (10.85)$$

The analogy of Eqs. (10.22) and (10.23) with Eqs. (10.63) and (10.83) suggests that the interaction quantity of Eq. (10.67) should produce a difference wave field, as is found in Eq. (10.13). Indeed, this difference wave field is derived in Chapter 6 and given in Eq. (6.37).

10.3 Time-lapse imaging

Consider the domain $\mathbb{D} = \{(\mathbf{x}_T, x_3) | \mathbf{x}_T \in \mathbb{R}^2, x_3^{\text{R}} = x_3^{\text{S}} < x_3 \leq x_3^{\text{tl}}\}$. In this section the interaction integral, as expressed by Eq. (10.85), is set in terms

of a time-lapse difference reflection operator. To enable this we introduce, according to Eq. (8.71), the following reflection operators, which transform the down-going wave field constituents to the up-going ones,

$$\hat{p}^{u,(1)} \stackrel{\text{def}}{=} \hat{\mathcal{R}}^{tl,(1)} \hat{p}^{d,(1)}, \quad \text{in } \mathbb{D}, \quad (10.86)$$

$$\hat{p}^{u,(2)} \stackrel{\text{def}}{=} \hat{\mathcal{R}}^{tl,(2)} \hat{p}^{d,(2)}, \quad \text{in } \mathbb{D}. \quad (10.87)$$

Following a similar procedure which yields Eq. (8.73), using the wave field composition of Eqs. (10.81), (10.82), (10.83) and (10.84), and the boundary conditions of Eq. (7.34), yields

$$\hat{\mathcal{R}}^{tl,(1)} = \left(\hat{\mathcal{Y}}^{(1)} + \hat{\mathcal{Y}}^{tl} \right)^{-1} \left(\hat{\mathcal{Y}}^{tl} - \hat{\mathcal{Y}}^{(1)} \right), \quad (10.88)$$

$$\hat{\mathcal{R}}^{tl,(2)} = \left(\hat{\mathcal{Y}}^{(2)} + \hat{\mathcal{Y}}^{tl} \right)^{-1} \left(\hat{\mathcal{Y}}^{tl} - \hat{\mathcal{Y}}^{(2)} \right). \quad (10.89)$$

Analogously to Eq. (8.17) we define the reference and monitor monopole Green's states as,

$$\hat{p}^{d,(1)}(\mathbf{x}_T, x_3; \mathbf{x}_T^R, x_3^R) \stackrel{\text{def}}{=} \hat{q}^{(1)} \hat{G}^{q,tl,(1)}(\mathbf{x}_T^R, x_3^R; \mathbf{x}_T, x_3), \quad (10.90)$$

$$\hat{p}^{d,(2)}(\mathbf{x}_T, x_3; \mathbf{x}_T^S, x_3^S) \stackrel{\text{def}}{=} \hat{q}^{(2)} \hat{G}^{q,tl,(2)}(\mathbf{x}_T^S, x_3^S; \mathbf{x}_T, x_3). \quad (10.91)$$

Eq. (10.85) becomes, after substitution of Eqs. (10.86), (10.87), (10.90) and (10.91), and subsequently, using the symmetry of $\hat{\mathcal{Y}}^{tl}$,

$$\begin{aligned} & \hat{I}^{\text{conv}}(x_3^{\text{tl}}; \mathbf{x}^R, \mathbf{x}^S) \\ &= 2\hat{q}^{(1)}\hat{q}^{(2)} \int_{\mathbf{x}_T \in \mathbb{R}^2} \left[\hat{G}^{q,tl,(1)}(\mathbf{x}_T^R, x_3^R; \mathbf{x}_T, x_3^{\text{tl}}) \hat{\mathcal{Y}}^{tl} \hat{\mathcal{R}}^{tl,(2)} \hat{G}^{q,tl,(2)}(\mathbf{x}_T^S, x_3^S; \mathbf{x}_T, x_3^{\text{tl}}) \right. \\ & \quad \left. - \hat{\mathcal{Y}}^{tl} \hat{\mathcal{R}}^{tl,(1)} \hat{G}^{q,tl,(1)}(\mathbf{x}_T^R, x_3^R; \mathbf{x}_T, x_3^{\text{tl}}) \hat{G}^{q,tl,(2)}(\mathbf{x}_T^S, x_3^S; \mathbf{x}_T, x_3^{\text{tl}}) \right] d\mathbf{x}_T. \end{aligned} \quad (10.92)$$

Assuming that there are no temporal contrasts inside the entire \mathbb{R}^3 , i.e. we have,

$$\hat{I}^{\text{conv}} = 0 \quad \text{and} \quad \hat{\mathcal{R}}^{tl,(1)} = \hat{\mathcal{R}}^{tl,(2)} = \hat{\mathcal{R}}^{tl}. \quad (10.93)$$

In terms of bilinear forms of scalar-valued functions (Section 7.5) Eq. (10.92) then yields,

$$\begin{aligned} & \left\langle \hat{G}^{q,tl,(1)}, \hat{\mathcal{Y}}^{tl} \hat{\mathcal{R}}^{tl} \hat{G}^{q,tl,(2)} \right\rangle_b(x_3^{\text{tl}}; \mathbf{x}^R, \mathbf{x}^S) \\ &= \left\langle \hat{\mathcal{Y}}^{tl} \hat{\mathcal{R}}^{tl} \hat{G}^{q,tl,(1)}, \hat{G}^{q,tl,(2)} \right\rangle_b(x_3^{\text{tl}}; \mathbf{x}^R, \mathbf{x}^S). \end{aligned} \quad (10.94)$$

Hence, we obtain the following symmetry relation

$$\hat{\mathcal{Y}}^{\text{tl}} \hat{\mathcal{R}}^{\text{tl}} = \left(\hat{\mathcal{Y}}^{\text{tl}} \hat{\mathcal{R}}^{\text{tl}} \right)^t. \quad (10.95)$$

Because this last relation must hold for arbitrary $\hat{\mathcal{Y}}^{\text{tl}} \hat{\mathcal{R}}^{\text{tl}}$ we can apply this latter symmetry to Eq. (10.92),

$$\begin{aligned} \hat{I}^{\text{conv}}(x_3^{\text{tl}}; \mathbf{x}^{\text{R}}, \mathbf{x}^{\text{S}}) &= 2\hat{q}^{(1)}\hat{q}^{(2)} \int_{\mathbf{x}_T \in \mathbb{R}^2} d\mathbf{x}_T \\ &\quad \hat{G}^{q, \text{tl}, (1)}(\mathbf{x}_T^{\text{R}}, x_3^{\text{R}}; \mathbf{x}_T, x_3^{\text{tl}}) \hat{\mathcal{Y}}^{\text{tl}} \Delta \hat{\mathcal{R}}^{\text{tl}} \hat{G}^{q, \text{tl}, (2)}(\mathbf{x}_T^{\text{S}}, x_3^{\text{S}}; \mathbf{x}_T, x_3^{\text{tl}}), \end{aligned} \quad (10.96)$$

with

$$\Delta \hat{\mathcal{R}}^{\text{tl}} = \hat{\mathcal{R}}^{\text{tl}, (2)} - \hat{\mathcal{R}}^{\text{tl}, (1)}, \quad (10.97)$$

and with $\hat{\mathcal{R}}^{\text{tl}, (1)}$ and $\hat{\mathcal{R}}^{\text{tl}, (2)}$ given in Eqs. (10.88) and (10.89), respectively. Defining the following extrapolation operator, similar to Eq. (9.8), as

$$\begin{aligned} \hat{\mathcal{W}}^{q, \text{tl}, (1)}(x_3, x_3') f(\mathbf{x}_T, x_3') \\ \stackrel{\text{def}}{=} 2 \int_{\mathbf{x}'_T \in \mathbb{R}^2} \hat{G}^{q, \text{tl}, (1)}(\mathbf{x}_T, x_3; \mathbf{x}'_T, x_3') \hat{\mathcal{Y}}^{\text{tl}} f(\mathbf{x}'_T, x_3') d\mathbf{x}'_T, \end{aligned} \quad (10.98)$$

Eq. (10.96) becomes

$$\begin{aligned} \hat{I}^{\text{conv}}(x_3^{\text{tl}}; \mathbf{x}^{\text{R}}, \mathbf{x}^{\text{S}}) \\ = \hat{q}^{(1)}\hat{q}^{(2)} \hat{\mathcal{W}}^{\text{tl}, (1)}(x_3^{\text{R}}, x_3^{\text{tl}}) \Delta \hat{\mathcal{R}}^{\text{tl}} \hat{G}^{q, \text{tl}, (2)}(\mathbf{x}_T^{\text{S}}, x_3^{\text{S}}; \mathbf{x}_T^{\text{R}}, x_3^{\text{tl}}). \end{aligned} \quad (10.99)$$

Likewise, defining,

$$\begin{aligned} \hat{\mathcal{W}}^{q, \text{tl}, (2)}(x_3, x_3') g(\mathbf{x}_T, x_3') \\ \stackrel{\text{def}}{=} 2 \int_{\mathbf{x}'_T \in \mathbb{R}^2} \hat{G}^{q, \text{tl}, (2)}(\mathbf{x}_T, x_3; \mathbf{x}'_T, x_3') \hat{\mathcal{Y}}^{\text{tl}} g(\mathbf{x}'_T, x_3') d\mathbf{x}'_T, \end{aligned} \quad (10.100)$$

and following Eqs. (9.5) and (9.10), Eq. (10.99) is written as

$$\begin{aligned} \hat{I}^{\text{conv}}(x_3^{\text{tl}}; \mathbf{x}^{\text{R}}, \mathbf{x}^{\text{S}}) &= \hat{q}^{(1)}\hat{q}^{(2)} \hat{\mathcal{W}}^{\text{tl}, (1)}(x_3^{\text{R}}, x_3^{\text{tl}}) \Delta \hat{\mathcal{R}}^{\text{tl}} \hat{\mathcal{W}}^{\text{tl}, (2)}(x_3^{\text{tl}}, x_3^{\text{S}}) \\ &\quad \times \left(2\hat{\mathcal{Y}}^{\text{tl}} \right)^{-1} \delta(\mathbf{x}_T^{\text{R}} - \mathbf{x}_T^{\text{S}}), \end{aligned} \quad (10.101)$$

in which $(2\hat{\mathcal{Y}}^{\text{tl}})^{-1}\delta(\mathbf{x}_T^R - \mathbf{x}_T^S)$ represents a dipole source. Eq. (10.101) expresses the interaction integral of Eq. (6.31) in terms of the 'WRW-model' of Berkhouit (1985), except for the difference that the operator $\Delta\hat{\mathcal{R}}^{\text{tl}}$ is a global operator with respect to the x_3 coordinate, whereas the reflection operator in the WRW model is local.

Using Eq. (6.37) we can express the difference reflection operator in terms of a difference wave field, by deconvolving \hat{I}^{conv} with $\hat{q}^{(1)}$, obtaining

$$\begin{aligned}\hat{p}^{\text{dif},u}(\mathbf{x}^R; \mathbf{x}^S) &= \hat{\mathcal{W}}^{q,\text{tl},(1)}(x_3^R, x_3^{\text{tl}}) \Delta\hat{\mathcal{R}}^{\text{tl}} \hat{\mathcal{W}}^{q,\text{tl},(2)}(x_3^{\text{tl}}, x_3^S) \\ &\quad \times \hat{q}^{(2)} \left(2\hat{\mathcal{Y}}^{\text{tl}}\right)^{-1} \delta(\mathbf{x}_T^R - \mathbf{x}_T^S).\end{aligned}\quad (10.102)$$

In this last equation, the difference wave field $\hat{p}^{\text{dif},u}$ is governed by Eqs. (6.21) to (6.24). The source function $\hat{q}^{(2)}$ appears in the right-hand side of Eq. (10.102) because of the source functions in Eqs. (6.25) and (6.26). Eq. (10.102) can be rewritten, in the real-frequency or Fourier domain, employing the symbol $\check{\cdot}$ of Eq. (B.6), to

$$\check{p}^{\text{dif},u}(\mathbf{x}_T^R, x_3^{\text{tl}}; \mathbf{x}_T^S, x_3^S) = \Delta\check{\mathcal{R}}^{\text{tl}} \check{p}^{\text{d},(2)}(\mathbf{x}_T^R, x_3^{\text{tl}}; \mathbf{x}_T^S, x_3^S), \quad (10.103)$$

relating an up-going difference wave field with a down-going wave field component through a difference reflection operator. In this last equation we applied, analogously to Eqs. (9.5) and (9.7), using Eq. (10.91), the forward extrapolation,

$$\check{p}^{\text{d},(2)}(\mathbf{x}_T^R, x_3^{\text{tl}}; \mathbf{x}_T^S, x_3^S) = \check{\mathcal{W}}^{q,\text{tl},(2)}(x_3^{\text{tl}}, x_3^S) \check{q}^{(2)}(2\check{\mathcal{Y}}^{\text{tl}})^{-1} \delta(\mathbf{x}_T^R - \mathbf{x}_T^S), \quad (10.104)$$

and, analogously to Eq. (9.46), the inverse extrapolation,

$$\check{p}^{\text{dif},u}(\mathbf{x}_T^R, x_3^{\text{tl}}; \mathbf{x}_T^S, x_3^S) = \check{\mathcal{W}}^{q,\text{tl},(1)}(x_3^{\text{tl}}, x_3^R) \check{p}^{\text{dif},u}(\mathbf{x}_T^R, x_3^R; \mathbf{x}_T^S, x_3^S). \quad (10.105)$$

Taking the kernel of $\Delta\check{\mathcal{R}}^{\text{tl}}$ after Eq. (9.29), Eq. (10.103) is written as

$$\begin{aligned}\check{p}^{\text{dif},u}(\mathbf{x}_T^R, x_3^{\text{tl}}; \mathbf{x}_T^S, x_3^S) \\ = \int_{\mathbf{x}'_T \in \mathbb{R}^2} \Delta\check{\mathcal{R}}^{\text{tl}}(\mathbf{x}_T^R, x_3^{\text{tl}}; \mathbf{x}'_T, x_3^{\text{tl}}) \check{p}^{\text{d},(2)}(\mathbf{x}'_T, x_3^{\text{tl}}; \mathbf{x}_T^S, x_3^S) d\mathbf{x}'_T.\end{aligned}\quad (10.106)$$

This last equation is inverted to obtain an image of the kernel $\Delta\check{R}^{\text{tl}}$. When the condition of Eq. (10.11) holds, and also $\hat{q}^{(1)} = \hat{q}^{(2)} = \hat{q}$, we have according to Eqs. (6.37) and (6.38)

$$\hat{p}^{\text{dif},\text{u}}(\mathbf{x}^{\text{R}}; \mathbf{x}^{\text{S}}) = \Delta\hat{p}^{\text{sct}}(\mathbf{x}^{\text{R}}; \mathbf{x}^{\text{S}}), \quad (10.107)$$

with

$$\Delta\hat{p}^{\text{sct}} = \hat{p}^{\text{sct},(2)} - \hat{p}^{\text{sct},(1)}. \quad (10.108)$$

Using Eq. (9.23) we then have

$$\Delta\hat{p}^{\text{sct}}(\mathbf{x}^{\text{R}}, \mathbf{x}^{\text{S}}) = \hat{q}\hat{\mathcal{W}}^{q,\text{b}}(x_3^{\text{R}}, x_3^{\text{tl}})\Delta\hat{\mathcal{R}}\hat{\mathcal{W}}^{q,\text{b}}(x_3^{\text{tl}}, x_3^{\text{S}})\frac{1}{2}\hat{\mathcal{S}}^{\text{b}}\delta(\mathbf{x}_{\text{T}}^{\text{R}} - \mathbf{x}_{\text{T}}^{\text{S}}). \quad (10.109)$$

with

$$\Delta\hat{\mathcal{R}} = \hat{\mathcal{R}}^{(2)} - \hat{\mathcal{R}}^{(1)}, \quad (10.110)$$

and, using Eq. (8.73), with

$$\hat{\mathcal{R}}^{(1)} = \left(\hat{\mathcal{Y}}^{(1)} - \hat{\mathcal{Y}}^{\text{u}}\right)^{-1}\left(\hat{\mathcal{Y}}^{\text{d}} - \hat{\mathcal{Y}}^{(1)}\right), \quad (10.111)$$

$$\hat{\mathcal{R}}^{(2)} = \left(\hat{\mathcal{Y}}^{(2)} - \hat{\mathcal{Y}}^{\text{u}}\right)^{-1}\left(\hat{\mathcal{Y}}^{\text{d}} - \hat{\mathcal{Y}}^{(2)}\right). \quad (10.112)$$

We can also write, in the Fourier domain, using the forward extrapolation of Eq. (9.7), and the inverse extrapolation of Eq. (9.46),

$$\Delta\check{p}^{\text{sct}}(\mathbf{x}_{\text{T}}^{\text{R}}, x_3^{\text{tl}}; \mathbf{x}_{\text{T}}^{\text{S}}, x_3^{\text{S}}) = \Delta\check{\mathcal{R}}\check{p}^{\text{inc}}(\mathbf{x}_{\text{T}}^{\text{R}}, x_3^{\text{tl}}; \mathbf{x}_{\text{T}}^{\text{S}}, x_3^{\text{S}}), \quad (10.113)$$

The representation of Eq. (10.109), and Eq. (10.113), for which the time-lapse contrast in the density and the compressibility vanishes for $x_3 < x_3^{\text{tl}}$, and for which the source functions are equal, is generalised by the representation of Eq. (10.102), and Eq. (10.103), respectively, which is valid for an arbitrary time-lapse contrast configuration.

10.4 Fundamental solutions

In the following analysis we apply the fundamental solution approach, according to Pazy (1983); Krueger and Ochs (1989); Wapenaar (1996a); Grimenbergen et al. (1998), and in particular we follow Haines and de Hoop (1996).

Taking the reference and monitor versions of Eqs. (9.48) to (9.51), and substitute these into Eqs. (10.1) and (10.3), we obtain the D-t-N operators $\{\hat{\mathcal{Y}}^{\text{d},(1)}, \hat{\mathcal{Y}}^{\text{u},(1)}\}$ and $\{\hat{\mathcal{Y}}^{\text{d},(2)}, \hat{\mathcal{Y}}^{\text{u},(2)}\}$, in accordance with Eq. (9.52), as solutions of the nonlinear Riccati equations,

$$\partial_3 \hat{\mathcal{Y}} - \hat{\mathcal{Y}} s \rho^{\text{b},(1)} \hat{\mathcal{Y}} + \frac{1}{s \rho^{\text{b},(1)}} \hat{\mathcal{H}}_2^{\text{b},(1)} = \mathcal{O}, \quad (10.114)$$

$$\partial_3 \hat{\mathcal{Y}} - \hat{\mathcal{Y}} s \rho^{\text{b},(2)} \hat{\mathcal{Y}} + \frac{1}{s \rho^{\text{b},(2)}} \hat{\mathcal{H}}_2^{\text{b},(2)} = \mathcal{O}, \quad (10.115)$$

respectively (Haines and de Hoop (1996)). The initial conditions are given by,

$$\hat{\mathcal{Y}} = \hat{\mathcal{Y}}^{\text{d},(1)} \Big|_{x_3=x_3^{\text{tl}}} \quad \text{and} \quad \hat{\mathcal{Y}} = \hat{\mathcal{Y}}^{\text{u},(1)} \Big|_{x_3=x_3^{\text{R}}}, \quad (10.116)$$

$$\hat{\mathcal{Y}} = \hat{\mathcal{Y}}^{\text{d},(2)} \Big|_{x_3=x_3^{\text{tl}}} \quad \text{and} \quad \hat{\mathcal{Y}} = \hat{\mathcal{Y}}^{\text{u},(2)} \Big|_{x_3=x_3^{\text{S}}}, \quad (10.117)$$

respectively. The densities $\rho^{\text{b},(1)}$ and $\rho^{\text{b},(2)}$, and the Helmholtz operators $\hat{\mathcal{H}}_2^{\text{b},(1)}$ and $\hat{\mathcal{H}}_2^{\text{b},(2)}$ of Eq. (7.29), are background medium parameters, given according to Eqs. (8.3) and (8.4) and Fig. (8.1), taking $x_3^{\text{sct}} = x_3^{\text{tl}}$. The reference and monitor normalised D-t-N operators, of Eqs. (10.24) and (10.25), are obtained, using Eqs. (8.47) and (8.48), as

$$\hat{\mathcal{Y}}^{\text{b},(1)} = \frac{1}{2} \left(\hat{\mathcal{Y}}^{\text{d},(1)} - \hat{\mathcal{Y}}^{\text{u},(1)} \right), \quad (10.118)$$

$$\hat{\mathcal{Y}}^{\text{b},(2)} = \frac{1}{2} \left(\hat{\mathcal{Y}}^{\text{d},(2)} - \hat{\mathcal{Y}}^{\text{u},(2)} \right). \quad (10.119)$$

Subsequently, the symplectic eigen D-t-N operator $\hat{\mathcal{Y}}^{\text{tl}}$ is calculated using Eq. (10.44), repeated here as,

$$\hat{\mathcal{Y}}^{\text{tl}} = \left(\hat{\mathcal{Y}}^{\text{b},(2)} \hat{\mathcal{Y}}^{\text{b},(1)} \right)^{\frac{1}{2}}. \quad (10.120)$$

Using Eqs. (10.1) and (10.3) we have in \mathbb{D}^{u} (Fig. (6.1)),

$$\partial_3 \hat{p}^{(1)} (\mathbf{x}_T, x_3; \mathbf{x}_T^R, x_3^R) + s \rho^{\text{b},(1)} (\mathbf{x}_T, x_3) \hat{v}_3^{(1)} (\mathbf{x}_T, x_3; \mathbf{x}_T^R, x_3^R) = 0, \quad (10.121)$$

$$\partial_3 \hat{p}^{(2)} (\mathbf{x}_T, x_3; \mathbf{x}_T^S, x_3^S) + s \rho^{\text{b},(2)} (\mathbf{x}_T, x_3) \hat{v}_3^{(2)} (\mathbf{x}_T, x_3; \mathbf{x}_T^S, x_3^S) = 0. \quad (10.122)$$

According to Eqs. (10.81) to (10.84) we have, in \mathbb{D}^u , the following wave field compositions

$$\hat{p}^{(1)} = \hat{p}^{d,(1)} + \hat{p}^{u,(1)}, \quad (10.123)$$

$$\hat{v}_3^{(1)} = \hat{\mathcal{Y}}^{tl} \hat{p}^{d,(1)} - \hat{\mathcal{Y}}^{tl} \hat{p}^{u,(1)}, \quad (10.124)$$

and

$$\hat{p}^{(2)} = \hat{p}^{d,(2)} + \hat{p}^{u,(2)}, \quad (10.125)$$

$$\hat{v}_3^{(2)} = \hat{\mathcal{Y}}^{tl} \hat{p}^{d,(2)} - \hat{\mathcal{Y}}^{tl} \hat{p}^{u,(2)}. \quad (10.126)$$

Substitution into Eqs. (10.121) and (10.122) yields

$$\partial_3 (\hat{p}^{d,(1)} + \hat{p}^{u,(1)}) + s\rho^{b,(1)} (\hat{\mathcal{Y}}^{tl} \hat{p}^{d,(1)} - \hat{\mathcal{Y}}^{tl} \hat{p}^{u,(1)}) = 0, \quad (10.127)$$

$$\partial_3 (\hat{p}^{d,(2)} + \hat{p}^{u,(2)}) + s\rho^{b,(2)} (\hat{\mathcal{Y}}^{tl} \hat{p}^{d,(2)} - \hat{\mathcal{Y}}^{tl} \hat{p}^{u,(2)}) = 0. \quad (10.128)$$

In accordance with Eqs. (9.48) and (9.49) we take, in order to satisfy Eqs. (10.127) and (10.128), the following evolution equations for $\hat{p}^{d,(1)} = \hat{p}^{d,(1)}(\mathbf{x}_T, x_3; \mathbf{x}_T^R, x_3^R)$ and $\hat{p}^{u,(1)} = \hat{p}^{u,(1)}(\mathbf{x}_T, x_3; \mathbf{x}_T^R, x_3^R)$,

$$\partial_3 \hat{p}^{d,(1)} + s\rho^{b,(1)} \hat{\mathcal{Y}}^{tl} \hat{p}^{d,(1)} = 0, \quad \text{in } \mathbb{D}, \quad (10.129)$$

$$\partial_3 \hat{p}^{u,(1)} - s\rho^{b,(1)} \hat{\mathcal{Y}}^{tl} \hat{p}^{d,(1)} = 0, \quad \text{in } \mathbb{D}, \quad (10.130)$$

with initial conditions

$$\hat{p}^{d,(1)} = \hat{p}^{d,(1)} (\mathbf{x}_T, x_3^R; \mathbf{x}_T^R, x_3^R), \quad (10.131)$$

$$\hat{p}^{u,(1)} = \hat{p}^{u,(1)} (\mathbf{x}_T, x_3^{tl}; \mathbf{x}_T^R, x_3^R). \quad (10.132)$$

For $\hat{p}^{d,(2)} = \hat{p}^{d,(2)}(\mathbf{x}_T, x_3; \mathbf{x}_T^S, x_3^S)$ and $\hat{p}^{u,(2)} = \hat{p}^{u,(2)}(\mathbf{x}_T, x_3; \mathbf{x}_T^S, x_3^S)$, we have

$$\partial_3 \hat{p}^{d,(2)} + s\rho^{b,(2)} \hat{\mathcal{Y}}^{tl} \hat{p}^{d,(2)} = 0, \quad \text{in } \mathbb{D}, \quad (10.133)$$

$$\partial_3 \hat{p}^{u,(2)} - s\rho^{b,(2)} \hat{\mathcal{Y}}^{tl} \hat{p}^{u,(2)} = 0, \quad \text{in } \mathbb{D}. \quad (10.134)$$

with initial conditions

$$\hat{p}^{d,(2)} = \hat{p}^{d,(2)} (\mathbf{x}_T, x_3^S; \mathbf{x}_T^S, x_3^S), \quad (10.135)$$

$$\hat{p}^{u,(2)} = \hat{p}^{u,(2)} (\mathbf{x}_T, x_3^{tl}; \mathbf{x}_T^S, x_3^S). \quad (10.136)$$

Eqs. (10.129) and (10.130), and Eqs. (10.133) and (10.134), show that we have obtained a parametrisation of the background medium in terms of $\{\rho^{b,(1)}, \hat{\mathcal{Y}}^{u,(1)}\}$ and $\{\rho^{b,(2)}, \hat{\mathcal{Y}}^{u,(2)}\}$, for the reference and monitor case, respectively. Because there is no time-lapse contrast in the admittance operator no difference reflections are generated in \mathbb{D}^u , i.e. for $x_3 < x_3^{tl}$. This new parametrisation, associated with the interaction integral \hat{I}^{conv} of Eq. (6.31), and the difference wave field $\hat{p}^{dif,u}$ (Eq. (6.37)), is illustrated in Fig. (10.1). Also shown is the parametrisation of the background medium in terms of densities, and admittance operators for the down- and up-going wave field constituents, $\rho^{b,(1)}$ and $\{\hat{\mathcal{Y}}^{d,(1)}, \hat{\mathcal{Y}}^{u,(1)}\}$, and $\rho^{b,(2)}$ and $\{\hat{\mathcal{Y}}^{d,(2)}, \hat{\mathcal{Y}}^{u,(2)}\}$, for the reference and monitor case, respectively, in case we evaluate the difference wave field $\Delta\hat{p}^{sct}$ of Eq. (10.108).

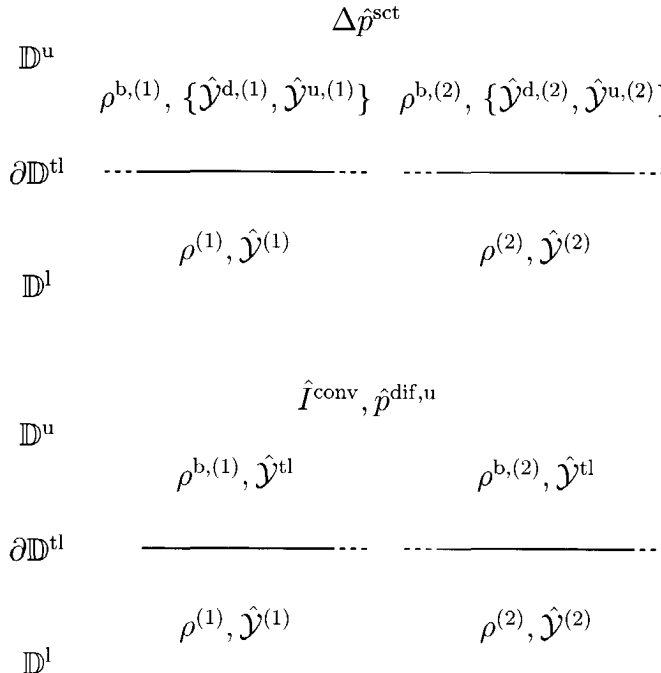


Figure 10.1: Parametrisation of $\Delta\hat{p}^{sct}$, in terms of $\rho^{b,(1)}$ and $\{\hat{\mathcal{Y}}^{d,(1)}, \hat{\mathcal{Y}}^{u,(1)}\}$, and $\rho^{b,(2)}$ and $\{\hat{\mathcal{Y}}^{d,(2)}, \hat{\mathcal{Y}}^{u,(2)}\}$ (top), and parametrisation of \hat{I}^{conv} and $\hat{p}^{dif,u}$, in terms of $\rho^{b,(1)}$ and $\hat{\mathcal{Y}}^{tl}$, and $\rho^{b,(2)}$ and $\hat{\mathcal{Y}}^{tl}$ (bottom).

In order to calculate the extrapolation operators, $\hat{\mathcal{W}}^{q,\text{tl},(1)}(x_3^R, x_3^{\text{tl}})$ and $\hat{\mathcal{W}}^{q,\text{tl},(2)}(x_3^{\text{tl}}, x_3^S)$, in Eq. (10.102), we need to obtain, according to Eqs. (10.98) and (10.100), the kernels or fundamental solutions, $\hat{G}^{q,\text{tl},(1)}(\mathbf{x}_T, x_3^R; \mathbf{x}'_T, x_3)$ and $\hat{G}^{q,\text{tl},(2)}(\mathbf{x}_T, x_3; \mathbf{x}'_T, x_3^S)$, respectively. Following Eqs. (9.57) and (9.55), the evolution equations for the latter two fundamental solutions are given by

$$\partial_3 \hat{G}^{q,\text{tl},(1)} - s \rho^{\text{b},(1)} \hat{\mathcal{Y}}^{\text{tl}} \hat{G}^{q,\text{tl},(1)} = 0, \quad \text{for } x_3 \in [x_3^R, x_3^{\text{tl}}], \quad (10.137)$$

$$\partial_3 \hat{G}^{q,\text{tl},(2)} + s \rho^{\text{b},(2)} \hat{\mathcal{Y}}^{\text{tl}} \hat{G}^{q,\text{tl},(2)} = 0, \quad \text{for } x_3 \in (x_3^S, x_3^{\text{tl}}], \quad (10.138)$$

respectively. Analogously to Eqs. (9.58) and (9.56), the initial condition are,

$$\hat{G}^{q,\text{tl},(1)}(\mathbf{x}_T, x_3^{\text{tl}}; \mathbf{x}'_T, x_3^{\text{tl}}) = \left(2\hat{\mathcal{Y}}^{\text{tl}}\right)^{-1} \delta(\mathbf{x}_T - \mathbf{x}'_T), \quad (10.139)$$

$$\hat{G}^{q,\text{tl},(2)}(\mathbf{x}_T, x_3^S; \mathbf{x}'_T, x_3^S) = \left(2\hat{\mathcal{Y}}^{\text{tl}}\right)^{-1} \delta(\mathbf{x}_T - \mathbf{x}'_T), \quad (10.140)$$

respectively. The fundamental solution $\hat{G}^{q,\text{tl},(1)}$ is parameterised with $\rho^{\text{b},(1)}$ and $\hat{\mathcal{Y}}^{\text{tl}}$, and solved upwards, whereas the fundamental solution $\hat{G}^{q,\text{tl},(2)}$ is parameterised with $\rho^{\text{b},(2)}$ and $\hat{\mathcal{Y}}^{\text{tl}}$, and solved downwards.

10.5 Numerical examples of the interaction integral

Consider the model of Fig. (10.2) which consists of 6 layers. Using this configuration reference and monitor wave speeds, $c^{(1)}$ and $c^{(2)}$, and densities, $\rho^{(1)}$ and $\rho^{(2)}$, are assigned according to Table (10.1). Time-lapse changes are modelled in layer 1, in which the source and receivers are placed, such that nonrepeatability of the time-lapse experiments is modelled, and in layer 3 and 5. In order to calculate the interaction integral of Eq. (6.31) we use a software code which simulates the pressure and vertical component of the particle velocity, response, p and v_3 , using finite differences in Eqs. (7.5) and (7.6). The compressibilities are calculated from Eq. (7.25). Equal monopole sources $q^{(1)} = q^{(2)}$ are employed. In Fig. (10.3) the difference wave field Δp^{sct} is shown, which is the time domain version of Eq. (10.108), obtained by placing the source and receiver array at 0 m depth. In this figure a difference direct wave, associated with the time-lapse changes in layer 1, and several difference reflections, associated with the time-lapse changes in layer

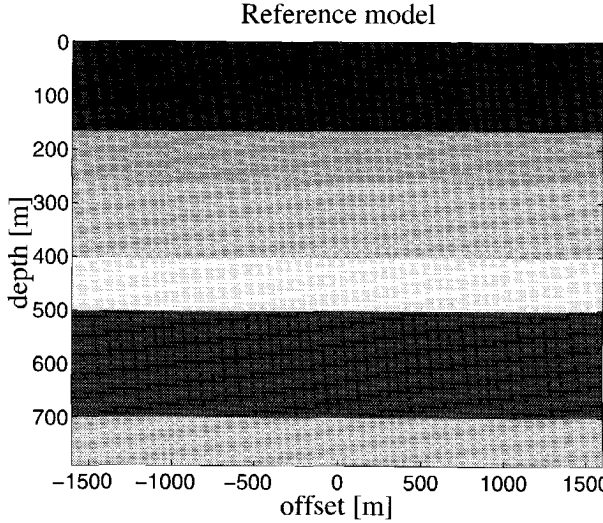


Figure 10.2: *Model for time-lapse finite difference simulations.*

1, 3 and 5, are observable. The difference wave field Δp^{sct} can be parameterised by the densities, and the down- and up-going admittance operators of the reference and monitor media, $\rho^{\text{b},(1)}$ and $\{\hat{\mathcal{Y}}^{\text{d},(1)}, \hat{\mathcal{Y}}^{\text{u},(1)}\}$, and $\rho^{\text{b},(2)}$ and $\{\hat{\mathcal{Y}}^{\text{d},(2)}, \hat{\mathcal{Y}}^{\text{u},(2)}\}$, respectively (Fig. (10.1) top). The parametrisation of the latter admittance or D-t-N operators, at a level surface $x_3 = x_3^{\text{sct}}$, in terms of $\{\rho^{\text{b},(1)}, \kappa^{\text{b},(1)}\}$ and $\{\rho^{\text{b},(2)}, \kappa^{\text{b},(2)}\}$, for $x_3 < x_3^{\text{sct}}$, is accomplished using Eqs. (7.26) to (7.28), Eqs. (8.3) and (8.4) and Fig. (8.1), Eqs. (8.14), (8.15), (8.17) and (8.18), and Eqs. (8.41), (8.42), (8.47) and (8.48). The expression for the reflection operator in Eq. (8.73) shows that a time-lapse contrast in $\{\hat{\mathcal{Y}}^{\text{d},(1)}, \hat{\mathcal{Y}}^{\text{u},(1)}\}$ and $\{\hat{\mathcal{Y}}^{\text{d},(2)}, \hat{\mathcal{Y}}^{\text{u},(2)}\}$ yields nonvanishing difference reflections for $x_3 < x_3^{\text{sct}}$, exemplified by Fig. (10.3). Calculating I^{conv} of Eq. (6.31) at $x_3^{\text{tl}} = 80$ m depth, i.e. halfway layer 1, using the finite difference code, we obtain Fig. (10.4). It appears that the difference direct wave associated with time-lapse contrasts for $x_3 < 80$ m has dissapeared, as compared to Fig. (10.3). Hence, differences in the medium parameters in the source and receiver domains are cancelled in the I^{conv} -gather of Fig. (10.4), thus solving the nonrepeatability problem associated with these time-lapse differences. For $x_3 < 80$ m we obtain a parametrisation in terms of $\rho^{\text{b},(1)}$ and $\hat{\mathcal{Y}}^{\text{tl}}$, and $\rho^{\text{b},(2)}$ and $\hat{\mathcal{Y}}^{\text{tl}}$ (Fig. (10.1) bottom). Therefore, a difference reflection is introduced at the interaction depth $x_3^{\text{tl}} = 80$ m through I^{conv} of Fig. (10.4), as compared

layer	$c^{(1)}$ [m/s]	$\rho^{(1)}$ [kg/m ³]	$c^{(2)}$ [m/s]	$\rho^{(2)}$ [kg/m ³]
1	1800	1500	2000	1600
2	2100	1700	2100	1700
3	2200	1800	2400	1900
4	2500	2000	2500	2000
5	3000	2400	3200	2500
6	2700	2300	2700	2300

Table 10.1: Reference and monitor velocities and densities, $c^{(1)}, \rho^{(1)}$ and $c^{(2)}$ and $\rho^{(2)}$.

to Fig. (10.3) in which this difference reflection does not appear. The difference reflections in Fig. (10.4) are associated with the operator $\Delta\hat{\mathcal{R}}^{\text{tl}}$ of Eqs. (10.88), (10.89) and (10.97) (Fig. (10.1) bottom), whereas the difference reflections in Fig. (10.3) are associated with the difference of the reference and monitor versions of the reflection operator of Eq. (8.73) (Fig. (10.1) top). The time shifts of the difference reflections in Fig. (10.3) depend on the time-lapse contrasts for $x_3 < 80$ m. In Fig. (10.4) the time-shifts of the difference reflections induced by the time-lapse contrasts for $x_3 < 80$ m have disappeared. Also the amplitudes of the difference reflections in Fig. (10.4) are corrected, as compared to Fig. (10.3), such that their dependencies on the temporal contrasts for $x_3 < 80$ m are cancelled. Hence, the corrective action of the interaction integral is both kinematically as well as dynamically valid.

In Figs. (10.5) to (10.7) the interaction integral I^{conv} is calculated at $x_3^{\text{tl}} = 164, 264$ and 404 m depths, i.e. just below the bottoms of layer 1, 2 and 3, respectively (Fig. (10.2)). One observes that in Fig. (10.5) the time-shifts and amplitudes of the difference reflections are such that these appear to be independent of the temporal contrasts in layer 1. Fig. (10.6) is the same as Fig. (10.5), confirming that I^{conv} is an invariant in a domain (for e.g. layer 2) in which no time-lapse changes have occurred. In Fig. (10.7) the difference reflections are associated with the time-lapse contrast in layer 3, and are independent of the time-lapse contrasts in layer 1 and layer 2. Observe that the first difference reflection, associated with the top of layer 3, is a pure amplitude difference, involving no time-shift, in contradistinction to the same difference reflection in Figs. (10.4) and (10.5), the former containing the sum of the time-shifts induced by the temporal contrasts in layer 1 and

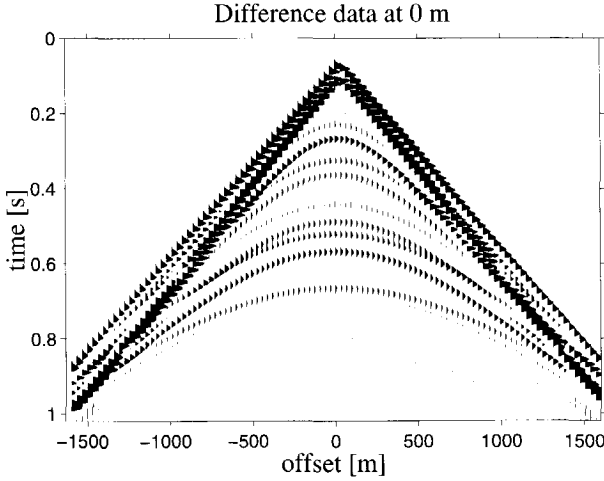


Figure 10.3: Difference wave field Δp^{sct} at $x_3 = 0$ m

2, the latter containing the time-shift induced by the temporal contrast in layer 2.

10.6 Longitudinal invariance

Consider the subdomain $\mathbb{D}^i = \{(\mathbf{x}_T, x_3) | \mathbf{x}_T \in \mathbb{R}^2, x_3^S < x_3^{i-1} < x_3 < x_3^i < x_3^{\text{tl}}\}$, in which the medium parameters are assumed to be invariant with respect to the x_3 -coordinate. Then, implementing longitudinal-invariance in Eqs. (10.114) and (10.115), similarly to Eq. (9.59), yields

$$\hat{\mathcal{Y}}_s \rho^{\text{b},(1)} \hat{\mathcal{Y}} - (s \rho^{\text{b},(1)})^{-1} \hat{\mathcal{H}}_2^{\text{b},(1)} = \mathcal{O}, \quad \text{in } \mathbb{D}^i, \quad (10.141)$$

$$\hat{\mathcal{Y}}_s \rho^{\text{b},(2)} \hat{\mathcal{Y}} - (s \rho^{\text{b},(2)})^{-1} \hat{\mathcal{H}}_2^{\text{b},(2)} = \mathcal{O}, \quad \text{in } \mathbb{D}^i. \quad (10.142)$$

From this last equation we take, analogously to Eqs. (9.60) and (9.61), the following solutions,

$$\{\hat{\mathcal{Y}}^{\text{d},(1)}, \hat{\mathcal{Y}}^{\text{u},(1)}\} = \{\hat{\mathcal{Y}}^{i,(1)}, -\hat{\mathcal{Y}}^{i,(1)}\}, \quad \text{in } \mathbb{D}^i, \quad (10.143)$$

$$\{\hat{\mathcal{Y}}^{\text{d},(2)}, \hat{\mathcal{Y}}^{\text{u},(2)}\} = \{\hat{\mathcal{Y}}^{i,(2)}, -\hat{\mathcal{Y}}^{i,(2)}\}, \quad \text{in } \mathbb{D}^i, \quad (10.144)$$

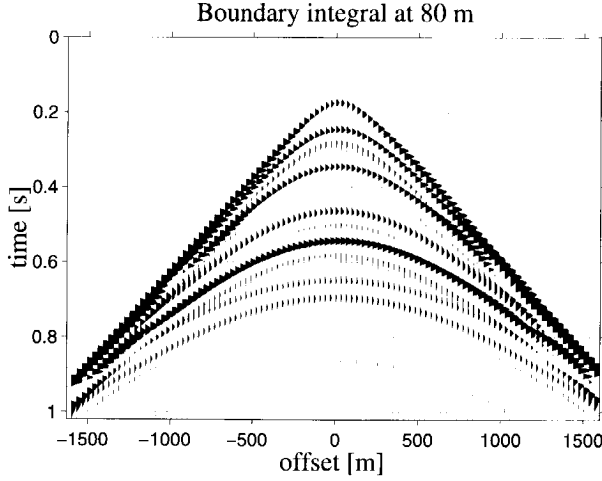


Figure 10.4: *interaction integral I^{conv} at $x_3^{\text{tl}} = 80 \text{ m}$.*

with

$$\hat{\mathcal{Y}}^{i,(1)} = (s\rho^{\text{b},(1)})^{-1} \hat{\mathcal{H}}_1^{\text{b},(1)}, \quad (10.145)$$

$$\hat{\mathcal{Y}}^{i,(2)} = (s\rho^{\text{b},(2)})^{-1} \hat{\mathcal{H}}_1^{\text{b},(2)}. \quad (10.146)$$

The symmetric pseudo-differential square-root operators $\hat{\mathcal{H}}_1^{\text{b},(1)}$ and $\hat{\mathcal{H}}_1^{\text{b},(2)}$ are given by

$$\hat{\mathcal{H}}_2^{\text{b},(1)} = \hat{\mathcal{H}}_1^{\text{b},(1)} \hat{\mathcal{H}}_1^{\text{b},(1)}, \quad \text{with} \quad \text{Re}(\lambda^{(1)}) > 0, \quad \forall \lambda^{(1)} \in \sigma(\hat{\mathcal{H}}_1^{\text{b},(1)}), \quad (10.147)$$

$$\hat{\mathcal{H}}_2^{\text{b},(2)} = \hat{\mathcal{H}}_1^{\text{b},(2)} \hat{\mathcal{H}}_1^{\text{b},(2)}, \quad \text{with} \quad \text{Re}(\lambda^{(2)}) > 0, \quad \forall \lambda^{(2)} \in \sigma(\hat{\mathcal{H}}_1^{\text{b},(2)}), \quad (10.148)$$

in which $\sigma(\hat{\mathcal{H}}_1^{\text{b},(1)})$ and $\sigma(\hat{\mathcal{H}}_1^{\text{b},(2)})$ designate the spectra of $\hat{\mathcal{H}}_1^{\text{b},(1)}$ and $\hat{\mathcal{H}}_1^{\text{b},(2)}$, respectively. The reference and monitor Helmholtz operators are, according to Eqs. (7.24) and (7.29), given by,

$$\hat{\mathcal{H}}_2^{\text{b},(1)} = \left(\frac{s}{c^{\text{b},(1)}} \right)^2 - \rho^{\text{b},(1)} \partial_\alpha \left[(\rho^{\text{b},(1)})^{-1} \partial_\alpha \cdot \right], \quad (10.149)$$

$$\hat{\mathcal{H}}_2^{\text{b},(2)} = \left(\frac{s}{c^{\text{b},(2)}} \right)^2 - \rho^{\text{b},(2)} \partial_\alpha \left[(\rho^{\text{b},(2)})^{-1} \partial_\alpha \cdot \right], \quad (10.150)$$

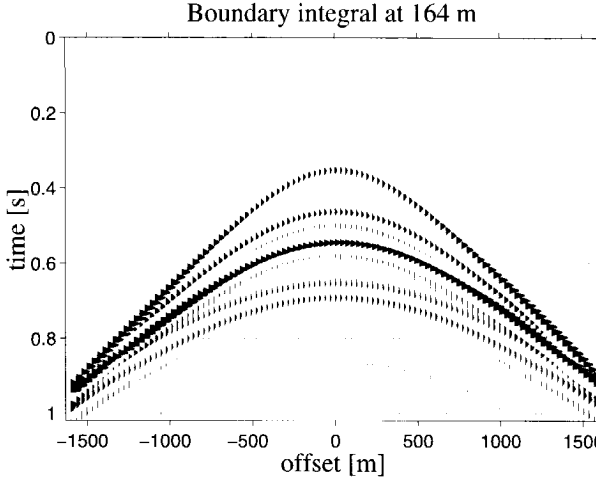


Figure 10.5: *interaction integral I^{conv} at $x_3^{\text{tl}} = 164 \text{ m}$.*

respectively. Because, according to Eq. (10.20), the admittance operators of Eqs. (10.145) and (10.146) are in normalised form, we have, using Eq. (10.120), for the symplectic eigenvalue operator,

$$\hat{\mathcal{Y}}^{\text{tl}} = \left(\hat{\mathcal{Y}}^{i,(2)} \hat{\mathcal{Y}}^{i,(1)} \right)^{\frac{1}{2}}. \quad (10.151)$$

Defining,

$$\hat{\mathcal{H}}_1^{\text{tl},(1)} \stackrel{\text{def}}{=} s\rho^{\text{b},(1)} \hat{\mathcal{Y}}^{\text{tl}}, \quad \text{in } \mathbb{D}^i, \quad (10.152)$$

$$\hat{\mathcal{H}}_1^{\text{tl},(2)} \stackrel{\text{def}}{=} s\rho^{\text{b},(2)} \hat{\mathcal{Y}}^{\text{tl}}, \quad \text{in } \mathbb{D}^i, \quad (10.153)$$

we obtain, according to Eqs. (10.137) and (10.138),

$$\partial_3 \hat{G}^{q,\text{tl},(1)} - \hat{\mathcal{H}}_1^{\text{tl},(1)} \hat{G}^{q,\text{tl},(1)} = 0, \quad \text{for } x_3 \in [x_3^i, x_3^{i+1}), \quad (10.154)$$

$$\partial_3 \hat{G}^{q,\text{tl},(2)} + \hat{\mathcal{H}}_1^{\text{tl},(2)} \hat{G}^{q,\text{tl},(2)} = 0, \quad \text{for } x_3 \in (x_3^i, x_3^{i+1}]. \quad (10.155)$$

The extrapolation operators of Eqs. (10.98) and (10.100) are, for a longitudinal-invariant medium, given by, according to Eqs. (9.73) and (9.74),

$$\hat{\mathcal{W}}^{q,\text{tl},(1)}(x_3, x_3^{i+1}) = \exp \left[- (x_3^{i+1} - x_3) \hat{\mathcal{H}}_1^{\text{tl},(1)} \right], \quad x_3^i \leq x_3 \leq x_3^{i+1}, \quad (10.156)$$

$$\hat{\mathcal{W}}^{q,\text{tl},(2)}(x_3^i, x_3) = \exp \left[- (x_3 - x_3^i) \hat{\mathcal{H}}_1^{\text{tl},(2)} \right], \quad x_3^i \leq x_3 \leq x_3^{i+1}. \quad (10.157)$$

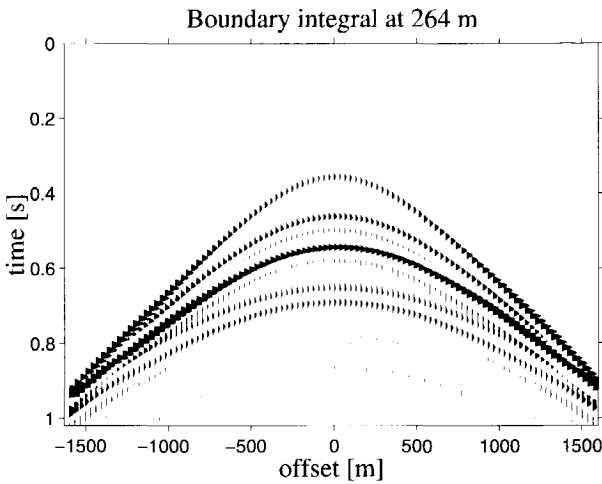


Figure 10.6: *interaction integral I^{conv} at $x_3^{\text{tl}} = 260$ m.*

Using a recursive scheme, assuming that the medium is piece-wise invariant with respect to the longitudinal x_3 -coordinate, one can construct, using the semi-group property of Eq. (9.19), using these last two equations, extrapolation operators for an inhomogeneous medium. Some examples are shown in the next section.

10.7 Proposed processing scheme

The objective of this thesis is to infer from time-lapse changes in the seismic velocities, and associated dynamic elasticity parameters, the change in the in-situ stress during two measurements. For acoustic waves we would try to estimate changes in the compressional-wave velocity and the dynamic compressibility. To do so I propose a recursive top-down approach which first solves the nonrepeatability problem and subsequently estimates the time-lapse changes, with respect to the reference measurement, as these occur, with increasing depth. The estimated time-lapse changes are then used to obtain a temporal contrast reflectivity image. Below I give an outline of the proposed processing steps. Consider an interaction depth x_3^{tl} , below expected nonrepeatability changes and above the expected time-lapse changes associated with e.g. reservoir activities.

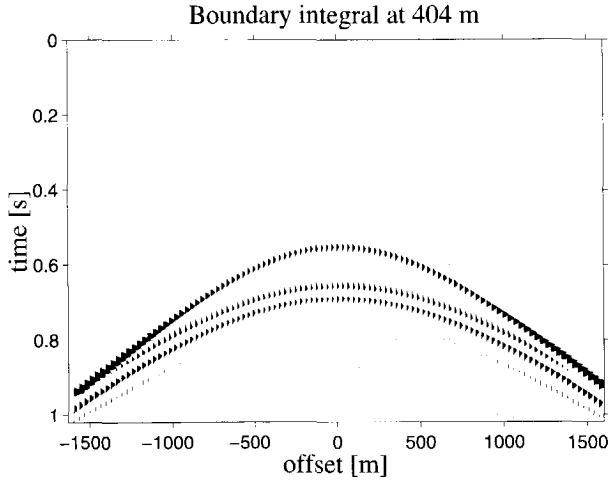


Figure 10.7: interaction integral I^{conv} at $x_3^{\text{tl}} = 404 \text{ m}$.

1. Transform the reference and monitor pressure data to the Fourier domain.
2. Equalise the reference and monitor source signatures (Eqs. (10.2) and (10.4)) such that $\check{q}^{(1)} = \check{q}^{(2)} = \check{q}$.
3. If necessary calculate $\check{p}^{\text{sct},(1)}(\mathbf{x}_T^S, x_3^S; \mathbf{x}_T^R, x_3^R)$ from $\check{p}^{\text{sct},(1)}(\mathbf{x}_T^R, x_3^R; \mathbf{x}_T^S, x_3^S)$, using source-receiver reciprocity.
4. Calculate the reference incident wave field $\check{p}^{\text{inc},(1)}(\mathbf{x}_T^S, x_3^{\text{tl}}; \mathbf{x}_T^R, x_3^R)$, at x_3^{tl} , using the reference forward extrapolation operator $\check{\mathcal{W}}^{q,b,(1)}(x_3^{\text{tl}}, x_3^R)$ of Eq. (9.15), applied to the reference dipole source $\frac{1}{2} \check{q} \check{\mathcal{S}}^{b,(1)} \delta(\mathbf{x}_T^R - \mathbf{x}_T)$ of Eq. (9.5).
5. Calculate the reference scattered wave field $\check{p}^{\text{sct},(1)}(\mathbf{x}_T^S, x_3^{\text{tl}}; \mathbf{x}_T^R, x_3^R)$, at x_3^{tl} , using the reference inverse extrapolation operator $\check{\mathcal{W}}^{q,b,(1)}^\dagger(x_3^{\text{tl}}, x_3^S)$ of Eq. (9.46), applied to the reference measurement $\check{p}^{\text{sct},(1)}(\mathbf{x}_T^S, x_3^S; \mathbf{x}_T^R, x_3^R)$.
6. Calculate the monitor incident wave field $\check{p}^{\text{inc},(2)}(\mathbf{x}_T^R, x_3^{\text{tl}}; \mathbf{x}_T^S, x_3^S)$, at x_3^{tl} , using an estimate of the monitor forward extrapolation operator $\check{\mathcal{W}}^{q,b,(2)}(x_3^{\text{tl}}, x_3^S)$ of Eq. (9.15), applied to an estimate of the monitor dipole source $\frac{1}{2} \check{q} \check{\mathcal{S}}^{b,(2)} \delta(\mathbf{x}_T - \mathbf{x}_T^S)$ of Eq. (9.5).

7. Calculate the monitor scattered wave field $\check{p}^{\text{sct},(2)}(\mathbf{x}_T^R, x_3^{\text{tl}}; \mathbf{x}_T^S, x_3^S)$, at x_3^{tl} , using an estimate of the monitor inverse extrapolation operator $\check{\mathcal{W}}^{q,b,(2)\dagger}(x_3^{\text{tl}}, x_3^R)$ of Eq. (9.46), applied to the monitor measurement $\check{p}^{\text{sct},(2)}(\mathbf{x}_T^R, x_3^R; \mathbf{x}_T^S, x_3^S)$.
8. Calculate the interaction integral $\check{I}^{\text{conv}}(x_3^{\text{tl}}; \mathbf{x}^R, \mathbf{x}^S)$ of Eq. (6.31), at x_3^{tl} , using Eq. (10.8).

A deviation of the true monitor model from the estimated monitor model leads to, using steps (6) and (7), an incorrect estimation of the monitor incident and scattered wave fields. This causes residual difference reflection energy, associated with the time-lapse contrasts in the medium parameters above the interaction depth x_3^{tl} . By updating the estimated monitor model, in steps (6) and (7), towards the true monitor model, we minimize the difference reflection energy. Application of the correct monitor model yields vanishing difference reflection energy, associated with the time-lapse contrasts in the medium parameters above the interaction depth x_3^{tl} , as is exemplified by Figs. (10.4) to (10.7).

9. Minimize difference reflection energy, associated with the time-lapse contrasts in the medium parameters above the interaction depth x_3^{tl} , by repeating steps (6), (7) and (8), using updating of the monitor model estimate towards the true monitor model.
10. Repeat steps (4) to (9) for subsequent depth levels, until below deepest time-lapse contrast, using the semi-group property of the extrapolation operator (9.19), resulting in a top-down recursive approach.

The previous steps yield an estimate of the unknown monitor model. The scheme depends on a sufficient accurate knowledge of the reference model. Depending on the uncertainty in the reference model, it might also be necessary to update the reference model. The estimated model(s) are used in the following steps to image the difference reflectivity.

11. Calculate the symplectic eigenvalue operator $\check{\mathcal{Y}}^{\text{tl}}$ using Eqs. (10.118), (10.119) and (10.120).
12. Deconvolve \check{I}^{conv} with the source signature \check{q} , according to Eqs. (6.37) and (10.102), to obtain $\hat{p}^{\text{dif},u}(\mathbf{x}_T^R, x_3^R; \mathbf{x}_T^S, x_3^S)$.

13. Calculate the down-going wave field component $\check{p}^{d,(2)}(\mathbf{x}_T^R, x_3^{tl}; \mathbf{x}_T^S, x_3^S)$, according to Eq. (10.104), by downward extrapolation of $\check{q}(\check{\mathcal{Y}}^{tl})^{-1}\delta(\mathbf{x}_T - \mathbf{x}_T^S)$, using $\check{\mathcal{W}}^{q,tl,(2)}(x_3^{tl}, x_3^S)$, through a medium parameterised by $\rho^{b,(2)}$ and $\check{\mathcal{Y}}^{tl}$.
14. Calculate the up-going difference wave field $\check{p}^{dif,u}(\mathbf{x}_T^R, x_3^{tl}; \mathbf{x}_T^S, x_3^S)$, according to Eq. (10.105), by downward extrapolation of $\check{p}^{dif,u}(\mathbf{x}_T^R, x_3^R; \mathbf{x}_T^S, x_3^S)$, using $\check{\mathcal{W}}^{q,tl,(1)}(x_3^{tl}, x_3^R)$, through a medium parameterised by $\rho^{b,(1)}$ and $\check{\mathcal{Y}}^{tl}$.
15. Estimate the kernel $\Delta\hat{R}^{tl}(\mathbf{x}_T^R, x_3^{tl}; \mathbf{x}_T^S, x_3^{tl})$ by inverting Eq. (10.106), using the results of steps (13) and (14).
16. Obtain angle-dependent difference reflectivity by applying a double Radon transform to $\Delta\hat{R}^{tl}(\mathbf{x}_T^R, x_3^{tl}; \mathbf{x}_T^S, x_3^{tl})$, with respect to the transverse receiver and source coordinates, \mathbf{x}_T^R and \mathbf{x}_T^S , respectively, and by subsequently applying the imaging condition, which amounts to an integration with respect to the frequency coordinate (see e.g. de Bruin et al. (1990)).

In Fig. (10.8) a numerical imaging example is shown, using steps (1) to (8), and steps (11) to (16), for a range of depth levels, using the model of Fig. (10.2), and the reference and monitor parameters of Table (10.1). Because the reference and monitor parameters are known the inversion update steps (9) and (10) are excluded. The forward and inverse extrapolation operators are calculated, using Eqs. (10.156) and (10.157), recursively, valid for a piece-wise depth-invariant medium. Fig. (10.8) shows the kernel $\Delta\hat{R}^{tl}$ as a function of horizontal ray parameter (Radon transform parameter dual to the horizontal receiver coordinate) and depth. Clearly, the temporal contrasts in layers 1, 3, and 5 are imaged as a function of horizontal ray parameter. In Fig. (10.9) the difference reflectivity at zero horizontal ray parameter (normal incidence) is shown. In Fig. (10.10) the difference reflectivity as a function of horizontal ray parameter, at a depth of 100 m, is depicted. The high values beyond $\pm 1 \times 10^{-4}$ are associated with evanescent waves.

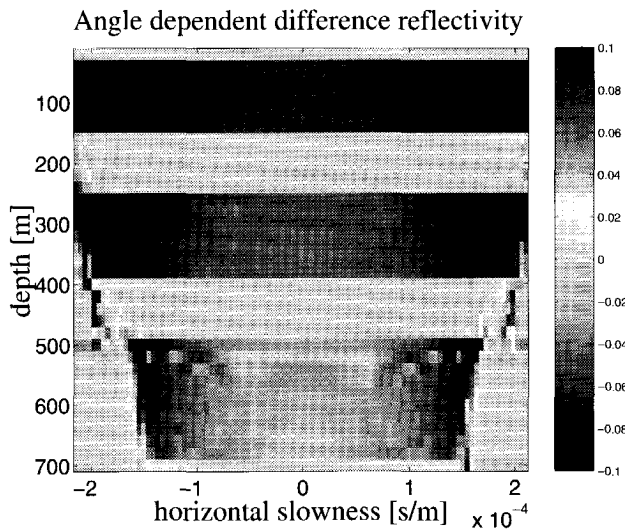


Figure 10.8: Imaged kernel of the difference reflection operator $\hat{\Delta}R^{\text{tl}}$ as a function of horizontal ray parameter and depth.

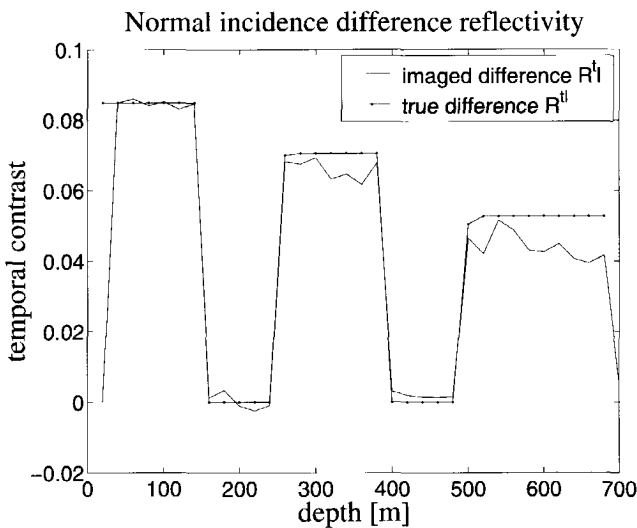


Figure 10.9: Difference reflectivity at zero horizontal ray parameter (normal incidence).

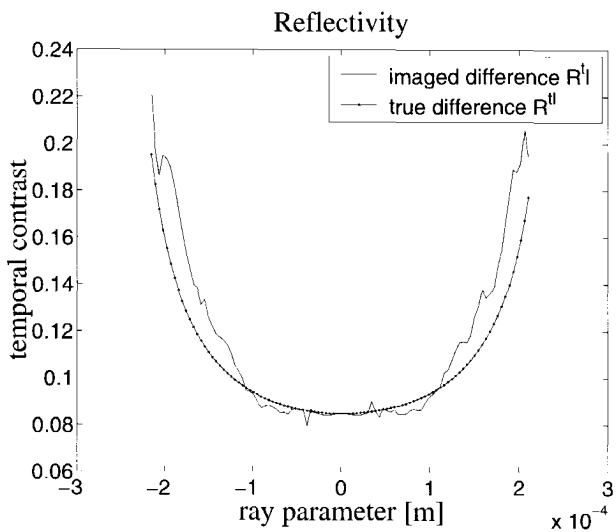


Figure 10.10: *The difference reflectivity as a function of horizontal ray parameter, at a depth of 100 m depth.*

10.8 Discussion

A recursive pre-stack processing scheme has been proposed, based on the full acoustic wave equation, for time-lapse datasets, involving reference wave fields, travelling through a reference medium, and monitor wave fields, which propagate through a monitor medium. To this end a boundary integral of the time-convolution type is employed which represents an up-going difference wave field, originating from temporal contrast sources below the boundary, at which this integral is evaluated. The up-going difference wave field is the temporal analogue of the up-going scattered wave field, which originates from spatial contrast sources.

The reflection operator is derived which, quantifying the scattering process, relates an up-going scattered wave field to a down-going incident wave field. This spatial scattering formalism is set in terms of spatial contrasts between a computational background medium and the actual medium. By comparison, the time-lapse scattering formalism, in terms of a difference reflection operator, uses temporal contrasts between the two actual reference and monitor media.

The reference and monitor wave fields, in the integrand of the boundary integral of the time-convolution type, are determined using computational background media, based on partial and insufficient knowledge of the actual media. The interaction of two actual wave fields is considered. This in contradistinction to spatial scattering formalisms, in which an actual measurement wave field interacts with a smooth computational wave field. For this reason may expect that with time-lapse seismic measurements a higher resolution can be attained than in single seismic measurements.

From the difference reflection operator, changes in the compressional-wave velocity or compressibility, and the density can be inferred. Using a suitable parametrization one could linearize this inversion, e.g. for small temporal contrasts, and carry out an AVO-type analysis. For stress inference one ideally needs a scheme based on elastodynamic waves in an anisotropic medium. The wave-vector formalism can be generalized, see e.g. de Hoop and de Hoop (1994), in terms of elastodynamic wave field quantities and anisotropic elastic moduli. The compressional- and shear-wave velocities inferred from such a scheme can be input to a stress-inversion scheme. For this we can use results from ultrasonic experiments, as are shown in the first part of this thesis. All under the assumption that we are able to translate the scaled experiments to the in-situ stress conditions.

Appendix A

Notations and conventions

In this thesis we consider the three-dimensional space \mathbb{R}^3 equipped with an Euclidean metric. Within this space a standard measuring rod is defined with respect to a Cartesian reference frame, consisting of three mutually perpendicular base vectors, $\{\mathbf{i}_1, \mathbf{i}_2, \mathbf{i}_3\}$, which form a right-handed system. A position in space, denoted by the vector \mathbf{x} , is specified by the Cartesian coordinates $\{x_1, x_2, x_3\}$, written as $\mathbf{x} = (x_1, x_2, x_3)$, and given by

$$\mathbf{x} = x_1 \mathbf{i}_1 + x_2 \mathbf{i}_2 + x_3 \mathbf{i}_3. \quad (\text{A.1})$$

To discriminate between the transverse direction, specified by the coordinates $\{x_1, x_2\}$, and the longitudinal direction, specified by the coordinate x_3 , the position vector is also denoted by $\mathbf{x} = (\mathbf{x}_T, x_3)$, with the transverse coordinate given by

$$\mathbf{x}_T = x_1 \mathbf{i}_1 + x_2 \mathbf{i}_2. \quad (\text{A.2})$$

We make use of Einstein summation convention and write

$$\mathbf{x}_T = x_\alpha \mathbf{i}_\alpha \quad \text{and} \quad \mathbf{x} = x_i \mathbf{i}_i, \quad (\text{A.3})$$

in which a repeated lower-case Greek subscript takes the values $\{1, 2\}$, and a repeated lower-case Latin subscript takes the values $\{1, 2, 3\}$. Time is given in the one-dimensional space \mathbb{R} , specified by the coordinate $\{t\}$ with respect to a standard clock, and denoted by t .

Appendix B

Integral transformations

In this appendix the one-sided Laplace transform pair with respect to time, of functions which represent causal or anti-causal wave fields, is introduced. Additionally, the Laplace-Fourier transform pair with respect to the time and transverse coordinates is given.

B.1 Laplace transform with respect to time

B.1.1 Causal wave fields

Consider a space-time wave field, $p(\mathbf{x}, t)$, originating from a source which excites at time $t = 0$. Because the wave field is causally related to the action of the source, we have the following causality condition

$$p(\mathbf{x}, t) = 0, \quad t < 0. \quad (\text{B.1})$$

The one-sided Laplace transform with respect to time of a causal space-time wave field $p(\mathbf{x}, t)$ is defined by

$$\hat{p}(\mathbf{x}, s) = \int_0^{\infty} \exp(-st) p(\mathbf{x}, t) dt, \quad \text{Re}(s) > 0, \quad (\text{B.2})$$

with the Laplace transform parameter $s \in \mathbb{C}$. The function $\hat{p}(\mathbf{x}, s)$ is regular in the right half-plane $\text{Re}(s) > 0$. The condition $\text{Re}(s) > 0$, together with the boundedness of the wave field $p(\mathbf{x}, t)$, ensures that the Laplace transform is a converging integral, which, when regarded as an integral equation, for a given $\hat{p}(\mathbf{x}, s)$, produces as a solution an unique space-time function $p(\mathbf{x}, t)$,

which vanishes for $t < 0$. Due to the analyticity of the Laplace transform kernel $\exp(-st)$, $\hat{p}(\mathbf{x}, s)$ is an analytic function in the region of convergence $\text{Re}(s) > 0$, see Widder (1946) and de Hoop (1995)[p. 1050]. Using the causality condition of Eq. (B.1) the Laplace transform integral is extended over the entire real line, according to

$$\hat{p}(\mathbf{x}, s) = \int_{t \in \mathbb{R}} \exp(-st) p(\mathbf{x}, t) dt, \quad \text{Re}(s) > 0. \quad (\text{B.3})$$

To be able to express the Laplace transform in terms of a Fourier transform s is separated into its real and imaginary parts,

$$s = j\omega + \epsilon, \quad \omega, \epsilon \in \mathbb{R}, \quad \epsilon > 0. \quad (\text{B.4})$$

Substituting this last definition for s into the Laplace transform of Eq. (B.3), we obtain

$$\hat{p}(\mathbf{x}, s) = \int_{t \in \mathbb{R}} \exp(-j\omega t) [\exp(-\epsilon t) p(\mathbf{x}, t)] dt, \quad \epsilon > 0, \quad (\text{B.5})$$

which constitutes a Fourier transform of the function $\exp(-\epsilon t)p(\mathbf{x}, t)$. Taking the limit $\epsilon \rightarrow 0$, we obtain

$$\lim_{\epsilon \rightarrow 0} \hat{p}(\mathbf{x}, s) = \hat{p}(\mathbf{x}, j\omega) = \check{p}(\mathbf{x}, \omega), \quad (\text{B.6})$$

in which $\check{p}(\mathbf{x}, \omega)$ is introduced for symbolic convenience and represents the Fourier transform of $p(\mathbf{x}, t)$.

The inverse Laplace transform is given by

$$p(\mathbf{x}, t) = \frac{1}{2\pi j} \int_{\epsilon-j\infty}^{\epsilon+j\infty} \exp(st) \hat{p}(\mathbf{x}, s) ds, \quad \epsilon > 0. \quad (\text{B.7})$$

Again, separating the real and imaginary parts of the Laplace parameter s , we can rewrite the inverse Laplace transform as

$$p(\mathbf{x}, t) = \exp(\epsilon t) \frac{1}{2\pi} \int_{\omega \in \mathbb{R}} \exp(j\omega t) \hat{p}(\mathbf{x}, s) d\omega, \quad (\text{B.8})$$

which constitutes an inverse Fourier transform of $\hat{p}(\mathbf{x}, s)$, multiplied by the real exponential function $\exp(\epsilon t)$.

B.1.2 Anti-causal wave fields

Consider an anti-causal space-time wave field $p^a(\mathbf{x}, t)$, anti-causally related to a source which excites at $t = 0$, which satisfies the following anti-causality condition

$$p^a(\mathbf{x}, t) = 0, \quad t > 0. \quad (\text{B.9})$$

The one-sided Laplace transform with respect to time of $p^a(\mathbf{x}, t)$ is given by

$$\hat{p}^a(\mathbf{x}, s^a) = \int_{-\infty}^0 \exp(-s^a t) p^a(\mathbf{x}, t) dt, \quad \text{Re}(s^a) < 0, \quad (\text{B.10})$$

in which s^a is the Laplace transform parameter and the function $\hat{p}^a(\mathbf{x}, s^a)$ is regular for the left half-plane $\text{Re}(s^a) < 0$. The Laplace transform parameter s^a is taken as

$$s^a = j\omega - \epsilon^a, \quad \omega, \epsilon^a \in \mathbb{R}, \quad \epsilon^a > 0. \quad (\text{B.11})$$

Substituting this last definition for s^a into the Laplace transform of Eq. (B.10), and using the anti-causality condition of Eq. (B.9), such that the integration is extended over the entire real line, we obtain

$$\hat{p}^a(\mathbf{x}, s^a) = \int_{t \in \mathbb{R}} \exp(-j\omega t) [\exp(\epsilon^a t) p^a(\mathbf{x}, t)] dt, \quad \epsilon^a > 0, \quad (\text{B.12})$$

which constitutes a Fourier transformation of the function $\exp(\epsilon^a t) p^a(\mathbf{x}, t)$. Using Eq. (B.5) we have

$$\hat{p}(\mathbf{x}, -s^a) = \int_{t \in \mathbb{R}} \exp(j\omega t) [\exp(-\epsilon^a t) p(\mathbf{x}, t)] dt, \quad \epsilon^a > 0. \quad (\text{B.13})$$

Suppose that an anti-causal wave field can be obtained by a time-reversal operation on a causal wave field according to

$$p^a(\mathbf{x}, t) = p(\mathbf{x}, -t). \quad (\text{B.14})$$

Applying time-reversal Eq. (B.13) can be rewritten as,

$$\hat{p}(\mathbf{x}, -s^a) = \int_{t \in \mathbb{R}} \exp(-j\omega t) [\exp(\epsilon^a t) p^a(\mathbf{x}, t)] dt, \quad \epsilon^a > 0. \quad (\text{B.15})$$

Hence, Eqs. (B.12) and (B.15) yields

$$\hat{p}^a(\mathbf{x}, s^a) = \hat{p}(\mathbf{x}, -s^a), \quad s^a = j\omega - \epsilon^a, \quad \epsilon^a > 0, \quad (\text{B.16})$$

(Fokkema and van den Berg (1993) and de Hoop (1995)). Because of Eq. (B.14) we can choose $\epsilon = \epsilon^a$, with ϵ given in Eq. (B.4). Hence, Eq. (B.12) can be rewritten as,

$$\hat{p}^a(\mathbf{x}, s^a) = \int_{t \in \mathbb{R}} \exp(-j\omega t) [\exp(\epsilon t) p(\mathbf{x}, -t)] dt, \quad \epsilon > 0. \quad (\text{B.17})$$

Using time-reversal of the right-hand side of Eq. (B.17) this equation can be written as

$$\hat{p}^a(\mathbf{x}, s^a) = \left\{ \int_{t \in \mathbb{R}} \exp(-j\omega t) [\exp(-\epsilon t) p(\mathbf{x}, t)] dt \right\}^*, \quad \epsilon > 0, \quad (\text{B.18})$$

where the star superscript denotes complex conjugation. Using Eq. (B.5) we obtain

$$\hat{p}^a(\mathbf{x}, s^a) = \hat{p}^*(\mathbf{x}, s), \quad \begin{cases} s &= j\omega + \epsilon \\ s^a &= j\omega - \epsilon \end{cases}, \quad \epsilon > 0. \quad (\text{B.19})$$

Taking the limit $\epsilon \rightarrow 0$ in Eqs. (B.16) and (B.19), as in Eq. (B.6), we have

$$\check{p}^a(\mathbf{x}, \omega) = \check{p}(\mathbf{x}, -\omega) = \check{p}^*(\mathbf{x}, \omega). \quad (\text{B.20})$$

B.1.3 Partial differentiation with respect to time

The Laplace transform of the partial derivative with respect to time of a causal wave field p , $\partial_t p$, is obtained by means of partial integration as

$$\begin{aligned} & \int_0^\infty \exp(-st) \partial_t p(\mathbf{x}, t) dt \\ &= \exp(-st) p(\mathbf{x}, t) \Big|_{0+}^\infty + s \int_0^\infty \exp(-st) p(\mathbf{x}, t) dt \\ &= -p(\mathbf{x}, 0+) + s \hat{p}(\mathbf{x}, s). \end{aligned} \quad (\text{B.21})$$

The term $-p(\mathbf{x}, 0+)$ accounts for the presence of a discontinuity at $t = 0$, when passing the instant $t = 0$ in the direction of increasing t (Fokkema and van den Berg (1993)[p. 19]). Hence, for vanishing $p(\mathbf{x}, 0+)$, differentiation with ∂_t in the time domain is equivalent to multiplication with s in the complex-frequency domain.

B.2 Spatial Fourier transformation

The three-dimensional Fourier transform, with respect to the spatial coordinate vector \mathbf{x} , is defined as

$$\bar{p}(\mathbf{k}, s) = \int_{\mathbf{x} \in \mathbb{R}^3} \exp(jk_q x_q) \hat{p}(\mathbf{x}, s) d\mathbf{x}. \quad (\text{B.22})$$

The inverse transform of Eq. (B.22) is obtained as

$$\hat{p}(\mathbf{x}, s) = \frac{1}{(2\pi)^3} \int_{\mathbf{k} \in \mathbb{R}^3} \exp(-jk_m x_m) \bar{p}(\mathbf{k}, s) d\mathbf{k}. \quad (\text{B.23})$$

The two-dimensional spatial Fourier transform, with respect to the transverse coordinate vector \mathbf{x}_T , is defined as

$$\tilde{p}(\mathbf{k}_T, x_3, s) = \int_{\mathbf{x}_T \in \mathbb{R}^2} \exp(jk_\alpha x_\alpha) \hat{p}(\mathbf{x}_T, x_3, s) d\mathbf{x}_T, \quad (\text{B.24})$$

in which the the argument list of the space-domain function and its transform is adjusted to distinguish between the transverse and longitudinal directions. The inverse transform of Eq. (B.24) is given by

$$\hat{p}(\mathbf{x}_T, x_3, s) = \frac{1}{(2\pi)^2} \int_{\mathbf{k}_T \in \mathbb{R}^2} \exp(-jk_\alpha x_\alpha) \tilde{p}(\mathbf{k}_T, x_3, s) d\mathbf{k}_T. \quad (\text{B.25})$$

B.2.1 Partial differentiation with respect to the spatial coordinates

Partial differentiation of the Laplace transformed wave field \hat{p} with respect to the m th spatial coordinate is given by

$$\int_{\mathbf{x} \in \mathbb{R}^3} \exp(jk_q x_q) \partial_m \hat{p}(\mathbf{x}, s) d\mathbf{x} = -jk_m \bar{p}(\mathbf{k}, s). \quad (\text{B.26})$$

Hence, partial differentiation in the spatial domain with the operator ∂_m is, in the wave-number domain, equivalent to multiplication with $-jk_m$.

Bibliography

Abraham, Ralph and Marsden, Jerrold E. *Foundations of Mechanics*. The Benjamin/Cummings publishing company, inc., second edition, 1978.

Aki, K. and Richards, P. G. *Quantitative seismology*. W. H. Freeman and Company, New York, 1980.

Al-Chalabi, M. and Huang, C. L. Stress distribution within circular cylinders in compression. *Int. J. Rock Mech. Sci. & Geomech. Abstr.*, 11:451–455, 1974.

Atkinson, B. K. Subcritical crack growth in geological materials. *J. Geophys. Res.*, 89:4077–4114, 1984.

Barends, F. B. J., van der Poel, J. T., and Teunissen, J. A. M. Geomechanical simulation of static and dynamic subsidence by reservoir compaction. In *Proc. Fifth Int. Symposium on Land Subsidence*, pages 237–245, The Hague, Netherlands, 1995.

Beishuizen, Jeroen. A proposal for 4-d seismic imaging. Master's thesis, Delft University of Technology, Department of Applied Geosciences, 1997. TA/TG 1997-07.

Berkhout, A. J. *Seismic migration: Imaging of acoustic energy by wave field extrapolation*. Elsevier, 1985.

Biot, M. A. General theory of 3-dimensional consolidation. *J. Appl. Phys.*, 12:155–164, 1941.

Biot, M. A. Theory of propagation of elastic waves in a fluid saturated porous solid i, low-frequency range. *J. Acoust. Soc. Am.*, 28:168–178, 1956a.

Biot, M. A. Theory of propagation of elastic waves in a fluid saturated porous solid ii, high-frequency range. *J. Acoust. Soc. Am.*, 28:179–191, 1956b.

Birch, F. The velocity of compressional waves in rocks to 10 kilobars , part 1. *Journal of geophysical research*, 65(4):1083–1102, 1960.

den Boer, E. G. The effect of stress on wave propagation in aeolian rotliegend sandstone. Master’s thesis, Delft University of Technology, Department of Applied Geosciences, 1996. MP/TG 1996-01.

den Boer, E. G., Dillen, M. W. P., Duijndam, A. J. W., and Fokkema, J. T. The effect of stress on wave propagation in aeolian rotliegend sandstone. In *EAGE 58th Conference and Technical Exhibition, Extended abstracts*, volume 1, page P071, Amsterdam, The Netherlands, 1996.

den Boer, E. G. and Fokkema, J. T. Scaling propagation phenomena as result of an externally applied isotropic stress on an aeolian rotliegend sandstone sample. In *SEG International Exposition and 66th Annual Meeting, Expanded abstracts*, volume 2, pages 1703–1706, Denver, Colorado, 1996.

Bojarski, N. N. Generalized reaction principles and reciprocity theorems for the wave equations, and the relationship between the time-advanced and time-retarded fields. *J. Acoust. Soc. Am.*, 74(1):281–285, 1983.

Brody, T. *The philosophy behind physics*. Springer-Verlag, 1993.

de Brouwere, L. J. Repeatability in time-lapse seismic monitoring. Master’s thesis, Delft University of Technology, Department of Applied Geosciences, 1998. TA/TG 1998-07.

Brown, R. and Korringa, J. On the dependence of the elastic properties of a porous rock on the compressibility of the pore fluid. *Geophysics*, 40: 608–616, 1975.

de Bruin, C. G. M., Wapenaar, C. P. A., and Berkhouit, A. J. Angle dependent reflectivity by means of prestack migration. *Geophysics*, 55:1223–1234, 1990.

Carroll, M. M. An effective stress law for anisotropic elastic deformation. *Journal of Geophysical Research*, 84:7510–7512, 1979.

Chen, Q. and Nur, A. Pore fluid pressure effects in anisotropic rocks: mechanisms of induced seismicity and weak faults. *Pure and applied geophysics*, 139(3/4):463–479, 1992.

Colton, D. and Kress, R. *Integral equation methods in scattering theory*. John Wiley & Sons, 1983.

Crampin, S. Effective anisotropic elastic constants for wave propagation through cracked solids. *Journal Royal Astronomical Society*, 76:133–145, 1982.

Crampin, S., Evans, R. S., and Atkinson, B. K. Earthquake prediction: a new physical basis. *Geophys. J. R. astr. Soc.*, 76:147–156, 1984.

Cruts, H. M. A. Experimental verification of stress-induced anisotropy. Master’s thesis, Delft University of Technology, Department of Applied Geosciences, 1995. MP/TG 1995-05.

Cruts, H. M. A., Groenenboom, J., Duijndam, A. J. W., and Fokkema, J. T. Experimental verification of stress-induced anisotropy. *Expanded abstracts, 65th SEG meeting, Houston*, pages 894–897, 1995.

van Dam, D. B. and de Pater, C. J. Influence of boundary conditions on the stress situation in true triaxial block tests. Technical Report TA/PF/97.014, Delft University of Technology, Department of applied Geosciences, 1995.

Dillen, M. W. P., Cruts, H. M. A., Groenenboom, J., Fokkema, J. T., and Duijndam, A. J. W. Ultrasonic velocity and shear-wave splitting behavior of a colton sandstone under a changing triaxial stress. *Geophysics*, pages 1603–1607, 1999.

Dillen, M. W. P., Fokkema, J. T., and Wapenaar, C. P. A. Convolution type interaction of time-lapse acoustic wave fields. In *SEG International Exposition and 66th Annual Meeting, Expanded abstracts*, volume 2, pages 0–0, Calgary, Canada, 2000.

Evans, R. Anisotropy: a pervasive feature of fault zones? *Geophys. J. R. astr. Soc.*, 76:157–163, 1984.

Fabre, D., Grasso, J. R., and Orengo, Y. Mechanical behaviour of deep rock core samples from a seismically active gas field. *Pure and applied geophysics*, 137(3):201–219, 1991.

Fokkema, J. T. Personal communications, 1993.

Fokkema, J. T. and van den Berg, P. M. *Seismic Applications of Acoustic Reciprocity*. Elsevier, 1993.

Fokkema, J. T., Wapenaar, C. P. A., and Dillen, M. W. P. Reciprocity theorems for time-lapse seismics. In *6th SBGf meeting, 325*, Rio de Janeiro, 1999.

Fung, Y.C. *Foundations of solid mechanics*. Prentice-Hall, New Jersey, 1965.

Gassmann, F. Über die elastizität poroser medien. *Vierteljahrsschr. der Naturforsh. Ges. Zürich*, 96:1–23, 1951.

Geertsma, J. The effect of fluid pressure decline on volumetric changes of porous rock. *Trans. AIME*, page 331, 1957.

Glennie, K. W., editor. *Introduction to the petroleum geology of the North Sea*, chapter 5. Blackwell Scientific Publications, third edition, 1990a.

Glennie, K. W., editor. *Introduction to the petroleum geology of the North Sea*, chapter 7. Blackwell Scientific Publications, third edition, 1990b.

Goldstein, J. A. *Semigroups of linear operators and applications*. Oxford University Press, New York, 1985.

Grasso, J. R., Fourmaintraux, D., and Maury, V. Le rôle des fluides dans les mécanismes d'instabilités de la croûte supérieure: l'exemple des exploitations d'hydrocarbures. *Bulletin de la société Géologique de France*, 163(1): 27–36, 1992.

Grimbergen, J. T. L., Dessing, F. J., and Wapenaar, C. P. A. Modal expansion of one-way operators in laterally varying media. *Geophysics*, 63: 995–1005, 1998.

Groenenboom, J. Progress report ultrasonic measurements, final report. Technical report, Delft University of Technology, Department of applied Geosciences, 1995.

Groenenboom, J. *Acoustic monitoring of hydraulic fracture growth*. PhD thesis, Delft University of Technology, 1998.

Haines, A. J. and de Hoop, M. V. An invariant embedding analysis of general wave scattering problems. *J. Math. Phys.*, 37(8):3854–3881, 1996.

Herrmann, F. J. *A scaling medium representation, a discussion on well-logs, fractals and waves*. PhD thesis, Delft University of Technology, 1997.

Hettema, M. H. H. *The thermo-mechanical behaviour of sedimentary rock: an experimental study*. PhD thesis, Delft University of Technology, 1996.

de Hoop, A. T. *Handbook of Radiation and Scattering of Waves*. Academic Press Limited, 1995.

de Hoop, M. V. *Directional decomposition of transient acoustic waves*. PhD thesis, Delft University of Technology, 1992.

de Hoop, M. V. and de Hoop, A. T. Elastic wave up/down decomposition in inhomogeneous and anisotropic media: an operator approach and its approximations. *Wave Motion*, 20:57–82, 1994.

Hubbert, M. K. and Rubey, W. W. Role of fluid pressure in mechanics of overthrust faulting. *Bull. Geol. Soc. Am.*, 70:115–205, 1959.

Hudson, J. A. Wave speeds and attenuation of elastic waves in material containing cracks. *Journal Royal Astronomical Society*, 64:133–150, 1980.

Jaeger, J. C. and Cook, N. G. W. *Fundamentals of Rock Mechanics*. Chapman and Hall, London, 1979.

Krueger, R. J. and Ochs, R. L. A green's function approach to the determination of internal fields. *Wave Motion*, 11:525–543, 1989.

Lang, S. *Algebra*. Addison-Wesley Publishing Company, third edition, 1993.

Lesne, Annick. *Renormalization methods: critical phenomena, chaos, fractal structures*. John Wiley & Sons Ltd, Chichester, England, 1998.

Lo, T., Coyner, K. B., and Toksöz, M. N. Experimental determination of elastic anisotropy of Berea sandstone, Chicopee shale, and Chelmsford granite. *Geophysics*, 51:164–171, 1986.

Main, Ian. Statistical physics, seismogenesis, and seismic hazard. *Reviews of Geophysics*, 34(4):433–462, 1996.

Maugin, Gérard A. *Material inhomogeneities in elasticity*. Chapman & Hall, 1993.

Mavko, G. M. and Nur, A. Melt squirt in the astenosphere. *J. Geophys. Res.*, 80:1444–1448, 1975.

McDonald, P. H. *Continuum mechanics*. PWS Publishing Company, Boston, 1996.

Moos, D. and Zoback, M. D. In situ studies of velocity in fractured crystalline rocks. *J. Geophys. Res.*, 88:2345–2358, 1983.

Mukerji, T. and Mavko, G. Pore fluid effects on seismic velocity in anisotropic rocks. *Geophysics*, 59:233–244, 1994.

Murphy III, W. F. Seismic to ultrasonic velocity drift: intrinsic absorption and dispersion in crystalline rock. *Geophys. Res. Lett.*, 11(12):1239–1242, 1984.

Nagelhout, A. C. G. and Roest, J. P. A. Investigating fault slip in a model of an underground gas storage facility. *Int. J. Rock Mech. & Min. Sci.*, 34 (3-4):212, 1997.

Nur, A. Effects of stress on velocity anisotropy in rocks with stress. *Journal of Geophysical Research*, 76(8):2022–2034, 1971.

Nur, A. and Simmons, G. Stress-induced velocity anisotropy in rock: an experimental study. *Journal of Geophysical Research*, 74(27):6667–6674, 1969.

Ouyang, Z. and Elsworth, D. A phenomenological failure criterion for brittle rock. *Rock mechanics and rock engineering*, 24:133–153, 1991.

Pazy, A. *Semigroups of linear operators and applications to partial differential equations*. Springer-Verlag, New York, 1983.

Plona, T. J. and Cook, J. M. Effects of stress cycles on static and dynamic young's moduli in castlegate sandstone. In Daemen&Schultz, editor, *Rock Mechanics*, pages 155–158. Balkema, Rotterdam, 1995.

Rai, Ch. S. and Hanson, K. E. Shear-wave velocity anisotropy in sedimentary rocks: A laboratory study. *Geophysics*, 53:800–806, 1988.

Rice, J. R. and Cleary, M. P. Some basic stress diffusion solutions for fluid-saturated elastic porous media with compressible constituents. *Rev. Geophys. and Space Phys.*, 14:227–241, 1976.

Roest, J. P. A. and Kuilman, W. Geomechanical analysis of small earth-quakes at the eleveld gas reservoir. In *Proc. Eurock 94 Symposium*, pages 573–580, Delft, Netherlands, 1994.

Roest, J. P. A. and Mulders, F. M. M. Overview modelling gas production-induced seismicity mechanisms. In *Proc. Eurock 2000 Symposium*, pages , Aachen, Germany, 2000.

Roest, J. P. A., Mulders, F. M. M., and Kuilman, W. Data-limited geomechanical modelling for investigating induced seismicity mechanisms. In *International Society for Rock Mechanics*, pages 1061–1064, Paris, France, 1999.

Sabatier, P. C. On the scattering by discontinuous media. In Colton, D., Ewing, R., and Rundell, W., editors, *Inverse problems in partial differential equations*, pages 85–100. SIAM, 1990.

Saucier, A. and Muller, J. Use of multifractal analysis in the characterization of geological formation. *Fractals*, 1(3):617–628, 1993.

Schutjens, P. M. T. M. Personal communications, 1996.

Schutjens, P.M.T.M. Experimental observations of the uniaxial compaction of quartz-rich reservoir rock at stresses of up to 80 mpa. In Barends and Brouwer&Schröder, editors, *Land Subsidence*, pages 389–408. Balkema, Rotterdam, 1995.

Segall, P. Induced stresses due to fluid extraction from axisymmetric reservoirs. *Pure and applied geophysics*, 139(3/4):535–560, 1992.

Skempton, A. W. Effective stress in soils, concrete, and rock. *Pore pressure and suction in soils*, page 1, 1960.

van Spaendonck, R. L. C. Pre-stack depth migration of time-lapse seismic data. Master's thesis, Delft University of Technology, Department of Applied Geosciences, 1996. TA/TG 1996-01.

Spencer, J. W. Stress relaxation at low frequencies in fluid saturated rocks: Attenuation and modulus dispersion. *J. Geophys. Res.*, 86:1803–1812, 1981.

Stuart, C. E. *Evaluation of anisotropic microcrack damage in cyclically stressed rock, characterized by contemporaneous acoustic emission and elastic wave velocity measurements*. PhD thesis, University College London, Department of Geological Sciences, 1992.

Swinnen, G. The effect of stress on wave propagation in reservoir rocks. Master's thesis, Katholieke Universiteit Leuven, Department of civil engineering, 1997.

Tao, G. and King, M. S. Shear-wave velocity and q anisotropy in rocks: a laboratory study. *Int. J. Rock Mech. Min. Sci. and Geomech. Abstr.*, 27 (5):353–361, 1990.

van Terzaghi, K. Die berechnung der durchlassigkeitsziffer des tones aus dem verlauf der hydrodynamischen spannungserscheinungen. *Sitzungsber. Akad. Wiss. Wien Math. Naturwiss. Kl. Abt. 2A*, 132:105, 1923.

van Terzaghi, K. *Theoretical Soil Mechanics*. Wiley, New York, 1943.

Todoeschuck, J. P. and Jensen, O. G. Scaling geology and seismic deconvolution. *Pure and Applied Geophysics*, 131(1/2), 1989.

Turner, P. *Continental Red Beds*. Number 29 in Developments in Sedimentology. Elsevier, Amsterdam, 1980.

Walden, A. T. and Hosken, J. W. J. An investigation of the spectral properties of primary reflection coefficients. *Geophysical Prospecting*, 33(3): 400–435, 1985.

Walker, T. R., Waugh, B., and Crone, A. J. Diagenesis in first-cycle alluvium of cenozoic age, south-western united states and north-western mexico. *Bull. Am. Geol. Soc.*, 89:19–32, 1978.

Walsh, J. B. The effects of cracks on the compressibility of rock. *Journal of geophysical research*, 70(2):381–389, 1965a.

Walsh, J. B. The effects of cracks on the uniaxial elastic compression of rocks. *Journal of geophysical research*, 70(2):399–411, 1965b.

Wang, Z. and Nur, A. Dispersion analysis of acoustic velocities in rocks. *J. Acoust. Soc. Am.*, 87(6):2384–2395, 1990.

Wapenaar, C. P. A. The infinite aperture paradox. *Journal of Seismic Exploration*, 1:325–336, 1992.

Wapenaar, C. P. A. One-way representations of seismic data. *Geophysical Journal International*, 127:178–188, 1996a.

Wapenaar, C. P. A. Reciprocity theorems for two-way and one-way wave vectors: a comparison. *J. Acoust. Soc. Am.*, 100(6):3508–3518, 1996b.

Wapenaar, C. P. A. and Berkhout, A. J. *Elastic wave field extrapolation*. Elsevier, 1989.

Weber, K. J. Personal communications, SEG-excursion guide, 1998.

Weston, V. H. Factorization of the wave equation in a nonplanar stratified medium. *J. Math. Phys.*, 29(1):36–45, 1988.

Widder, D. V., editor. *The Laplace transform*, page 243. Princeton University Press, seventh edition, 1946.

Winkler, K. W. Dispersion analysis of velocity and attenuation in berea sandstone. *J. Geophys. Res.*, 90:6793–6800, 1985.

Wyllie, M. R. J., Gregory, A. R., and Gardner, L. W. Elastic wave velocities in heterogeneous and porous media. *Geophysics*, 21:41–70, 1956.

Wyllie, M. R. J., Gregory, A. R., and Gardner, L. W. An experimental investigation of factors affecting elastic wave velocities in porous media. *Geophysics*, 23:459–493, 1958.

Summary

In this thesis the time-lapse seismic method is investigated with regard to its application in monitoring the subsurface stress. The objective is to use this method to study the temporal changes of the stress field associated with the geomechanics of an earthquake. In particular, the application towards small earthquakes, induced by fluid injection or extraction operations such as in oil and gas production, is investigated. The derived processing scheme is generic enough to be used for other time-lapse seismic problems, e.g. monitoring hydrocarbon saturation changes.

The elastodynamic response of seismic waves to a changing stress field is considered as a possible precursor to earthquakes. The major problem that must be solved is that quasi-static (large spatio-temporal scale) mechanical parameters which govern earthquake precursor mechanisms must be inferred from dynamical (small spatio-temporal scale) mechanical parameters which underlie wave propagation theory. Ultrasonic stress experiments are conducted to serve as scaled physical model studies which enable to investigate the relationship between elasto-quasi-static theory, which governs crustal deformation, and elastodynamic theory, describing seismic wave propagation.

Three series of experiments were conducted on a triaxial pressure machine, involving the Colton, the Flechtinger, the Niederhausen and the Bad Dürckheim sandstones. The machine can not apply a controlled pore pressure to the rock since it is an open system. According to the effective stress concept a decrease/increase of the fluid pressure results in an increase/decrease of the effective stress. Hence, up-/down-loading in the triaxial pressure machine simulates the effective stress during extraction/injection of fluids from a reservoir. During the experiments, phenomena such as anisotropy, hysteresis, and anelasticity are studied with respect to quasi-static finite strains (stress-strain curves) and dynamic infinitesimal strains (wave propagation).

The ultrasonic experiments show that effective stress changes lead to dis-

tinct anisotropic velocity changes in compressional-waves and shear-waves. The stress imprint can be recognized from the associated velocity pattern. The ultrasonic velocities indicate that the sensitivity of the different waves to stress predominantly depends on stresses applied in the polarization and propagation directions of the particular wave mode. Also, stress-induced changes in shear-wave splitting are observed. The wave velocity change per unit stress increment decreases with increasing effective stress, for all velocities, showing a decreasing sensitivity of ultrasonic waves to stress with increasing effective stress. Hysteresis, apparent through a different behaviour during up- and down-loading, is less significant for wave velocities than for quasi-static strains. Anelasticity, which depends on the mineralogy, appears as a permanent deformation and a permanent wave velocity increase after a first loading experiment. Depending on the anelastic effect, first up-loading wave velocities are smaller than first down-loading velocities. Dynamic elastic moduli, calculated from wave velocities, are larger than the quasi-static moduli, calculated as the tangent of stress-strain curves. Static and dynamic elastic moduli are approximately parallel during up-loading, suggesting a simple explanation which enables to relate the two moduli.

In seismic exploration the earth's elastodynamic response to an acoustic source (e.g. dynamite or air guns) is measured. Data from a multitude of such measurements are processed in order to obtain an image of the subsurface from which geological structures are identified which might enclose a hydrocarbon reservoir. Time-lapse seismic monitoring is a technique in hydrocarbon production which uses repeated seismic experiments, employing optimal time intervals, to obtain difference maps such that reservoir operations can be optimized.

With time-lapse seismic measurements one can obtain compressional- and shear-wave velocity changes induced by pore fluid pressure changes. The velocity changes appear as travel time and reflection amplitude changes in a difference seismogram. Using an integral representation of the time-convolution type, which contains in the integrand the total wave fields of the reference and the monitor states, a new difference wave field is computed, generated by temporal contrasts located below the interaction depth, at which the integral is calculated, whereas temporal contrasts above the interaction depth do not contribute to the interaction integral. This enables to obtain pure difference amplitudes at every depth level from which an image can be constructed of the temporal contrasts. The recursive annihilation of phase shifts above the interaction depth also offers an inversion scheme which aims to invert for

wave velocity changes above the interaction depth.

The integral representation of the time-convolution type constitutes a bilinear form. Substitution of the reference and monitor wave field decomposition operations, in terms of Dirichlet-to-Neumann (D-t-N) operators of the wave field components, and subsequently applying a normalization, one obtains a symplectic matrix operator with respect to this bilinear form. Assuming equality of the reference and monitor D-t-N operators of the wave field components, the matrix operator becomes alternating. In case of inequality of these D-t-N operators, application of a symplectic eigenvalue decomposition yields an alternating matrix operator. On this new basis a difference wave field can be constructed with vanishing difference reflections above the interaction depth. At the interaction depth a pure amplitude reflection is obtained while deeper reflections are dynamically corrected in contradistinction to the difference wave field constructed from the reference and monitor wave fields measured at the acquisition surface.

The implementation of the ultrasonic scale results (Part I) to the seismic scale (Part II) is discussed but not carried out. The time-lapse seismic monitoring theory in Part II is derived for acoustic waves, whereas Part I assumes elastic wave theory. The analysis in Part II is done for acoustic waves in order to keep the calculations within reasonable limits. The elastic wave theory can be derived in an analogous manner involving similar operators. The derived theory on time-lapse seismic wave fields is generic and not just applicable towards stress inference, but can handle arbitrary time-lapse problems, such as a combination of pore fluid saturation changes and effective stress changes.

Samenvatting

Het onderzoek dat in dit proefschrift beschreven wordt heeft betrekking op de in tijd herhaalde seismische methode en meer specifiek op de toepassing ervan in het meten van de ondergrondse spanningen. Het doel is om deze methode te gebruiken voor een studie van het spanningsveld en de veranderingen ervan in de tijd die gerelateerd zijn aan de geomechanica van aardbevingen. Wat vooral wordt bestudeerd is de toepassing met betrekking tot kleine aardbevingen die geïnduceerd worden door vloeistofinjectie- of extractieprocessen zoals bij olie- en gasexploitatie. Het hier afgeleide dataverwerkingsschema is voldoende algemeen om ook bij andere in de tijd veranderlijke seismische problemen gebruikt te kunnen worden, zoals het meten van de veranderingen in olie- of gassaturaties.

Het elastodynamische effect van een veranderend spanningsveld op seismische golven wordt onderzocht als een mogelijke voorbode van aardbevingen. Het grootste probleem dat opgelost moet worden is dat quasi-statische mechanische parameters (op een grote ruimte-tijd schaal), die aardbevingsmechanismen beheersen, afgeleid moeten worden uit dynamische mechanische parameters (op een kleine ruimte-tijd schaal), die ten grondslag liggen aan de golfvoorplantingstheorieën.

Drie reeksen van experimenten zijn uitgevoerd op een triaxiale drukbank met Colton, Flechtinger, Niederhausen en Bad Dürckheim zandstenen. De drukbank kan geen gecontroleerde vloeistofdruk aanbrengen aangezien het een open systeem betreft. Volgens het concept van effectieve spanning resulteert een toename/afname van de vloeistofdruk in een respectieve wijze afname/toename van de effectieve spanning. Daarom simuleert de toename/afname van de belasting in de triaxiale drukbank de effectieve spanning tijdens extractie/injectie van vloeistoffen uit/in een reservoir. Gedurende de experimenten worden fenomenen zoals anisotropie, hysterese en inelasticiteit bestudeerd met betrekking tot quasi-statische eindige rek (spannings-

rekcurves) en dynamische infinitesimale rek (golfvoorplanting).

De ultrasone experimenten laten zien dat veranderingen in de effectieve spanning leiden tot duidelijke anisotrope snelheidsveranderingen in druk- en schuifgolven. De spanningstoestand kan herkend worden aan de hand van het bijbehorende snelheidspatroon. De ultrasone snelheden wijzen erop dat de gevoelighed van verschillende golven op de spanning voornamelijk afhangt van de spanningen aangebracht in de polarisatie- en voorplantingsrichtingen van de specifieke golfvorm. Ook spanningsgeïnduceerde veranderingen in de splitsing van schuifgolven zijn waargenomen. De ratio tussen de verandering van de golfsnelheid en de toename van spanning neemt voor alle snelheden af met een toenemende effectieve spanning, en laat dus een afnemende gevoelighed van ultrasone golven voor de spanning zien bij het toenemen van de effectieve spanning. Hysterese, zichtbaar door verschillend gedrag tijdens het vergroten en verkleinen van de belasting, is minder significant voor golfsnelheden dan voor quasi-statische rek. Inelasticiteit, die afhangt van de mineralogie, blijkt uit een permanente deformatie en golfsnelheidstoename na een eerste belastingsexperiment. Afhankelijk van het inelastische effect, zijn de golfsnelheden, voor een bepaalde eerste spanningsbelasting, bereikt door een toename van de belasting kleiner dan na een afname van de belasting. Dynamische elastische moduli berekend uit golfsnelheden, zijn groter dan quasi-statische moduli, berekend als de raaklijn aan spannings-rekcurves. Statische en dynamische elastische moduli lopen bij benadering parallel tijdens een toename van de belasting. Dit suggereert dat er een eenvoudige verklaring bestaat hoe deze twee moduli aan elkaar gerelateerd zijn.

In seismische exploratie wordt de elastodynamische respons van de aarde ten gevolge van een akoestische bron (bijvoorbeeld dynamiet of airguns) gemeten. Gegevens van zeer vele van dat soort metingen worden verwerkt om een beeld van de ondergrond te verkrijgen. Het doel is de geologische structuren te bepalen die een olie- of gasreservoir zouden kunnen bevatten. 'Time-lapse seismic monitoring' (het monitoren m.b.v. in tijd herhaalde seismiek) is een techniek, die gebruikt maakt van, na bepaalde optimale periodes herhaalde, seismische experimenten, om veranderingen in kaart te brengen zodat de produktie van olie of gas uit het reservoir geoptimaliseerd kan worden.

Met time-lapse seismische experimenten kan men druk- en schuifgolfsnelheidsveranderingen opsporen die het gevolg zijn van veranderingen in de vloeistofdruk in de poriën. De snelheidsveranderingen manifesteren zich als veranderingen in de looptijden en reflectie-amplitudes in verschilseis-

mogrammen. Gebruikmakend van een integraalrepresentatie van het tijd-convolutie type, dat in de integrant de totale golfvelden van de referentie- en herhalingstoestanden bevat, wordt een nieuw verschilgolfveld berekend, dat voortkomt uit temporele contrastbronnen onder het interactie-niveau waarop de integraal wordt berekend, terwijl contrasten boven dit niveau niet bijdragen aan de integraal. Dit maakt het mogelijk dat op ieder diepteniveau zuivere verschilamplitudes verkregen kunnen worden, zodat uiteindelijk een totaalbeeld van de temporele contrasten opgebouwd kan worden. De recursieve verwijdering van fasedraaiingen boven het interactieniveau geeft ook de mogelijkheid van een inversie schema met als doel het inverteren voor de veranderingen in de golfsnelheden boven dat niveau.

De integraalrepresentatie van het tijd-convolutie type vormt een bi-lineaire vorm. Substitutie van de ontbindingsoperaties van de referentie- en herhalingsgolfvelden in termen van Dirichlet-naar-Neumann (D-n-N) operatoren van de golfveld componenten, en hierna een normalisatie, geeft een symplectische matrix operator met betrekking tot die bi-lineaire vorm. Dit wordt een alternerende matrix operator als we aannemen dat de referentie en herhalings D-n-N operatoren van de golfveld componenten gelijk zijn. In het geval van ongelijkheid van deze D-n-N operatoren, leidt het toepassen van een symplectische eigenwaardenontbinding tot een alternerende matrix operator. Op deze nieuwe basis kan een verschilgolfveld gemaakt worden uit verschilreflecties die verdwijnen boven het interactie niveau. Op dit niveau verkijgt met een zuivere amplitude reflectie terwijl de diepere reflecties op een dynamische manier gecorrigeerd worden, in tegenstelling tot het verschilgolfveld dat gemaakt wordt uit de referentie- en herhalingsgolfvelden gemeten op het acquisitie oppervlak.

De transformatie van de resultaten van de ultrasone schaalexperimenten (Deel I) naar de seismische schaal (Deel II) wordt besproken maar is niet geïmplementeerd. De time-lapse seismische theorie in Deel II is afgeleid voor akoestische golven, terwijl Deel I de theorie van elastische golven aanneemt. De analyse in Deel II is gedaan voor akoestische golven om de omvang van de berekeningen binnen de perken te houden. De elastische golftheorie kan op een vergelijkbare manier afgeleid worden met gebruikmaking van eenzelfde soort operatoren. De afgeleide theorieën met betrekking tot time-lapse seismische golfvelden zijn zeer algemeen en ook toepasbaar buiten het bepalen van alleen spanningen. Zij kunnen arbitraire time-lapse problemen aan, zoals een combinatie van saturatieveranderingen van de porievloeistof en effectieve spanningsveranderingen.

Acknowledgement

I thank Prof. Fokkema for confiding in me and giving me freedom to explore after setting the original boundaries. His scientific insights were always a valuable challenge to whatever I came up with. I also thank Prof. Wapenaar for his significant contributions and his meticulous proof-reading. I acknowledge the assistance of Adri Duijndam for trying to keep my research within practical bounds. I thank the members of the Ph.D. committee for their contributions. I thank the former M.Sc. students Helma Cruts, Evert den Boer, Rutger van Spaendonck, Gerd Swinnen, Gerald Breimer, Jeroen Beishuizen, and Leen de Brouwere, who contributed to this thesis. I thank Peter Schutjens for providing the location of two sandstone quarries and for suggestions concerning the experiments. I thank Gerard Diephuis for providing data and advice concerning seismic reservoir modelling. I thank Hans Roest for providing his expertise on geomechanics and stress experiments. With regard to the technical support, I thank Rob Witting and Gerard Mathu for assisting with the tri-axial pressure machine, Leo de Groot for his help with the repeatability experiments, Remco Romijn and Dirk Jan van Dam for their help with the ultrasonic data acquisition and processing, and Arno Mulder and Wim Verwaal for their help with the core experiments. I thank Karl Heinz Wolf and Ruud Ephraim for their help with the thin sections. I thank my room mates Michel Schonewille, Rob Witting, and Jeroen Goudswaard for their company and their help with many software problems. I thank Tiny van Heerden, Jacob Dillen, Betty Zwart en John Dillen for supporting me during this thesis writing. I thank Jaap Haartsen for his phone calls. And I thank Edith van den Bosch and Corinne van den Bosch for their support as paraniinfen.

Curriculum vitae

Personalia

Family name	Dillen
First names	Meindert (Menno) Wichert Dillen
Date of birth	august 11th 1966
Nationality	Dutch

Education

1978-1984	Secondary school VWO Harderwijk, The Netherlands
1984-1992	M.Sc. Delft University of Technology Faculty of Mining and Petroleum Engineering Section of Applied Geophysics Delft, The Netherlands

Employment

Position	Ph.D. student
Duties	Research in lithologic inversion Software development
Supervisor	Prof. A. J. Berkhou

apr 1995 - may 1999	Delft University of Technology Faculty of Applied Geosciences Associate Researcher in the NAM project 'Measuring earth stress buildup by seismic measurements in the time-lapse mode'
Position	
Duties	Quarterly reporting to the NAM End report in the form of a Ph.D. thesis Assisting students with M.Sc. thesis
Supervisor	Prof. J. T. Fokkema
juli 1998 - sep 1998	Amoco Houston
Position	Intern in Gulf of Mexico subsalt team
Duties	Ray trace modelling of base of salt seismic amplitudes
jun 1999 - aug 2001	Delft University of Technology Subfaculty of Applied Physics Postdoc in STW project 'Acoustic wave propagation in self-similar media and its application to seismic imaging'
Position	
Duties	Research
Supervisor	Prof. C. P. A. Wapenaar

